UNIVERSIDAD DE CHILE

FACULTAD DE CIENCIA FÍSICAS Y MATEMÁTICAS

DEPARTAMENTO DE GEOLOGÍA

COMPLEX ACTIVE FAULTING ALONG THE LIQUIÑE-OFQUI FAULT SYSTEM: THE LINK BETWEEN CRUSTAL EARTHQUAKES AND POSTGLACIAL GEOMORPHOLOGICAL IMPRINTING IN THE PATAGONIAN ANDES

TESIS PARA OPTAR AL GRADO DE DOCTOR EN CIENCIAS

MENCIÓN GEOLOGÍA

ANGELO ALEXANDER VILLALOBOS CLARAMUNT

PROFESOR GUÍA:

DR. GABRIEL EASTON VARGAS

MIEMBROS DE LA COMISIÓN:

DR. SERGIO RUIZ TAPIA

DR. RODRIGO FERNÁNDEZ VASQUEZ

DR. GREGORY DE PASCALE

SANTIAGO DE CHILE

2021

RESUMEN DE LA TESIS PARA OPTAR AL GRADO DE:
Doctor en Ciencias, Mención Geología
POR: Angelo Alexander Villalobos Claramunt
FECHA: 31/03/2021
PROF. GUÍA: Dr. Gabriel Easton Vargas

FALLAMIENTO ACTIVO COMPLEJO EN EL SISTEMA DE FALLAS LIQUIÑE-OFQUI: VINCULO ENTRE TERREMOTOS CORTICALES Y LA IMPRONTA GEOMORFOLÓGICA POSGLACIAL EN LOS ANDES PATAGÓNICOS

Esta tesis se enfoca en la comprensión del comportamiento tectónico activo del Sistema de Fallas Liquiñe-Ofqui (SFLO) tanto en la escala temporal de corto plazo como en la escala de largo plazo, durante el Cuaternario tardío, entre ~45° and ~46° S. El SFLO es un sistema de fallas intraarco de más de 1000 kilómetros de extensión, que recorre la Cordillera de Los Andes desde el centro-sur de Chile hasta el Itsmo de Ofqui frente al punto triple de la subducción de las placas tectónicas de Nazca y Antártica bajo la placa Sudamericana. Para abordar la naturaleza activa del SFLO durante tiempos post-glaciales se realizaron observaciones y toma de datos geofísicos marinos (perfiles de reflexión sísmica y batimetría), junto al levantamiento geomorfológico en el continente a lo largo de una transecta (~45,5° S) que considera tres dominios morfotectónicos en este sector de los Andes: fiordos, cordillera principal y pampas en la vertiente oriental de la cordillera.

El último evento sísmico importante en el área corresponde a la Secuencia Sísmica de Aysén de 2007, la cual comenzó el 10 de enero de 2007 con un pequeño sismo (M_L 3) a una profundidad entre 8 – 10 km, extendiéndose hasta febrero del siguiente año. Los sismos más importantes correspondieron a M_w 6.1, asociado a la Falla Quitralco, y el evento principal y más destructivo dentro de esta secuencia, de M_w 6.2, generado a lo largo de la Falla Punta Cola con ruptura del lecho marino, que gatilló inmensos deslizamientos de roca de gran volumen, de los cuales cuatro impactaron el lecho del Fiordo de Aysén, provocando destructivas olas de tsunami. Además de estas estructuras, en el área se encuentran otras fallas con potencial sismogénico como la Falla Río Cuervo. El estudio de registros similares a aquellos provocados durante el evento de 2007, permite proponer siete paleoterremotos previos de características similares, basado en el análisis paleosismológico fundamentado en el estudio de facies sísmicas y estimaciones de las tasas de sedimentación en el lecho marino del Fiordo de Aysén.

Con el fin de estimar la edad máxima de rasgos geomorfológicos y paleosismológicos subaéreos y submarinos asociables a SFLO, se presenta por primera vez una transecta de registros geológicos del último retroceso glacial en la región de estudio (45,5° S) en los Andes Patagónicos. Se estudiaron varios sectores utilizando análisis morfoestratigrafico con geocronología de radiocarbono en depósitos paraglaciales, enfocados en determinar la evolución ambiental durante las glaciaciones cuaternarias y la posición de la capa de hielo durante este período. Los resultados se interpretan como un retroceso de casquete glacial que en esta región ocurrió sincrónicamente en ambos flancos de la cordillera principal de los Andes después de 12 ka.

Se propone una estrecha relación entre tectónica y clima en la configuración geomorfológica pleistocena-holocena en los Andes Patagónicos, de modo tal que el retiro del casquete glacial luego de la Última Glaciación, habría generado un rebote glacio-isostático el cual provocó una reestructuración de la carga de esfuerzo estático a niveles de la corteza superior, favoreciendo la morfogénesis y los procesos sismogénicos en el SFLO, en particular. Sin embargo, esto sería un proceso secundario sobreimpuesto al proceso mayor según el cual la corteza inferior transfiere esfuerzo tectónico a la corteza superior, generando la transcurrencia dextral que caracteriza dominantemente a este sistema de fallas, tal como ocurrió en el caso de la secuencia sísmica del año 2007 en el Fiordo de Aysén.

PHD THESIS ABSTRACT:
PhD in Geological Sciences
BY: Angelo Alexander Villalobos Claramunt
DATE: 31/03/2021
ADVISOR: Dr. Gabriel Easton Vargas

COMPLEX ACTIVE FAULTING ALONG THE LIQUIÑE-OFQUI FAULT SYSTEM: THE LINK BETWEEN CRUSTAL EARTHQUAKES AND POSTGLACIAL GEOMORPHOLOGICAL IMPRINTING IN THE PATAGONIAN ANDES

This thesis focuses on understanding the active tectonic behavior of the Liquiñe-Ofqui Fault System (LOFS) over both short-term and long-term scales between ~45° and ~46° S during postglacial times (Late Quaternary) in Chile. Field observations, acquisition of marine geophysical data (seismic reflection profiles and bathymetry) and a geomorphological survey were carried out along a transect (~45.5° S) that comprises three morphotectonic domains: the fjordland, the main Andes mountain range, and the pampas located east of the Andes. From a seismotectonic perspective the study region is situated immediately north of the Chilean triple junction, where the Nazca and Antarctic Plates subduct beneath the South American Plate. LOFS is an intra-arc fault system of more than 1,000 kilometers in length, which runs through the Cordillera de Los Andes from the Ofqui Isthmus towards the north along south-central Chile.

The most recent seismic event in the area corresponds to the 2007 Aysén Seismic Sequence, which began on January 10, 2007, with a small earthquake (M_L 3) at a depth between 8 - 10 km, extending until February of the following year. Major earthquakes corresponded to M_w 6.1, associated with Quitralco Fault, and the event considered the main and most destructive within this sequence, M_w 6.2, generated along with the Punta Cola Fault with a rupture of the seabed, which also triggered massive landslides of significant volume, of which four entered into the Aysén Fjord, causing destructive tsunami/displacement waves. Other faults with seismogenic potential are known, such as the Río Cuervo Fault, in addition to these structures. The study of records similar to those caused during the 2007 event allows proposing seven previous paleo-earthquakes with similar characteristics, based on the paleoseismological analysis supported by seismic facies features and sedimentation rates estimates.

In order to temporarily constrain the maximum age of subaerial and submarine geomorphological and paleoseismological features associated to the fault system, we realized a geomorphological transect (45.5° S) along this area of the Patagonian Andes. Several sectors were studied using a morphostratigraphic approach, and radiocarbon-based geochronology on glacial drifts focused to determine the environmental evolution during Quaternary glaciations and the position of the ice sheet during the Last Glacial Maximum, to constrain the activity of the LOFS. The results show that icesheet retreat in this region occurred synchronously on both flanks of the main mountain range after 12 ka BP.

A close relationship between tectonics and climate is proposed in the Pleistocene-Holocene geomorphological configuration in the Patagonian Andes. After the Last Ice Age, the retreat of the icesheet would have generated a glacio-isostatic rebound, which caused a restructuring of the static stress load at levels of the upper crust, favoring morphogenesis and seismogenic processes in the LOFS, in particular. However, this would be a secondary process superimposed on the broader process according to which the lower crust transfers tectonic stress to the upper crust, generating the dextral passage that dominates this fault system, as occurred in the case of the seismic sequence of the year 2007 in the Aysén Fjord.

Agradecimientos

Primero que todo, entrego mis formales agradecimientos a ANID (ex CONICYT) y su programa de Becas de Doctorado Nacional por el financiamiento de mis estudios de posgrado.

También quisiera expresar mi más sincero agradecimiento y gratitud hacia todas las personas que me han apoyado a lo largo de mis años de estudio en el Programa de Doctorado en Ciencias mención Geología. Agradezco a mis profesores de la comisión, en especial a mi profesor guía, Dr. Gabriel Easton Vargas, por su confianza y continuo apoyo desde el primer día que llegué a la Universidad de Chile a finales del año 2013 a presentarle mis intensiones de continuar mis estudios en tectónica activa. Agradezco a los profesores Sergio Ruiz, Gregory De Pascale y Rodrigo Fernández por sus correcciones y observaciones que me entregaron diferentes perspectivas que han hecho este trabajo mucho más completo y satisfactorio a nivel personal.

A todos mis colegas, coautores y a todos los miembros del Laboratorio de Tectónica Activa, en especial a José “Pepe” González por las incalculables y nutritivas horas de discusión (y verborrea) científica-filosófica que han sido una base fundamental para la construcción de nuevas ideas e hipótesis, y a Jean-Baptiste Ammirati por sus enseñanzas en los aspectos geofísicos y sismológicos. Incluyo además a los estudiantes de posgrado del periodo 2014 -2018 que sumado al intercambio de conocimiento interdiciplinario entregado durante esos años, su agradable compañía hizo que mi estadía en la Universidad de Chile haya sido mucho más grata. Particularmente a Danielle Tardani, Diego Aravena, Manuel García, Laura Lagos, Verónica Mardones, Matías Peña, Bárbara Salomé, Lea Israel, Estefanía Camus, Rayén Gho, María Angélica Contreras, Eduardo Morgado, Camila Leal, Carolina Geoffroy y Marcela Pizarro, muchas gracias por su buena onda.

Un agradecimiento (o una gran disculpa) a mi familia, mis padres y hermano, por su eterna paciencia y ayuda durante todos estos años de cambios de humor.

Por último se me hace imposible no recordar a todos los miembros de los proyectos de investigación CIMAR-24 y CIMAR-25, con los cuales pude aventurarme y aprender en terreno gran parte de las técnicas de geología marina usadas en esta tesis. Especialmente quisiera agradecer también al Dr. Galderic Lastras y toda la tripulación de la expedición marítima DETSUFA, por haber facilitado los datos geofísicos que sirvieron a esta tesis.

Table of Contents

Table of Figures

Chapter 1: Introduction

1.1 Overview

The Chilean subduction margin, characterized by moderate to large earthquakes (M_w>6 up to M_w 9.5), is one of the most seismically active regions globally. The greatest instrumentally recorded earthquake was the 1960 Valdivia Earthquake with a magnitude M_w 9.5 (Figure 1.1), and a rupture zone over 1,000 kilometers long (Plafker & Savage, 1970; Barrientos & Ward, 1990; Moreno et al., 2009). This massive megathrust earthquake caused thousands of casualties and hundreds of millions of dollars damage (e.g., Rothé, 1969; Dunbar et al., 1996; Utsu, 2002; Lomnitz, 2004).

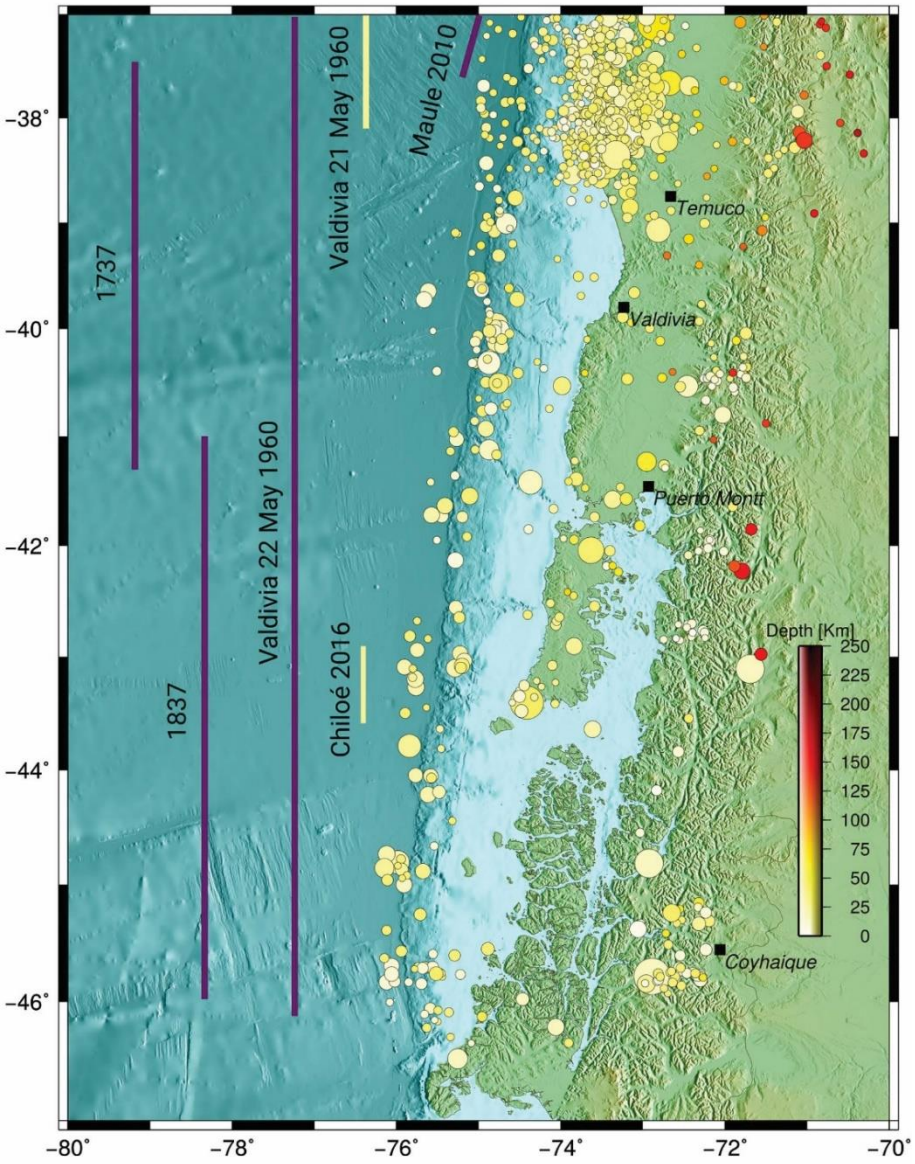

Figure 1.1. South-Central Chile seismicity. Dots are epicenters of events larger than M 4.5 from the NEIC catalog from 1900 to 2017. The color bar is related with the depth of the hypocenters. The purple line is the estimated rupture extent the giant 1960 and 1737 and 1837 Valdivia earthquakes, and the yellow color lines are the rupture lengths of smaller events that ruptured a partial zone of the interplate contact (from Ruiz & Madariaga, 2018).

Earthquakes in active tectonic margins characterized by oblique convergence do not only originate at the subduction zone, but also along large fault systems parallel to the margin. In the North Patagonian Andes, the oblique convergence is partitioned into two components: the dip-slip is accommodated along with the subduction interface, and the strike-slip component is mainly accommodated by the Liquiñe-Ofqui Fault System (LOFS) (Figure 1.1b), a dextral strike-slip fault system (e.g., Cembrano et al., 2002, 1996a; Lavenu & Cembrano, 1999; Legrand et al., 2011). Other strike-slip faults occur in similar settings. The most known are the left-lateral Philippine Fault (parallel to the Luzon and Philippine Trenches), the right-lateral Median Tectonic Line (parallel to the Nankai trough, Japan), and the Sumatran Fault Zone (parallel to the Sunda Subduction zone). All of which have demonstrated a high-destructive potential in historical and prehistorical times (e.g., Besana & Ando, 2005; McCarthy & Elders, 1997; Nakanishi et al., 2004; Natawidjaja & Triyoso, 2007; Tsutsumi et al., 1991). Attempts to understand the link of these structures parallel to the subduction margin with the mountain-building in these areas are scarce, especially in Southeast Asia. Despite this, it has been observed that they can behave in different ways. Those mainly focused on geomorphic features in the western deformation front of the Philippine Fault Zone stand out (e.g., Rimando & Rimando, 2020) that have allowed proposing greater participation of this fault and an overestimation associated with thrust faults. In the case of the Sumatra Fault, studies focused on this relationship have not been developed. In Japan, the current understanding of the Median Tectonic Line long history tells us about a paleo-subduction zone behavior during Mesozoic times and a strike-slip reactivation and current state of deformation (Isozaki et al., 2010; Sato et al., 2015). Concluding that it currently does not participate significantly in the generation of relief (Townend & Zoback, 2015; Sato et al., 2015).

In the Aysén Fjord area, a seismic swarm was felt between January 2007 and February 2008 (Figure 1.2). The seismic activity's peak stage occurred in April 2007 and was characterized by two main earthquakes that occurred on 2 April, M_w 6.1, and on 21 April, M_w 6.2. The last one triggered several landslides that induced tsunami waves of several tens of meters on the fjord (Lastras et al., 2013; Naranjo et al., 2009). However, there is no certainty about which structures were responsible for the seismic activity or the mechanisms in which these events took their course.

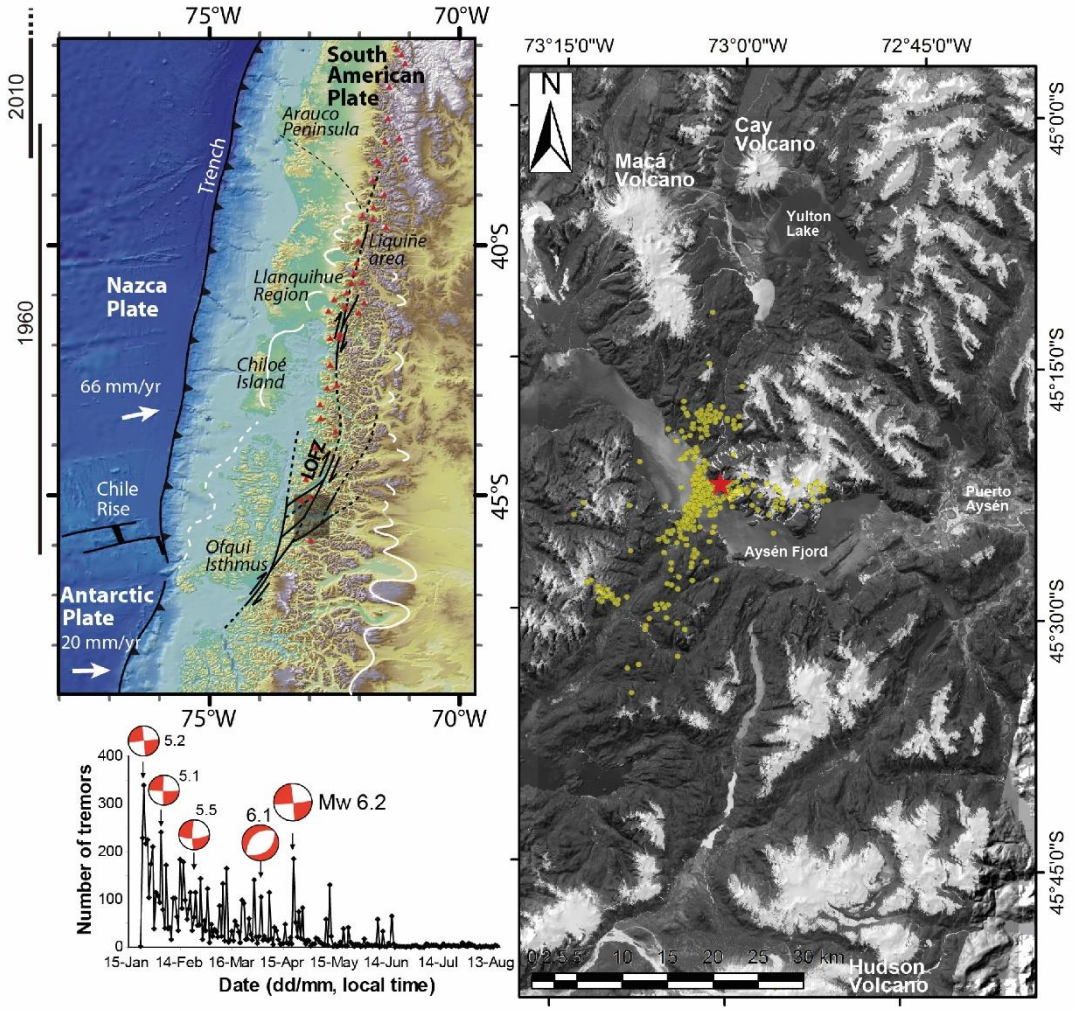

Figure 1.2. Regional tectonic context at the triple junction of the Nazca, Antarctic and SouthAmerican plates, and location of the 2007-AYSS. Left top: Regional tectonic plate's context of the Patagonian Andes, indicating the main regional trace of the intra-arc Liquiñe-Ofqui Fault Zone and Late Pleistocene-Holocene large volcanoes. Black lines to the left show the latitudinal rupture of the 1960 Valdivia earthquake, and the 2010 Maule earthquake. White lines show the approximate maximum extend of the Pleistocene ice sheet during the Last Glacial Maximum (from Thomson et al., 2010). Right: Location of the April 2007-AYSS in the area of the Aysén Fjord (Legrand et al., 2011), and the relief shown by the means of a SPOT satellite image over a Digital Elevation Model (DEM). Circles represent seismic events of Mw ≤3.0, as well as some events of M>5. The red star indicates the location of the main shock (M_w 6.2), according to GUC (2007). The location of the Macá, Cay and Hudson volcanoes is also shown. Left bottom: Distribution of number of events versus time, and focal mechanisms for the main shocks according to GUC (2007) and HRV (2007). Taken from Vargas et al. (2013).

The detailed and continued sedimentary records in fjords are idealized archives to reconstruct an area's seismic history. The assessment of the degree and style of activity of the structures also can give the foundation for studies conducted by other disciplines, focused on the interaction of these seismogenic structures and potential impact on societies. Several lakes and fjords characterize the study area located on the Patagonian Andes of Southern Chile. Before this work, few efforts regarding the identification of active segments have been made, and most of them are focused on the study of the 2007 Aysén Seismic Swarm (2007-AYSS) (e.g., Agurto et al., 2012; Lara et al., 2008; Legrand et al., 2011; Mora et al., 2010; Russo et al., 2011).

However, there is no certainty as to which structure(s) was (or were) responsible for the seismic activity or the mechanisms in which these events took their course. Although, some of these faults have been suggested as responsible (Vargas et al., 2013).

Given the lack of information regarding the complex structural setting, and doubts about the origin of seismic events at the Aysén Region, my thesis provides geomorphic, structural, sedimentary, and paleoseismological data. With this data I have built a 3D structural and hazard assessment models of the LOFS in the area. Along with the above, earthquake geology, paleoseismological and marine geology techniques help to better understand the seismic history in this portion of the North Patagonian Andes. Thus, a better framework for the seismic and geological risk of the area and similar zones.

1.2 The 2007 AYSS along the LOFS (a state-of-the-art before this presentation)

The first investigations about the 2007-AYSS focused mainly on the effects caused by the main event of April 21 (M_w: 6.2) (e.g., Naranjo et al., 2007; Naranjo et al., 2009; Sepúlveda & Serey, 2009). This was mainly due to the limitations in the seismic monitoring of this area of Southern Chile, particularly the direct damage caused by the tsunami-wave that affected the few functional stations in the fjord. Barrientos et al. (2007) and Comte et al. (2007) were the first to present the earthquakes recorded during this first period of 2007-AYSS. From these first works, it was possible to calculate the focal mechanism tentatively propose an association to the LOFS without complete certainty (Cembrano et al., 2007a; Comte et al., 2007). More detailed work on the effects of mass wasting was carried out by Naranjo et al. (2007) (Figure 1.3), Pavez et al. (2007), Arenas et al. (2008), Sepúlveda et al. (2008a, 2008b), Naranjo et al. (2009). This kind of studies focused on generating a catalog and detailed mapping of these phenomena, managing to classify them into landslides, rock falls, rock avalanches, and debris flows (Figure 1.4). More recently, Sepúlveda & Serey (2009) discussed in advance associated with the tsunami-wave of April 21.

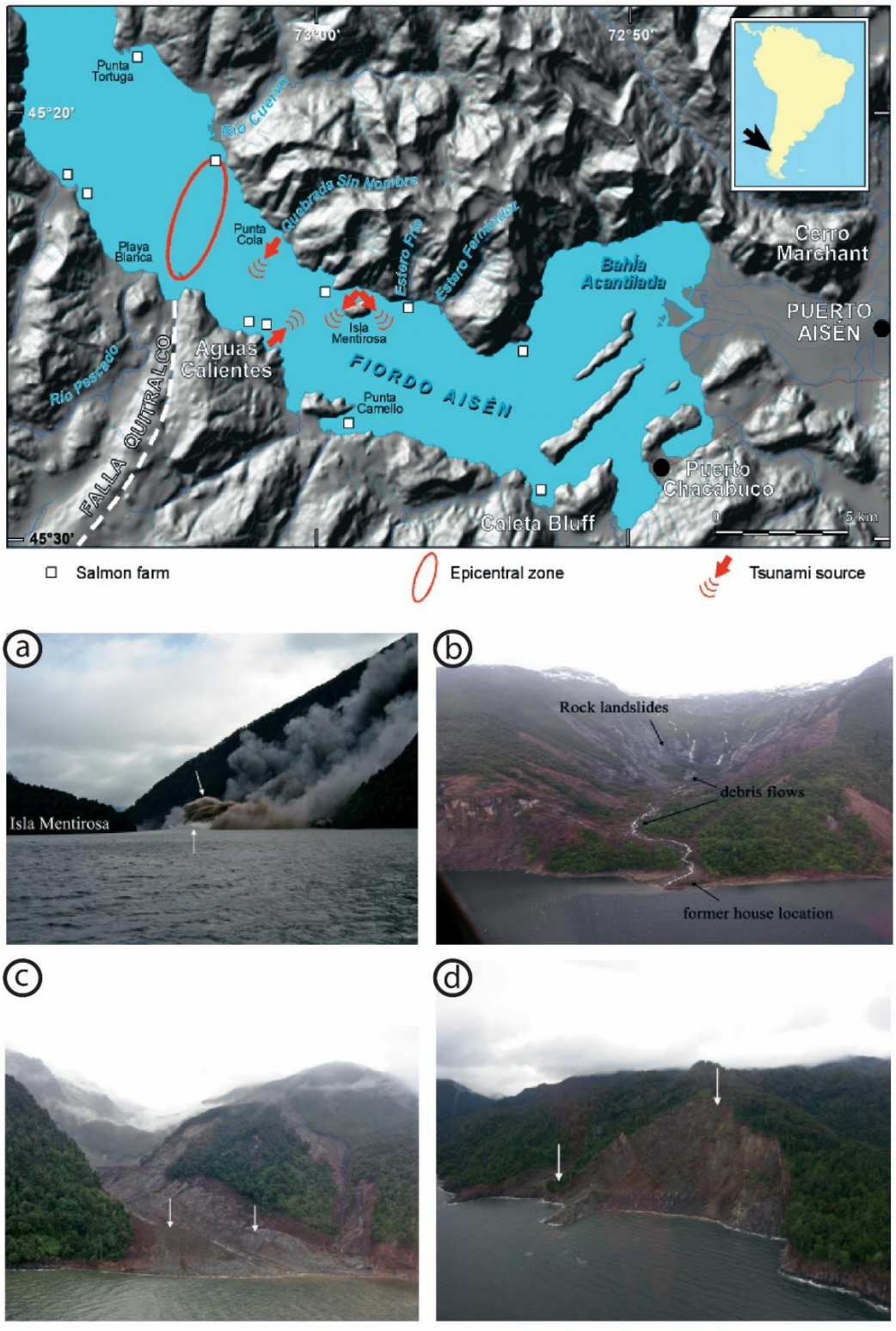

Figure 1.3. Map describing the events triggered by the Mw 6.1 earthquake in Aysén Fjord. (a) Mentitosa Island landslide entering the fjord. (b) Rock landslides and debris flows deposits on Quebrada Estero Frío. (c) Punta Cola landslide deposits. (d) Scars associated to Aguas Calientes landslide (from Naranjo et al., 2007).

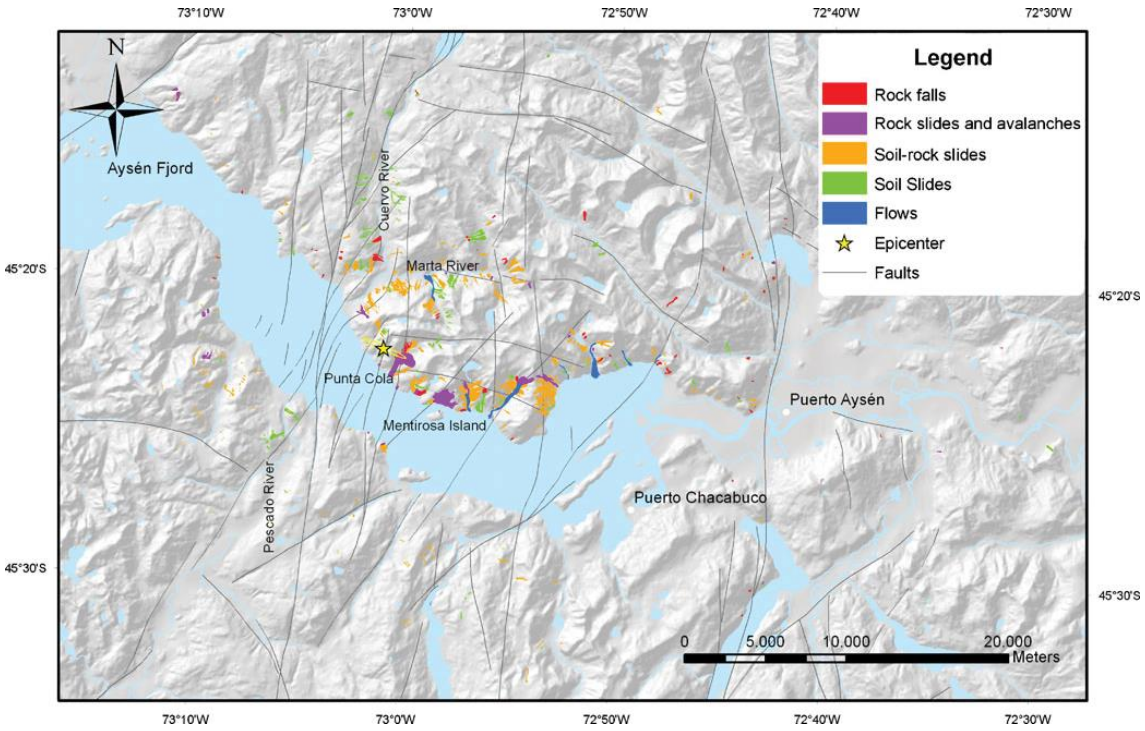

Figure 1.4. Shaded relief map with the inventory of landslides triggered during the 2007 earthquake (from Sepúlveda et al., 2010).

Mora et al. (2010) were the first using a Joint Hypocenter Determination relocation method to propose and present a restricted distribution of the events of 2007-AYSS and reported that the hipocenteres ranged between 0 and 8 km depth (Figure 1.5), located in a small area along the domain of the the Liquiñe-Ofqui Fault System. Meanwhile, Sepúlveda et al. (2010) shed light on the effects of a seismogenic fault with shallow earthquakes and the amplification of the waves caused during the earthquake and its direct effects on landslides.

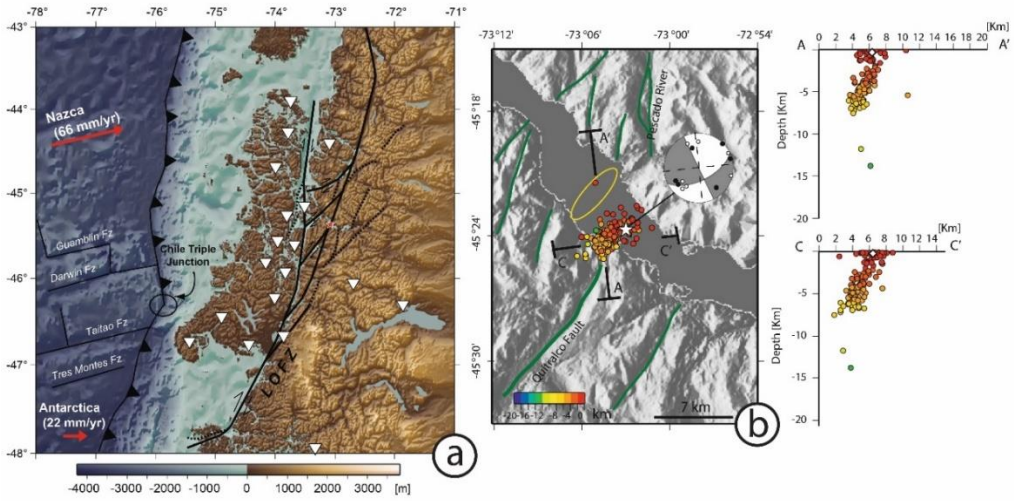

Figure 1.5. (a) Active stations from CRSP temporal network for this study shown as white inverted triangles. Red star denotes Aysén swarm location. (b) Calculated relocation using JHD methoid (from Mora et al., 2010).

Legrand et al. (2011) propose a tectonic-volcanic origin based on the spatial and temporal distribution and the size of the earthquakes, making an association with the known monogenetic cones in the vicinity of the fjord (Figure 1.6) and the active nature of the volcanic arc in this sector of the Andes. For their part, Russo et al. (2011) used a combined earthquake relocation methodology using P and SH wave arrival times together with Joint Hypocenter Determination with questionable results. He also implemented a coulomb effort change methodology for proposed faults in his work.

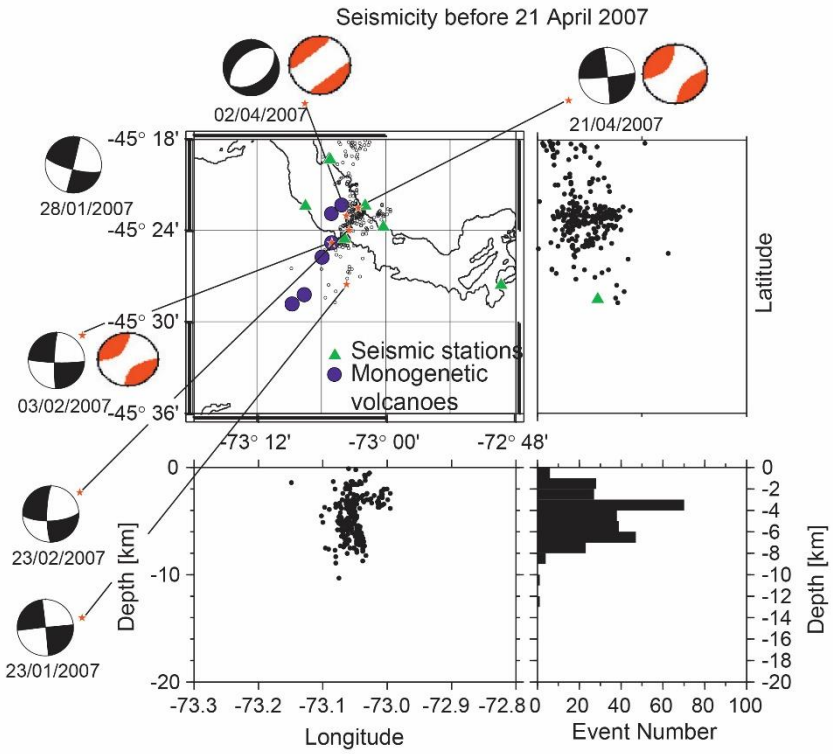

Figure 1.6. Earthquakes located by the local network (triangles) before 21 April 2007 and focal mechanisms determined by the GCMT catalogue. The focal mechanism of 28 January 2007 is shown but not associated with a location (from Legrand et al., 2011).

Agurto et al. (2012), using new data from a network of 15 seismographs and an observation window of seven months, characterized the seismogenic structure of the fjord area through a 1D velocity model (Figure 1.7). This made it possible to relocate many earthquakes from the 2007-AYSS, which facilitated the visualization of patterns associable with structures. In addition to the above, many focal mechanisms were calculated, providing valuable information on the association of these events with seismogenic structures.

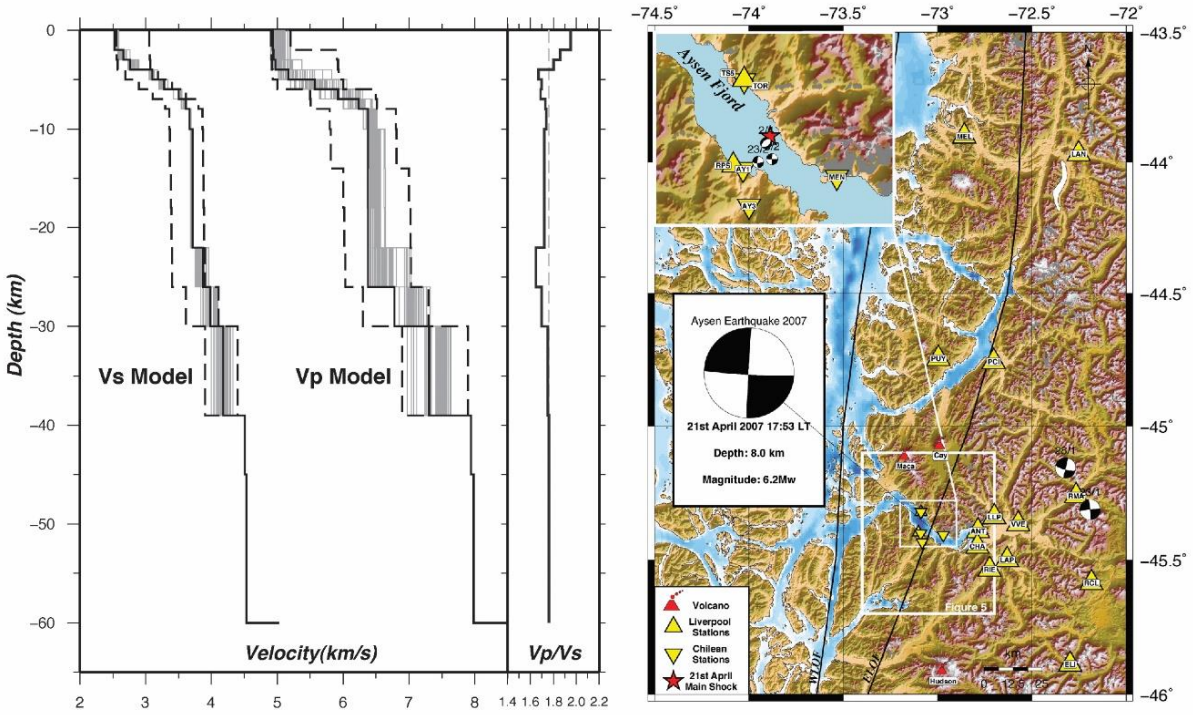

Figure 1.7. Left-hand side: 1-D velocity model for P and S velocities as well as Vp/Vs ratio. Dashed lines indicate range of starting models, grey lines indicate final models and the bold black line represents the best final model with the lowest overall rms. Right-hand side: Study area and distribution of seismic network around Aysén Fjord including largest events (M > 5) of the 2007 seismic sequence. Focal mechanisms from GCMT Catalogue except main shock from USGS Catalogue. Location of largest events from this work except events January 23 and 28 from NEIC catalogue. From Agurto et al. (2012).

1.3 State-of-the-art on active faulting and surface rupture

1.3.1 Study of the faulting-earthquake relationship

The causal relationship between faulting and earthquakes has been well described for more than 100 years (e.g., Gilbert, 1884; Kotô, 1893). Studies conducted in the context of the Great California Earthquake of 1906 cleared any doubt of such a connection (Lawson, 1908). Simultaneously, the first physical geodesy-based earthquake faulting models began to develop, also incorporating the concept of elastic rebound (Reid, 1910). From this type of research, the study of the mechanics of faulting and earthquakes has been kept under constant progress, mainly due to the occurrence of mid to high magnitude earthquakes with surface rupture in continental crust faults and old Quaternary alluvial deposits.

Understanding this phenomenon led to the development of empirical equations that allow us to relate different features found on the surface. Those physical phenomena involved in the generation of an earthquake also gave way to seismic risk analysis methodologies. As expected, have many uncertainties because the historical and instrumental record of fault activity is often restricted to a short period of time. Along with this, the understanding of physics after fracture generation and propagation have advanced, following mainly two approaches, the analog, with “sandbox” type

studies, and the numerical-deductive approaches, where simple dislocation models stand out, as do those more complex using finite elements modelling

The following is a summary of the types of study devoted to crustal faulting with surface rupture and part of the paleoseismological vision of the problem.

1.3.2 Field studies

When an earthquake occurs, a fault's motion generates two types of ground motion: a permanent quasi-static displacement on the fault, and transient dynamic oscillations moving away from the source (Ambraseys & Jackson, 1984). Oscillatory displacement is the result of waves generated at each point of the fault as the slip takes place on the fault and can propagate for great distances across Earth.

The study of surface rupture earthquakes has always been a topic that has focused significant attention on geoscientists. It corresponds to evidence that is commonly easy to associate with the seismogenic source (McCalpin & Nelson, 2009). Most of this work has been concentrated on areas where the fault trace is well exposed. In the case of investigations carried out in terrestrial environments, a shallow level of burial facilitates trenches. Technical-economic foundations influence this decision, which tries to avoid deep excavations.

The generation of flexures in the hanging wall of a reverse fault and the formation of extensional cracks or secondary faulting is also a type of surface deformation triggered by the faulting of a crustal structure. In this case, the footwall is, in most cases, practically intact. In normal faults, the opposite happens; the footwall is most affected by secondary deformation. Contrastingly, recurrent faults produce the least amount of secondary deformation since their rupture zone is restricted and narrow, although, as expected, there are always exceptions.

Geological field studies typically focus on surface faulting features left, relatively shallow exploration trenches (<6m depth), and interpretation of surface geological evidence. There are few studies of coseismic faulting where the surface rupture characteristics are linked to the displacement in-depth and are well documented. For this, it is necessary to study this phenomenon through physical modeling of the rupture propagation, which can reproduce the deformation observed on the surface.

The following is a variety of techniques used in the ground phase to study earthquakes with surface rupture, which is based on paleoseismological methodologies.

1.3.2.1 Inland environments

i. Characterization of surface ruptures

Currently, there is a wide variety of techniques for detecting deformation zones associated with active faulting. The logical sequence for this type of study starts at the regional scale (remote sensing methods), then the local scale (geomorphological mapping), and ends at the site scale (geophysics methods, trenches) (McCalpin, 2009).

ii. Characterization of subsurface ruptures

When studying a seismogenic fault, one of the objectives that is kept in mind is reconstructing its seismic history by determining the recurrence and displacement of paleoearthquakes (Sieh, 1981). This is achieved by digging trenches, which are usually up to 15 m deep (Bray et al., 1994), which cut or are parallel to the fault trace, depending on its kinematics. The main objective of this phase is the identification of event indicators within the stratigraphy that allows defining earthquake horizons (sensu Scharer et al., 2007).

The implementation of trenches is conditioned by the monetary factor, so relatively accessible places with little sediment depth are usually chosen in young sediments. Numerous paleoseismological studies have shown that this procedure allows recognizing a maximum of two paleoearthquakes (McCalpin, 2009). If it is necessary to know the behavior of a surface fault, it is necessary to extend the search to older deposits. One way to avoid the high costs that this would entail is the implementation of geophysical methods.

The implementation of geophysical methods has three advantages in this studies. The most elemental ones include the search for targets for paleoseismological trenches, as an alternative to the use of trenches and drilling, and the most interesting for this study as a follow-up of the geometry of the rupture at greater depths, even down to crustal scales (tens thousands of meters). In the literature, the most widely implemented methods are reflection and refraction seismic, GPR (Ground-Penetrating Radar), and some electrical methods such as resistivity tomography. Electromagnetic methods such as the EM-31 induction method and magnetic methods such as Aero-magnetic campaigns and magneto-telluric profiles are common—finally, those gravimetric as those using residual Bouguer anomalies.

1.3.2.2 Underwater environments

i. Characterization of surface ruptures in the seafloor

The methods used in paleoseismological campaigns in underwater environments are based on traditional subaerial techniques and the most advanced technical-methodological developments of marine geosciences (Gràcia et al., 2013). Most of the current seafloor mapping techniques that allow rapid identification of geomorphic evidence correspond to geophysical methods based on acoustic waves (e.g., Gràcia et al., 2003, 2006; Lamarche et al., 2006). This is due to the low underwater transmission of light and electromagnetic waves. Other techniques such as ship-mounted laser scanning images and LiDAR bathymetries performed by low-flying aircraft require special conditions in very shallow, shallow waters.

To find first-order evidence of active faulting, the most widely used seafloor mapping technique is multibeam sonar bathymetry (e.g., Beck et al., 2012; Cattaneo et al., 2012; Escartín et al., 2016; Gràcia et al., 2006, 2012; Pondard & Barnes, 2010). Another way to carry out the mapping is to use lateral scanning sonars that deliver a high-quality image for the detection of tectonic features, delivering 3D surface mappings that integrate morphology and material properties of the study area. To obtain acoustic quality data, the sonars must be attached to vehicles capable of reaching high depths, such as autonomous vehicles (AUVs), remotely operated (ROVs), or submarines.

ii. Characterization of subsurface ruptures

The visualization of the subsurface structures is carried out using seismic reflection techniques correlated with soundings when possible (e.g., Beck et al., 2012; Gràcia et al., 2012). Like the techniques in the previous section, seismic reflection is based on acoustic waves but with a lower frequency (10–150 Hz), which allows the penetration of the seafloor substrate. In general, all these techniques use arrays of sound sources and receivers to improve the definition of the weak signal through a stacking process. In the study of active faults, a low penetration system focused on the subsurface's first meters is used, which uses slightly higher frequencies to detect faults in detail, their termination, and deformed strata. Today, the most widely used techniques use as source, air guns or acoustic pulses such as CHIRP (Compressed High-Intensity Radar Pulse) or others.

1.3.3 Elaboration, interpretation and use of empirical equations for earthquake related geomorphic features

Relationships between different features generated by earthquakes with surface rupture were established based on global catalogs (e.g., Wells & Coppersmith, 1994;

Anderson et al., 1996; Vakov, 1996; Wesnousky, 2008). These equations' main objectives are the assessment of the seismogenic potential of an active fault that generates a surface expression, and the prediction of the characteristics and dimensions of the morphological features associated with a new rupture for a given magnitude of a new seismic event. The most used features to evaluate are the maximum rupture length and maximum or average displacement per event (e.g., Wells & Coppersmith, 1994; Mason, 1996; Dowrick & Rhoades, 2004; Manighetti et al., 2007). It was observed that several measurable parameters in a fault with surface expression are correlated with each other and the magnitude (M_w) of the earthquake.

The construction of these empirical equations began long before the widely used Wells & Coppersmith (1994)'s equations. The first studies focused mainly on finding the relationship between the earthquake magnitude and the surface rupture length (Tocher, 1958; Solonenko, 1973; Slemmons, 1977; Nikonov, 1977). In parallel with this, other researchers were advancing in understanding this link, including the surface rupture length of the aftershocks (Chinnery; 1969; Kanamori & Anderson, 1975; Geller, 1976). Later, this type of correlation began to be used as a way of understanding the earthquake source mechanics (Scholz, 1982a; Steinberg, 1983; Bonilla et al., 1984; Wesnousky, 1986; Wells & Coppersmith, 1994).

The way of interpreting the correlation of the data obtained in the field with those measured instrumentally has changed as we understand more about this phenomenon's mechanics. Works such as that of Bonilla et al. (1984) statistically analyzed the relationship between surface earthquake wave's magnitude, surface rupture length, and surface displacement (offset) at fault. Those authors suggest that the relationship between the evaluated parameters is stochastic. Subsequently, Shaw & Scholz (2001) demonstrated by comparing earthquakes with large aspect ratios and analogous dynamic models of smaller-scale earthquakes that the physical results were consistent and unchanging at scale. Contrarily, Stirling et al. (2002) using an improved version of the Wells & Coppersmith (1994)'s catalog, an international database with pre-instrumental and instrumental data. They compared the largest earthquakes, those of medium magnitude and less, suggesting that those larger-scale earthquakes have different scalar relationships than other minor ones. Additionaly, Manighetti et al. (2007) have analyzed length and slip data to understand the origin of the significant variability of stress drops in large earthquakes, proposing that this variability comes from a variable number of breaks in the main fault segments during earthquakes. The authors proposed new parameterizations for maximum displacement and length based on the idea of several segment breaks. Wesnousky (2008), using an international database of 38 earthquakes, provides an initial statistical basis for predicting the end tip-point for a rupture and the expected amount of surface slip along the fault strike.

This research's practical use corresponds to the theoretical basis of seismic hazard analysis methodologies, both deterministic and probabilistic. If there is no historical instrumental record for a similar event, the rupture parameters are taken as the basis of the methodology. Examples of these types of assessments can be found on submarine fault lines in Cascadia, California, and New Zealand (e.g., Barnes & Pondard, 2010; Goldfinger et al., 2003; Stirling et al., 2012). In this sense, the most critical data is the earthquake with the maximum magnitude that the seismogenic source can generate, which is commonly calculated with the surface rupture length

and surface displacement (e.g., Wells & Coppersmith, 1994; Wesnousky, 2008), and lately with a velocity rate value (Anderson et al., 1996). For the construction of these relationships, the geological and geomorphological data fulfill the function of reconstructing the geometry (determination of the trace and segmentation of the fault), dating of events, and the amount of displacement (deformation) per event, which later through statistical regressions or physical equations serve to estimate the magnitude of the seismic moment of each event.

1.3.4 Analog and numerical models: factors that control surface rupture

Another approach taken to understand the surface rupture earthquake phenomenon is using models, either analog or numerical. These models are constrained with the information obtained in the field.

When these features are observed in trenches and in seismic imagery, a great variety of ways in which a rupture is possible to differentiate. Due to the great variety of geological materials (rheology), stratigraphy (rheological contrast and geometric control), and involved processes.

Typically most of the fault trace offset is defined in one or more distinctive rupture segments within a more extensive shear zone as often more complex discontinuous patterns develop in an area that can vary in thickness over time along the trace of the fault. Within this complexity, there are usually repetitive patterns commonly observed in the field. Most of this information forms a reliable source for studies of the materials' physical behavior in the rupture process.

How a rupture behaves when entering close to the ground-air/water interface varies depending on its kinematics and geometry. Reverse (thrust) faults typically decrease in the dip as they are approaching the ground-floor (Roth et al., 1981; Cole et al., 1984). Normal faults usually refract at the bedrock-sediment interface and increase their dip as they approach the ground-floor (Roth et al., 1981; Cole et al., 1984). Strike-slip faults tend to maintain a sub-vertical dip, although, on some occasions, they divide into branches forming positive or negative flowers close to the ground-floor interface.

Using finite element modeling, Anastasopoulos et al. (2007) manage to determine that for normal and reverse faults, the increase and decrease of its surface dip angle is a function of the frictional angle's peak the angle of dilatation. For a rupture to be able to propagate to the surface, it depends on the ratio between a base value of the depth separation defined as "h" which is relative to the thickness of the coverage "H" of unconsolidated material on the bedrock. This h/H ratio is a function of increasing upwelling ductility. In reverse faults, significantly higher ratios are calculated compared to normal faults (Anastasopoulos et al., 2007).

The fault movement can be classified into two types: one relative and the other differential. Relative motion is usually concentrated in a narrow strip on the bedrock, while differential movement is generally found in the rupture zone in small fault planes. Fortunately, most of the differential movement in a fault zone is usually concentrated in a single rupture, making it easier to locate the deformation. For its part, the remaining movement, about 20%, is generally found in secondary faults or at a distance not more than 12 km from the main fault trace (Bonilla, 1970).

1.3.7 Surface rupture and geological risk

The process of surface rupture earthquakes has historically been responsible for significant structural damage during earthquakes, making this topic more significant in civil engineering projects. Several examples of the impact that this type of deformation can generate on infrastructure were observed during four earthquake events. The most damaging corresponds to the event that took place in the Japanese city of Kobe. The M_w 6.9 earthquake occurred in 1995 along the Nojima Fault. This event generated ground accelerations greater than 80% g, locally more than 100% g, and a surface rupture that dislocated the soil from a few decimeters vertically to a few meters horizontally (Kanamori, 1995; Yamaguchi & Yamazaki, 2001). The earthquake caused significant damage to the buildings arranged directly on this geological fault and the loss of some 6,000 people. In Turkey in 1999 (Kocaeli and Duzce Earthquakes) and the Chi-Chi Earthquake in Taiwan the same year. To avoid the destruction caused by this phenomenon, many countries located in seismotectonically active areas have developed seismic regulations, building codes, and maps that show the regions identified with active faults. These codes require the non-construction of buildings in the vicinity of active faults or, at least, not without a substantial number of analyzes or unique construction designs. Examples of the above are the European Seismic Code (EC-8), which indicates a distance from the trace of the specific active fault, depending on the case, which must be based on studies. Following a different approach, in California, the seismic code prewrites a single distance of 50 feet (15.3 m) from both sides of the fault trace, despite variations in fault zone characteristics and ground conditions. Geological and historical evidence has shown that earthquakes' surface deformation in active crustal faults can reach distances of 10 - 40 m from the fault trace. Compared to the first, more specific one, this last seismic code is not sustainable in a robust scientific source.

This problem is increased if we consider the points already mentioned above for the cases of faults with mainly a dip component (reverse and normal faults) where the rupture propagation cannot necessarily be projected from the fault plane location in the bedrock in deep.

1.4 Hypothesis

This thesis intend to test the hypothesis that the seismic sequence occurred on 2007 in the fjordland of the Aysén Region was caused by a reactivation of several fault branches of the Liquiñe-Ofqui Fault System (LOFS). Previous works in this area, indicate that the LOFS is formed by a complex arrangement of structures involving

shallow and deep parts of the crust with the capacity to generate earthquake surface ruptures.

In testing the aforementioned hypothesis, I examine critical questions associated with the earthquake surface rupture and active faulting characteristics of the Aysén Fjords sedimentary infill. These questions include:

- What and how was the seismotectonic origin of the 2007 Aysén seismic sequence?
- Is there evidence of surface seismic rupture associated with the M_w 6.2 and M_w 6.1 earthquakes?
- Is it possible to determine similar events in the recent geological past?
- How does tectonics contribute to the relief building along the LOFS in this portion of the Patagonian Andes?

Understanding the paleoseismic history and faults offsets, such as the Punta Cola, Quitralco, and Río Cuervo faults and other related structures —the fault branches of the Liquiñe-Ofqui Fault System studied in this thesis— have important implications for the seismic hazard assessment and stress regime in the Aysén zone and the wide North Patagonian Andes.

1.5 General and specific goals

The main objective of this thesis is to establish the active tectonic behavior of the Liquiñe-Ofqui Fault System both in the short-term time scale (seismogenic point of view, at the scale of the 2007 earthquake episode), and long-term scale (geomorphological landscape evolution), in the Patagonian Andes of the Aysén Region during postglacial times.

To meet this objective, the following specific objectives are proposed.

- Explore and identify the presence and continuity of geological faults and their deformation patterns within the sedimentary infill of the Aysén Fjord.
- Recognize and discriminate the presence and Late Quaternary tectonic activity (paleoseismic history) as discrete events associable to the active structures located within the study area.
- Elucidate and explain the deformation at a crustal-scale to link the deep rupture mechanisms with the surface rupture processes for this segment of the LOFS.

This aims have necessary implications for the seismic hazard model and stress regime in the Aysén Fjord zone and other similar tectonics settings. The improvement of the characterization of the geometry and seismic activity migration through, across, and along these strike-slip faults mechanics is required to assess the paleoseismic ruptures in complex settings such as transfer zones that often have highly distributed fault zones.

- Constrain the presence and delimit the location of the ice sheet this sector of the North Patagonian Andes to validity of the paleo-earthquake record ages found in the fjord sedimentary infill.

- Assess the link between deep fault mechanical processes and surface deformation occurred in the complex segment of the LOFS in the Aysén Fjord area, and the seismic history, and link it to the mountain uprising on a long-term timescale (since the last glaciation) of this segment of the Patagonian Andes.

This aims needs a paleoclimatic and palaeoenvironmental study understand the ice sheet retreat framework and how it relates to the tectonic structures studied in this area.

1.6 Methodology

To identify the submerged continuation of the LOFS branches, I used high-resolution bathymetry and sub-bottom profiles. The area where data was obtained is located westward of Puerto Aysén, in the inner-fjord (73.13° - 72.68° W and 45.32° - 45.47° S; Figures 1.9 and 1.10). The data set used was obtained in the DETSUFA project's geophysical campaign between 4 and 17 March 2013, project focused on the detection of deposits associated with mass wasting events, in which Dr. Gabriel Easton along with other professors from the Department of Geology of the University of Chile participated. The maritime campaign was on board the R/V BIO Hésperides of the Spanish Navy (Figure 1.8).

Figure 1.8. Photography of the R/V BIO Hésperides of the Spanish Navy.

1.6.1 Bathymetry

Multi-beam data was used to create a high resolution bathymetry map (4x4 m). The data was acquired using a KONGSBERG SIMRAD multi-beam (EM120 and EM1002 models). The equipment works with 111 beams at a sonar frequency of 96 kHz with a maximum ping rate of >10 Hz. The equidistant mode was used for swath bathymetry acquisition (Figure 1.9). This array maximized the number of beams, facilitated data acquisition, and produced a homogenized final grid. During the campaign, the vessel followed parallel lines of navigation, using a mosaic method separated every 150 m. Also, swaths' thickness had the same width, which generated a 50% overlap with the only exception of those areas near the coast that was not covered for the safety of the mission.

1.6.1.1 Data adquisition

Both ecosounders can operate with fully adjustable angular coverage. During the limited usage of the EM-120, it was used in full swath mode. While the EM-1002S was used in equidistant mode (swath width independent of water depth). This maximizes the number of usable beams, eases the survey planning. Survey planning involved parallel navigation lines with full seafloor coverage (Figure 1.9). Lines were separated 300 m in the outer-fjord area, and 150 m in both Mentirosa and Acantilada areas (inner fjord). Swath width was adjusted to 300 m and 150 m respectively so that lines can overlap in a 50%, except for the lines closer to the coastline or in turns. In these lines, the side located at shallower water depths and that was not going to be further surveyed was fully opened, in order to obtain as much coverage as possible. Total overlapping was designed to follow navigation safety requirements. Lines that were designed to seismic profiles were generally operated with a 500 m swath width. XBT (Expendable Bathythermograph) probes were used at specific sites to measure changes in sound velocity on water due to ever-changing conditions associated with a restriction of fresh water circulation, tides, and sediments.

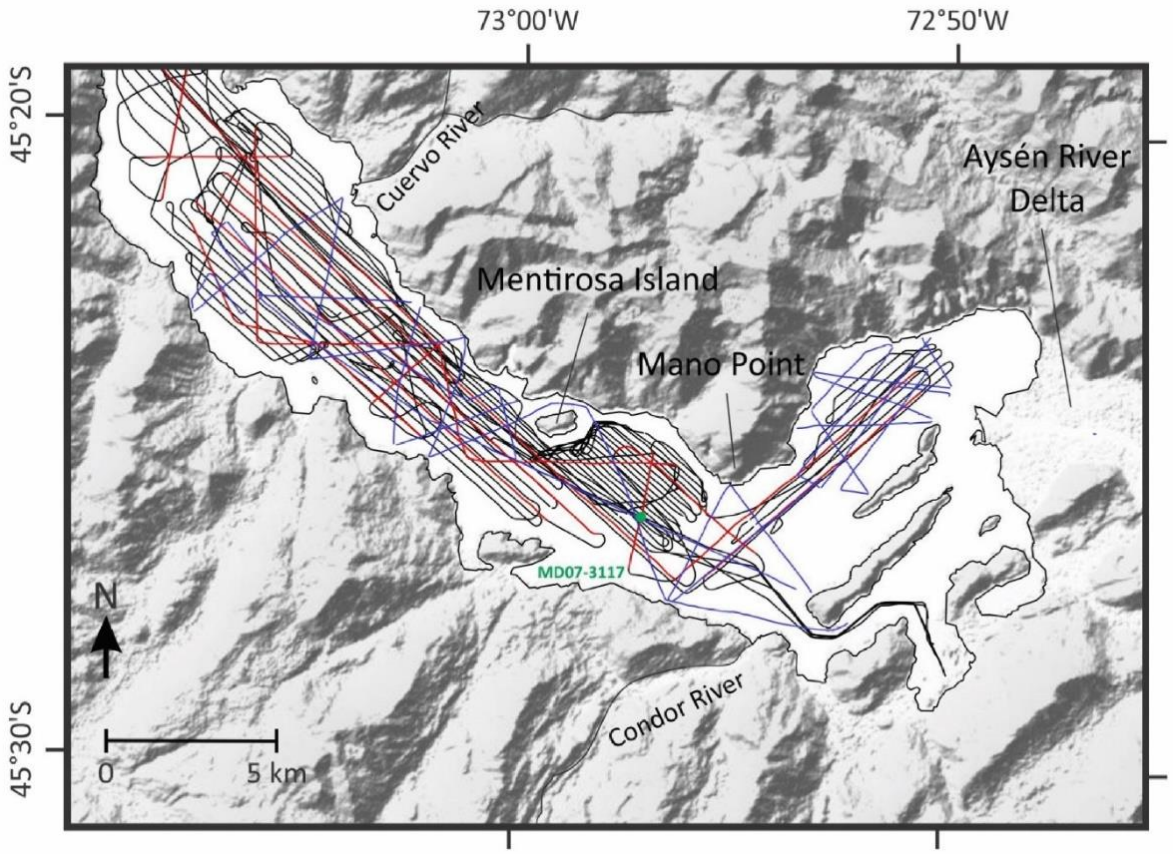

Figure 1.9. Hillshade map of the inner Aysén Fjord area showing the different track lines where the geophysical data was adquire. Black lines are TOPAS profiles, red are the airgun lines and blue lines were acquired with a sparker source. MD07-3117 core is indicated with a green dot.

1.6.1.2 Data processing

Preliminary processing of bathymetric data was made onboard using Caris HIPS and SIPS softwares, which provides manual or automatic processing tools. Data were corrected for local velocity profiles and tidal changes when necessary. The final grid obtained has a maximum resolution of 4 m per cell. Bathymetry, slope, and aspect maps were produced using ArcGIS 10.3 (Figures 1.10 and Appendix A1).

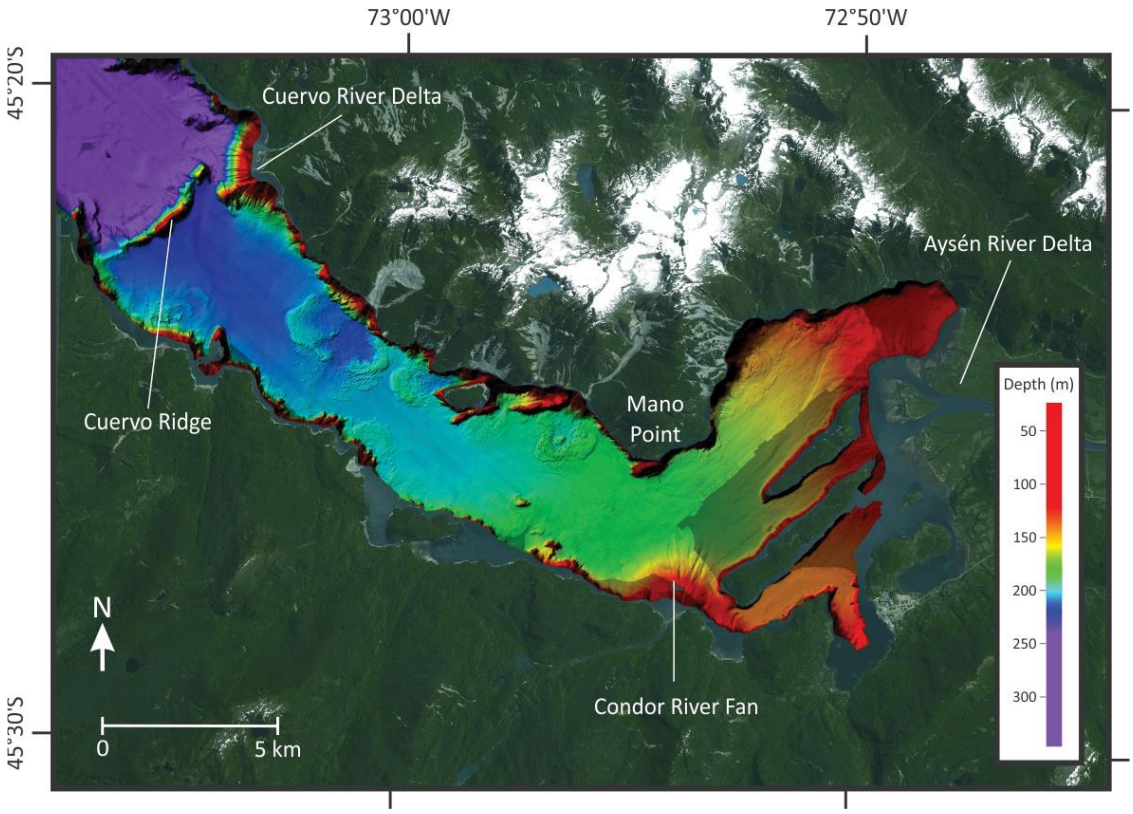

Figure 1.10. Data from the EM 1002S multibeam echosounder are in bright colours and complemented by the darkercoloured Seabeam 1050 bathymetry data (extracted from Wils, 2016).

1.6.2 Air-gun seismic reflection profiling

The used air-gun seismic data was also acquired during the DETSUFA survey to detect and map landslide deposits. It was used to detect older landslide deposits and neotectonic structures deforming sedimentary infill. The mapping of other features such as the Cuervo Ridge and also the basement of this area were also considered.

According to the above, the system was designed so the higher resolution of the seismic reflectors was preferred over large penetrations, taking into account the shallow water depths and the presence of the first multiple.

1.6.2.1 Acquisition system and recording setup

The sub-bottom seismic profiles were obtained using two BOLT air guns (165 and 175 cubic inches), which were towed behind the vessel stern. The configuration used in the seismic sources was 2,000 psi, a depth of the gun of 3 m, and a firing rate of 15 m over the seafloor. The recording system used was DELPH SEISMICPLUS mini-streaming with a recording length of 4 s and a pre-gain of 8 Hz.

1.6.2.2 Data logging

To decide which recording system was better for the Aysén Fjord characteristics, two streamers were used during the first five lines of the seismic survey. A SIG streamer (225 m long, 150 m active section, three channels along 50 m long sections) and a mini-streamer (100 m long, 25 m active section, one record channel). During the development of this survey was evident that the mini-streamer was better in imagery resolution. Thus SIG streamer was recovered to ease the sailing.

1.6.2.3 Pre-processing

Raw seismic lines were obtained in SEG-Y (Figure 1.11) format in conjunction with the vessel navigation file. Preliminary processing was carried out on seismic lines' raw files, which included removing electrical noise using a 50 Hz filter and applying a gain amplifier (Cruise report DETSUFA). Other basic processes, such as mute and step-band filters, were carried out.

1.6.2.4 Re-interpretated lines

In the case of the Lake Riesco, a previously-published 3.5 kHz subbottom seismic profile (Vargas et al., 2013) was used to discuss the continuity of the morfostratigraphical units observed inland. Methodological details are described in Vargas et al. (2013). Briefly, the seismic data were obtained with a Bathy2000 sub-bottom profiler system, recorded digitally, and seismic units were defined based on the amplitude and reflectors' frequency. The vertical resolution of the 3.5 kHz seismic profiles is 20 – 30 cm, so only the sedimentary units thicker than ~50 cm can be accurately detected and mapped.

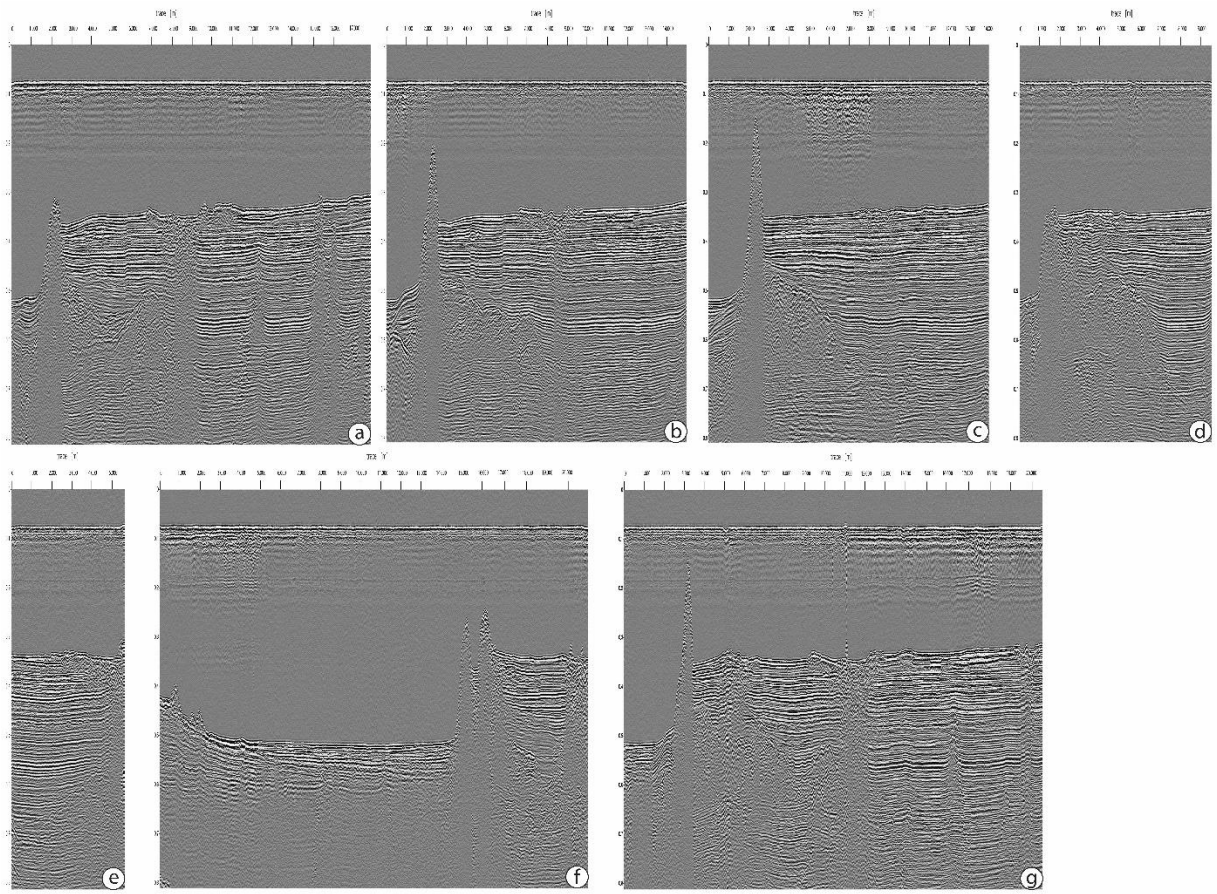

Figure 1.11. Raw seismic lines. (a) SL-05, (b) SL-06, (c) SL-07, (d) SL-08, (e) SL-09, (f) SL-10, (g) SL-15.

1.6.3 Seismic event locations

I compiled information regarding the 2007-AYSS hypocenters location from data recorded by the Chilean National Seismological Center (CSN, Universidad de Chile) (Barrientos et al., 2007; Legrand et al., 2011) (Figure 1.6) and the University of Liverpool (Agurto et al., 2012) (Figure 1.7).

To associate seismic activity with geological structures and propose a geometric model at a crustal-scale, I used two seismic catalogs covering most of the 2007-AYSS. I used data from the CSN local seismic network between 27 January and 21 April 2007. During this first stage, the seismic network consisted of five 3-component seismometers installed around the epicentral area of the M_w 5.2 earthquake (Barrientos et al., 2007). 284 events were recorded before 21 April 2007 (Barrientos et al., 2007; Russo et al., 2011), when the tsunami triggered by the M_w 6.2 earthquake destroyed it. For the following period, I used seismic data published by Agurto et al. (2012), corresponding to the University of Liverpool seismic network. This seismic network consisted of 15 stations and recorded seismic data between July 2007 and February 2008. This dataset is characterized by precise hypocenter relocation based on a 1D crustal velocity model (Agurto et al., 2012). The model is well constrained for

the shallower ~30 km, encompassing the expected seismogenic zone (Lange et al., 2008; Agurto et al., 2012).

In order to support our seismotectonic model of the LOFS in the area, I analyzed the 3D point source position of the studied earthquakes using MOVE 2016.1 software (Figure 1.12). By comparing this last information with active faults defined from seismic profiles and bathymetric data, together with hypocenter clusters and focal mechanisms solutions of the main earthquakes (Agurto et al., 2012), I developed 3D surfaces representing the LOFS branches in Aysén Fjord at upper-crustal scale.

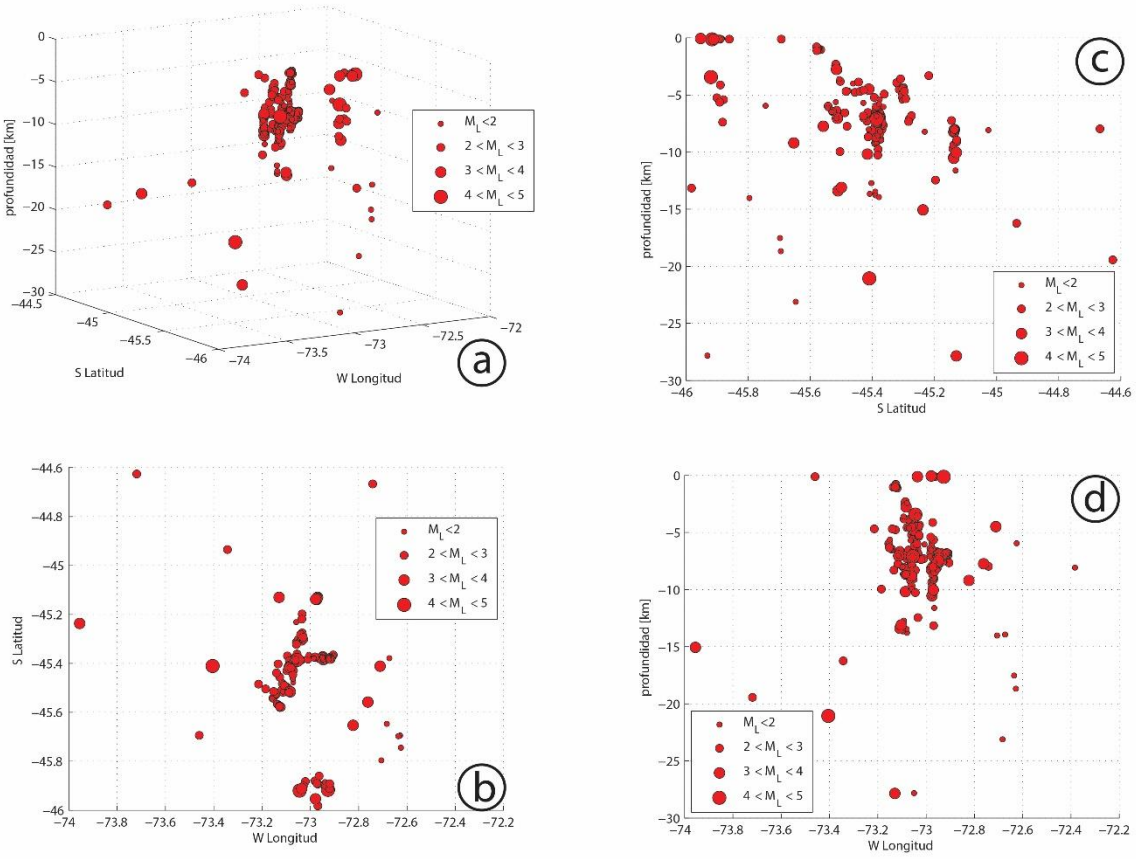

Figure 1.12. Hypocenter distribution of the 2007-AYSS in a 3-D environment of the MOVE software. (a) 3-D view, (b) N-S profile view, (c) W-E profile view, (d) Plan view.

1.6.4 Geomorphological mapping

Due to some times harsh meteorological conditions and thick vegetation cover, the presence of geomorphic features linked to current tectonics activity is difficult to establish. However, it is possible to observe escarpments and other features associated with the LOFS (Vargas et al., 2013; Jara & Melnick, 2009).

I mapped glacial geomorphological features in several zones of the Aysén Region, inside the LGM limits from satellite imagery and in the field. Glacial geomorphological features including frontal and lateral moraines, trim lines, meltwater channels, sandar, alluvial fans, glacial lineations, and cirques, together with other related landforms, were mapped from remotely sensed images and during two field visits in 2004 and 2019. Remotely sensed images include Landsat 7 ETM+ scenes (30 m spatial resolution), pan-sharpened Landsat 7 scenes, and ASTER-GDEM (30 m spatial resolution) satellite images were used to update the maps (Figure B12) already made by Arqueros (2004). Satellite images were overlaid on a Digital Elevation Model (DEM) based on 30 m cell size to provide topographic context and aid landform identification in complex terrain areas. All mapped features were done in ArcMap GIS software.

In addition, three high-resolution remote sensing dataset were used for geomorphology mapping: DEMs with a spatial resolution of 55.6 cm/px, 1.8 m/px, 48.6 m/px (Lake Riesco, Pampa el Diablo, Coyhaique Alto zones, respectively) derived from imagery captured using an unmanned aerial vehicle (UAV) during aerial surveys the first week of July 2019 (Figures B10, B11, B12). The images were taken using a DJI Phantom 4 UAV (Figure 1.13) with an integrated DJI-FC330 camera (3.61 mm focal length, sensor resolution 12.4 MP, 4,000 x 3,000 pixels). Surveys were flown at an altitude of 183, 383, and 314 m, respectively, yielding images with a resolution of 12.4 MP. A total of 192, 141, and 281 images were used to construct the DEMs, selected based on image quality and lighting coherence.

Figure 1.13. Photography of the drone used in our survey. DJI Phantom 4 UAV with an integrated DJI-FC330 camera.

However, the dataset does not provide complete coverage of the study sites in the Aysén Region, covering 0.896, 2.56, and 2.62 km^2, respectively. Thus, the aerial photographs and satellite imagery were primarily used in large and medium-scale geomorphological maps.

Processing of 2019 UAV-captured imagery was undertaken in Agisoft Photoscan Version 1.3.2 build 4,205, which utilizes a Structure-from-Motion (SfM) approach. SfM operates under the same basic principles as stereoscopic photogrammetry, namely that 3D structure can be reconstructed from a series of overlapping, offset two-dimensional images. However, it differs fundamentally from conventional photogrammetry in that the geometry of the scene, camera positions, and orientation are solved automatically without the need to specify a priori a network of targets with known 3D positions (e.g., Westoby et al., 2012). Instead, these are solved simultaneously using an iterative bundle adjustment procedure, based on a database of features automatically extracted from a set of multiple overlapping images (e.g., Ryan et al., 2014; Westoby et al., 2012). Position information can then be introduced after model production in an arbitrary coordinate system, meaning that errors in ground control points (GCPs) will not propagate in the DEM.

The first stage of processing in Agisoft Photoscan involves image alignment. The software implements SfM algorithms to track features through a sequence of overlapping images to estimate the relative location of camera positions for each image and generate a 3D point-cloud of the tracked features. The point-cloud can subsequently be optimized and georeferenced using GCPs or using onboard telemetry data. Following image alignment, a multi-view reconstruction algorithm is applied to produce a 3D polygon mesh based on pixel values (Ryan et al., 2014).

1.6.5 Fieldwork

Field observations on the moraines and other deposits and landforms were made at Coyhaique River Basin for the first time in 2004 (Arqueros, 2004). During 2019 between 1 and 7 July, I visit the Coyhaique River, Emperador Guillermo, and Mañihüales rivers confluence zone, several sites at Aysén River Basin, and the Lake Riesco zone again.

In the 2004 field trip, a geological and geomorphological survey at 1:50,000 scale of an area close to 700 m^2 was done. This survey focused on the identification of quaternary morphostratigraphic units. The area was traveled by van, walks, and difficult areas were carried out by helicopter sampling.

Moraine morphology was characterized using profiles constructed in the field with tape and hand-held GPS. Lithofacies were described in the field based on texture, particle-size characteristics, and clast-shape analyses. A sediment description using binocular loupe and a microscope was made where the sandy sediments were analyzed according to the criteria of Friedman & Sanders (1978). The characterization of the sedimentary facies using the data collected in the field for the subsequent construction and interpretation of 8 stratigraphic columns and stratigraphic profiles of glacial drifts and other geomorphological features as talweg river profiles and glacial terraces.

1.6.6 Radiocarbon dating

As is widely known, radiocarbon dating is one of the first radiometric techniques to be developed. Despite being useful only on Quaternary objects (~50,000 years BP), it is the most widely used dating technique. The first radiocarbon measurements were published in 1949, and since then, hundreds of thousands of dates were produced by more than 100 laboratories worldwide. Below are the basic theoretical concepts and an explanation of the specific technique used in one of the investigations that form this work.

1.6.6.1 Basic principles

Radiocarbon (^{14}C) is one of three isotopes of carbon, the others being ^{12}C and ^{13}C. The most abundant of these is ^{12}C, which comprises around 98.9% of all naturally occurring carbon. ^{13}C forms around 1.1% and ^{14}C one part in 10^{-10}%. Both ^{12}C and ^{13}C are stable isotopes, but ^{14}C is not, and it decays to a stable form of nitrogen, ^{14}N, through the emission of beta (β) particles (one β particle is released from the nucleus for every atom of ^{14}C that decays). It is this instability, or radioactivity, which gives us the name radiocarbon.

In the upper atmosphere, ^{14}C atoms form through the interaction between cosmic ray neutrons, which reach the Earth's atmosphere from deep space, and nitrogen (Lingenfelter, 1963; Castagnoli & Lai, 1980). The process involves neutron capture by the nitrogen (^{14}N) atom, and the loss of a proton, to create ^{14}C. The ^{14}C atoms produced by this process combine with oxygen to form a particular form of carbon dioxide ($^{14}CO_2$), which mixes with the non-radiocarbon containing molecules of CO_2. In this way, ^{14}C becomes part of the global carbon cycle and is assimilated by plants through the photosynthetic process and by animals through plants' ingestion. Oceans absorb most of ^{14}C (more than 95%) as dissolved carbonate, which means that organisms living in seawater will also take up ^{14}C during their life cycle.

Although the ^{14}C in the terrestrial biosphere and the oceans are continuously decaying, it is continually replenished from the atmosphere. Therefore the quantity of ^{14}C stored in plant and animal tissue and the world's oceans, the global carbon reservoir, remains roughly constant. In effect, a position has been reached where the carbon used to build plant and animal tissue is in isotopic equilibrium with the atmosphere (^{14}C activity in plants and animals are the same as that in the atmosphere). The ^{14}C reservoir can therefore be likened to a car with a drip-feed to the fuel tank; the car will use fuel as the engine runs, but as the tank is continuously being topped-up, the fuel will remain at more or less the same level.

Once an organism dies, however, it becomes isolated from the ^{14}C source. No further replenishment of ^{14}C can occur, and the radiocarbon clock runs down by radioactive decay, which occurs at a constant rate. Thus, by measuring the amount of ^{14}C that remains in a sample of fossil material and comparing this to modern ^{14}C in standard material, age can be inferred for the organism's death. In order to be able to

do this, however, we need the ^{14}C decays rate. Experimental results have shown that the ^{14}C decay rate is 1% every 83 years. Rates might imply that after 8,300 years, all residual activity in a sample will have ceased. However, as with all radioactive isotopes, the decay curve for ^{14}C is not linear but exponential (Figure 1.14), and this means that materials significantly older than this can still be dated. The half-life of a ^{14}C atom is 5,730 years, and under normal circumstances, the limit of measurement of ^{14}C activity is eight half-lives. It is modifying the upper age limit of around 45,000 years. Samples older than this are usually described as being of infinite age and are expressed, for example, as >45 000 years.

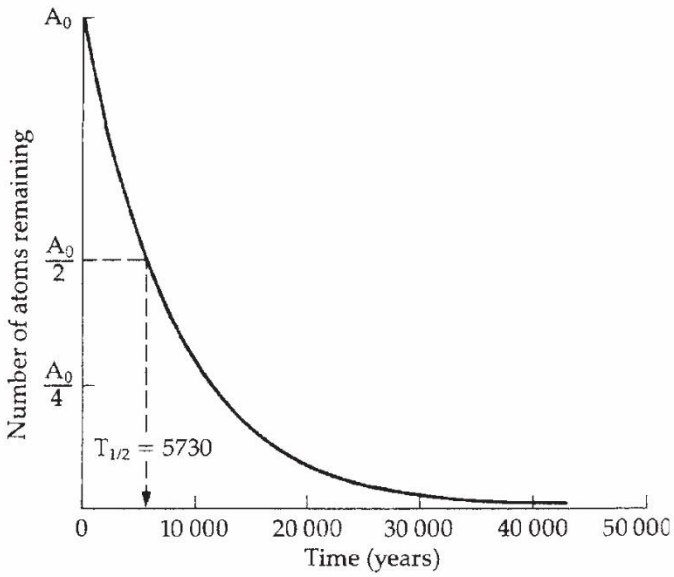

Figure 1.14. The dacay exponential curve for radiocarbon. The percentage decrease in number of atoms in a given unit of time is constant (after Bowman, 1990).

Under exceptional circumstances and by employing relatively large sample sizes, the maximum range can be extended to about 60,000 years (e.g., Geyh, 1965; Stuiver et al., 1979). With isotopic enrichment, ages up to 75,000 years have been reported on a small number of samples (Grootes et al., 1975; Stuiver et al., 1978; Erlenkeuser, 1979). Accelerator mass spectrometry (AMS) technology, combined with approaches to the enrichment of the ^{14}C content in milligram size samples using laser technology, allow the practical extension of the ^{14}C time frame beyond 50,000 years on a routine basis for the typical archaeological sample if the stringent requirements in the exclusion of contaminants both infield and laboratory contexts can be met (Hedges et al., 1980; Stuiver, 1978).

1.6.6.2 Radiocarbon Measurement

Radiocarbon dates can be obtained on a range of biogenic materials. These include i.e., wood, peat, organic lake sediment, plant remains, charcoal, shell, and coral. More problematic are bone and soil, while radiocarbon dates have also been obtained on more unconventional materials, such as cloth, metalwork, or fossil pigment. Two approaches are employed to measure residual ^{14}C activity in samples of

these materials relative to modern standards: beta counting, which involves the detection and counting of β emissions from ^{14}C atoms over some time, working on the principle that the rate of emissions will reflect the residual level of ^{14}C activity within the sample, and accelerator mass spectrometry (AMS), which employs particle accelerators as mass spectrometers to count the relative number of ^{14}C atoms in a sample, as opposed to the decay products. In this thesis, I have used the AMS methodology. Therefore I will focus on explaining this technique in depth below.

1.6.6.3 Accelerator Mass Spectrometry

In the 1980s, a significant breakthrough was made in radiocarbon dating with particle accelerators' employment as mass spectrometers. Mass spectrometers are used to detect atoms of particular elements based on differences in atomic weights. Conventional mass spectrometers cannot discriminate between ^{14}C and other molecules of similar weights, such as ^{14}N. However, by accelerating particles to very high speeds, the small ^{14}C signal can be separated from other isotopes, therefore the term AMS. However, it is essential to emphasize that it is not the absolute number of ^{14}C atoms measured; the abundance of ^{14}C atoms is so small that it would be challenging to measure total amounts. Instead, AMS determines the isotope ratio of ^{14}C relative to the stable isotopes of carbon (^{13}C or ^{12}C). The age is determined by comparing this ratio with that of a standard of known ^{14}C content. The measure is often referred to as isotope ratio mass spectrometry.

The most commonly used system, which involves two separate acceleration phases, is a tandem accelerator (Figure 1.15). Samples are converted to graphite (or a CO_2 source) and mounted on a metal disc. Cesium ions (Cs^+) are then fired at the metal disc with the sample, and the negatively ionized carbon atoms (C^-) produced are accelerated towards the positive terminal. During passage through the stripper, four electrons are lost from the C^- ions (five in some AMS systems), and they emerge with a triple positive charge (C^{3+}, or C^{4+} if five electrons are stripped). The positive terminal's repulsion leads to a second acceleration of the carbon ions through focusing magnets, where deflection occurs according to mass. The signal of the stable isotope ^{13}C (and sometimes ^{12}C) can be measured using Faraday cups, the ^{14}C signal being collected by ion detectors.

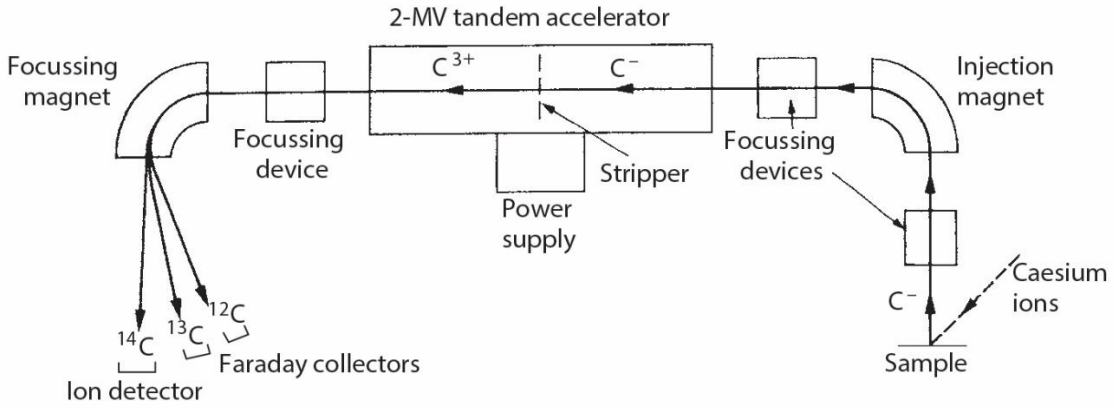

Figure 1.15. Schematic diagram of a tandem accelerator for the detection and counting of ^{14}C atoms (after Bowman, 1990).

Radiocarbon ages can be obtained by comparing the ^{14}C to ^{13}C or ^{12}C ratios of the sample material with those for targets in the same set that have been made up of material of known modern age. The error term that accompanies all AMS dates reflects, as in conventional dating, statistical uncertainties relating to the ^{14}C decay curve, random and systematic errors that occur during the measurement process, and uncertainties that arise in measuring the oxalic acid standards and in quantifying the natural background ^{14}C.

1.6.6.4 Calibration of the Radiocarbon Timescale: Wiggle-Match Dating

To avoid the problems caused by fluctuations in the radiocarbon curve is useful to apply the wiggle-match dating approach. The technique takes advantage of the short-term fluctuations in the radiocarbon calibration curve and can provide more accurate chronologies than individual radiocarbon dates. The simplest example involves the use of tree rings. In that case, high-precision radiocarbon dating is carried out on individual rings whose age differences are known precisely. A resulting curve of dendro-age plotted against radiocarbon age can be fitted (wiggle-matched) to the radiocarbon calibration curve's shape. Wiggle-matching dating has also been applied to peat sequences. However, only the radiocarbon age of individual horizons is known, and the independent (i.e., non-radiocarbon-based) timescale has to be derived by making assumptions about the rate of peat accumulation (Blaauw et al., 2003; 2004). The wiggle-matching technique is best used over a short section of the calibration curve where, in some cases, it may prove possible to match the dated section to within a few years on the calendar timescale (e.g., Hogg et al., 2002). Various statistical approaches to wiggle-matching have been developed, some again including Bayesian analysis (Christen & Litton, 1995), and these can generate dating ranges that are even tighter than the combined errors in the original radiocarbon measurements. The result is a higher level of overall dating precision (Ramsey et al., 2001). Computer programs are now available for curve fitting, and these are available via the Internet. They include Cal25 (Van Der Plicht, 1993) and OxCal, which can perform radiocarbon calibration and automatic wiggle-matches (Ramsey, 1995; 1997).

1.6.6.5 My Work

In my second investigation, I used radiometric techniques to constrain the ages of glacial fluctuations. The new data allow us to elucidate two significant problems within the Patagonian Andes. (i) Assess the palaeoclimatic significance of the moraine systems and associated glacier fluctuations; (ii) to limit –have a reference framework– the age of the fjords' sedimentary infill and recognizable buried moraines. The latter aims to constrain the paleoearthquake ages detected in the Aysén Fjord and similar situations within other nearby glacial basins.

I dated eight samples and re-used four samples from glacial and glaciofluvial sediments at sites located on the moraines' northern and southwestern flanks using radiocarbon methods. In some places as the Lake Riesco zone, dense vegetation

obscures most of the moraine, so sample collection was limited to natural exposures. Critical to the sampling strategy was to find sedimentary facies containing organic material but without current bioturbation. Therefore, I targeted localities with exposures of muddy sediments and glaciofluvial sand, where it occurs either within outwash sediments or within discrete meltwater channels cut into the moraine. The total number of samples is therefore limited because, for the central part, the moraine is composed of diamicton.

Most of the samples came from the interdrift fine deposits, particularly where glacial sediments overlay ancient undisturbed surfaces. I calculate radiocarbon ages using the CALIB v.7.0.4 software calibration tool (Stuiver et al., 2018) and ShCal13 Southern Hemisphere Curve (Hogg et al., 2013). Ages are presented in the text as average age cal. Ka BP (Appendix Figures B5 – B8).

Chapter 2: Geodynamics and Climate

2.1 Geological setting

2.1.1 General geology

Longitudinal domains with an N-S strike characterize the geology of the North Patagonian Andes (Figure 2.1). In the west of the region, there is a metamorphic domain formed by a Paleozoic Mes-Cenozoic basement and meta-sedimentites, with meta-volcanites of Cretaceous age (Traiguén Formation), a central Meso-Cenozoic plutonic complex, and a westward Pleistocene-Holocene volcano-sedimentary domain (Cembrano et al., 2002; Niemeyer et al., 1984; Pankhurst et al., 1999).

North Patagonian Batholith (NPB) crops out along the axis of the Southern Andes. It is mainly composed of Cenozoic and Mesozoic granitoids, where the hornblende-biotite tonalities and granites are the primary lithology (Pankhurst et al., 1999; Parada et al., 2007). NPB is limited to the west by Mesozoic metamorphic rocks, which on Chonos Archipelago western side and the Taitao Peninsula, and eastward by Mesozoic volcanic rocks (Parada et al., 2007).

Five of the thirteen quaternary volcanoes that are part of the Southern Segment of the Southern Volcanic Zone (42° - 46° S) are close to my study zone (Melimoyu, Mentolat, Cay, Macá, and Hudson volcanoes). Except for the Cay volcano, all the volcanoes have erupted during the Holocene, with the Hudson volcano being the most active (Stern et al., 2007). Their lithologies are dominated by basaltic to dacitic lavas and pyroclasts composition (Naranjo & Stern, 1998; D'Orazio et al., 2003).

The soils in this area are dominated by andosols, which are soils developed on volcanic deposits (Gut, 2008; Vandekerkhove, 2014).

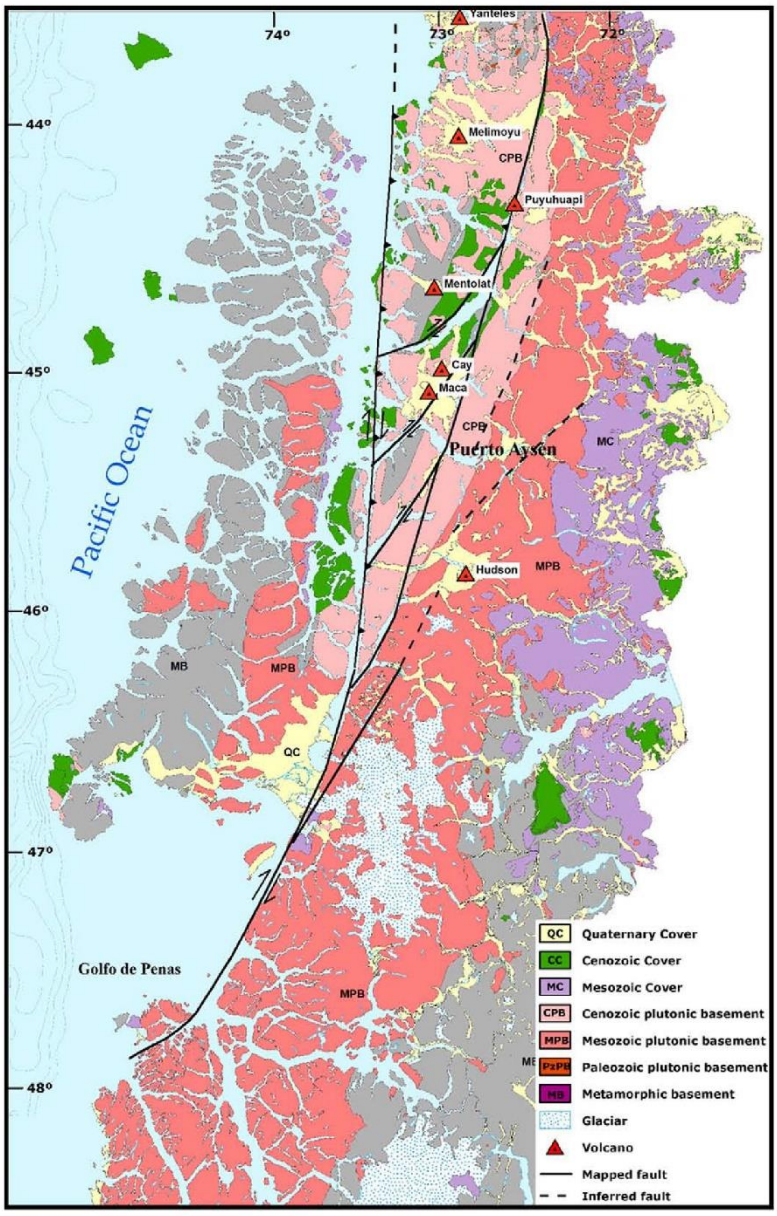

Figure 2.1. Regional scale geology of the Chilean Andes between 43.5°S and 48.5°S, modified from 1:1.000.000 scale map, Servicio Nacional de Geología y Minería, Chile and previous compilations by various authors (Cembrano et al., 1996a, 2002; Thomson, 2002). The present-day volcanic arc, located along the axis of the main cordillera, is built on top of a Meso–Cenozoic plutonic basement of the Patagonian Batholith. Extracted from Cembrano & Lara (2009).

2.1.2 Sedimentary infill in patagonian fjords

Silva & Prego (2002) generated a division of the entire Patagonia fjord infill into three large macro-zones based on carbon and nitrogen concentrations distribution in the sediments: the northern (from Puerto Montt to Taitao Peninsula), central (from Golfo de Penas to Magellan Strait), and southern zones (from Magellan Strait to Cabo de Hornos).

Patagonian fjordland macro-zones have organic carbon values ranging from 0.38 to 1.7% (northern zone), 0.44 to 1.43% (central zone), and 0.29 to 0.90% (southern zone) (Silva, 2008). Terrigenous organic matter in the sedimentary infill increases from the oceanic areas towards the fjords headwaters. The latter is associated in most cases to the main river discharge (Pinto & Bonert, 2005). Sediments deposited by glaciers have a meager amount of organic matter due to the dilution associated with a large amount of inorganic matter (Silva, 2008).

High sedimentation rates characterize Chilean fjordland. ^{210}Pb depositional rates (estimations) range between 0.26 and 0.3 cm/yr in Aysén Fjord and Canal Costa (Rojas, 2002; Salamanca & Jara, 2003; Van Daele et al., 2013). Meanwhile, in Cupquelán and Quiltralco fjords, these values have an average of 0.15 cm/yr and 0.67 cm/yr, respectively (Salamanca & Jara, 2003). In the Puyuhuapi Channel case, the values range between 0.25 and 0.75 cm/yr (Rebolledo et al., 2005; Sepúlveda et al., 2005).

Terrigenous organic matter in these fjords comes from surroundings, mainly from the evergreen rain forest (Villagrán, 1988). The anthropogenic contribution to organic matter is mainly confined to the region's major cities: Puerto Montt, Castro, Puerto Aysén, Coyhaique, and Punta Arenas.

Sediments of the region were initially formed by glacial debris deposition, followed later by glaciofluvial deposition (Araya-Vergara, 1997). Recent marine sedimentation began during the last ice age when ice melting raised sea level in 120 m. Close to 12,000 years BP, glacial lobes were well expanded and occupied the entire basin (Clapperton, 1994).

2.2 Plate boundaries settings

The Central-Southern Chilean margin is one of the most active plate boundaries on Earth. This extensive margin encompasses the Great Chilean (Valdivia) earthquake rupture zone (M_w 9.6), the largest earthquake on record, with 1,000 km long in the forearc between the parallels ~37° and 46° S (Plafker & Savage, 1970; Cifuentes, 1989) (Figure 1.1a).

From Aysén Fjord to Coyhaique Basin, the study areas are located close to the southern end of an oblique subduction margin between Nazca and South American plates. The convergence rate is ~6.6 cm/yr (Angermann et al., 1999) (Figure 1.2), or 7.4 cm/yr based on paleomagnetic analysis data from the seafloor (DeMets et al., 2010).

In this segment of the Patagonian Andes, the Chile Ridge (CR), an active structure currently subducting offshore Taitao Peninsula (Herron et al., 1981; Cande et al., 1987; Tebbens et al., 1997) in the called Chilean Triple Junction. This tectonic configuration is unique in the world as it is the only Trench-Ridge-Trench collision in

which the ridged plate corresponds to a continental lithosphere (Agurto-Detzel et al., 2014). Northward of the triple junction, a younger and buoyant portion of the slab is subducted at a rate of 6.6 cm/yr, while southward Antarctic Plate is subducted at 2 cm/yr under the South American Plate (DeMets et al., 2010; Wang et al., 2007).

Features associated with the CR subduction under the triple junction were observed by several authors such as tectonic erosion, plutonism close to the trench, the Late Cretaceous uprising (Cande & Leslie, 1986), and the presence of an ophiolite complex in the Taitao Peninsula (Forsythe et al., 1986), and the displacement of a microplate (sliver) in the forearc (Wang et al., 2007). Another essential characteristic of this tectonic feature is generating a ~350 km long volcanic gap within the arc (Ramos & Kay, 1992). In the back-arc, a basaltic plateau-like is widely distributed (Ramos & Kay, 1992; Gorring et al., 1997). This basaltic plateau would be associated with a period where the slab-window passed through that place (Ramos & Kay, 1992).

Northward triple junction, Bohm et al. (2002) defined a 30° Wadati-Benioff zone eastward with earthquakes reaching 150 km depth between 36° and 40° S. Lange et al. (2008) found seismicity between 12 and 70 km depth, defining a Wadati-Benioff zone with inclination ranging between 30° and 33° eastward, between 41.5° and 43.5° S.

Another important feature within the Nazca Plate in Southern-Central Chile is the Valdivia Fracture Zone at 40° S (Figure 1.1b). This lithospheric discontinuity separates the oceanic crust generated by CR southward from that formed in the Eastern Ridges of the Pacific northward (Tebbens & Cande, 1997). It has been proposed that these features could influence coseismic and inter-seismic sliding patterns.

2.3 History and evolution of the convergent margin

The convergence vector between the two plates has changed both in direction and velocity at geological time-scale (Pardo-Casas & Molnar, 1987; Somoza, 1998; Quinteros & Sobolev, 2013) (Figure 2.2). These changes are mainly associated with South American Plate deformation stages (Somoza, 1998) or the Nazca Plate passage in the transitional zone and lower mantle (Quinteros & Sobolev, 2013).

The Farallon Plate began subducting under South America ~50 Ma ago with a NE strike and a highly oblique angle. Between 26 and ~20 Ma ago, in response to Farallon Plate fragmentation (in the Nazca and Coco oceanic plates), the convergence vector changed again to be almost orthogonal to the trench, and the velocity rate increased between 10 to ~15 cm/yr (Pardo-Casas & Molnar, 1987; Somoza, 1998) which coincides with the beginning of the uprising in the Andes (Somoza, 1998). About 20 Ma ago, the convergence vector adopted its current state (N77°E) (Pardo-Casas & Molnar, 1987; Kendrick et al., 2003) with a velocity rate ranging between 6.3 and 7.9 cm/yr (Angermann et al., 1999; Kendrick et al., 2003).

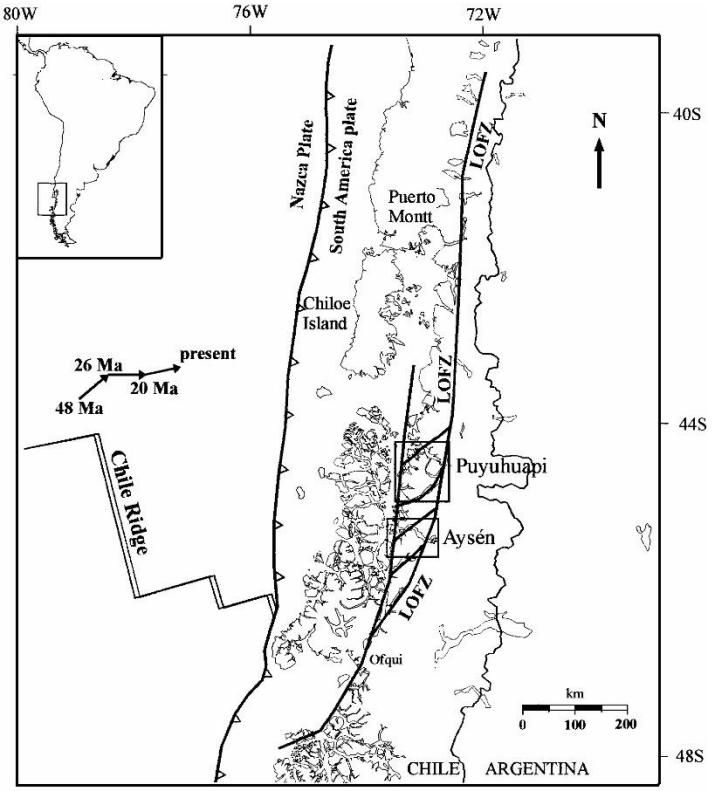

Figure 2.2. Regional scale geometry of the Liquiñe–Ofqui fault zone and geotectonic setting of the southern Chilean Andes. Relative Nazca–South America plate motion vector was highly dextral-oblique to the trench between 49 and 26 Ma, nearly orthogonal between 26 and 20 Ma, and slightly dextral-oblique after 20 Ma (modified from Pardo-Casas & Molnar, 1987). Extracted from Cembrano et al. (2000)

During the Late Miocene (10 Ma), the Chile Ridge started to collide with the South American Plate generating the triple junction (Forsythe & Nelson, 1985). The steady right-lateral oblique convergence vector between Farallon (Nazca) and South American plates since Eocene (50 Ma) induced strain partitioning with a W-E shortening in the forearc and right-lateral shear strain in the arc. The latter defined a transpressive tectonic setting confirmed by the regional seismicity (e.g., Cifuentes, 1989; Dewey & Lamb, 1992; Murdie et al., 1993).

2.4 Regional geomorphology

Southern Chile is characterized by an extensive fjord and channels area, which extends between Puerto Montt (41° 30' S) and Cape Horn (55° 30' S). It covers 241,000 km^2. Southern Chile is also characterized by an extensive coastline, made up of many islands, fjords, straits, and gulfs.

This estuarine system's basins resulted from the glacial erosional activity and tectonic sinking of the longitudinal valley (Borgel, 1970). This system is part of the most extensive coastal estuarine system in the world as Alaska, British Columbia, Iceland, Greenland, and Norway (Cameron & Pritchard, 1963; Rabassa, 2008; Rabassa et al., 2011).

Pickard (1971) subdivides the Chilean fjords into three segments based on their geomorphological features:

1. Northern fjords (Puerto Montt to San Rafael Lagoon)
2. Central fjords (Golfo de Penas to Strait of Magellan western mouth)
3. Southern fjords (from Magellan Strait to the Almirantazgo Fjord)

My study area, which corresponds to Aysén Fjord, is located in the northern segment of the Chilean fjord zone. The study area corresponds to an estuarine area. It has restrictive circulation and dilution of salty water by freshwater flows of terrestrial origin (Cameron & Pritchard, 1963). This region receives significant contributions of particulate terrestrial material with high sedimentation rates occurring in fjords. Sediment accumulation is high.

Sediments of the region were initially formed by glacial debris deposition, followed later by glaciofluvial deposition (Araya-Vergara, 1997). Recent marine sedimentation began during the last ice age when ice melting raised sea level in 120 m. Close to 12,000 years BP, glacial lobes were well expanded and occupied the entire basin (Clapperton, 1994). The remainder of this glaciation in this segment corresponds to the northern ice fields (~46° S).

The northward segment of the fjord and channels area can be divided into two sub-segments based on its ocean waters – freshwaters exchange regime. (a) Chiloé Island inland coastal zone, which is composed of two basins, including Golfo Ancud, connected to the Pacific Ocean through Chacao Channel, and Golfo Corcovado connected to the ocean by the Boca Del Guafo. Desertores Islands partially separates these large basins. The few fjords in this area include Reloncaví, Comau, and Reñihue. (b) The southern basin has the broad and deep Moraleda Channel as its central axis. One of its relevant hydrographic characteristics is the narrowing of this channel and the presence of constriction and sill with a variable depth between 50 and 60 m at its southern end known as Meninea Narrowing (45° 16' S; 73° 38' W) (Silva et al., 1995).

This constriction separates the sector into two areas. Puyuhuapi and Jacad fjords northward; Aysén, Quitralco, and Cupquelán southward all connected by Moraleda and Elefantes channels, ending at Laguna San Rafael. This lagoon is in front of an active glacier, part of the northern ice fields (Ahumada & Rudolph, 2004). With depths close to 150, this southernmost area is isolated from the oceanic influence due to the damming effect of its narrow entrance (Guzmán & Silva, 2002).

2.4.1 Southern sub-segment fjords and Aysén Fjord

The fjords in this sub-segment have irregular shapes with deep beds. These have numerous constrictions and elevations that inhibit circulation (Silva & Prego, 2002). This complexity is also reflected on a regional scale, with narrow channels and numerous separating islands that separate the Pacific Ocean from the mainland.

Bathymetric surveys have shown deep valleys, reaching about 600 m at the mouth of the fjords, and several moraine sills (Araya-Vergara, 1997, Rodrigo, 2008). The presence of these sedimentary structures control the water exchange with the Pacific Ocean and also allowing high sedimentation rates and organic material preservation (Sepúlveda et al., 2005; Silva & Guzmán, 2006; Sievers, 2008).

The Aysén Fjord has a strike ranging from EW to NW-SE with the typical u-shape of a glacial valley. This fjord is cut by the Liquiñe-Ofqui fault system branches and other secondary tectonic structures (Vargas et al., 2013).

2.4.2 Glacier Ice

Currently, Patagonia has three major glacial systems: Northern Patagonian Ice Field (between 46° - 47° S); Southern Patagonian Ice Field (48° - 52° S); and Cordillera Darwin Ice Field (54° - 55° S). Immediately southward the study area, there is the Northern Patagonian Ice Field, covering 4,200 km^2. It consists of about 70 glaciers larger than 0.5 km^2 (Rivera et al., 2007).

2.5 Seismotectonics of Southern-central Chile

The Chilean subduction zone in its southern segment has presented several large megathrust earthquakes during the last hundreds of years (Figures 1.1 and 2.3). Based on historical documents that recorded the impact of these events in the Southern Chile since the arrival of the Spanish colonizers in 1551 (i.e., historical earthquakes), geoscientists have proposed two large adjacent seismotectonic segments usually delimited in the subduction zone: the Constitución Segment (Maule) and the Valdivia Segment, which were affected by the 2010 Maule and 1960 Great Chilean earthquakes, respectively (Métois et al., 2012).

The last major event in the central and southern segments of the Chilean subduction zone was the 2010 Maule Earthquake (Figure 2.3). The event magnitude was M_w 8.8, and it had a ~500 km long rupture, covering the Constitution (Maule) Segment (Moreno et al., 2012). In anticipation of this event, a large seismic potential (seismic gap) was suspected based on historical events (Campos et al., 2002) and geodetic measurements (Moreno et al., 2008; Ruegg et al., 2009). Coastal uplift data (Farías et al., 2010), as well as slip models (Lay et al., 2010; Tong et al., 2010), suggest that the Maule Earthquake extended approximately between the 33.5° parallels and

38.5° S. Interseismic models with their coupling patches calculated from GPS observation inversions during the decades before the event (Madariaga et al., 2010; Moreno et al., 2010) suggest that the plane was highly blocked but in a heterogeneous way.

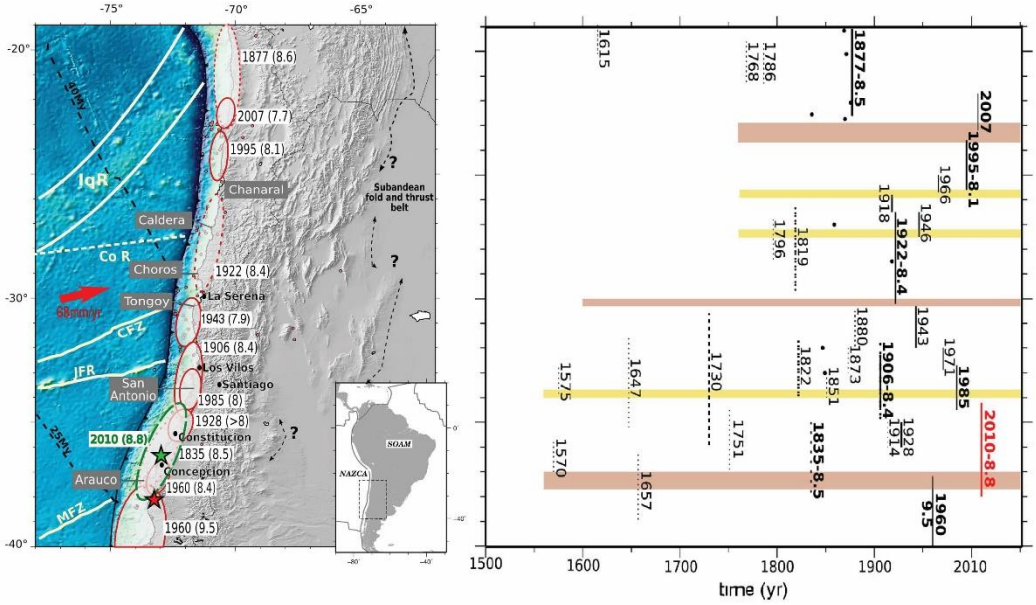

Figure 2.3. Left-hand side: Seismotectonic background of the Nazca playe and South American plate's convergence zone and main geological features. Topography and bathymetry are from ETOPO1. Red contoured ellipses: maximal rupture zones of the M>7.5 historical (dashed) and instrumental (solid) earthquakes since 1830 (Beck et al., 1998; Comte & Pardo, 1991; Biggs & Robinson, 2009). Green ellipse: rupture zone of the 2010 Maule earthquake. Green star: relocated hypocenter for the Maule event (Vigny et al., 2011). Red circles: Mw>6 events since 1976. Right-hand side: Largest estimated rupture lengths of the main identified historical earthquakes since 1500 against time. Dashed and solid lines mean high and low uncertainty on those ruptures, respectively (Lomnitz, 1970; Beck et al., 1998; Campos et al., 2002)

The Valdivia Segment covers from 37.5° to 46° S and is mainly recognized for generating the 1960 Great Chilean (Valdivia) Earthquake, the largest seismic event recorded by seismological instruments (Plafker & Savage, 1970; Cifuentes, 1989; Moreno et al., 2009) (Figure 1.1). The rupture was ~1,000 km long, with a 17 m average, and a 44 m local maximum was modeled (Barrientos & Ward, 1990; Moreno et al., 2009). Within the Valdivia Segment, contemporary surface deformation includes a prolonged post-seismic effect of mantle rebound and blocking the seismogenic zone (Hu et al., 2004; Khazaradze et al., 2002). The interpretation is based on the fact that the GPS vectors within the rupture zone are smaller than those located northward. Those GPSs located further inland (along the intra-arc and the trans-arc) move in the direction of the sea, opposite to the inter-seismic contraction deformation.

This megathrust rupture zone is correlated with the LOFS. Furthermore, another critical feature parallel to this segment is the forearc close to the LOFS, corresponding to the Chiloé Micro-plate (sliver). It was described as a decoupled block from a stable South America plate using geological (Rosenau et al., 2006), seismological (Lange et al., 2008), and geodetic data (Wang et al., 2007).

The existence of tectonic control in the inter-seismic earthquake cycle is evident. These two seismotectonic segments overlap in the Arauco Peninsula area, which corresponds to the prominent promontory along the Pacific margin of South America. It has remained stable since the Pliocene and is characterized by a rapid uplifting during the Quaternary (Melnick et al., 2009). Several hypotheses were proposed to explain the barrier between these two seismotectonic segments (37.5° to 38.5° S): i) a significant continental basement discontinuity (Melnick et al., 2009). It was associated with the Lanalhue Fault, a presumed crust-scale structure inherited from Permian times (Glodny et al., 2008); ii) significant bathymetric features on the oceanic plate (Sparkes et al., 2010; Moreno et al., 2011), or massive landslides deposits (Geersen et al., 2013). This would generate low interplate coupling; iii) activity along the fault systems branches realizing coseismic slip, and producing permanent shortening in the upper plate (Moreno et al., 2012).

The most crucial megathrust earthquake after the Maule Earthquake was an M_w 7.1 in January 2011. It corresponds to the largest replica related to the M_w 8.8.

2.5.1 Historical Earthquakes in South-Central Chile

Until the 2010 Maule Earthquake, the area was dominated by a post-seismic deformation linked to the M_w: 9.5 Valdivia Earthquake (Plafker & Savage, 1970; Cifuentes, 1989; Barrientos & Ward, 1990; Klotz et al., 2001; Wang et al., 2007; Moreno et al., 2009; Ruiz et al., 2017). Ruiz et al. (2017) proposed that some historical events within this seismogenic segment could have been overlooked due to low or no population density. Some of these recognized historical earthquakes are 1575, 1737, 1837, and 1960. They were first proposed as earthquakes with similar characteristics to M_w: 9.5 Valdivia Earthquake, and an average recurrence of 128 ± 62 years were calculated (Nishenko, 1985). Later in the work of Cisternas et al. (2005), evidence was presented that the earthquakes in Southern Chile are widely diverse in the rupture length (e.g., Cisternas et al., 2017a). Among these, the 1575 earthquake may have had a great similarity to the 1960 event (Ruiz & Madariaga, 2018). It has also been recognized that the 1737 earthquake may have occurred in the northern segment of the 1960 rupture and broke the deeper zone of the plate interface, and so far, no evidence of tsunamis is recognized, but damaged distant towns (Cisternas et al., 2017b; Ruiz & Madariaga, 2018). In contrast to the previously named earthquake, 1837 earthquake was studied using paleoseismological approach (e.g., Cisternas et al., 2005; 2017a; 2017b; Moernaut et al.; 2014; 2018) shown that it generated a transoceanic tsunami but with an estimated rupture lower than 1960 (Cisternas et al., 2017a, 2017b).

This part of subduction zone (from 37° S to 47° S) is characterized by deformation and slip partitioning of the horizontal component (dextral slip) associated with the oblique convergence of the Nazca and South American plates in the Liquiñe-Ofqui Fault System (Cembrano et al., 1996a). This fault system, which corresponds to the main object of study of this thesis, was tentatively associated with the M_w: 9.5 Valdivia Earthquake through an M_w: 7.7 slow aftershock (Kanamori & Rivera, 2017).

This main event (M_w: 9.5 1960 Valdivia Earthquake) is also recognized as precursor earthquakes, highlighting the event M_w: 8.1 of May 21, 1960, which is considered the beginning of the sequence that gave rise to the M_w: 9.5 Valdivia earthquake (Cifuentes, 1989; Cifuentes & Silver, 1989), named by Ruiz & Madariaga (2018) as the 1960 Concepción Earthquake. Another of this group of earthquakes is the M_s: 7.8 event that occurred 15 minutes before the mainshock (Duda, 1963; Kanamori & Cipar, 1974). These earthquakes have been classified as interplate events by Ojeda et al. (2017) through an inversion of the data provided by Plafker & Savage (1970).

2.5.2 Liquiñe-Ofqui fault system

The main structural feature in the Patagonian Andes is the intra-arc transpressional Liquiñe-Ofqui Fault System (LOFS), a predominantly dextral transcurrent fault system, parallel to the trench (Cembrano et al., 1996a; 2007b) (Figure 3.1).

The LOFS extends for ~1,200 km long between 38° and 47° S (Forsythe & Prior, 1992; Hervé, 1994; Cembrano et al., 1996a; Lavenu & Cembrano, 1999; Cembrano et al., 2002; Legrand et al., 2011). In the study area, the system is formed by two NNE parallel regional lineaments connected by at least four NE en-échelon lineaments that define a duplex structure (Hervé, 1994). In Aysén Fjord and surroundings areas, quaternary volcanoes, such as the Macá-Cay volcanic complex to the north, and Hudson volcano to the southeast (Niemeyer et al., 1984; D'Orazio et al., 2003), are associated with dozens of Holocene monogenetic cones located along lineaments parallel to the main faults or directly along traces of the major structures in the area (Vargas et al., 2013). A structural control by the LOFS in the distribution of Quaternary volcanism was proposed by Cembrano & Lara (2009).

After its discovery by Steffen (Steffen, 1944; Hauser, 1991), several authors have provided estimations of the fault system length, or at least to its main lineaments. It is currently accepted that the LOFS starts immediately south of the Chilean Triple Junction, in the Golfo de Penas area (47° S), and is considered as an extension of the Cenozoic basin and the trailing edge of the Chiloé Microplate (Forsythe & Nelson, 1985; Cande & Leslie, 1986; Rojas et al., 1994). Northward, the LOFS prolongs until Copahue volcano (38° S) (Lavenu & Cembrano, 1999; Rosenau et al., 2006), where it reaches Argentina and continues through the Arauco transfer zone in a dextral jump to the right and merge with the Cenozoic Corral Antiñir - Copahue thrust-and-fold belt (Folguera et al., 2004; Melnick et al., 2006, Melnick & Echtler 2006).

Its detailed geometry and, also, the continuity in-depth, remains poorly controlled. As previously mentioned, LOFS is frequently described at a regional scale, taking into account only those works where onland fault traces were mapping or inferred by lineaments (e.g., Cembrano et al., 1996a; Pérez-Flores et al., 2016), published and unpublished data on fragile deformation (Cembrano et al., 2000; Vargas et al., 2013; Pérez-Flores et al., 2016), shallow earthquakes hypocenters and scarce focal mechanisms (Agurto et al., 2012; Chinn & Isacks, 1983; Dziewonski et al.,

1990;1995; 1999; Lange et al., 2008). The mapping of quaternary volcanoes and ephemeral eruptive centers (monogenetic cones) has also been used.

The duplex area was interpreted as a positive flower-shaped structure with uplifted blocks evidenced by different cooling ages as indicated by fission tracks thermochronology studies (Thomson, 2002) (Figure 2.4). It could be inferred that the presumed structures that form the western lineament would dip slightly eastward.

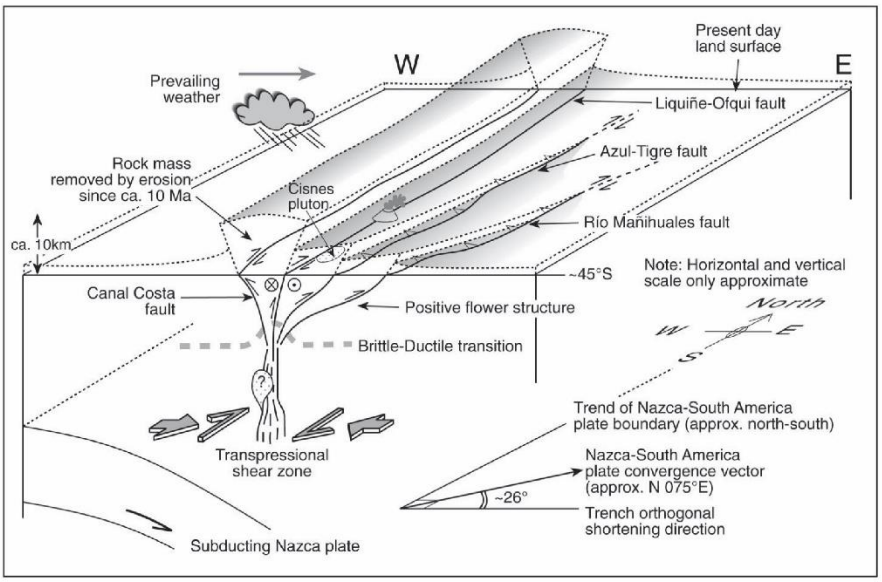

Figure 2.4. Three-dimensional block diagram interpretation of the Liquiñe-Ofqui Fault System at 44°–45°S. The LOFS and the major oblique-slip or reverse faults to the east are interpreted as a positive transpressional flower structure by Thomson (2002).

The seismicity and shallow depth focal mechanisms recorded both in the northern (Lange et al., 2008) and southern (Agurto-Detzel et al., 2014) parts of the LOFS has allowed to identify fragile deformation within the LOFS and prolong it between 12 and 20 km depth. Mylonite outcrops demonstrate internal shear structures with kinematics and ages consistent with tectonic evolution history (Cembrano et al., 2000). The latter suggests a development at depths beyond the brittle-ductile transition zone. Furthermore, investigations such as those carried out by Lara et al. (2008) on several monogenetic cones located along the fault trace show a tholeiitic chemical signature, defining the presence of poor-evolved magmas (e.g., Caburgua, Ralún-Cayutué, and Puyuhuapi), suggesting that these faults could work as pipes pumping asthenospheric magmas (Cembrano & Lara, 2009).

The latter hypothesis gives more robustness to the idea of a fully decoupled lithospheric block west of the LOFS (Chiloé microplate) (Beck et al., 1993; Lavenu & Cembrano, 1999; Rosenau et al., 2006; Wang et al., 2007) (Figure 2.5).

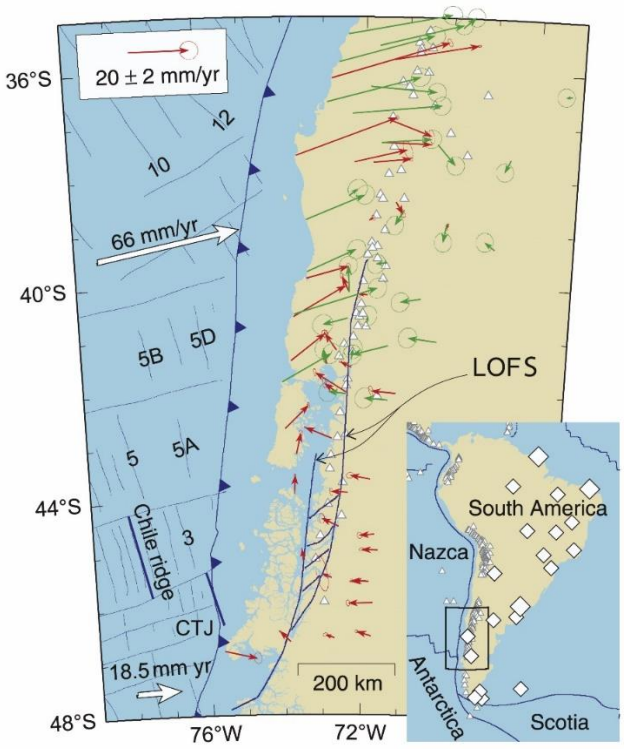

Figure 2.5. Tectonic setting of the Chile margin and GPS velocities. Labeled large arrows are plate motion vectors relative to South America. Triangles indicate locations of volcanoes. GPS velocities published by Wang et al. (2007) are shown with red arrows. GPS velocities published by Klotz et al. (2001) are shown with green arrows. LOFS: Liquiñe Ofqui Fault System, CTJ: Chile triple junction. Modified from Wang et al. (2007).

The oblique convergence of the Nazca Plate beneath the South American Plate, at an ~18° angle (respect to the orthogonal to the trench) (Angermann et al., 1999), explains a significant part of the total partitioning in trench parallel transcurrent and compressional deformation, defining a dominant transpressional mechanism along the LOFS (Beck, 1988; Cembrano et al., 1996a, 2000, 2002; Rosenau et al., 2006).

Other factors may influence such a deformation, such as a strong interplate coupling and a thermally weakened continental crust (De Saint Blanquat et al., 1998; Legrand et al., 2011). Forsythe & Nelson (1985) and Cembrano et al. (2002) proposed an indenter-type mechanism produced by a CR-trench interaction, a mechanism that would generate decoupling of the Chiloé sliver from the continental plate along the LOFS. Cembrano et al. (2002) also proposed that both transfer mechanisms may work simultaneously and could control short- and long-term deformation, respectively, along with this fault system.

2.5.3 Other faults (diagonal to LOFS)

Other regional scale structures recognized in the Southern Andes are NW-SE striking curved lineaments extending west of the LOFS main trace (Hervé, 1976; Hervé & Thiele, 1987; Cembrano & Hervé, 1993). The most studied of these lineaments are Bío-Bío Fault Zone (Bohm et al., 2002), Mocha-Villarrica Fault (Melnick et al., 2003),

and Lanalhue Fault (Glodny et al., 2008). These lineaments are interpreted as reactivated ancient basement structures apparently with left lateral-reverse kinematics shown by offsets in the LOFS trace (Glodny et al., 2008; Lange et al., 2008; Melnick et al., 2009).

Conversely, Rosenau et al. (2006), relying on fault-contact, proposes that these left lateral faults are coeval with LOFS. As already mentioned, some of them extend from the coast to the main mountain range and could be accommodating the Chiloé microplate, hence separating blocks with different histories (Bohm et al., 2002; Hackney et al., 2006; Melnick et al., 2009).

Eastward LOFS between 44° and 46° S, two major structures with NNE-SSW strikes are described: Azul - Tigre Fault (sensu Romero, 1983, Thomson, 2002) and Río Mañihuales Fault. J. Cembrano studied the Azul -Tiger Fault in a Queulat shear zone segment. There several hundred meters of shear zones with right lateral-inverse kinematic indicators are exposed.

2.5.4 Kinematic regime history and evolution

The LOFS partition part of the margin parallel component of the oblique convergence between the Nazca and South American plates. Additionally, the existence of a structural control quaternary volcanism disposal was proposed (Cembrano & Hervé, 1993; Cembrano & Moreno, 1994; Cembrano & Lara, 2009).

Several types of mechanisms were proposed for the LOFS displacement. Some authors consider only oblique subduction (e.g., Hervé 1976; Beck 1988; Cembrano et al. 1996a; 2000; 2002). Others incorporate an indenter mechanism caused by Chile Ridge subduction (e.g., Forsythe & Nelson 1985; Cembrano et al. 2002). This indenter could be causing a detachment along the fault plane in the forearc, between the Chiloé microplate and the continental margin. Cembrano et al. (2002) propose that both oblique subduction and indenter mechanism generate transpressive deformation along the continental border and give oblique convergence a long-term deformation during the collision of CR the short-term control. Cembrano et al. (2000) proposed strong interplate coupling due to the subduction of a young, buoyant oceanic lithosphere northward of the triple junction and a thermally weakened continental crust.

The LOFS is characterized as a continental scale shear zone. The structure would have its origin from the Farallon Plate convergence (Cembrano et al., 1996a; 1996b). A wide variety of kinematic and thermochronological evidence supports this hypothesis. Pankhurst et al. (1999) and Cembrano et al. (1996a, 2000) described mylonitic belts and 1 to 2 km wide cataclastic zones in the LOFS northern segment (ca. 41.8° S). Also, they described left-lateral reverse shear indicators dated in ca. 100 Ma (pre-Late Cretaceous). The Late Eocene - Early Miocene sedimentary basin formations close to LOFS (~46° S) (Rojas et al., 1994) recorded a transtensional regimen that coincides with right-lateral oblique subduction between 48 and 26 Ma (Pardo-Casas & Molnar, 1987). At 26 Ma, when the convergence closely orthogonal to

the trench, the basins were uplifted, thrust, and affected by calc-alkaline granitic intrusions (Pardo-Casas & Molnar, 1987; Cembrano et al., 1996b).

At 20 Ma, a right-lateral oblique convergence vector to the trench with high rates (Pardo-Casas & Molnar, 1987), and strong coupling favored a transpressive left-lateral regime along the arc (Cembrano et al., 1996a, 1996b). Evidence supporting this is the complex, fragile deformation patterns associated with dominant right-lateral reverse faulting in LOFS northern segment (ca. 41° S) (Cembrano et al., 2000). These fault rocks are much younger and cut Miocene plutons (Cembrano et al., 2000). Furthermore, intrusive bodies and metamorphic rock studies in the LOFS central segment (30° - 42° S), as well as syntectonic plutonic sites (Nakamura, 1977; Cembrano et al., 1996a; 2007b).

During the Late Miocene (ca. 6 Ma), the collision of three Chile Ridge segments between 46.5° and 47° S caused a transpressional regime and rapid exhumation (Cembrano et al., 2002; Thomson, 2002). Lavenu & Cembrano (1999) and Cembrano et al. (2000) proposed that this series of collisions generated the most recent right-lateral kinematics stage in the LOFS (42° - 47° 30’ S). Evidence of this right-lateral deformation stage is observed in a 4 to 5 km wide brittle-ductile deformation zone cutting North Patagonian Batholith rocks ca. 42° S. Muscovites and synkinematic biotites ^{40}Ar - ^{39}Ar ages ranging between 10 and 4 Ma (Cembrano et al. 1999; 2000). Rocks younger than 3.3 Ma also shown brittle deformation.

Southward 43.8° S, LOFS is expressed by a single fault trace showing brittle and ductile deformation with oblique right-lateral slip. Synkinematic biotites ^{40}Ar - ^{39}Ar ages range between 4.2 and 3.8 Ma (Cembrano et al., 1999). Similar ages were found in mylonites further south (4.4 ± 0.3 Ma between 45 and 46° S).

Two phases characterize the current Plio-Quaternary kinematic history of the Patagonian Andes (38° - 47° S). The first one is dominated by E-W shortening contemporaneous with the volcanic arc thickening. Later, the second phase (started ca. 1.6 Ma) generated a narrowing of the volcanic arc, with a right-lateral deformation along with the fault system (Lavenu & Cembrano, 1999; Lara & Folguera, 2006; Rosenau et al., 2006). Thermochronological studies provided important information on the evolution of the deformation state of the LOFS (e.g., Cembrano et al. 1996; 2000; 2002). Based on these studies, these faults are active since the end of the Mesozoic, first as a left-lateral fault, then as a right-lateral fault during the mid-Miocene. Brittle features were identified in Pliocene and post-Pliocene rocks, together with high uplift rates during the Holocene (Cembrano et al. 1996).

Present day right-lateral shear deformation along the LOFS was first reported by Wang et al. (2007). Using a geodetic network located between 42° and 44° S, they calculate an average velocity rate of 6.5 mm/yr. This would be equivalent to a 75% convergence movement accommodated in a parallel to the trench component.

The latest advances come from mapping of paleo-surface ruptures, offsets, and lithological separations along the master fault allowing to constrain geologic slip rates for the first time with dextral rates of 11.6–24.6 mm/yr (Quaternary) and 3.6–18.9 mm/yr (Late-Cenozoic) respectively (De Pascale et al., 2021).

2.6 Climate and Paleoclimate settings

2.6.1 Regional climate

The Westerly winds strongly influence the southern Pacific Ocean and Southern Chile (southward 40° S). At the same time, westerlies are controlled by the Pacific Subtropical Anticyclone and the Antarctic Convergence location. These dynamics result in a strong latitudinal gradient of rainfall and temperature (Strub et al., 1998).

North Patagonian Andes has a temperate and humid oceanic climate, with cooling levels generally over 1 km a.s.l. (Garreaud et al. 2013). It shows low seasonality and a strong east-west gradient, ranging from >3,000 mm/yr on the Andes western side and <600 mm/yr on the Chile-Argentina frontier (Miller, 1976; Aravena & Luckman, 2009). Precipitations on the Andes western side are almost entirely controlled by the westerlies and the orographic effect, given by its abrupt topography (Garreaud et al., 2013).

Furthermore, Miller (1976) subdivides Southern Chile at 42° S, with a cold temperature band southward, and with a warmer band northward this latitude. The southernmost band has a westerlies predominance, with little seasonality.

The Aysén Fjord area's climate is cold and humid, with an annual average of rain-fall close to 2,600 mm in Puerto Aysén, but with a maximum of 4,000 mm in the same fjord. Glacial ice is found from an elevation of ~1,100 m within the fjord to the south of the study area in the northern part of the Northern Ice Fields, which correspond to the largest ice fields in the southern hemisphere outside of Antarctica (Glasser et al., 2011; Rivera et al., 2007).

2.6.2 Late Quaternary Glaciations in the North Patagonian Andes

The mapping and dating of the glacial extension have been done mainly along the eastern flank of the main mountain range. The geomorphological record here is well preserved due in part to the arid climate on Andes' eastern side. Here, moraine systems can be found in nearly every valley between 38° S and 56° S, and often are associated with, or confine large lakes.

In the past decade, the application of cosmogenic nuclide surface exposure dating and optically stimulated luminescence (OSL) has led to an increase in the

concentration and geographic range of glacial chronologies. Before focusing on the current knowledge, it is necessary to know the distribution of these glacial systems and their spatial associations. Here, in this section, I will review the history of the main work carried out in the Patagonian Andes, and how the understanding of paleoclimatic evolution and glacial history was built.

2.6.2.1 Glacial landforms detection and distribution

The extension of the ice sheets during the Late Quaternary in South America and, mainly, Patagonia, has been the object of extensive studies since the last century. The presence of palaeoenvironmental records largely depends on natural archives (e.g., peat bogs, lakes). In Patagonian Andes, the location of study sites is biased eastward due to the limited accessibility of the Chilean fjords. The exception is Isla Grande de Chiloé in north-western Patagonia, and the Chonos Archipelago and Taitao Peninsula in central-western Patagonia. Submarine geomorphological evidence of glacial landforms, in the southern Chilean fjords (e.g., Dowdeswell et al., 2016; Dowdeswell & Vásquez, 2013).

The first glacial landform observations are associated with the Antarctica surveys at the end of the 19th century and the 20th century (Nordenskjöld, 1898; Quensel, 1910). Antevs (1928) mapped the extent of Pleistocene ice sheets in South America, showing a continuous extension from the current south end to 27° S. According to this map, ice covered a large part of Patagonia. Caldenius (1932) mapped the Quaternary frontal moraine deposits, establishing the moraine systems located eastward of the main mountain range formed four different systems.

Feruglio (1944) proposed that deposits near Argentino Lake and Nahuel Huapi Lake can be associated with two systems: one before the last glaciation and another that has a double moraine system, in which two advances of the last glaciation are presented separated by an interstadial period. Feruglio (1949) proposed an extension of the Pleistocene Patagonian Icesheet, considering complete ice coverture of the Patagonian and Tierra del Fuego archipelagos, also reaching the Chonos Archipelago to the north.

Further eastward of the main mountain range, the ice sheet's limits were irregular, arriving until the exit of the mountain valleys and on the sub-Andean plateaus. Auer (1956) extended the eastern limit but without referring to the Pleistocene Patagonian Icesheet, instead referring to the moraine systems.

Flint & Fidalgo (1964, 1969) worked eastward of the Andes between 39 - 43° S. Using the degree of moraines weathering as a criterion. They suggested that there are three subdivisions for the drifts of Northern Patagonia: Nahuel Huapi, El Cóndor, and Pichileufú drifts (moraine systems). The latter would belong to the penultimate glaciation. Rabassa & Evenson (1987) and Lapido et al. (1990) suggested that only the Nahuel Huapi drift belongs to the Upper Pleistocene, and El Cóndor and Pichileufú drifts were deposited during the Middle and Lower Pleistocene, respectively.

More detail exists for the Upper Pleistocene glaciations in the Southern Andes, and I will focus mainly on these due to my studies' scope. The best-dated moraine sequence is located in the Chilean Lake District (Región de Los Lagos). In this zone, three phases of glacial advance were defined (Porter, 1981). From the oldest to the youngest, they correspond to the Llico River, Santa María, and Llanquihue, the first two assigned to the Lower and Middle Pleistocene. The last glaciation was well dated due to the abundant organic matter (Rabassa & Clapperton, 1990). This phase corresponds to the last glaciation and has been divided into three sub-stadiums. The Llanquihue state I is older than the radiocarbon dating range and was assigned to the isotopic stage 4 (~70,000 years BP) (Mercer, 1983). The Llanquihue stage II would have developed between 20,000 and 19,000 BP, corresponding to the Last Glacial Maximum (LGM). Llanquihue stage III, although it does not have an associated frontal moraine system, was interpreted by Porter (1981) and Marcer (1983) as a re-advance between 15,000 and 14,000 years BP. In its entirety, the Llanquihue event would have been equivalent to the Wisconsin and Weichel events in North America and Europe, respectively (Clapperton, 1990).

Geomorphological, stratigraphic, and radiocarbon dating works in another 105 localities in the Chilean Lake District (Denton et al., 1999; Andersen et al., 1999), extended the LGM time lapse between 29,400 and 14,550 years BP. In this almost 15,000 years, these authors recognize glacier advances at 26,797 years BP, 22,295 years BP, 21,000 years BP, 17,800 years BP, and 15,730 years BP. The maximum occurred at 22,295 years BP. It is known as the most extensive in the northern sector of the region (Rupanco Lake), while to the south (Chiloé, Dalcahue), the maximum advance would have been recorded at 14,800 years BP.

On the eastern flank of the main mountain range, Mörner & Sylwan (1989) have provided other geomorphological data supported by paleomagnetic data, in the sector of General Carrera - Buenos Aires Lake, where Caldenius (1932) would have defined its moraine systems. These authors concluded that only the four innermost ones were deposited during the last glaciation of the fifteen frontal moraines. The four easternmost moraine arches are associated with reverse magnetic polarity sediments, interpreted as the Matuyama epoch (> 780,000 years). In contrast, the four following frontal moraines correspond to the Matuyama/Bruhnes polarity limit (the outermost with reverse polarity and the internal with normal polarity). The remaining seven frontal moraines would be more recent than 700,000 years.

Douglass et al. (2001, 2002) have also studied the frontal moraine series at the oriented General Carrera - Buenos Aires Lake. Using ^{40}Ar-^{39}Ar dating in basaltic flows and cosmogenic radionuclide dating (^{10}Be and ^{26}Al) in eleven moraines, determined that five of them have an age range between 1,016 ± 10 ka and 760 ± 14 ka, which they named as Telken Moraine System.

Kaplan et al. (2001) dated two younger moraines assigned to the penultimate glaciation, identified as Moreno Moraine System, at 135 ka BP. The majority of their dates are from the Fénix Moraine System. They identify the maximum extent during

the LGM at 23 ka BP and several detentions during the deglaciation a few kilometers west of the maximum position. They also identify a more significant retreat at the 15 ka BP that left the lake's eastern margin free of ice for several hundred years. This allowed the formation of 900 varves in 18 meters. Later, a new advance was represented by the Menucos moraine system dated 11.8 ka BP, but with scanty certainty due to its youth. On the south-western margin of Buenos Aires Lake, Turner et al. (2001) suggest, based on geomorphological mapping, tephrochronology, and radiocarbon dating, which Patagonian Northern Ice Field receded 30 km to their current range between 13,500 and 14,000 years BP, and that since then there has been no further progress. This would indicate the absence of a stage similar to the Younger Dryas.

In the Alto Mayo River's hydrographic basin, southeastward of the Coyhaique River Basin, Beltramone (1991) correlated La Elvira and Nahuel Huapi drifts, corresponding to the last glaciation. The deposits of La Elvira Drift form a frontal moraine system located further west of Alto Mayo River. Other drifts, located to the west, called Río Mayo and Ricardo Rojas drifts, have been correlated with El Cóndor and Pichileufú drifts.

2.6.2.2 Current studies and evidence

Between latitudes 44° and 49° S, the Pleistocene Patagonian Icesheet drained eastwards from ten topographically controlled outlet glaciers and ice lobes. It extended onto the Andean plains during the LGM, leaving behind a series of moraines (Glasser & Jansson, 2005; Glasser et al., 2008). To date, most of the research is focused on just two of these formerly glaciated basins: General Carrera - Buenos Aires Lake and Cochrane – Pueyrredón Lake. In this zone, $^{40}Ar/^{39}Ar$ dating of basaltic lava flows interbedded with the glacial deposits, cosmogenic nuclide surface exposure dating, soil formation rates, and OSL dating are used to date glacial advances spanning from the Greatest Patagonian Glaciation (ca.1.1 Ma) through to the last glacial cycle (e.g., Singer et al., 2004; Douglass & Bockheim, 2006; Kaplan et al., 2004; Smedley et al., 2016; Hein et al., 2010). Moraine systems in other basins, as Coyhaique and Ausen basins are probably related to the last glacial cycle, or older, have received little attention. Younger, likely Lateglacial to Holocene moraines are found within the Andean valleys and present-day mountain glaciers. On the Andes' western side, terrestrial geomorphological evidence is confined to the Taitao Peninsula, as already indicated.

Westward main mountain range, several peats bog, and lake cores have been obtained from the Taitao Peninsula and the Chonos Archipelago, covering the Lateglacial and Holocene period. A marine core (MD07-3088) recovered off the Taitao Peninsula (46° S) provides high-resolution pollen, clay mineralogy, and major geochemistry record covering the last 22 ka (Siani et al., 2010; Montade et al., 2013). Multiple peat bog and lake cores have been sampled from valleys along the Andes' eastern flank and provide a record covering the Lateglacial and Holocene. Minimum radiocarbon ages for deglaciation are also typical.

2.6.2.3 Western Andes

Hubbard et al. (2005) proposed that during the LGM, the Paleocene Patagonian Icesheet was extended over the western islands and terminated in the ocean close to the continental shelf edge. This implies that there is no direct field evidence for glacier advances during the LGM. However, a terrigenous sediment record recovered from immediately offshore of the Taitao Peninsula was used to infer glacial advances at 21.6 - 20.9 ka, 20.2 - 20 ka, 19.6 - 19.1 ka, and 18.5 - 18 ka, based on rapid, short-term fluctuations of smectite/ (illite+chlorite) and titanium/potassium (Siani et al., 2010). This record was interpreted as an increased erosion of the Coastal Range due to glacier dynamics until ca. 18 ka. The increase in the sediment input from the main mountain range after 18 ka suggests the ice margin withdrawal from the western island zone by this time (Siani et al., 2010). Minimum radiocarbon ages from Stibnite Lagoon suggest that the Taitao Peninsula was ice-free by 17.4 ± 0.2 cal ka BP (Lumley & Switsur, 1993), and the northern parts of the Chonos Archipelago by 16.3 ± 0.2 cal ka BP (Haberle & Bennett, 2004).

Taitao Peninsula presents a series of arcuate terminal moraines that indicate valley glaciers flowing east and south from the peninsula's central area drained an independent ice cap (Heusser, 2002; Glasser et al., 2008). Just in one locality, at least twelve distinct moraines indicate multiple re-advances or still-stands (Heusser, 2002). Ages of these moraines are unknown, but based on a minimum radiocarbon age (17.4 ± 0.2 cal ka BP) (Lumley & Switsur, 1993), Heusser (2002) proposed that it may correspond to the LGM. If correct, this would imply either a limited westward expansion of the ice sheet at the LGM or control linked to the deep Golfo Elefantes prevented the ice sheet from overrunning the Taitao Peninsula (Glasser et al., 2008). In the first hypothesis, the climatological conditions that would allow for growth of an ice cap on the low-lying peninsula, but not support ice expansion from the Cordillera (Glasser et al., 2008), and also is difficult to reconcile with LGM ice expansion northward in the Chilean Lake District (Denton et al., 1999). The second hypothesis seems discardable given the extensive moraine deposits evidence showing that the outlet glaciers advanced over Golfo Elefantes (Heusser, 2002). An alternative is that the moraines on the Taitao Peninsula were deposited during late LGM still stands, shortly after the separation of the Taitao ice cap from the PIS, and before rapid deglaciation on the peninsula.

2.6.2.4 Eastern Andes

The Patagonian Ice Sheet between 44° S and 49° S is represented by several moraines located at the eastern end of the formerly glaciated basins (Glasser et al., 2008). The drifts are mainly undated, but the innermost moraines are correlated to the LGM (Glasser et al., 2008). In the absence of direct dating of the moraines, radiocarbon ages from lake and peat bog cores provide a minimum deglaciation age. In the Cisnes River valley (44.7° S), an age from an intermorainic lake (Shaman Lake) indicates a retreat before 18.9 ± 0.1 cal ka BP (de Porras et al., 2012). Further upstream, a core from Mallín El Embudo suggests that the middle part of the Cisnes River valley was occupied by a proglacial lake until ca. 13 cal ka BP (de Porras et al., 2014). Southward

in the Simpson River basin (45.6° S), a minimum radiocarbon age of 41.2 ± 0.3 cal ka BP was obtained from Castor Lake.

At the 46.5° S, cosmogenic ^{10}Be ages from moraine boulders (Fénix V) revealed that General Carrera - Buenos Aires Lake outlet lobe reached its maximum extent 27-25 Ka. Four subsequent re-advances or still-stands are indicated by the Fénix IV-I moraines, with a final advance at ca. 19.3 ka (^{10}Be peak age, Fénix I) (Douglass et al., 2006; Kaplan et al., 2004). At the 47.5° S ages from moraine boulders on the Blanco River Moraine System showed that the Pueyrredón Lake ice lobe reached its maximum extent at ca. 28.0 ka (^{10}Be peak, Blanco River I), a little earlier than General Carrera - Buenos Aires Lake outlet (Hein et al., 2009; Hein et al., 2010). Blanco River II-III moraines are also interpreted as three subsequent re-advances or still-stands, with the last event dated at ca. 21.6 ka (^{10}Be peak) (Hein et al., 2009, 2010). ^{10}Be ages from boulders and bedrock along a transect separating the Pueyrredón Lake and Chacabuco valleys were used to reconstruct ice surface profiles (Boex et al., 2013). Lateral moraines on Sierra Colorado yielded ^{10}Be ages of 23.8 ± 3.9, 28.3 ± 1.4, and 24.3 ± 5.3 ka, thus corresponding to the Blanco River terminal limits. Profiles revealed that the Pueyrredón Lake lobe had a low surface gradient and a maximum thickness of ~1,100 m. This result is consistent with the Hubbard et al. (2005) model.

OSL ages also have been used in the segment of Patagonia. Smedley et al. (2016) reported ages of 30.8 ± 5.7 ka and 34.0 ± 6.1 ka from glaciolacustrine deposits linked to the Fénix moraines. The authors interpreted an earlier ice advance without a preserved moraine. They proposed that an ice advance overrun or removed by meltwater the moraine deposits. According to these results, LGM occurred earlier than indicated based on the preserved moraine record. The ice margin retreat was initiated at approximately the same time in General Carrera – Buenos Aires Lake and Cochrane – Pueyrredón Lake at ca. 19 ka. The initial deglaciation in both valleys was interrupted by subsequent re-advances. General Carrera – Buenos Aires Lake outlet lobe initially retreated to an unknown distance, leading to a proglacial lake. A subsequent re-advance then deposited the Menucos moraine above varved lake sediment (Douglass et al., 2006; Kaplan et al., 2004; Turner et al., 2005). ^{10}Be ages from Menucos moraine yielded between 18.3 ka and 15.2 ka (Douglass et al., 2006). Smedley et al. (2016) reported an OSL age of 14.7 ± 2.1 ka from glaciofluvial sediment stratigraphically older than Menucos moraine, and thus there remains an element of uncertainty on the age of the Menucos moraines. After their deposition, the glacier most likely retreated permanently back into General Carrera – Buenos Aires Lake basin.

Hein et al. (2010) also proposed a re-advance or still-stand for the Cochrane – Pueyrredón Lake and Chacabuco valleys depositing the Lago Posadas and Lago Columna moraines. A boulder on the Columna moraine yielded a ^{10}Be age of 19.2 ± 2.4 ka (Boex et al., 2013), and a boulder on bedrock in the Cochrane – Pueyrredón Lake valley, which provided a minimum age for the re-advance, had a ^{10}Be age of 17.3 ± 1.1 ka (Hein et al., 2010). This data also is used to infer an ice sheet retreat of more than 80 km.

Chapter 3: Active Faulting, Submarine Surface Rupture, and Seismic Migration along the Liquiñe-Ofqui Fault System, Patagonian Andes

Published in Journal of Geophysical Research: Solid Earth, 2020, Volume 125, Issue 9, 26 pp.

Angelo Villalobos; Gabriel Easton; Andrei Maksymowicz; Sergio Ruiz; Galderic Lastras; Gregory P. De Pascale; Hans Agurto-Detzel

Abstract

The intra-arc Liquiñe-Ofqui Fault System (LOFS) is an active transpressive fault zone located in the Patagonian Andes of Chile. In 2007, a seismic sequence occurred in the Aysén Fjord region of Chilean Patagonia along the LOFS, with a Mw 6.2 main earthquake that triggered dozens of landslides, some of which induced tsunami waves that caused severe damage and casualties. Through the analysis of high-resolution seismic reflection and bathymetric data, we identify six submarine faults cutting the Late Quaternary postglacial sedimentary infill of the fjord. The most conspicuous are the dextral-normal NE-SW striking Quitralco fault (QF) and the N-S striking strike-slip Río Cuervo (RCF) and Punta Cola faults (PCF). Our paleoseismological analysis reveals at least seven paleolandslide events buried in the fjord sediments that were triggered by local paleoearthquakes, which occurred since local ice sheet retreat, that is, circa 12 kyr. By combining tectonic observations with local seismicity data, we propose a seismotectonic model for the evolution of the 2007 seismic sequence where three structures were progressively activated from the depth toward the upper continental crust, causing surface rupture along the PCF and with earthquakes, suggesting only partial ruptures along other faults. Because the other faults did not rupture to the seafloor they remain important sources of seismic hazard. Thus, the last seismic sequence was a consequence of a stress transfer from the lower-ductile toward the upper-brittle continental crust, close to the triple junction of the Nazca, South American, and Antarctica Plates. Our results emphasize on the potential synergies between multiple geological and geophysical methods to assess complex events.

Plain Language Summary

When crustal faults rupture, the energy released is the earthquakes we feel at the surface of the Earth. Recent studies along strike-slip faults demonstrate that these phenomena are often not only related to a single fault but instead take place along several faults like was seen in the 2016 Kaikoura earthquake in New Zealand. Using novel high-resolution seismic reflection imagery and bathymetric data together with the reanalysis of local seismicity, we show (i) multiple active faults in the Aysén Fjord area along the Liquiñe-Ofqui Fault System in the Patagonian Andes; (ii) several of these faults were activated during the last 2007 seismic sequence and one of them (the Punta Cola fault), ruptured to the surface causing a Mw 6.2 earthquake that generated massive landslides and local tsunami; and (iii) mapping of similar landslides in the fjord

sediments demonstrates similar events occurred at least seven times since the last ice sheet retreat in the area, that is, in the last 12,000 yr. This demonstrates the necessity for including the possibility of complex ruptures involving multiple faults regarding seismic hazard assessment along crustal faults, especially for faults near populated areas.

3.1 Introduction

The identification and characterization of fault geometry and prehistoric earthquakes in the geological records are the basis for the study of multiple seismic cycles, evaluation of seismogenic source behavior, stress distribution, interaction among different faults, and seismic hazard assessment (e.g., Healy et al., 2004; Kilb et al., 2002; Nostro et al., 2005). Active faulting onshore can generate surface ruptures that are eventually easily recognizable in the geomorphology. In contrast, the recognition and study of these types of geomorphologic markers are more difficult in the case of the marine environment, at which point the application of geophysical techniques becomes crucial to improving the geologic structural analysis. In addition, the absence of records of recent seismic activity, either instrumental or in the historical archives, can generate a false sense of security regarding the seismic hazard associated with these active faults. When fault rupture in a submarine environment or near shore other coseismic geohazards such as tsunamis, soil liquefaction, landslides, and associated displacement waves can occur, as it was the case of the last 2007 seismic swarm in the Aysén region of the Patagonian Andes in southern Chile (Naranjo et al., 2009; Oppikofer et al., 2012; Sepúlveda et al., 2010; Vargas et al., 2013).

In recent decades, the study of active faults in earthquake geology and paleoseismology on land has improved our knowledge about faulting mechanisms and earthquake occurrence based upon direct observations of geological records (e.g., De Pascale & Langridge, 2012; McCalpin, 2009; Meghraoui et al., 1988; Rockwell & Ben-Zion, 2007; Vargas et al., 2014; Wallace, 1981; Yeats et al., 1997). However, submarine faults pose a number of challenges. Much work along the submarine portions of the Alpine Fault in New Zealand (e.g., Barnes, 2009; Barnes et al., 2005, 2013), the Northern Anatolian Fault in Turkey (e.g., Armijo et al., 2005; Beck et al., 2007; Cormier et al., 2006; McHugh et al., 2006; Sunal & Erturaç, 2012), in California (e.g., Hardebeck, 2013), and northern Chile (e.g., Vargas et al., 2011) demonstrates that the combination of high-resolution multibeam bathymetric data with subbottom profiling yields excellent insights into active fault investigations and provides critical information about slip rates and the timing of paleosurface ruptures. In addition, paleoseismological studies can focus on secondary active faulting evidence, such as tsunami records, turbidites, slumps or soft sediment deformation features (e.g., Goldfinger et al., 2013; Nelson et al., 2012; Pouderoux et al., 2012; Smedile et al., 2012). Because of their fast sedimentation rates and often long sedimentary records, fjords constitute ideal archives to explore the seismic history of an area and to assess the structural style and degree of activity of faults that directly disrupt the sedimentary infill. However these environments can represent a challenge for paleoearthquake investigations based on indirect records of paleostrong ground motions, such as turbidites (e.g., Atwater et al., 2014; Van Daele et al., 2013; Wils et al., 2018), due to the supply of sediment coming from adjacent rivers, as in the case of the Aysén River in the homonymous fjord.

The Patagonian Andes of southern Chile are characterized by a main crustal-scale transpressional intra-arc tectonic feature, which is the Liquiñe-Ofqui Fault System (LOFS—or fault zone) and runs roughly parallel to the continental margin (Figure 3.1). The LOFS has been characterized as a major transpressive fault system, along which N-S striking faults accommodate mostly strike-slip movement with local reserve component, with local extension driving normal faulting. The convergent margin in this region is characterized by oblique subduction between the Nazca beneath the South American plates. Between January 2007 and February 2008, an intense seismic sequence occurred in the Aysén Fjord area (2007 Aysén Seismic Sequence: 2007-AYSS). The peak of seismic activity occurred on April 2007 and was characterized by two main earthquakes: a M_w 6.1 magnitude on 2 April and a M_w 6.2 magnitude on 21 April (Agurto et al., 2012; Lara et al., 2009; Legrand et al., 2011; Mora et al., 2010; Russo et al., 2011; Vargas et al., 2013). The seismic swarm encompassed a spatial extension of 52 by 24.5 km^2 and occurred along the main branches of the LOFS (Figure 3.1).

In this study, we analyze submarine evidence of surface faulting activity that resulted from the last 2007-AYSS and prior events by using multibeam bathymetric data and high-resolution seismic profiles in the inner part of the Aysén Fjord. The results allow us to identify submarine active fault segments of the LOFS, which we compare to previous surface faulting mapping in this area. Through a reanalysis of the seismicity data, we find a migration of the seismic sequence among the main faults that resulted in a surface rupture triggering large rockslides and submarine landslides, especially on 2 April 2007. Finally, we propose a seismotectonic model suggesting that the 2007-AYSS resulted from a stress transfer from the lower-ductile toward the upper-fragile crust in this region.

3.2 Seismotectonic setting

3.2.1 Liquiñe-Ofqui Fault System and related tectonic features

The study area is located near the southern termination of the subduction margin between the Nazca and South American plates (Figure 3.1), with a convergence rate estimated at ~6.6 cm/yr (Angermann et al., 1999). The main structural feature in this region is the intra-arc transpressional LOFS, which extends for ~1,200 km between 38° S and 47° S (Cembrano et al., 1996a, 2002; Forsythe & Prior, 1992; Hervé, 1994; Lavenu & Cembrano, 1999; Legrand et al., 2011). In general, the system is formed by two NNE parallel regional lineaments connected by at least four NE en échelon lineaments that define a duplex structure (Hervé, 1994). A structural control by the LOFS in the distribution of Quaternary volcanism was proposed by Cembrano & Lara (2009), while a strong role of the Quaternary glaciations was proposed as constructive control on the Patagonian Andes mountain building (Thomson et al., 2010).

In the Aysén Fjord and surroundings areas, Quaternary volcanoes, such as the Macá-Cay volcanic complex (D'Orazio et al., 2003; Niemeyer et al., 1984), are associated with dozens of Holocene monogenetic cones located along lineaments parallel to the main faults or directly along traces of the major structures in the area (Vargas et al., 2013). These Quaternary volcanoes overlay granitic rocks with mafic intrusions and locally gneisses, constituting the North Patagonian Batholith (Bartholomew, 1984). The landscape is dominated by U-shaped valleys associated with the Quaternary glacial erosion, which are characterized by steep slopes reaching up to 2,000 m above sea level (a.s.l.) with landslides, glacial and fluvial geomorphologies, and volcanic deposits related to the Southern Volcanic Zone sources (Sepúlveda et al., 2010; Vargas et al., 2013). The climate of the region is cold and humid, with average annual rainfall of approximately 2,600 mm in Puerto Aysén, reaching maximum values of 4,000 mm in the fjord (Dirección General de Aguas), with mapped glaciers located at elevations down to ~1,100 to ~1,500 m a.s.l. (Vargas et al., 2013). The Aysén Fjord is EW to NW-SE oriented and corresponds to a typical U-shaped glacier valley with steeped flanks that was fully glaciated during the Last Glacial Maximum (LGM), which here occurred around 17.3 kyr (e.g., Glasser et al., 2012; Heusser, 1990). Active branches of the LOFS were recognized across the fjord, and despite strong erosion rates and sediment supply to the valleys, especially by the Aysén River, which drains the overall Patagonian Andes at this latitude, geomorphologic markers of faulting activity occurred in the last 12,000 Cal yr BP, after the last ice sheet retreat in the area, were found on land and at the seafloor (Figure 3.2), suggesting rapid tectonic rates associated with active structures of this major fault system (Vargas et al., 2013). These active tectonic rates would be responsible for significant seismogenic activity along active faults, as previously inferred from a study of the shallow sedimentary infill of the Aysén Fjord (e.g., Wils et al., 2018).

The Chile Rise (CR) is a major tectonic feature that is currently subducting ~260 km southwest of Puerto Aysén (Figure 3.1), offshore the Patagonian Andes (Cande et al., 1987; Herron et al., 1981). This first-order tectonic configuration forms the Chile Triple Junction (CTJ), which currently occurs offshore of the Taitao Peninsula in the Aysén region but has migrated to the north circa 14 Ma since the ridge collided with the trench (Bangs & Cande, 1997). The oblique convergence of the Nazca Plate beneath the South American Plate, at an ~18° angle with respect to the orthogonal direction to the trench (Angermann et al., 1999), explains a significant part of the total partitioning in trench parallel transcurrent and compressional deformation, defining a transpressional dominant mechanism along the LOFS (Beck, 1988; Cembrano et al., 1996a, 2000, 2002; Rosenau et al., 2006). Other factors may influence such a deformation such as a strong interplate coupling and a thermally weakened continental crust (De Saint Blanquat et al., 1998; Legrand et al., 2011). Forsythe and Nelson (1985) and Cembrano et al. (2002) proposed an indenter-type mechanism produced by a CR-trench interaction, a mechanism that would generate decoupling of the Chiloé sliver from the continental plate along the LOFS. Cembrano et al. (2002) proposed that both transfer mechanisms may work at the same time and could control short- and long-term deformation respectively along this fault system.

Most knowledge about changes in the states of deformation along the LOFS is based on structural and thermochronological evidence, proposing left-lateral (sinistral) kinematics during the Late Mesozoic and right-lateral (dextral) kinematics since the Late Cenozoic (Middle Miocene to present) (Cembrano et al., 1996a, 2000, 2002;

Thomson, 2002). Recent tectonics are characterized by right-lateral lower crust ductile and upper crust brittle deformation during the Pliocene and post-Pliocene times, with high uplifting and crustal exhumation rates during the Quaternary, as estimated from fission track thermochronology and plutonic rocks (Rosenau et al., 2006; Thomson, 2002).

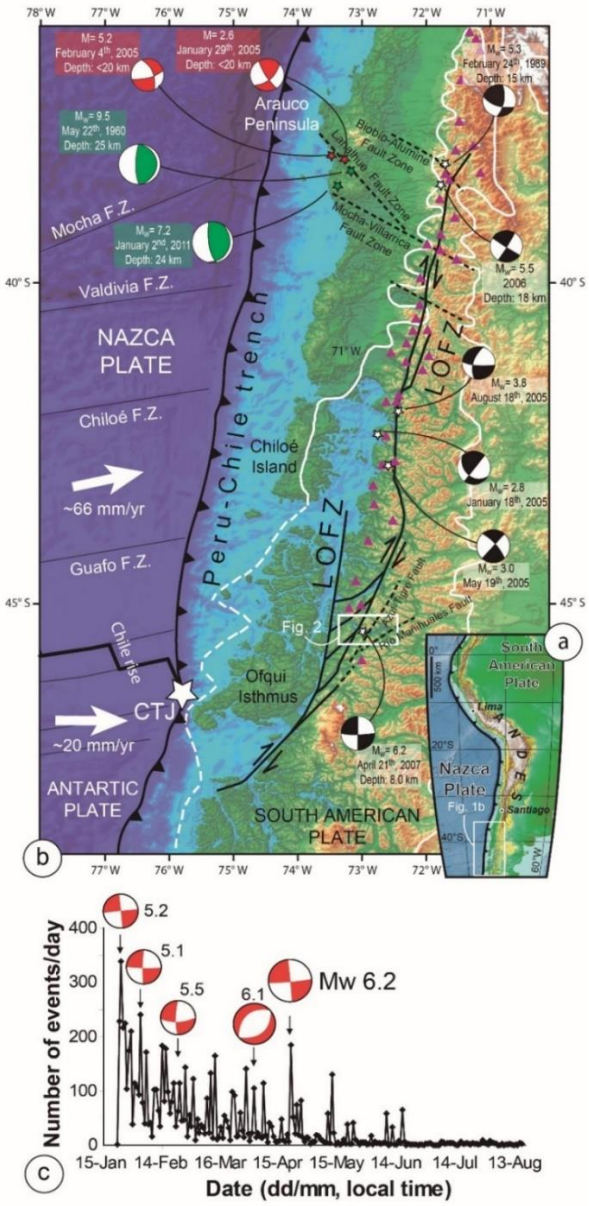

Figura 3.1 (a) Geotectonic framework of South America showing regional tectonics (b) Regional tectonic context at the triple junction of the Nazca, Antarctic and South American plates. Composite Digital Elevation Model (DEM) of the Nazca and South American plates. Regional map showing the location and extent of LOFS (continuous black lines), transverse fault systems (TFS; segmented black lines) and main volcanoes (purple triangles) (after Hervé, 1994; Moreno & Naranjo, 2003; Rosenau et al., 2006; Cembrano & Lara, 2009). Previously published focal mechanisms of crustal earthquakes are shown for the LOFS (black), TFS (red) and megathrust earthquakes (green) (Cifuentes, 1989; Barrientos & Acevedo-Aránguiz, 1992; Haberland et al., 2006; Lange et al., 2008; Legrand et al., 2011). Convergence velocity vectors after Angermann et al. (1999). White lines show the approximate maximum extension of the Pleistocene ice sheet during the Last Glacial Maximum (modified from Thomson et al., 2010). (c) Distribution of number of events versus time of the 2007-AYSS swarm and focal mechanisms for the main shocks according to Geophysics, University of Chile GUC (2007) and Harvard Seismology HRV (2007).

3.2.2 The 2007-AYSS

The Aysén Fjord is located in a remote part of southern Chile that was colonized at the beginning of the 20th century, explaining the limited historic seismic record.

Seismicity along LOFS is poorly characterized, mainly due to the scarcity of permanent local networks. Shallow crustal events were recorded since the early 1980s by temporary arrays (Figure 3.1b), which were most commonly deployed to monitor volcanic activity (Agurto-Detzel et al., 2014; Barrientos & Acevedo-Aránguiz, 1992; Lange et al., 2008). The 2007-AYSS began on 10 January 2007 with a small earthquake (M_L < 3) nucleated at 9–10 km below the inner fjord. Many similar events took place on 14, 18, 19, and 21 January until a M_w 5.2 earthquake struck the area on 23 January, generating aftershocks with >20 events per hour (Figure 3.1c; Barrientos et al., 2007; Russo et al., 2011). From this initial stage, five major events each with increasing size (M > 5; U.S. Geological Survey National Earthquake Information Center (USGS NEIC) catalog) occurred on 28 January (M_w 5.2), 3 February (M_w 5.3), 23 February (M_w 5.7), 2 April (M_w 6.1), and finally, 21 April (M_w 6.2) (Figure 3.1c). These last two events are considered the peak stage of this seismic sequence (Agurto et al., 2012).

The M_w 6.2 earthquake caused 538 mass movements, including large rockslides and rock avalanches (Figures 2 and 3; Naranjo et al., 2009; Sepúlveda et al., 2010). Among these, the three largest mass movements occurred at Punta Cola (12 Mm^3), north of Isla Mentirosa (8 Mm^3), and at Aguas Calientes (1.7 Mm^3; Naranjo et al., 2009; Sepúlveda & Serey, 2009; Sepúlveda et al., 2010; Oppikofer et al., 2012), causing direct damage and triggering local tsunami waves when the landslide material entered the fjord. The runups of these waves were tens of meters at Isla Mentirosa and close to 10 m at the southern side of the fjord (Naranjo et al., 2009; Vargas et al., 2013), causing 10 deaths and significant damage to infrastructure and the local economy.

Figure 3.2. (a, b) Holocene littoral sediments cut by the Río Cuervo Fault in the northern shore of the Aysén Fjord. (c) Outcrops associated to the Punta Cola Fault, in the northern shore of the Aysén Fjord, showing the rockslide deposit produced by the M_w 6.2 episode during the 2007 Aysén Seismic Sequence. Location of both sites corresponds to (c) and (d) points in Appendix Figure A16, respectively.

3.3 Data and Methodologies

To study submarine segments of the LOFS, we used high-resolution bathymetry and seismic reflection profiles obtained in the inner fjord west of Puerto Aysén (between 73.13°-72.68°W and 45.32°-45.47°S; Figures 3.1 and 3.3a). The data set was obtained during a geophysical study as part of the DETSUFA project (Deslizamientos Tsunamigénicos en el Fiordo de Aysén; Lastras et al., 2013), which took place between March 4th and 17th, 2013, aboard the BIO Hésperides.

3.3.1 Bathymetry

To obtain a high-resolution bathymetric map, a KONGSBERG SIMRAD multibeam EM-1002S was used. This system uses 111 beams at a 96 kHz sonar frequency and with a maximum ping rate of >10 Hz. Equidistant mode was used for swath bathymetry acquisition. This array maximized the number of beams facilitating data acquisition and obtaining a homogenized final grid with improved resolution, with tracks separated every 150 m. The swath thickness was the same regardless of width, generating a 50% overlap between each track, with the exception of areas located near the coast. Expendable Bathythermograph (XBT) probes were used at specific sites to measure changes in water sound velocity due to variability in fresh water circulation.

The processing of bathymetric data was done using Caris HIPS and SIPS software. The final grid of the bathymetric data have a grid size of 4 m, and from these data, bathymetric, slope, and aspect maps were derived using ArcGIS software (Figures 3.3b and Appendix A1).

3.3.2 Seismic profiling

The seismic reflection data were acquired using an array of two BOLT air guns (165 and 175 inches^3), which were towed behind the vessel stern. The configuration used in the seismic sources was 2,000 psi, a depth of 3 m for the gun, with a firing rate of 15 m over the seafloor. A 100 m long mini-streamer with a 25 m active section, corresponding to one single channel, recovered the shots. The seismic data were recorded by using the DELPH SEISMICPLUS system with a recording length of 4.0 s and a preamplifier gain of 8 Hz. The raw seismic data were processed aboard the SMT Kingdom Suite, including the navigation and standard processes of electrical noise removing (50 Hz filter), gain amplifier and bandpass filtering, to improve data visualization. Postprocessing included the migration of the sea bottom diffractions and the muting of the water column performed in Seismic-Unix.

We use a P-wave velocity (V_P) = 2000 m/s for migration from time (TWT) to distance (m) because it corresponds to an average value for shallow marine sediments located in the trench of the Nazca beneath the South American plates along Central-Southern Chile (e.g., Maksymowicz et al., 2012). These sediments were classified as fluvial and glaciomarine in origin (e.g., Bangs & Cande, 1997; Thornburg & Kulm, 1987). A more detailed explanation concerning the physics and empirical values is presented in the appendix (Appendix Text A1).

Finally, the seismic interpretation was generated using Move and Adobe Illustrator. We estimate a maximum error of $\pm$0.33 m for vertical distance estimations from our seismic profiles (Appendix Figure A5).

3.3.3 Seismic event locations

Information regarding the 2007-AYSS hypocenter location was compiled from data recorded by temporary stations at the Chilean National Seismological Center (CSN, Universidad de Chile; Barrientos et al., 2007; Legrand et al., 2011) and the University of Liverpool (Agurto et al., 2012).

To associate seismic activity with geological structures and to propose a geometric model at a crustal scale, we used two seismic catalogs covering most of the 2007-AYSS. We used data from the CSN local seismic network for the period between 27 January and 21 April 2007. During this first stage, the seismic network consisted of five 3-component seismometers installed around the epicenter of the M_w 5.2 earthquake (Barrientos et al., 2007). A total of 284 events were recorded before 21 April 2007 (Barrientos et al., 2007; Russo et al., 2011), when the tsunami triggered by the M_w 6.2 earthquake destroyed this network. For the following period, we used seismic data published by Agurto et al. (2012) corresponding to the University of Liverpool seismic network. This temporary deployment consisted of 15 stations and recorded seismic data between July 2007 and February 2008. This dataset is characterized by precise hypocenter relocation based on a new 1-D crustal velocity model for the area (Agurto et al., 2012), well constrained for the shallower ~30 km, encompassing the expected seismogenic zone (Agurto et al., 2012; Lange et al., 2008).

To support our seismotectonic model of the LOFS in the area, we analyzed all the earthquakes in a three-dimensional diagram using MOVE 2016.1. By comparing this latest information with active faults defined from seismic profiles and bathymetric data, together with the hypocenter clusters and focal mechanisms solutions of the main earthquakes (Agurto et al., 2012), we developed 3D surfaces representing the QF, RCF and PCF at the upper-crustal scale.

3.4 Results and interpretation

3.4.1 Geomorphology of the inner-fjord seafloor

The submarine geomorphology of the Aysén inner Fjord is characterized by a flat seafloor with a regional slope of ≤2.5° (Figure 3.3). Its northern and southern boundaries are high-angle slopes between ~30° and ~80°. The inner part of the Aysén Fjord is bounded to the west by the Cuervo Ridge, which is a conspicuous feature composed of NE-striking elongated seamounts, with ~80° slopes. The inner fjord deepens westward from 150 m below sea level (b.s.l.) near Bahía Acantilada, in front of the Aysén river mouth (Figure 3.3a), to ~220 m in front of Isla Mentirosa. West of the Cuervo Ridge, the sea bottom of the fjord is characterized by a noticeably steep drop-off of ~100 m, reaching depths of ~340 m.

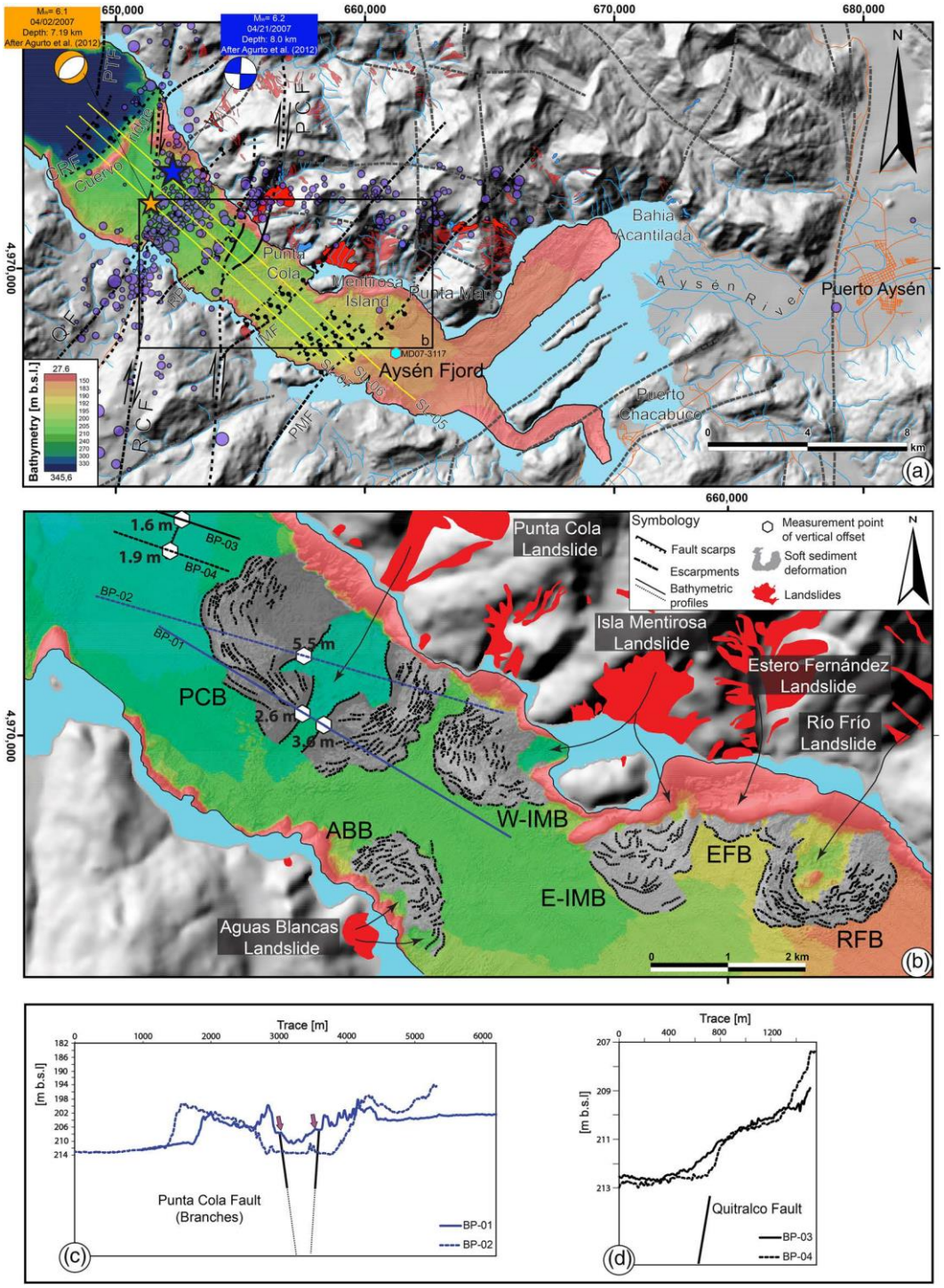

Figure 3.3. (a) Topo-bathymetric map of the inner Aysén Fjord. Digital elevation model based on 1:50,000 topographic sheets from the Chilean Army Geographic Institute (IGM). The location of the seismic profiles (SL-05, SL-05 and SL-07) in Figures 3.4–3.6 is shown. Epicenters of the 2007-AYSS (transparent purple circles) and the focal mechanism solutions for M_w = 6.1 and M_w = 6.2 are indicated. Continuous black lines show surface rupture features. Segmented black and gray lines show fault traces and lineaments, respectively. Mapping of faults onshore from Van Daele et al. (2013; Appendix Figure A16). The light blue point corresponds to a ~21 m piston core extraction site (Wils et al., 2018). (b) Geomorphic analysis of the segment affected by the 2007-AYSS, PCB (Punta Cola Bulge), W-IMB (Western Isla Mentirosa Bulge), E-IMB (Eastern Isla Mentirosa Bulge), ABB (Aguas Blancas Bulge), and EFB (Esterno Fernández Bulge). Escarpments related to PCF and QF are shown. (c, d) Bathymetric profile (BP) traces are shown using blue and black continuous and segmented lines.

The submarine continuation of fault scarps is difficult to assess in bathymetric maps, mostly due to the high sedimentation rates associated with the sediment input from the Aysén River as well as the obliteration of the sea bottom geomorphology imposed by the deformation associated with the submarine impact of rockslides and rock avalanches (Figure 3.3b). This deformation appears as bathymetric highs with differences of up to ~8 m with respect to the surrounding flat surfaces in the seafloor bathymetry. These abrupt changes will be referred to as “escarpments” hereafter, except in those cases associated with active faults, which will be referred to as “fault scarps.” Some of these bulges, especially in front of Punta Cola (Figure 3.3b), were interpreted as pressure ridges and fault scarps by Vargas et al. (2013), while these are generally considered basin-plain deformation associated with the submarine impact of rockslides according to Van Daele et al. (2013), following the model established by Schnellmann et al. (2005). The model proposes that slope-adjacent landslides induced deep- and far-reaching deformation in the basin-plain sedimentary sequence (Van Daele et al., 2013). The deformation zone typically displays a geometry similar to a fold-and-thrust belt structure in cross section, which is created from an increase loading of the basin-plain sediment during a mass flow because the slope-adjacent landslide wedge growth leads to a successive propagation of the thrust front (Schnellmann et al., 2005). The compression and deformation of the flat fjord floor is favored by the peculiar geometry of glaciogenic lakes and fjords; this geometry comprises steep slopes with sharp lower slope breaks (Schnellmann et al., 2005).

The bulges are characterized by curved traces on the map at ~370–750 m long, and each of them is associated with a subaerial landslide that entered the fjord (Lastras et al., 2013; Oppikofer et al., 2012; Van Daele et al., 2013; Figure 3.3b). Using bathymetric profiles and aspect maps, we distinguished a main slope delimiting each bulge as well as several internal curved slopes with lower heights that limit tilted surfaces (Figure 3.3c).

Specifically, the Punta Cola Bulge (PCB) is interrupted by a NNE rectilinear sag limited by two escarpments with vertical offsets that range between 1.6–5.5 m (Figures 3.3b and 3.3c). Northwest of the PCB, a 650 m long escarpment-oriented NE-SW with vertical offsets that range from 1.6 to ~2 m can be observed (Figures 3.3b and 3.3d).

3.4.2 Seismic stratigraphy

We differentiate the sedimentary fjord infill into three main seismic-stratigraphic units based on SBP data. We use Belknap and Shipp's (1991) criteria, which are based on (1) the character of the reflections, (2) the intensity of the acoustic contrast, and (3) the general geometry of the deposit, including the stacking pattern of the reflectors. Additionally, we interpret and relate these units to different geomorphologic and stratigraphic features. As a result, we map and interpret three seismic profiles located along the inner part of the fjord (Figures 3.3–3.6).

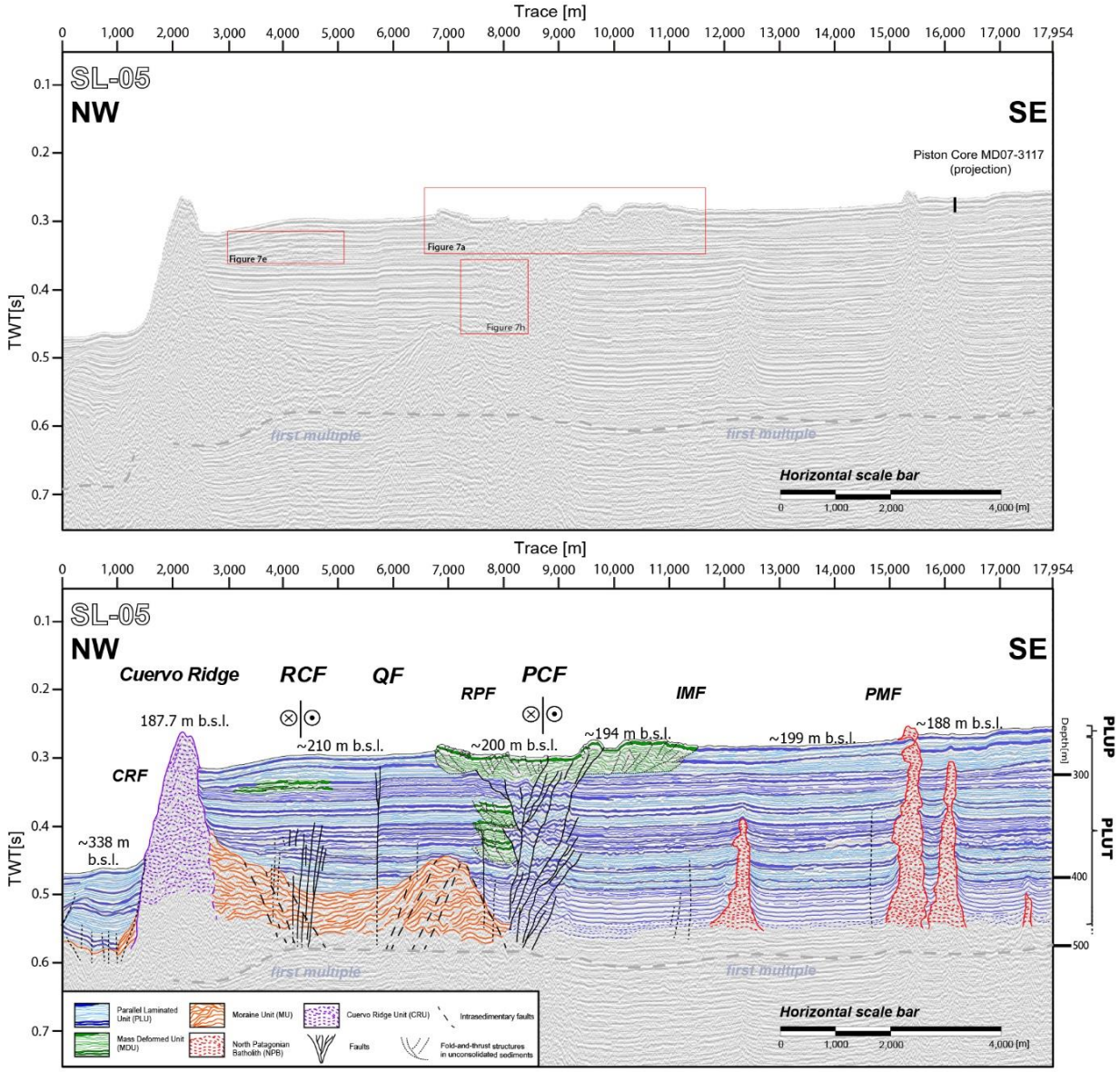

Figure 3.4. (a) Uninterpreted seismic reflection profile (SL-05; location in Figure 3.3a) showing the location of insets in Figure 3.7. (b) Interpreted profile showing main fault offshore segments of the LOFS transfer zone. Seismic facies color coding corresponds to the Parallel Laminated Unit (PLU, bluish color), Mass Deformed Unit (MDU, green), Moraine Bank Unit (MU, orange), Cuervo Ridge (purple), and North Patagonian Batholith (NPB, red). Continuous lines and discontinued lines represent faults, with continuous lines indicating less uncertainty. Fault names from NW to SE are Cuervo Ridge (CRF), Río Cuervo (RCF), Quitralco (QF), Río Pescado (RPF), Punta Cola (PCF), Isla Mentirosa (IMF), and Punta Mano faults (PMF).

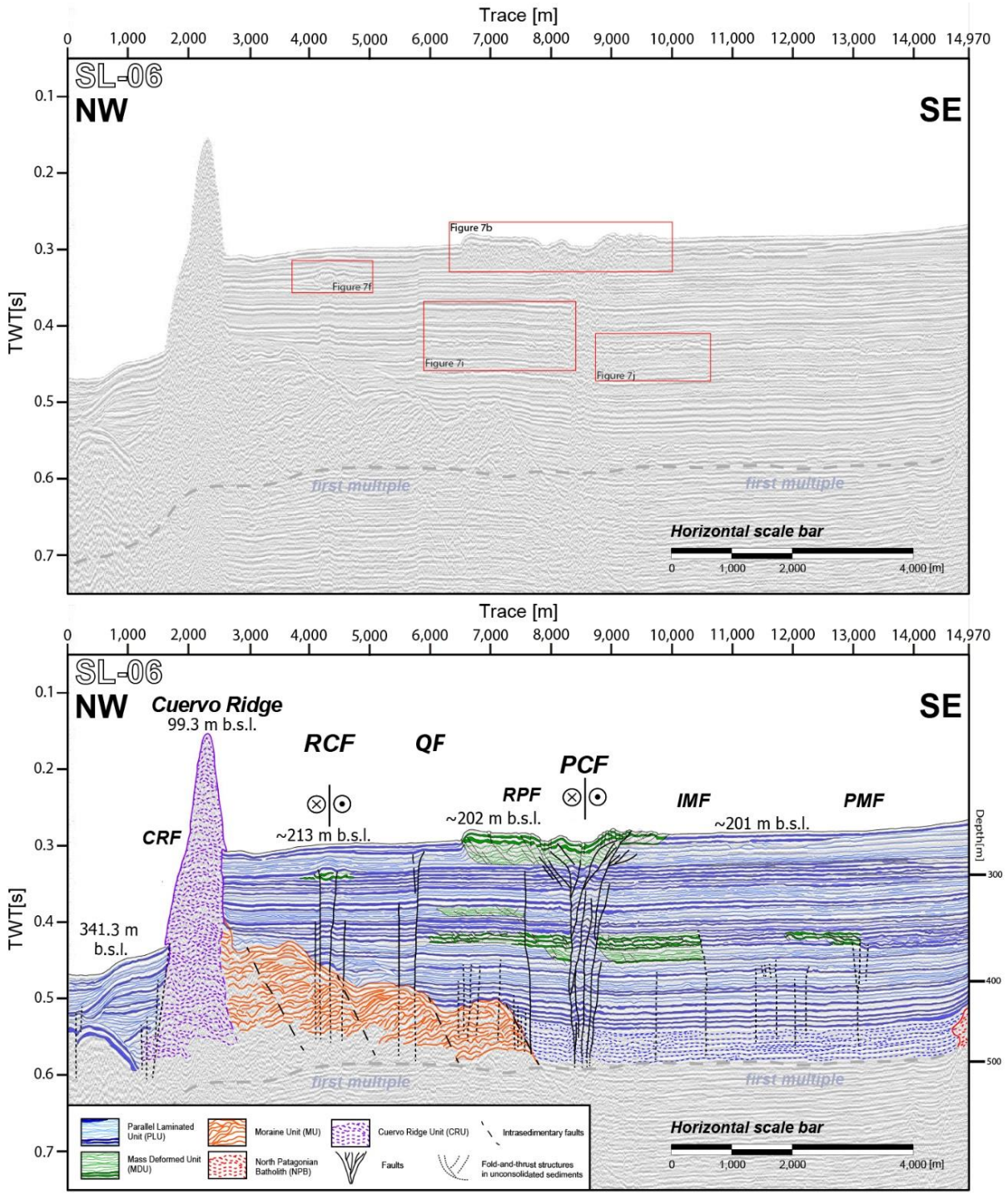

Figure 3.5. (a) Uninterpreted seismic reflection profile (SL-06; location in Figure 3.3a) showing the location of insets in Figures 3.7 and 3.10. (b) Interpreted profile showing main fault offshore segments of the LOFS transfer zone. Color coding for seismic facies units and abbreviations labels for the faults are the same as in Figure 3.4.

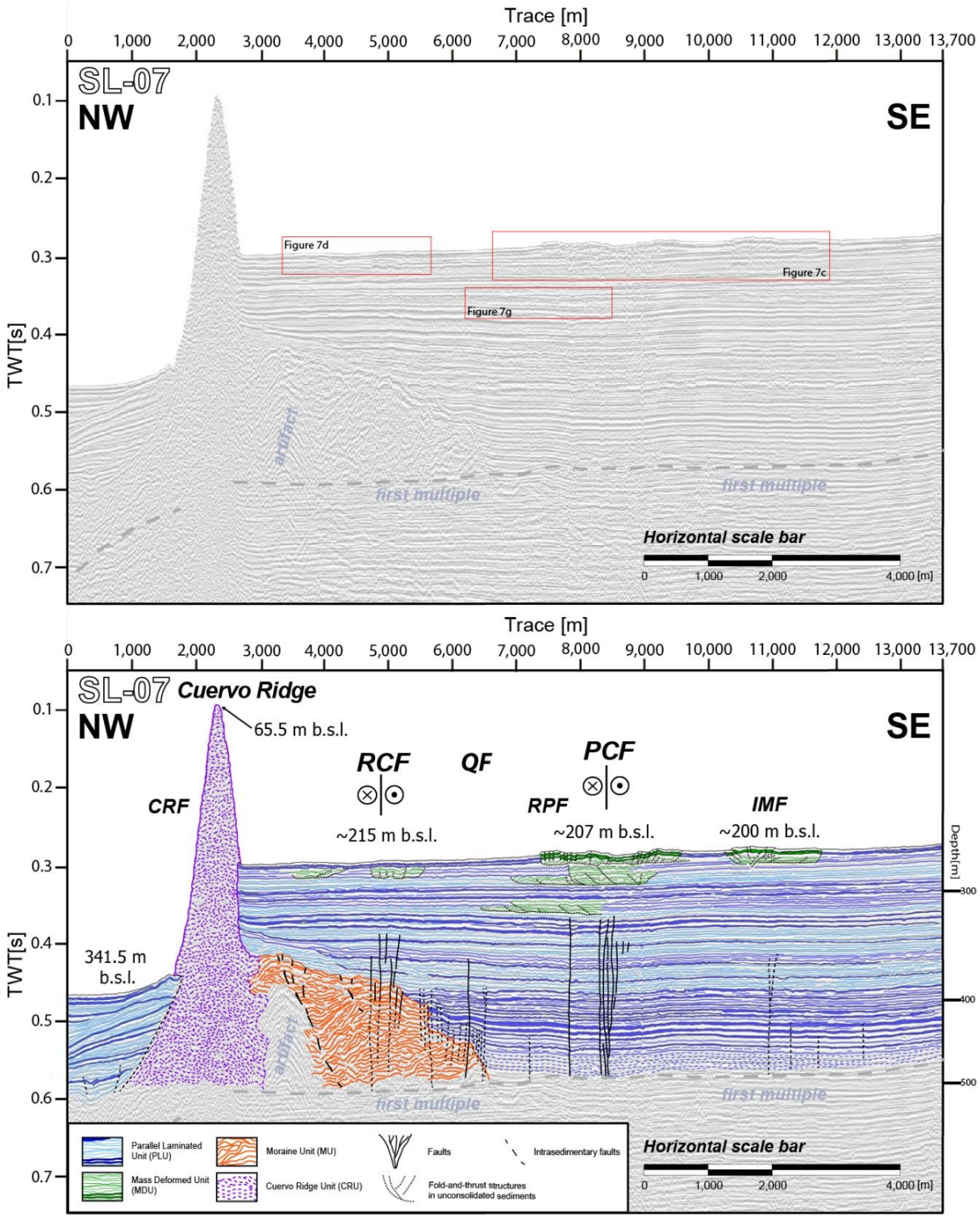

Figure 3.6. (a) Uninterpreted seismic reflection profile (SL-07; location in Figure 3.3a) showing the location of insets in Figures 3.7 and 3.10. (b) Interpreted profile showing main fault offshore segments of the LOFS transfer zone. Color coding for seismic-facies units and abbreviations labels for the faults are the same as in Figure 3.4.

3.4.2.1 Cuervo Ridge Unit (CRU)

We observe the internal structure of Cuervo Ridge and other bodies, which are characterized by semicontinuous and discontinuous chaotic to transparent seismic facies. Lara et al. (2009) interpreted the Cuervo Ridge as at least partly a monogenetic cone based on the dredging of a basalt sample. Vargas et al. (2013) also suggested a volcanic component in at least part of this ridge based on the observation of 3.5 kHz subbottom profiles. Because extensive glaciations occurred in this zone, an alternative interpretation for at least part of this type of unit would be a frontal moraine, where glaciers entrained local volcanic rocks and deposited them here (Boyd et al., 2008).

Seismic facies here have semicontinuous to discontinuous reflectors constituting the Cuervo Ridge, and it can be interpreted as formed by hard rocks, eventually partly volcanic, and constituting the Northern Patagonian Batholith such as, for example, in the eastern portion of profile SL-05 (Figure 3.4). Based on these observations, it is possible to discard a submerged moraine as an origin for the Cuervo Ridge. Clearly, more dredge samples in this area are needed to clarify this hypothesis.

3.4.2.2 Moraine Unit (MU)

This unit has continuous to semicontinuous irregularly shaped reflectors with moderate to intense acoustic contrast in lateral contact with the Cuervo Ridge, most possibly onlapping this last feature (Figures 3.4–3.6). The unit has a multicrested mound with a hummocky internal shape that we interpret as a moraine, following the similarities in geometry and semichaotic facies seen in previous seismic surveys in Chilean fjords (e.g., Boyd et al., 2008; Breuer et al., 2013). This glacial deposit, described for the first time here, appears at ~0.42 s (~107 m below the seafloor, b.s.f.) from eastern flank of the Cuervo Ridge up to the vicinities of Punta Cola, covering ~7 km along the inner fjord. The estimated thickness of this Moraine Unit (MU) ranges at least between ~14 and 33 m (until the first multiple). The stepped geometry of the MU, as found in the seismic profiles, is characteristic of push frontal moraines (Figures 3.4–3.6). Furthermore, the considerable thickness of the deposit could indicate successive phases of advancements and retreats of the glacier that likely occurred during the Late Quaternary here.

3.4.2.3 Parallel Laminated Unit (PLU)

The best represented seismic-stratigraphic unit is the Parallel Laminated Unit (PLU), characterized by seismic facies with parallel continuous to semicontinuous, medium to high intensity reflectors exhibiting laminar and sometimes wedge geometries. The estimated minimum thicknesses for this unit (using V = 2,000 m/s, until the first multiple) ranges from ~107 to ~307 m, thinning from Bahía Acantilada, in front of the Aysén River mouth, toward the Cuervo Ridge. The PLU overlays the MU and the CRU, with well-recognized onlap terminations denoting an important aggradation of the sedimentary infill of the inner fjord, mostly due to the strong sediment supply from the Aysén River (Figures 3.4–3.6). Wedge geometries and

chaotic seismic facies occur within this unit mainly in the west section, close to the CRU.

DaSilva et al. (1997) characterized different seismic facies and seismic-stratigraphic units in Chilean fjords, including part of the Aysén Fjord. They indicated that the first 0.15 s of the subsurface sedimentary infill correspond to an ice proximal facies (i.e., marine proximal glacial deposits), whereas in Vargas et al. (2013), the PLU was observed up to the first ~40.4 m and was subdivided into two seismic-stratigraphic units: the more recent shallower unit characterized by continuous laminations and a poorly laminated deeper unit, interpreted as the result of postglacial sedimentation during the deglaciation since 12 kyr and the Holocene sea level high stand post-7 kyr.

The seismic reflection data used in this work allowed us to extend the observations ~250 m deeper than in previous studies. The images show that the general characteristics of PLU are similar for several meters more of depth (Figures 3,4a, 3,5a, 3.6a). Within this unit, we generated a subdivision based on the contrast and lateral continuity of the reflectors, and we will later discuss the possible origin of this seismic facies.

3.4.2.4 Mass Deformed Units (MDU)

We differentiate reflectors characterized by chaotic to semicontinuous seismic facies, some of which have low acoustic amplitude. We named these packages, based on their depth and location, Mass Deformed Units (MDU-00 to MDU-07).

Located on the seafloor, MDU-00 is interpreted as deformed sediment caused by rockslides and rock avalanches that entered the fjord triggered by the M_w 6.2 earthquake, following Van Daele et al. (2013). These units are the seismic expression of the bathymetric bulges previously seen on the seafloor (Figure 3.3b) and are directly related to the three major rock avalanches that entered into the fjord at Punta Cola (PCLS, Fig. 7a), Isla Mentirosa (IMLS, Fig. 3.7b) and Aguas Calientes (ACLS, Figure 7c; Lastras et al., 2013). Continuous reflectors in the upper section of the deposits indicating velocity contrasts between seawater and sedimentary infill show conspicuous vertical offsets. These reflectors are deformed, slightly folded and dislocated, revealing reverse faults that coincide with the curved traces found on the deformed seafloor that we associate with soft-sediment fold-and-thrust belts based on Van Daele et al. (2013) and Lastras et al. (2013), following Schnellmann et al. (2005).

Seismic profiles show thrust faults verging in opposite directions, a geometry that can be related to a semicircular deformation front linked to the propagation of a submarine landslide (Figure 3.3b). Thrust fronts are high-angle dislocations that separate MDU from PLU facies. The location of basal décollement zones varies between each profile and each sedimentary wedge. In the case of PCB and the Western Isla Mentirosa Bulge (W-IMB), thrust fronts (related to the landslides deforming the seafloor) detach at ~36 and ~47 m below the seafloor (b.s.f.), respectively, as observed in the northern seismic profile SL-05 (Figure 3.4). In profile

SL-06, the PCB décollement zone is at ~41 m b.s.f, but in W-IMB, it becomes shallower at ~16 m b.s.f. (Figure 3.5), while in the southern profile SL-07, the PCB and Aguas Calientes Bulge décollement zones are located at ~19 and ~21 m b.s.f., respectively (Figure 3.6). Through the analysis of ~1.3 kHz seismic reflection data, Van Daele et al. (2013) describe similar seismic facies in profiles perpendicular to ours, covered by massflow-related deposits they interpreted as mega-turbidites.

In the deep sedimentary infill, we identified seven levels with similar features and structures to the seismic facies described upward (MDU-00) embedded within the Parallel Laminated Unit. These packages, MDU-01 to MDU-07 (Figure 3.7), also exhibit wedge geometries, and most can be followed at the same depth in at least two of the seismic profiles. Similar to MDU-00, sedimentary wedges, fold-and-thrust belts structures can be found. These MDUs are located at minimum depths of ~24.2 m, ~30.5 m, ~48.2-51.8 m, ~65.8 m, 70.4-82.4 m, ~100.3-198.6 and ~121.9-137.1 m b.s.f. in the case of MDU-01, 02, 03, 04, 05, 06 and 07, respectively.

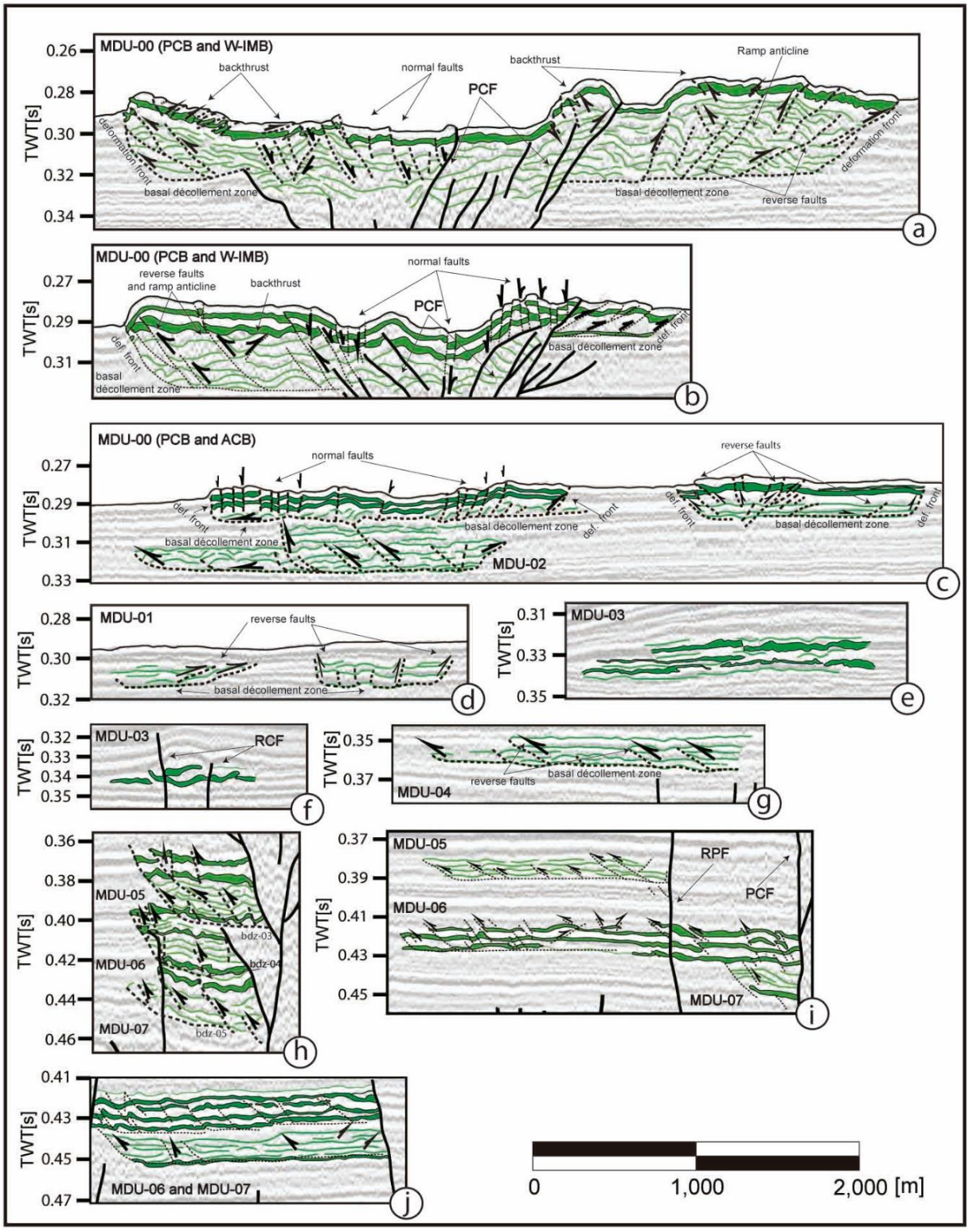

Figure 3.7. Detail of the sedimentary deformed wedge (MDU) internal structure interpreted in SL-05, SL-06 and SL-07 seismic profiles. Each structural feature, together with kinematics, are indicated in at least one Fig. (a), (b) and (c) show present day seafloor deformation (MDU-00) associated with PCB, W-IMB and ACB. The Punta Cola Fault (PCF) is clearly differentiable from the synsedimentary deformation. (c) Shows MDU-02 (d) shows MDU-01, (e) and (f) show MDU-03, (g) shows MDU-04, (h), and (i) and (j) show MDU-05, 06 and 07.

3.4.3 Active faulting in the Liquiñe-Ofqui Fault System

Through the analysis of seismic profiles, we describe active faults rupturing the postglacial sedimentary infill of the inner Aysén Fjord in the study area, including the Punta Cola Fault (PCF), Quitralco Fault (QF) and Río Cuervo Fault (RCF), as previously mapped by Vargas et al. (2013), and we present new submarine structures identified in this work.

3.4.3.1 Punta Cola Fault

Vargas et al. (2013) described PCF as an ~20 km long dextral-reverse fault based on the observation of rock outcrops affected by intense brittle deformation, with fault planes and fractures that range between centimetric shear zones and damage zones several dozen meters in width (Figure 3.2c). From south to north, its onshore style varies from a simple N-S striking fault trace, observable for ~8.2 km until it reaches the fjord bank (Appendix Figure A16).

Here we find ~4.2 km of submarine continuation of this fault is observed in seismic profiles, showing an asymmetrical positive flower structure geometry (Figures 3.4 and 3.5). This structural feature was not found in the fjord near a pressure ridge, and, on the contrary, the existence of a small depression limited by escarpments masks it (Figure 3b). The faulted zone associated with this structure narrows southward from an average width of ~1,080 to ~243 m (SL-05 and SL-07; Figures 3.4 and 3.6). Branch tips of fault segments in this system can be observed reaching the surface in northern seismic profiles SL-05 and SL-06 (Figures 3.4 and 3.5). In addition, reflector offsets generate a pop-up structure within the deformation zone on profiles SL-05 and SL-06. In contrast, seismic profile SL-07 shows fault ruptures terminating at ~0.35 s, below the sea floor. This difference in the behavior of the reflector offset with respect to the northern profiles could be associated to a local bend striking N30–50°E shown in plan geometry (Figure 3.3a), due to a change in the slip along the fault plane. We interpret this change as a product of reduced slip along the southward fault segment of the PCF across the fjord (Figure 3.3a).

To the north, the fault strike changes slightly toward the west (N-S to N10°E) for ~12 km until the northern fault termination.

3.4.3.2 Río Cuervo Fault

The RCF is the most prominent NS striking fault in the area, which extends ~100 km, with fault segments ~30–40 km long (Appendix Figure A16; Vargas et al., 2013). Damage zones up to hundreds of meters wide show evidence of brittle deformation affecting granitic rocks as well as sediments near the northern bank of the fjord (Figures 3.2a and 3.2b; Vargas et al., 2013). However, no trace of this fault can be directly observed in the geomorphology of the seafloor, as revealed by high-resolution

bathymetric data (Figure 3.3b). Despite this data, seismic profiles show at least four parallel, well-defined branches affecting the sedimentary infill of the fjord in the area of the RCF. In the three profiles SL-05, SL-06 and SL-07, the estimated deformation zone width is ~500 m, and the tip position of the faults can be observed 0.32 to 0.39 s below the sea floor, never reaching the surface, which suggests that the most recent rupture here occurred dozens to hundreds of years prior to 2007 (Figures 3.4–3.6).

3.4.3.3 Quitralco Fault

The QF is a NE-SW striking fault with ~70 km length as a part of a major LOFS transfer zone (Appendix Figure A16). It comes from the outer Moraleda Fjord in the western lineament of the system, ending east in the area where it connects with PCF, interacting with the RCF (Thomson, 2002; Vargas et al., 2013). Like other faults and lineaments with a similar strike in the area, right-lateral displacement has been inferred for the QF from geomorphologic observations. Using our fault traces projected from our seismic profiles, together with the onshore mapping of this structure based on field and remote sensing observations of fault scarps (Vargas et al., 2013), we estimate an ~636 m minimum lateral offset. Seismic profiles show QF to be a simple trace accompanied by synthetic and antithetic faults that are best expressed in seismic profiles SL-05 and SL-06. The fault defines two blocks as the western hanging block depressed with respect to the eastern–footwall block. Despite this, the QF inclination is ambiguous, with a tendency to dip to the west (Figure 3.6). We attribute such ambiguity to its subvertical nature and possibly to a lesser slip in the fault plane correlated with the change in the tip position toward its termination within the study area.

According our analysis, the fault tip does not reach the seafloor (stopping at ~0.31 s reflector), where a smooth fault scarp is observed (Figures 3.3b, 3.3d, and 3.4). Meanwhile, southward, its tip location is deepened, reaching 0.47 s below the seafloor in the SL-06 and SL-07 profiles located to the south (Figures 3.5 and 3.6).

3.4.3.4 Other NE-SW striking normal faults

Other faults suggested previously as lineaments in previous work (Vargas et al., 2013) were found in our seismic images. These faults are parallel to QF, and we named them, from west to east, the Cuervo Ridge Fault (CRF), Río Pescado Fault (RPF), Isla Mentirosa Fault (IMF) and Punta Mano Fault (PMF).

The CRF is located near a bathymetric steep of ~100 m close to the Cuervo Ridge. Seismic profiles SL-05 and SL-06 show that sediment immediately west of the ridge presents an eastward tilting, which can be interpreted as a rollover anticline. Furthermore, antithetic and synthetic normal faults deform sediment in the hanging-wall block. We associate the presence of these features to normal fault kinematics of CRF. Unlike other main fault traces clearly shown in seismic profiles, the Cuervo Ridge masks CRF.

RPF limits the eastern flank of the Río Pescado Valley. Seismic profiles SL-06 and SL-07 show that RPF dips slightly eastward and that its fault tip is located at ~0.34 s (Figures 3.5 and 3.6). In SL-05, the tip falls at ~0.4 s (Figure 3.4).

Finally, IMF and PMF have greater degrees of uncertainty in our interpretations. Unlike the structures described above, these faults do not present a discontinuity in the reflectors that allow easy recognition in the seismic profiles, possibly due to small accumulated offsets. It is possible to identify deformed zones across the three seismic profiles defining fault branches that we have categorized as main and secondary faults. The main faults delimit an uplifted block and have continuity with lineaments proposed by Vargas et al. (2013).

3.5 Discussion

3.5.1 Architecture of postglacial sedimentary infill in the inner Aysén Fjord

The inner Aysén Fjord, which is limited to the west by the Cuervo Ridge and associated bathymetric step (Figure 3.3a), is characterized by a well-stratified sedimentary cover (PLU; Figure 3.4) that can be interpreted as a postglacial unit overlaying the MU, defined here, exhibiting characteristic wedge architecture to the west. The sedimentary thickness ranges between >300 m, near the Aysén River mouth, to ~109 m, near the Cuervo Ridge (Appendix Figures A6–A8). This wedge architecture thinning to the west in PLU implies a strong contribution from the Aysén River during the last deglaciation in the Patagonian Andes and the modern global sea level high stand after 7 kyr (Lambeck et al., 2002). Considering local observations of fluvioglacial sediment and moraines covered by tephra layers with buried soil in the area of the Aysén River mouth (Vargas et al., 2013), it is possible to infer an age close to ~12 kyr for the last ice sheet retreat in the area, giving a maximum age for the well-stratified sediment constituting the PLU. Or viewed from another perspective, time averaged sedimentation rates of 25 to 9 mm/yr are possible here, assuming that all laminated sediments from prior glaciations were removed by the Aysén Glacier during the LGM.

A ~21 m long sediment core (MD07-3117, Figures 3.3a, 3.4a) was extracted from the Aysén Fjord (SW of Punta Mano, Figures 3a and 4a) in a pre-2007 campaign (aboard RV Marion Dufresne). From the analysis of this core, Van Daele et al. (2013) and Wils et al. (2018) observed three sandy layers (~5, ~17, and ~20 m core depth), as well as a pumice layer (~10 m core depth), and tentatively correlated these layers with stratigraphic horizons in SBP data (which provide a higher resolution at the near surface than our seismic data), referred to as reflectors SL-F and SL-D for two of the sandy layers and SL-E for the pumice layer.

Van Daele et al. (2013) tentatively correlated a ponding unit observed in the Condor River fan, with the H_1 Hudson volcano eruption deposits (~8,260 yr BP) assuming similarities in the lamination and stratigraphic configuration. Based on the

previous inference, they interpreted sedimentation rates of approximately 3.0 mm/yr; these rates are similar to previous estimates of approximately 1.9 mm/yr (using ^{210}Pb; Salamanca & Jara, 2003). Upon assuming a constant sedimentation rate, they estimated the age of the pumice layer as ~3,170 yr BP (Van Daele et al., 2013), correlating it to the H_2 Hudson eruption (3,600 ^{14}C yr BP). More recently, Wils et al. (2018), using a combination of radiocarbon dating with tephrochronology correlation, built an age-depth model for the first ~21 m represented in the MD07-3117 core, confirming that the pumice layer at ~10 m would correspond to the SL-E reflector. The age for this deepest layer would correspond to 4,050–4,190 ^{14}C Cal yr BP. Within the ~21 m sedimentary record encompassed by the MD07-3117 core, they propose five paleoevents based on the interpretation of layers/reflectors as megaturbidites, dated as 710–830, 1,850–1,980, 1,970–2,120, 7,460–7,540, and 8,710–8,890 ^{14}C Cal yr BP, respectively. Additionally, they propose four paleoevents, from which the oldest associated with the SL-A reflector (RL-023 = 0.4 ms or ~55 m depth in our seismic profiles) would be dated between ~18,600 and 20,000 ^{14}C Cal yr BP (Wils et al., 2018).

Geomorphological features and radiocarbon ages available on a regional scale support the occurrence of large ice sheets covering the Northern Patagonian Andes during the Last Glacial Maximum between ~20-18 kyrs BP, with frontal systems likely located in the Pacific Ocean (Heusser, 1990; Thomson et al. 2010; Figure 3.1). Furthermore, Vargas et al. (2013) dated soils buried by tephra layers directly overlying moraines and outwash sediment in the Aysén Fjord area as ~12,000 ^{14}C yr BP, indicating the age for the last ice sheet retreat at the local scale.

Considering that no glacio-deformed sediment can be observed in the sedimentary infill of the Aysén Fjord from our seismic reflection data, we suggest that all of this sediment is postglacial in origin. Additionally, seismic facies interpreted as moraine banks (MU) are clearly visible at ~200 m depth in the profiles. By assuming a minimum age of ~12,000 yr for the top of the MU (Figure 3.4), it is possible to infer a postglacial age for the entire stratified sediment forming the PLU overlaying the MU (Figure 3.4). Our inferences provide a new perspective with respect to the previous interpretation of Wils et al. (2018), who assigned an age of ~18-20 kyr for the reflectors located at ~55 m b.s.f., within the PLU, based on the extrapolation of sedimentation rates from surface sediment core.

We propose that PLU contains two subunits: a lower one corresponding to a transgressive phase (PLUT), which was generated during the deglaciation in the area, and overlying strata corresponding to the progradational phase (PLUP), generated after the sea level stabilization during the early to mid-Holocene (~7-6 kyr BP; Lambeck et al., 2002; 2014). Our characterization is based on the following points. Reflectors with high contrast acoustic impedance characterize the PLUT, reflecting high amplitude changes. Greater amplitude is generally associated to sediments with greater density. We interpret this as coarser sediments (sand-gravel) constituting the PLUT with respect to PLUP (Figures 3.8, Appendix A6-A8). This unit could correspond to deposits associated with the first stages of a local glacial retreat. Radiocarbon ages reported by Wils et al. (2018) from the core MD07-3117 are stratigraphically consistent, suggesting an age of approximately 8,723-9,030 Cal yrs BP at the bottom of the sediment core, i.e. ~21 m of core depth. From these same ages, the 7.0-6.0 kyrs chronostratigraphic horizon would be located between 17-15.5 m of core depth. We

can recognize this stratigraphic horizon as a toplap defining the base of the PLUP in our seismic profiles (Figure 3.8d).

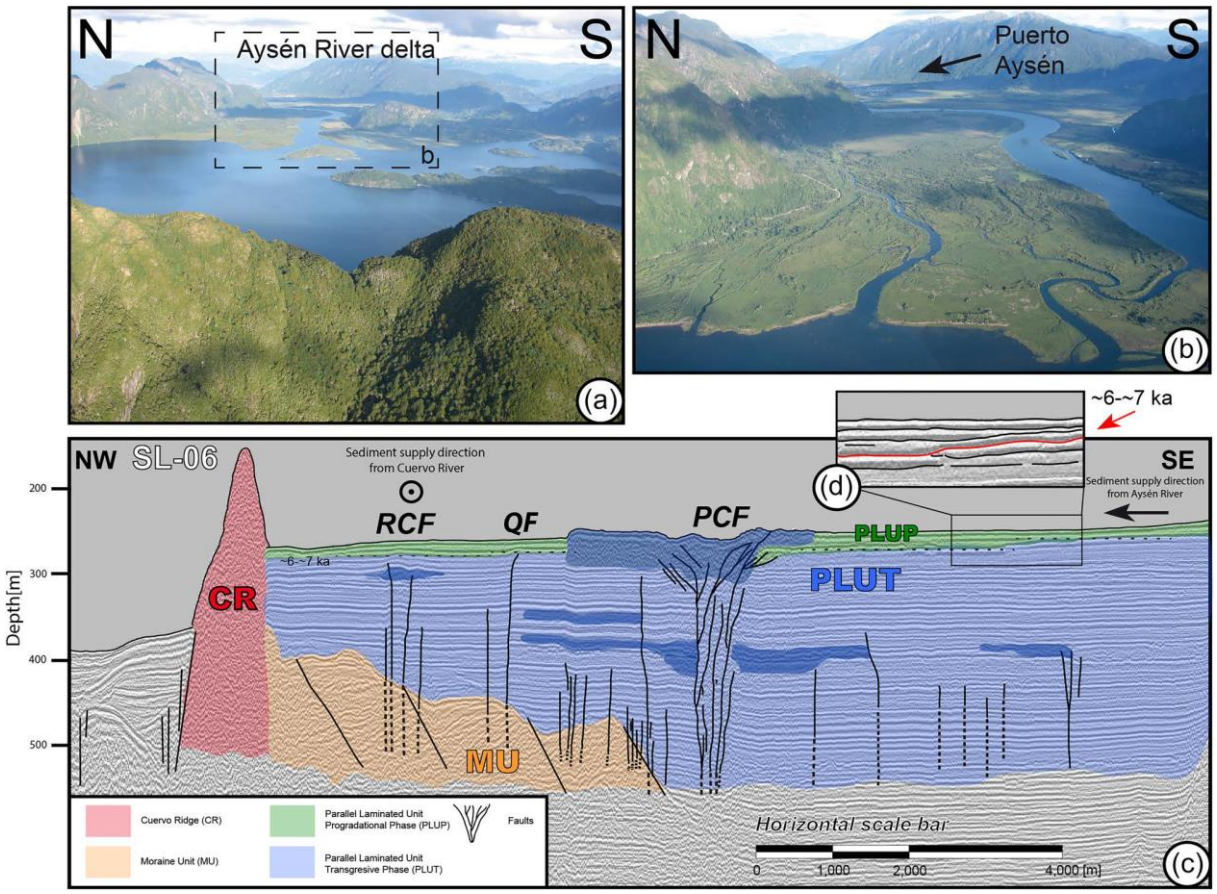

Figure 3.8. (a, b) Photographs taken from a helicopter showing the Aysén River delta. (c) Seismic reflection profile (SL-06) migrated to distance (m) using V_P = 2,000 m/s. PLU (postglacier sedimentary infill) contains two subunits: a lower one corresponding to a transgressive phase (PLUT, blue) and overlying strata corresponding to the progradational phase (PLUP, green). The limit correspond to the ~6 to ~7 kyr limit (found in Piston Core MD07-3117) when the sea level stabilized in the area during the early to mid-Holocene (Lambeck et al., 2002, 2014). Inset (d) shows a top-lap inside the sedimentary infill that matches with the sea level stabilization limit.

Using a simple geometric calculation, we can roughly estimate sedimentation rates values between ~15.6 and ~36.1 mm/yr (average of ~25 mm/yr) for the time period between ~12,000 and ~6,000 Cal yr BP. This large variation is mainly due to the geometry of MU and the simplicity of our approach. In addition, upon considering 17.3 kyr as a maximum age for the last ice sheet retreat in the region (Glasser et al., 2012; Hein et al., 2010; Sugden et al., 2005) and then for the top of the MU in our seismic profiles (Figures 3.4–3.6), it is possible to infer sedimentation rates ranging between ~8.3 and ~19.1 mm/yr (average of ~13.3 mm/yr) for the period between 17.3 and 6 kyr Cal BP. These last estimates are comparable to modern sedimentation rates inferred from ice-retreat processes in fjords (e.g., Morehead, 2001; Syvitski & Shaw, 1995). We interpret these values as the product of the strong contribution of sediment due to the melting of the Patagonian ice sheet during the deglaciation and by an increase in the accommodation space due to the increase of the sea level, despite the not well-constrained isostatic rebound in the area. Lower sedimentation rates deduced from the available radiocarbon data from the sediment core MD07-3117 (Wils et al.,

2018) that are similar to the previous estimates in the same area by Van Daele et al. (2013) can be explained by the progradation of the fluvial system into the fjord, due to the strong influence of the Aysén river and limited accommodation since the global sea level stabilization during the Holocene (Lambeck et al., 2002, 2014), originating the PLUP.

3.5.2 Surface rupture and paleoseismological record

High-resolution bathymetric data and seismic profiles from the inner Aysén Fjord area provide evidence for surface and subsurface submarine earthquake ruptures during the 2007-AYSS, associated with active faulting along main branches of the LOFS (Figures 3.4–3.6). The surface and subsurface submarine rupture that resulted from the 2007 M_w 6.2 dextral strike slip earthquake can be directly interpreted from the observation of deformed strata in seismic profiles (Figures 3.4–3.6), in which the fault rupture reaches up to the surface (profiles SL-05 and SL-06; Figures 3.8a and 3.8b). In addition to that, ~1.5–5.0 m height escarpments can be observed not only disrupting the PCB, but also affecting the seafloor outside this unit (Figure 3.3b). Moreover, the longitudinal sag limited by these submarine escarpments are aligned in the position of the PCF faulted zone (Figures 3.3b, 3.3c, 3.7a, and 3.7b). Finally, no sags delimited by submarine escarpments can be observed disrupting the other bulges caused by the landslides driven by the M_w 6.2 event in 2007. Thus, our interpretation differs from Van Daele et al. (2013) and Lastras et al. (2013), who proposed the sags on PCB exclusively as a break-through formed by the direct impact of the Punta Cola landslide. We propose these features resulted from an earthquake seafloor rupture with greater slip along the northern segment of PCF, evidenced by a well-developed fault zone reaching up to the seafloor surface in the northern profiles (SL-05 and SL06; Figures 3.4 and 3.5), with respect to the southern profile (SL-07; Figure 3.6). A local subsidence occurred associated to a relaxation lapse generated in the transpressive structure, overimposed by submarine landsliding phenomena (i.e., Kodaira et al., 2012). This would has produced a local rotation of blocks driving an apparent amplification of the vertical offset along the escarpments, with secondary normal faulting at shallow depths (Figures 3.7a, 3.7b, and 3.7c). The 3.5 kHz shallow seismic profiles carried out in 1995 (CIMAR-1) did not show any evidence of deformation of the sea floor in front of the PCF area (Araya-Vergara, 2011), supporting our hypothesis of submarine earthquake surface rupture driven by the M_w 6.2 event during the 2007-AYSS (Appendix Figures A13 and A14). Sedimentary flows driven by the impact of PCLS may have used this tectonic depression as a preferential path for deposition. This stresses the previous interpretation of Van Daele et al. (2013), who suggest that the entire deformation affecting the Aysén Fjord in front of Punta Cola (Figure 3.3b) is sedimentary in origin, involving deeper layers of the sedimentary infill (Type 4 after the model by Schnellmann et al., 2005). In contrast, our interpretation can explain this variant of the model considering these deeper levels, not exclusively as a ramp-flat system but rather as a part of the faulted zone along the PCF (Figures 3.7a and 3.7b), where it is possible to differentiate between tectonic deformation —affecting from deeper strata up to the seafloor— and synsedimentary deformation limited to shallower levels. Therefore, the singular geometry of PCB seen in the plan (opened in contrast to the other bulges) is in partly related to surface submarine rupture of PCF.

Seismic profiles SL-05 and SL-06 clearly show sediment layers disrupted by a normal fault in the area, where a 650 m long escarpment is visible (Figure 3.3b), with a bathymetric change of ~2 m associated with the QF trace (Figure 3.3d). This escarpment is parallel to the fault trace projected into the Aysén Fjord, proposed by Vargas et al. (2013). However, alternatively to the statement of Wils et al. (2018), we suggest that this escarpment does not correspond to a 2007 event fault scarp but rather to an ancient fault scarp draped by the younger sedimentary infill because our profiles SL-05 and SL-06 show the fault tip between ~17.9 and 14.6mb.s.f. (Appendix Figures A9 and A10). Thus, we interpret that the M_w 6.1 dextral-normal event that occurred during the 2007-AYSS along the QF, could not have reached the surface at the Aysén Fjord sea bottom.

No surface rupture feature can be associated with 2007-AYSS along the RCF according to our observations in our seismic profile data, in which the tip of the RCF ranges between ~109.2 and 27.2 m b.s.f (Appendix Figures A9 and A10).

The complex geometry of the structures in the area could generate several scenarios for paleo-earthquakes that may have left a record inside the fjord in the form of soft-sediment deformation and/or vertical offset distribution of the reflectors on both sides of a single structure. The action of these faults could have been presented in several ways but with two extreme scenarios. The first one involves individual faulting for each structure through time, resulting in different recurrences for each fault, and, therefore, each paleo-event would be associated with a single structure. For us, this approach does not appear to fit as well with the complex tectonic setting of the area and even less so with the structural domain —the transfer zone— in the LOFS. We would expect interaction between structures, as evidenced by the record of the recent events during 2007, as discussed later in this work.

The second group of scenarios could imply multifaulting events that can occur when coseismic ruptures between two or more structures exist. These events can be favored by other factors such as the presence of fluids (Legrand et al., 2011) and static stress transfer between structures constituting the same fault system or the megathrust itself. Examples of such events, but over shorter time scales, are the 2010 Canterbury earthquake sequence in New Zealand (e.g., Beavan et al., 2012), the 2011 El Mayor-Cucapah in Mexico (e.g., Fletcher et al., 2014) and the 2016 Kaikoura earthquakes in New Zealand (e.g., Hamling et al., 2017). These types of phenomena show difficult paleoseismological inferences and seismic hazard assessment from simplistic models based on single fault ruptures (Stirling et al., 2017).

By considering average sedimentation rates from the PLU (~25 mm/yr, between 12 and 6 kyr Cal BP), representing the transgressive phase of the sedimentary infill of the inner Aysén Fjord, we speculate that the last seven paleolandslides, with a similar sedimentary imprint that resulted from earthquakes nucleated along active faults in the area, similar to the M_w 6.2 during the 2007-AYSS. Evidence show that landslides related to the 1960 M_w 9.5 Valdivia earthquake have been superficial, restricted to soil and of relatively small volume (Wright & Mella, 1963) while landslides related to the 2007 M_w 6.2 Aysén earthquake several tens of million m^3 large deep seated and in bedrock (Oppikofer et al., 2012). Thus, the deep seated landslides that enter Aysén

Fjord should only be from large, local ruptures and not from the subduction zone (e.g., 1960-style events). Using our estimations these paleoevents occurred close to ~8,315 to ~7,115 (MDU-07), ~6,837 to ~6,238 (MDU-06), ~5,576 to ~4,675 (MDU-05), ~4,353 (MDU-04), ~3,576 (MDU-03), ~2,648 (MDU-02), and ~1,344 (MDU-01) yr BP. If our assumptions about sedimentation rates and timing are correct, these events occurred approximately every ~1,100–1,500 kyr in the Holocene epoch (Appendix Figure A12).

3.5.3 Seismic migration and seismotectonic model

Shallow earthquakes recorded here are generally located in the first 10 km of the upper crust (Figure 3.9a). At a preliminary view, these events appear to have a random distribution. To explore this, we generated a first-order 4-D seismotectonic model (space and time; Figure 3.9). By using different observation windows (day-to-day and month-to-month), it is possible to distinguish patterns of seismic activity revealing cluster-like behavior. We establish a first-order association between each seismic cluster and the spatial location of the QF, RCF, and PCF, as well as with other minor faults proposed as lineaments in the area that would have been involved in later phases during the 2007-AYSS.

On January 2007, two NE-SW shallow and deeper clusters of epicenters occurred close to the QF trace (Figure 3.9b). The depth of the earthquakes ranges between 6.0–8.2 km with local magnitudes of $2.0 \leq M_L \leq 4.7$. The distinction between the two clusters, which we have interpreted as an expression of two independent ruptures, is clear in terms of time and depth (Figure 3.9a). The association of both clusters with some of the nearby structures was done by (a) proximity, (b) projection of the structure in depth, and (c) the degree of deformation absorbed by each fault recorded in the geological record. In this way, we associate the deepest cluster to the PCF and the shallowest cluster with the QF (green and purple circles and envelopes, respectively, in Figures 3.9a and 3.9b).

Later, in February 2007, seismicity migrated southward, with depths ranging between 3.9 and 8.7 km and magnitudes between $1.3 \leq M_L \leq 5.0$. We tentatively associate two clusters to the RCF (blue circles and envelopes; Figures 9a and 9c). Well-defined clusters were located near the RCF-QF intersection, with depths ranging between 3.3–6.1 km and magnitudes between $1.5 \leq M_L \leq 3.2$. We interpreted this seismic activity as a prolongation of the seismicity developed in January. Seismicity depths ranged from 1.7–7.4 km with magnitudes from $1.1 \leq M_L \leq 5.3$. In addition, some minor epicenters appeared near PCF in contrast with the deeper seismic activity previously seen (depths: 2.0–3.4 km; $1.0 \leq M_L \leq 3.1$; green circles and envelopes in Figures 3.9a and 3.9c). We interpret this shallowing in the seismicity as subsequent earthquake ruptures propagated toward the surface.

QF concentrates most of the seismic activity in March (Figure 3.9d). Hypocenters range between 2.0 and 6.8 km in depth with magnitudes of $1.0 \leq M_L \leq 4.8$. This seismic activity moves closer to the surface on the following days (Figure 3.9a). Additionally, a small cluster north of the study area and west of the RCF trace is also well defined (depths: 5.0-6.4 km; $\sim 1.0 < M_L \leq 4.1$).

April 2007 is the most interesting observational time window in the sequence due to the energy released and other phenomena triggered by the two main earthquakes (M_w 6.1 and M_w 6.2). Despite this, as can be observed in Figures 9a and 9e, the concentration of earthquakes in each area associated with QF and PCF is lower than in the previous months. This is mainly due to and is more noticeable in the case of the PCF, a void in the information caused by the damage to the seismological equipment associated with the M_w 6.2 event. Nevertheless, activity associated with these faults is distinguishable within our model. PCF plays a more important role due to the presence of an NW cluster characterized by shallow depths (1.8–3.7 km, green circles and envelope in Figures 3.9a and 3.9e) located near the area where the surface rupture is observed. In addition to the geophysical and geological observations already exposed, this clarifies the moment when the subsurface rupture of QF and superficial rupture of PCF were generated.

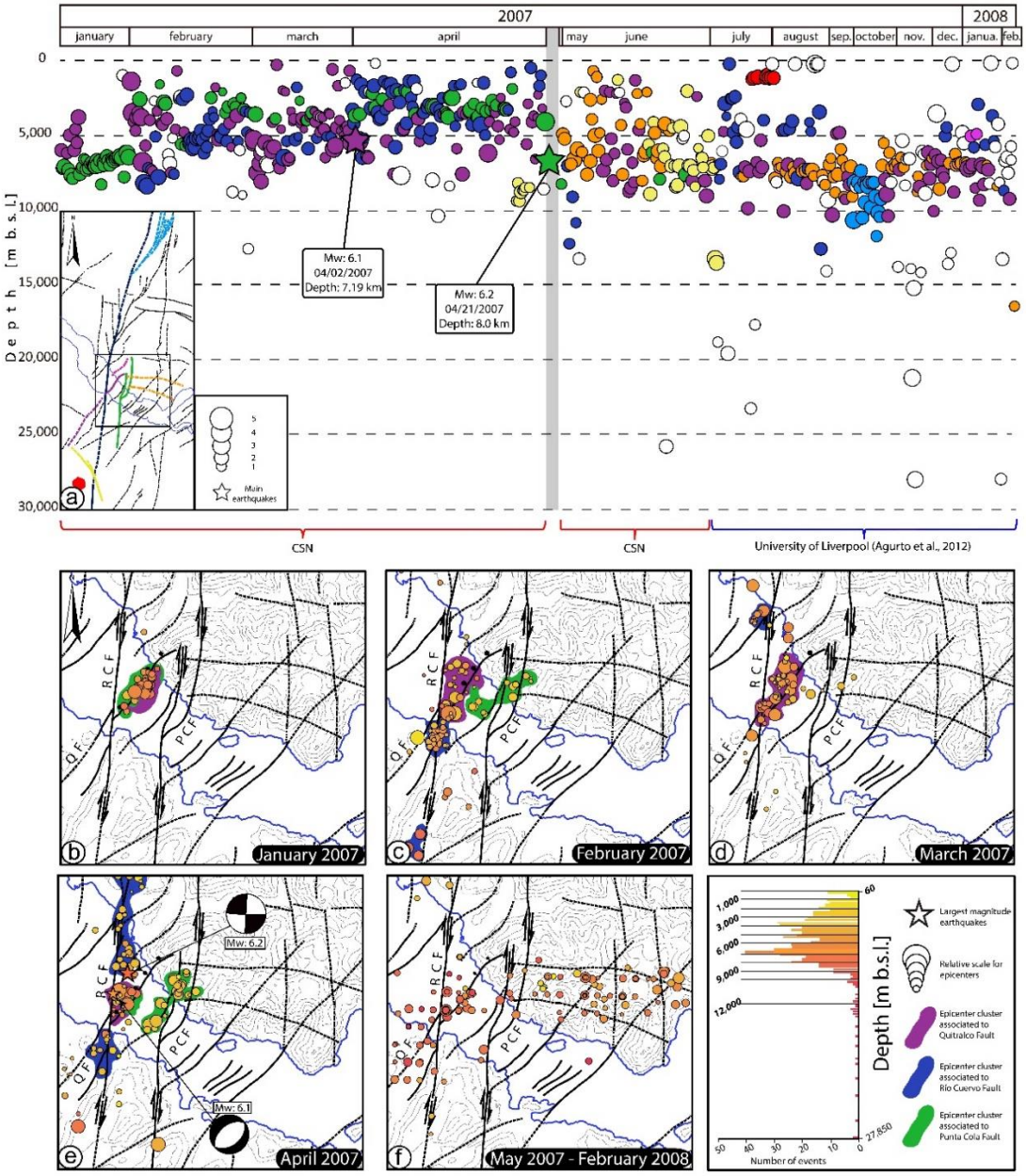

Figure 3.9. Seismic migration of the 2007-AYSS. Fault map and seismological data (Agurto et al., 2012; Barrientos et al., 2007) were used. (a) Temporal evolution of the seismic sequence vs. the depth. Green circles correspond to earthquakes associated with PCF. Purple circles indicate QF. Blue circles indicate RCF. Orange circles indicate the group of guidelines identified on the northern flank of the fjord. Yellow circles indicate a NW-SE line located south of the study area, and light blue circles indicate a branch of the RCF located north of the study area. The mini-map specifies each fault and lineaments with its corresponding color. (b) January, 2007. (c) February, 2008. (d) March, 2007. (e) April, 2007. (f) May, 2007 to February 2008. A warm color-scale is used to highlight the depth of each event. Epicenters of M_w 6.1 and M_w 6.2 are marked with stars. Epicenter clusters, which we associate with each active fault involved in 2007-AYSS, are colored with purple (QF), blue (RCF) and green (PCF) envelopes.

It is plausible to expect that during the period without local seismic networks (i.e., no data); aftershocks occurred in QF and PCF. We have summarized the period between May 2007 and February 2008 in Figure 3.9f for the inner fjord area, and more data are shown in Figure 3.9a. Unlike previous months where seismic activity was approaching the surface and ended mostly within the first 5 km, the phase after the peak stage of the 2007-AYSS was characterized by a deepening of the activity

(between ~5 and ~10 km) and by a more important role of other structures, some of which are located outside the study area (yellow and light blue in Figure 3.9a). In the inner fjord area, a W-E migration was predominant and can be associated with the approximately E-W lineaments (orange circles in Figure 3.9a) located on the northern flank of the fjord (Vargas et al., 2013).

Finally, we present a 3-D seismotectonic model of the faults across the Aysén Fjord involved in the 2007-AYSS (Figure 3.10). The constraints used are mostly the hypocenter clusters, focal mechanisms solutions of the main earthquakes, interpretations of the seismic profiles, and our structural view based on previous field observations (Thomson, 2002; Vargas et al., 2013). All of these data were used to draw planes fitting the hypocentral distribution (e.g., Alparone & Gambino, 2003; Wan et al., 2008; Appendix Figure A15). The proposed fault planes present soft angle breaks according to the general geometry observed for this type of structure (e.g., Sylvester, 1988; Thomson, 2002). Our seismotectonic model presents similarities with the theoretical model of Thomson (2002), characterized by approximately NS LOFS structures forming a positive flower structure at a crustal scale, together with main NE striking dextral-normal branches of the LOFS, defining a major fault transfer zone in the area (Thomson, 2002; Vargas et al., 2013).

According to our seismotectonic model (Figure 3.10), we suggest that the 2007-AYSS and prior similar-sized events found in our seismic profiles could be the result of static stress transfer and seismic migration from the lower-ductile to the brittle continental crust. This has been widely demonstrated in the literature, where the tendency is for earthquakes of a medium to large magnitude in crustal faults nucleates at the base of the brittle crust (e.g., Das & Scholz, 1983; Scholz, 1988). This condition, observed in other faults in similar tectonic contexts (e.g., Sumatran Fault: Bellier & Sébrier, 1994; Muraoka et al., 2010), would explain the beginning of the sequence at low depths. We propose this phenomena mainly based on the hypocenters general tendency at deep during the first four months (Figure 3.9). We do not rule a mixed origin related to a combined fluid-driven mechanism and intra-arc tectonic activity, as other works have proposed (Agurto et al., 2012; Legrand et al., 2011). Geologic slip rates along this fault system are unknown in the study region, but once considering modeled based on extremely limited input data slip rates in the order of 32 ± 6 m/kyr since theMiocene, as inferred from thermochronology and displaced granites along the LOFS to the north from our study region (Adriasola & Stöckhert, 2008; Rosenau et al., 2006), it is possible to infer an important seismic potential along active faults of this major fault system (Vargas et al., 2013), which is necessary to consider in future seismic hazard assessment in the region. In light of the evidence we present here showing shorter recurrence intervals between events than postulated previously, having new slip rates here will be of great importance.

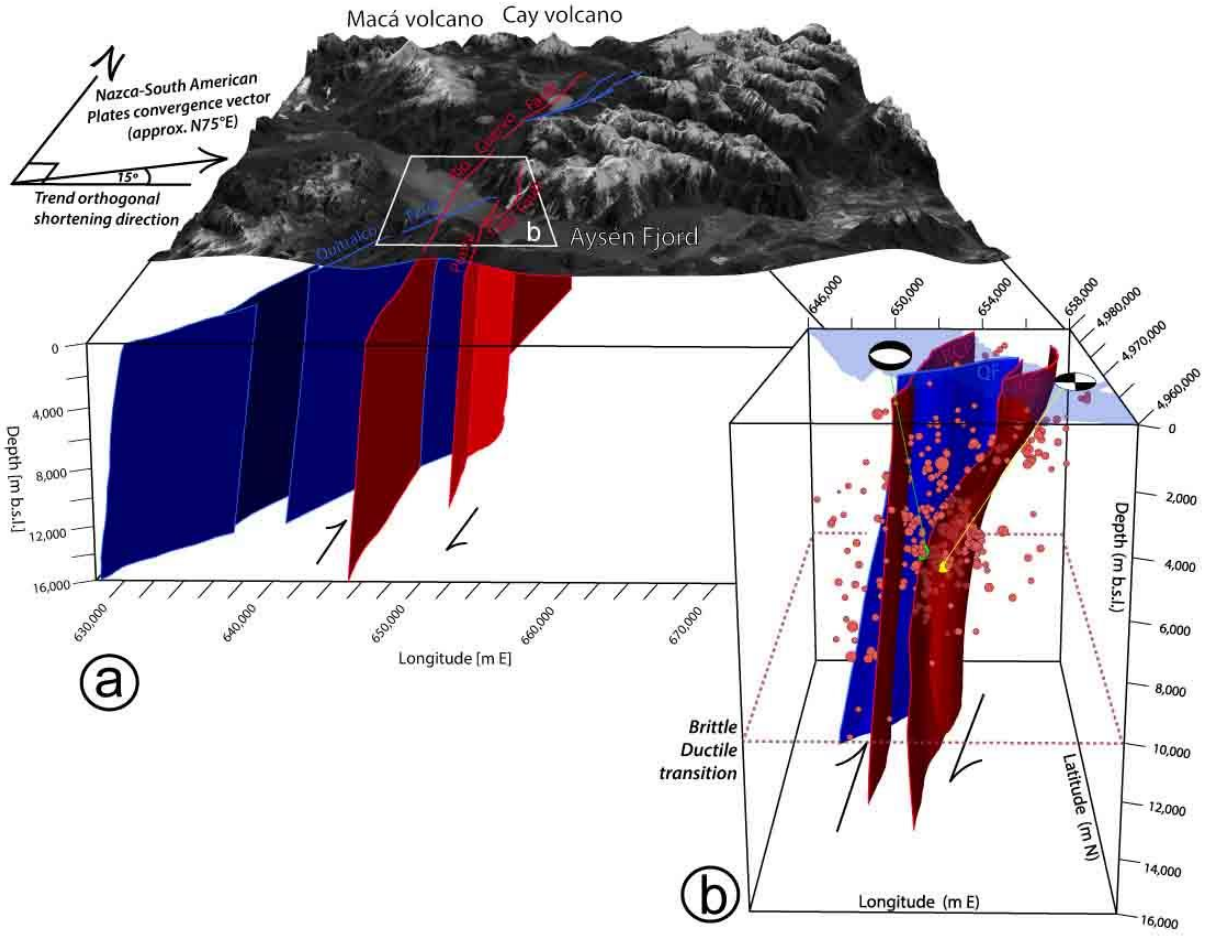

Figure 3.10. 3D geometric model of the LOFS in the study area. (a) Seismogenic faults projected at the scale of the fjord and its surroundings. A digital elevation model based on 1:50,000 topographic sheets from the Chilean Army Geographic Institute (IGM) with a SPOT-image is superimposed on the fault model. (b) Close to the main structures (RCF, QF and PCF) involved in 2007-AYSS. Red spheres correspond to earthquakes used for the generation of fault planes. The green sphere corresponds to M_w 6.1. The yellow sphere corresponds to M_w 6.2.

3.6 Conclusions

To understand earthquake phenomena along active fault systems, it is necessary to have an extensive and detailed recognition of the structures and assess fault behavior at millennial time scales. Aysén Fjord is located in the Patagonian Andes of Chile and found in a unique tectonic setting adjacent to a trench-ridge-trench triple junction, along which stress partitioning induces active faulting along the major LOFS. Here, the 2007-AYSS occurred from January 2007 to February 2008, which culminated with a M_w 6.2 event. Faults within the LOFS (Vargas et al., 2013) were responsible for the crustal seismicity that occurred during this period that lead to casualties (e.g., Naranjo et al., 2009; Sepúlveda et al., 2010; Sepúlveda & Serey, 2009). Extensive landslides that occurred during 2007 were the main factor, due to generation of large displacement waves when rock avalanches that were triggered during the earthquakes entered Aysén Fjord, in the economic impacts and life loss.

Seismicity data based on two local seismic networks were deployed from January and April 2007 (Barrientos et al., 2007; Russo et al., 2011), and July 2007 and February 2008 (Agurto et al., 2012) show involvement in the seismic sequence of the Punta Cola, Río Cuervo, and Quitralco faults. Geological data in the field (Vargas et al., 2013) show evidence for recent fault activity at Punta Cola and Río Cuervo faults. Active source seismic data from Aysén Fjord show long term Late Quaternary evidence of post-LGM (and likely post-12 kyr) deformation of marine fjord infill sedimentation, due to faulting in Punta Cola, Río Cuervo, and Quitralco faults. Detailed analysis of the seismic data shows that Punta Cola Fault ruptured the seafloor along its northern segment during the main M_w 6.2 earthquake in 2007. Meanwhile, Río Cuervo, and Quitralco faults, likely did not rupture through the seafloor sediments in 2007, although there is evidence based on disrupted seafloor sediments for pre-2007 deformation along these faults. Seismic activity in the 2007 AYSS reflects ruptures that begin near the brittle-ductile interface approaching the seafloor and appears to show that the entire fault plane is rupturing at the peak stage within the sequence.

The analysis of seismic profiles also reveals more evidence of the active nature of faults affecting the fjord in the form of seismic facies with similar characteristics to those generated by major landsliding caused by the M_w 6.2 earthquake. In the seismic stratigraphy, we detected seven other examples of pre-2007 major landsliding events within Aysén Fjord. Because the Giant M_w 9.5 Valdiva earthquake in 1960 did not trigger notable landslides more than small volume rock fall and soil slips in Aysén Fjord (Wright & Mella, 1963), likely due to the distance from the subduction zone source of that event, and because crustal events are well known to be responsible for large coseismically inducted earthquakes, local paleostrong ground motions that triggered these pre-2007 landslides were likely from ruptures along local LOFS fault sources. Thus, strong ground motions during a local crustal earthquakes are the most likely source of these buried landslide deposits in the fjord sediments, mainly because of the intensity of the shaking behavior, which strongly depends on the magnitude and distance from the fault source.

Our seismotectonic analysis suggests that during the last seismic sequence the seismicity started at ~8 km depth within the Punta Cola and Quitralco faults, subsequently migrating to the other structures driving multiple episodes of active faulting in the area. We propose that earthquake nucleation along these active faults was a product of stress transfer from the ductile lower crust to the fragile upper crust, favored by the thermal weakening due to the proximity of the triple junction of the subduction contact of the Nazca and Antarctica Plates beneath the South American Plate. Importantly, through a combination of seafloor morphology derived from multibeam sonar data, plus fjord basin stratigraphy from subseafloor seismic profiles when combined with local seismicity data allowed for a more comprehensive assessment of structures from within the LOFS than using any of these methods in isolation. We suggest that the synergies obtained through combining these data could be of use in other regions where these three types of data may be available from historic fault ruptures (both onshore and offshore) and yield additional insight into the both regional and local neotectonics and associated coseismic geohazards (including major landslide events).

Ultimately, because of both the lack evidence for full ruptures (i.e., to the seafloor surface) along the Río Cuervo and Quitralco faults in 2007 combined with the strong evidence for recurrence of strong ground motions here in the past 12 kyr as revealed from buried landslides deposits in Aysén Fjord sediments, these faults should be considered important sources of seismic hazard and require further analysis to better understand the recurrence of events and potential hazard associated with these structures.

Chapter 4: Glacial Quaternary geology of the Patagonian Andes across the Coyhaique-Puerto Aysén transect constrains neotectonics and paleoseismological observations along the Liquiñe-Ofqui Fault System

To be submitted to Quaternary Science Reviews

Angelo Villalobos, Gabriel Easton, Rita Arqueros, Gregory De Pascale

Abstract

Quaternary glaciations in the Southern Andes are widely studied in the mountain areas of both the Lakes Region and the Magellan Region. Aysén Region is an area well known for having held the former Patagonian Ice Sheet, whose length along this mountain range is estimated up to 2,000 km long (38° - 55° S) during the Last Glacial Maximum (LGM). Icesheets, and also mountain glaciers, leave a rich geomorphological record of their advances. Particularly, they are well represented in the eastern piedmont. This offers a great opportunity to study and understand fluctuations of the ice cover through glacial cycles. In this work, we present for the first time a geological transect (45.5° S) including geomorphology, stratigraphy, and radiocarbon-based geochronology of glacial drifts in the Coyhaique River basin, Emperador Guillermo and Mañihuales rivers confluence, and close to Puerto Aysén city. Furthermore, we present evidence of underwater buried moraines in Lake Riescoand Aysén Fjord. We focus on to determine the environmental evolution during Quaternary glaciations and the position of the ice sheet during this period, to constrain the activity of the Liquiñe-Ofqui Fault System. We propose based on radiocarbon ages that the last icesheet retreat in this region occurred synchronously on both flanks of the main mountain range after 12 ka. Therefore, constraining the maximum age of subaerial and submarine geomorphological and paleoseismological features associated with this fault zone in the area.

4.1 Introduction

During the Quaternary, Earth was cyclically affected by a series of glaciations whose probable origin is associated with variations in the amount and distribution of the incident solar radiation (Zachos et al., 2001). These variations would be due to orbital changes that would induce glacial and interglacial periods every ~100 ka (Zachos et al., 2001). The study of the regional implications of these global variations is essential for both palaeoenvironmental and paleoclimatic reconstructions. Quaternary glaciations in the Patagonian Andes of Southern Chile are widely studied in the mountain areas of both the Lakes Region (Clapperton, 1993; Porter, 1981; Denton et al., 1999) and the Magallanes Region (Marden et al., 1995), where there is still considerable ice bodies present including the Northern (NPI) and Southern Patagonian Icesheets.

In the North Patagonian Andes (i.e. Aysén Region), although there are a number of studies focused around the margins of the NPI near Lake General Carrera-Buenos Aires and Laguna San Rafael (e.g., Singer et al., 2004; Turner et al., 2005; Kaplan et al., 2004; 2005; Douglass et al., 2006; Araneda et al., 2007; Ackert et al., 2008; Hein et al., 2010; Bertrand et al., 2012; Glasser et al., 2012; 2016), studies further to the north and thus further away from the modern NPI are lesser (e.g., Anderssen et al., 1999; Denton et al, 1999a; 1999b; Abarzúa et al. 2004; Moreno et al., 2015). Despite this, this sector of the Andes is an area well known for been covered by the Patagonian Ice Sheet (PIS), whose length along this mountain range is estimated up to 2,000 km long (~38° S - ~55° S; Figure 4.1a) during the Last Glacial Maximum (LGM) which occurred from ~25 to 18 ka (Glasser & Jansson, 2005; Glasser et al., 2008; 2016; Hein et al., 2010; Bendle et al., 2017). Deposits and erosive evidence of these icesheets, and also mountain glaciers, leave a rich geomorphological record of the limits of this ice. Particularly, they are well represented in the dryer-climate and less vegetation covered eastern piedmont, in comparison to the wet temperate rainforests found to the west of the study area near the fiords. This offers a great opportunity to study and understand the fluctuations of the ice through the glacial cycles and gain additional insight into the paleoclimate in this area. Examples of this kind of study are those performed on Lago General Carrera-Buenos Aires shores (e.g., Ton-That et al., 2000; Douglass et al., 2001; 2002). These investigations have focused on clarifying geological and tectonic aspects of the pre-Quaternary basement. Under this context, the studies of geological mapping conducted by Skármeta & Charrier (1976), Skármeta (1978), and Niemeyer et al. (1984) recognized the existence of geomorphological units and glacial, periglacial, and river deposits eastward Coyhaique city.

In this paper, we present the geomorphology, stratigraphy, and radiocarbon chronology of extensive moraine belts and associated deposits in the Coyhaique River Hydrographic Basin (CRB), the confluence of Emperador Guillermo and Mañihuales rivers (EMC), and close to Puerto Aysén, in the Aysén Region. This provides insight across the Andes from the fjords in the west to the pampas in the east. Also, we present evidence of submarine moraines in the Lake Riesco and Aysén Fjord. Along with the associated glacial drifts morphology and stratigraphy, our objective is to determine the evolution of the environment during the Quaternary glaciations, as a first contribution to the environmental evolution of this sector. A secondary objective use the timing of glacial deposit deposition relative to the active Liquiñe-Ofqui Fault System (LOFS) in order to constrain motion along these faults.

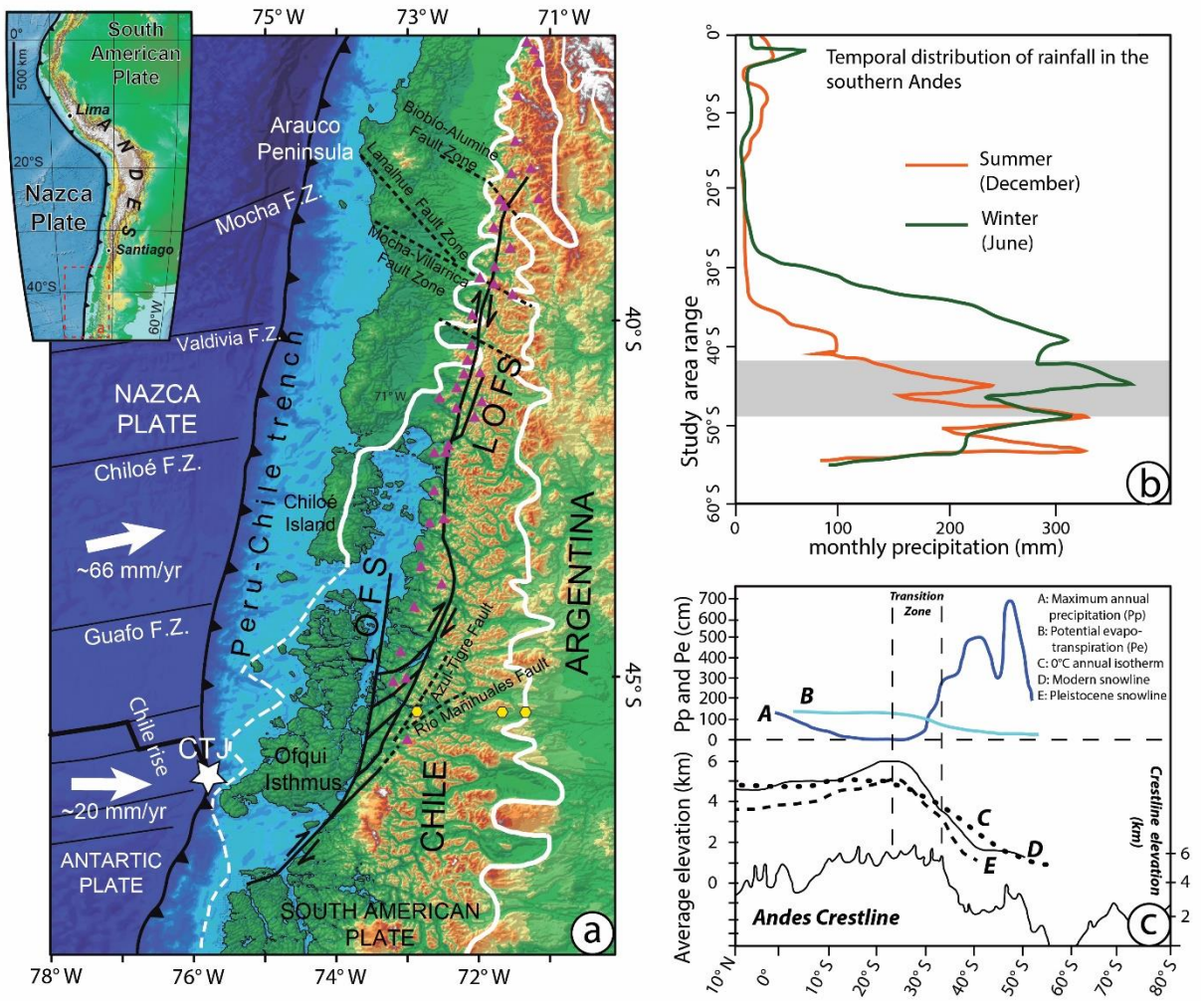

Figure 4. 1. Up to the left inset: Geotectonic framework of South America showing regional tectonics (a) Regional tectonic context at the triple junction of the Nazca, Antarctic, and South American plates. Composite Digital Elevation Model (DEM) of the Nazca and South American plates. Regional map showing the location and extent of LOFS (continuous black lines), transverse fault systems (segmented black lines), and main volcanoes (purple triangles) (after Hervé, 1994; Moreno & Naranjo, 2003; Rosenau et al., 2006; Cembrano & Lara, 2009). Convergence velocity vectors after Angermann et al. (1999). White lines show the approximate maximum extension of the Pleistocene ice sheet during the Last Glacial Maximum (modified from Thomson et al., 2010). Yellow dots show (from west to east) Puerto Chacabuco, Coyhaique, and Coyhaique Alto meteorological stations. (b) Annual rainfall and average temperatures in the Southern Andes (modified from Hollin et al., 1981). The gray fringe highlights our study area range. (c) Noth-south profile along the Andes. It shows rainfall gradients (modified form Clapperton, 1993).

4.2 Study area

4.2.1 Regional physiological settings

Our study area is divided into six key field sites distributed approximately between 45.2° and 45.6° S (Figure 4.2a). It encompasses the three geomorphological domains, from west to east, found in the Aysén Region geomorphology: fjord, main mountain range, and pampa areas. Also, it can be broadly summarized using a W-E

profile (Figure 4.2b, parallel to 45° 38.5 'S). This profile starts in the Aysén Fjord and finishes approximately in the Chile-Argentina border (Figure 4.2a).

The main mountain range, where four of our sites are located (Figures 4.22 and 4.25), is characterized by steep-sloped peaks (Figures 4.1c and 4.2b). These summits could represent paleo-ice field nunataks (Arqueros, 2004), which would have been stayed in this area during the Quaternary glacial phases. At present, most of the summits are covered by permanent ice. The characteristic features in the fjord area are the steepen walls delimiting it, were ancient glacial valleys where glaciers moved westward. At present, they are flooded by the sea and constitute the base level and discharge zones of many rivers of the region. Eastward of the Andes axis, in the transition zone between the main mountain range and pampa area, CRB is located (Figures 4.3 and 4.5). Both in Coyhaique River and in the Ñireguao, Pollux, and Simpson rivers basins, glacial lobes generated during the Quaternary glaciations from the ice fields hold in the main mountain range would have advanced eastward, generating the glacial landforms and deposits observed in the region.

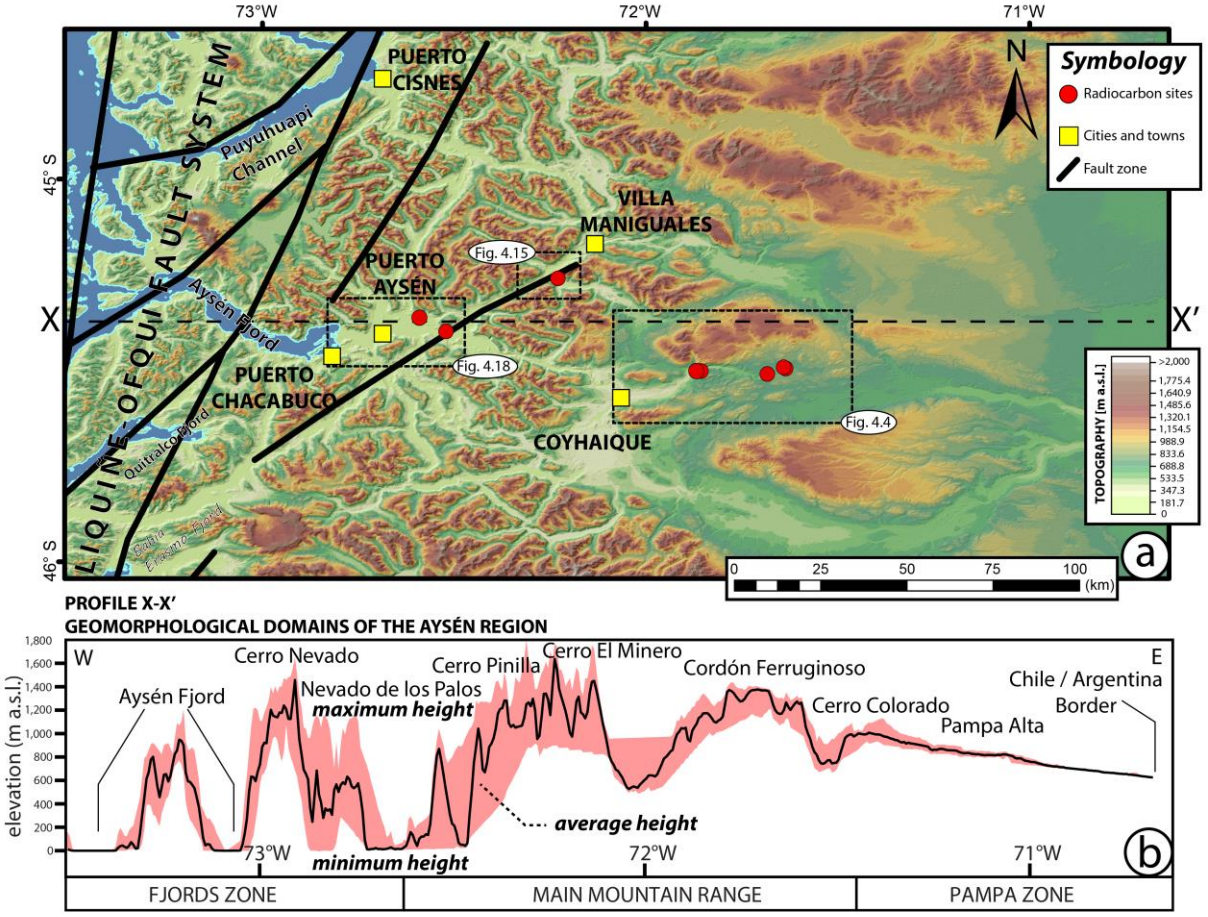

Figure 4.2. (a) Regional physiological setting of the Norpatagonian Andes (Chilean Aysén Region) highlighting the Profile X-X'. It is shown in each study area by an inset. Sampling sites for radiocarbon dating (red circles, and translucent white boxes indicates non-calibrated ages), cities and other localities (yellow squares), and fault zones (heavy blue lines). (b) West-east Profile X-X' in the Aysén Region. Regional features are shown using a swath profile, with a 5 km buffer both north and south, where the average height is indicated by a black line, and minimum and maximum heights are expressed by the red area borders. This defines a three geomorphological domains segmentation (fjord area, main mountain range, pampa area).

4.2.2 Geological Settings

The regional geology of the Southern Andes is dominated by the Northern Patagonian Batholith (NPB) however a number of other key geological units are found. In detail, in our study area, the mountain range is dominated by Paleozoic metamorphic basement rocks, which are unconformably overlain by upper-middle Jurassic to Cretaceous volcanic and marine sedimentary sequences (Niemeyer, 1975; Aguirre-Urreta & Ramos, 1981; Diemer et al., 1997; De la Cruz et al., 2004). The latter are unconformably overlain by tertiary continental sedimentary rocks and basalts (Espinoza & Fuenzalida, 1971). All these units are intruded by granitic bodies associated with the Lower Cretaceous NPI (Lagabrielle et al., 2004; Vandekerkhove et al., 2016). Quaternary volcanic bodies associated with the southern volcanic zone are key elements recognized in the area, with historical and recent activity (Stern 2004; Naranjo & Stern, 1998; 2004). The basins located east of the main mountain range are filled by Pliocene-Quaternary and glaciofluvial and glacial sediments.

Of all these units previously named, CRB exposes Jurassic and Cretaceous stratified rocks associated with Ibáñez Formation (JKi; Niemeyer, 1975), Coyhaique Group (Kic; Lahsen, 1966; Haller & Lapido, 1980), and Divisadero (Kid; Heim, 1940) and Toro formations (Kset) and Cerro Mirador – Casa Piedra Domes Complex (Covacevich et al., 1994). Finally, a series of Quaternary deposits that includes glacial, glaciofluvial, glaciolacustrine and fluvial deposits, infill the main valleys of the region. In addition, deposits of mass removals associated with steep topography are recognized cover all the above-named units.

4.2.3 Climate Settings

The climate of the Aysén Region is controlled by the influence of (i) the rainfall associated with the westerlies, determined by the seasonal variation of the polar front (Strub et al., 1998) that conditions increased rainfall during the winter months, (ii) polar cell, (iii) storm tracks, (iv) the position and intensity of the SE Pacific high, and (v) the orographic factor induced by the main mountain range (Figure 4.1b). The latter involved a drastic decrease in the amount of rainfall from the mountains to the east, which has not changed, at the least, from the Upper Pleistocene (McCulloch et al., 2000).

The maximum rainfall occurs in the coastal sector characterized by a temperate maritime climate. According to data from Puerto Aysén station in this area, annual precipitation is 2,150 mm/yr. Mean summer temperature (December–February) is 12.7°C, whereas mean winter temperature (June–August) is 4.4°C (Puerto Aysén weather station, 32 m a.s.l; Dirección General de Aguas, 2013– 2018).

In the vicinity of Coyhaique city, there is the transition from a cold rainy temperate maritime climate to an Andean with steppe degeneration. In Coyhaique

station, the mean annual rainfall falls to 930 mm/yr (Reserva Nacional Coyhaique weather station, 400 m a.s.l.; Dirección General de Aguas, 2013–2018) with a slight drop in precipitation in February, and the mean summer temperature (December–February) is 11.2°C, whereas mean winter temperature (June–August) is 1.7°C.

Towards the central-eastern sector of the basin, an Andean climate with cold steppe ecoregion (Hepp et al., 1996) is well developed (Patagonian dry climate), with characteristics of semi-arid desert. This climate corresponds to a transition to the cold stage, where annual precipitation that continues to decrease eastward ranging from 400 to 700 mm/year (mean annual temperature of 6.5 °C, mean maximum temperature of 11.2 °C and mean minimum temperature of 2.2 °C).

The vegetation present in the study area corresponds to the Cold Temperate Notofagus Forest, also known as the Deciduous Native Forest. They are Lenga (Nothofagus Pumilio), Ñirre (Nothofagus Antarctica), and Coigüe (Nothofagus Donbeyi, Nothofagus Betuloides) forests associated with an undergrowth of grasses. There is also the presence of shrubs, such as calafate, michay, and maitencillo. Towards the Coyhaique sector, the vegetation transforms into the Patagonian Steppe, also known as the Steppe Herbaceous Biome, which dominates the border with Argentina. It comprises perennial herbaceous plants and some scattered shrubs, dominated by the grass of coironales and semi-shrubby vegetation such as sting and muddy bush, and herbaceous cardillo and the pimpernel (Acaena Pinnatifida).

4.2.3.1 Equilibrium Line Altitude and Location of modern glaciers

In marine and temperate glaciers, snow line location determine approximately the Equilibrium Line Altitude (ELA). ELA corresponds to an imaginary line that separates the glacier accumulation and ablation zones. In the temperate zone of the Aysén Region, between 40° and 46° S, ELA coincides with the 0° C summer isotherm, located between 3,000 - 2,000 m a.s.l. (Figure 4.1c) (Clapperton, 1993).

The snow line height rises eastward, both in modern ELA and LGM-ELA (Figure 4.1c) (Porter, 1981), which indicates a source from the west for rainfall in both periods. To the south, as the precipitation increases due to the influence of the westerlies and the polar front, the position of the ELA decreases reaching temperatures below the 0° C summer isotherm (Figure 4.1c). This condition allows glaciers to develop between the 36° and 46° S on the rocky massifs in the area.

Northern Patagonian Ice Field comprises 28 glaciers covering 4,200 km^2 (Aniya, 1988), while Southern Patagonian Ice Field includes 48 glaciers covering an area of 9,659 km^2 (Aniya et al., 1996). There are many small mountain glaciers outside the area of the ice fields, which are mostly not inventoried (Rivera et al., 2000). Regional antecedents indicate that during the LGM, the extension of the glaciers would have reached an area greater than the current one, reaching about 540,000 km^2 (Hollin et al., 1981), covering the entire study area.

4.2.4 General hydrography

The CRB belongs to the Simpson River hydrographic basin. Its confluence is located just outside Coyhaique city (Figure B1a), on the western edge of this point of interest. It covers an approximate area of 630 km^2, its height range between 200 and 1,765 m a.s.l. It is 45 km long and a width ranging between 6 km, near Coyhaique city, and 20 km in the Meseta Boscosa-Pampa El Diablo zone. The main tributaries of CRB are Las Cascadas, Seguel, Los Corrales, El Zorro Chico, Zanjón Hondo, Pedregoso-Las Nieves, El Culebra, and Los Tres Puentes-Casa Piedra estuaries (Figure B1). Together they present a dendritic pattern.

The hydrographic basin also has a large number of lagoons covering ~5 km^2. The most important are Baguales, El Toro, Escondida, Las Perdices, Las Mellizas, El Zorro, Horqueta, El Principio, Los Patos, Los Cóndores, Tranquilo, Verde, and Los Flamencos (Figure B1). With the exception of the last three, these lagoons constitute a remnant of a supraglacial environment in the transition to an environment of ice disintegration and another of frontal moraines (Arqueros, 2004).

4.3 Methodology

A variety of methods were used in order to characterize and constrain timing of glacial advance and retreat in the study area. A literature review was conducted to better understand the Quaternary and pre-Quaternary geological history. Additionally remote sensing mapping of the area was done at a regional scale in addition to fieldwork for validation of remote mapping and sample collection and field characterisation. The details of these various methods will be discussed below.

We follow five steps to establish a radiocarbon chronology of the drifts (moraine systems) and their landforms. The ancient extent of the glaciers was established through geomorphological mapping, using aerial photography, satellite images, and ground observation.

The first step was to generate glacial geomorphological maps of the drifts distributed eastward main mountain range. Moraine deposits located northward Puerto Aysén city and at Emperor Guillermo and Mañihuales rivers confluence were also mapped. Extensive aerial photographic analysis (taken by SAF-81 and SAF-83 flights) resulted in the production of preliminary maps (scale 1:60,000), which were extensively field verified. Glacial geomorphological features, including frontal moraines, outwash plains (sandars), molten water channels (eskers), glacial lines (striaes and roche moutonnée), and glacial cirques, along with other geomorphic features related to other landforms, were mapped using remote and field sensors imagery. Remote sensing images include Landsat 7 ETM+ (30 m spatial resolution) and ASTER GDEM. Satellite

images were superimposed on a digital elevation model (DEM) to provide topographic context and help to identify glacial features in areas with complex accessibility.

All maps were generated in ArcMap software. Moraines field observations were carried out in CRB during the 2004 and July 2019 field survey. In addition, moraine landforms were characterized using field profiles using tape and handheld GPS, as well as using a DEM. Although some glacial landforms modeled using a DEM produced by satellite images, however many times, these landforms are often too small to be mapped by these sources (e.g., recently uncovered areas). Examples of these features are eskers, crevasse squeeze ridges, and glacial flutes. All these features were mapped using aereal photography.

On the opposite side, when deglaciation exposes these glacial landscapes to a subaerial environment and are relatively small-sized or exposed high erosional rates (or prolonged low-rates), the landscape can be modified, masked, or removed (Rose, 1991). In cases that do not require concern satellite image spatial resolution, some smaller-scale features such as certain frontal moraines and terraces are insufficient for correct visualization and analysis. Which, added to the fact that high-resolution commercial aerial photographs (and satellite images) are expensive. An alternative technique that works in topographic and geomorphology quantitative analysis is the high-resolution orthophotos and DEM from short-range aerial photography using unmanned aerial vehicles (UAV or drones; Chandler et al., 2015; Evans et al., 2016; Hackney & Clayton, 2015; Rippin et al., 2015; Ely et al., 2017). The use of UAVs in geomorphology is facilitated by the application of Structure from Motion (SfM) (e.g., Harwin & Lucieer, 2012; Westoby et al., 2012; Micheletti et al. 2015). SfM uses overlapping imagery acquired from multiple viewpoints to reconstruct the camera position and camera geometry. From these reconstructed camera locations it is then possible to generate spatial relationships between common feature points and thereby generate a feature's structure (Westoby et al., 2012; Fonstad et al. 2013; Micheletti et al. 2015). The horizontal accuracy and precision of resultant aerial imagery and Digital Elevation Models (DEMs) generated through SfM can be better than satellite imagery and aerial LIDAR (±0.2 m; Fonstad et al., 2013; Hugenholtz et al., 2013), whilst vertical accuracy is typically better than ±0.1m (Fonstad et al., 2013).

We used a DJI Phantom 4 drone to collect high resolution photos from moraines of Coyhaique Alto, El Diablo, and Riesco systems. This drone has a FC330 single-lens digital camera attached to the UAV. The camera lens was fixed at a 3.61 mm focal length to have a constant field view, which facilitates and maximizes image overlapping. Each of these images has metadata that includes, among other information, its positioning using a GPS attached to the UAV. The UAV was flown at a 183 m average height, using an automatic stabilization system, which allowed better control against strong winds which are common in the area. After these photo were collected, they were modelled using Agisoft PhotoScan Professional 1.3.2 Build 4205 software. These data were then exported for use in Arcmap software.

The UAV collected air photographs from which were a DEM was developed where the Coyhaique River cuts some frontal moraines cords of this drifts (Appendix Figure B1). A total of 281 orthophotos were taken at an average height of 314 m above

the floor, with which a 2.62 km^2 orthomosaic was made (Figure 4.5a). Our DEM has 1.7 million faces (Figures 4.5b and 4.5c). This allows us to define the geometry in detail of two moraine crests, both using 3D modeling and a series of transverse profiles to the moraine axis.

We flew our UAV over the zone between Zanjón Hondo Estuary and Cerro La Compañía. We took 141 orthophotos at an average height of 383 m above the floor, with which a 2.56 km^2 orthomosaic was made (Figure 4.9a). There are an associated 3.0, 2.2, and 1.1 m errors, on x (longitude), y (latitude), and z (altitude) axes, respectively. The total error is 3.9 m. We made a DEM with more than 308,000 faces (Figures 4.9b, and 4.9c) to highlight landform features. It was possible to observe two of the three frontal moraine of this series in this place, located at a different height, with their ridges-axes at 695 (701) m, and 720 (725) m a.s.l., respectively (profiles i-i ’and ii-ii’ in Figure 4.9). The most conspicuous feature is the front moraine cord closest to Pampa El Diablo. A slight slope divides both moraines; a broken slope is observed in the northern profile, while in the southern profile, there is only a continuous slope reaching the glaciofluvial plain.

We also flew our UAV over the westernmost moraine cord, henceforth Riesco frontal moraine. 192 orthophotos were taken at an average height of 183 m above the floor, with which a 0.896 km^2 orthomosaic was made (Figure 4.19a). There are an associated 2.9, 2.9, and 1.4 m errors, on x (longitude), y (latitude), and z (altitude) axes, respectively. The total error is 4.4 m. We made a DEM with more than 733,780 faces (Figures 4.19b, and 4.19c) to highlight and measure geomorphic features.

In addition to collecting additional remote sensing data, fieldwork focused on the characterization of the sediments exposed in test-pits, road cuts, and natural sections, within each morphological unit distinguished in our maps.

The third step was to describe the main stratigraphic sections. Lithofacies were field described using textures criteria, particle size, their characteristics, and clast shapes. Facies were adapted from those developed by Miall (1977) and Eyles et al. (1983). Sedimentary deposits and geomorphological units of different systems differ mainly due to their stratigraphic relationships and erosional-weathering degree. The concepts and criteria used for environment interpretation of the facies associations have been taken from Edwards (1986) and Miller (1996) based on the glacial landscape zonation model of Sugden & John (1976).

The fourth step was the collection of field samples for purposes of radiocarbon dating from stratigraphic sections, particularly where glacial sediments overlay ancient undisturbed surfaces. Most of the samples came from the interdrift fine deposits and a total of 8 samples were collected for radiocarbon analysis. These samples were processed in the sedimentary laboratory of the University of Chile and sent to Beta Analytic Inc. Lab for radiocarbon analysis. We calculate radiocarbon ages using CALIB v.7.0.4 software calibration tool (Stuiver et al., 2018) and ShCal13 Southern Hemisphere Curve (Hogg et al., 2013). Ages are presented in the text as average calibrated age in cal. ka BP (before present).

To constrain timing of deposition in which the glaciers remained in a quasi-static position in Coyhaique River Basin, we have sampled datable material in the field. Samples contained organic matter in the right conditions to be treated under the radiocarbon method. We have selected three sites under this criteria: RC-01, RC-02, and RC-03 (Appendix Figures B13 and B14).

The first two correspond approximately to the first and second moraine series of the El Diablo System, at Pedregoso Estuary and Coyhaique River confluence, and on Coyhaique River northern bank close to Pampa El Diablo, respectively. The third site is correlated with El Toro System close to Los Corrales Estuary and Coyhaique River confluence.

To better understand the sample locations and context, three schematic stratigraphic columns are shown, and all ages are in Table 4.1.

Table 4.1. It shows the type of material sampled and their conventional radiocarbon age (non-calibrated) for each sample. Samples were processed in the sedimentary laboratory of the University of Chile and sent to Beta Analytic Inc. Lab for radiocarbon analysis. CALIB v.7.0.4 software calibration tool (Stuiver et al., 2018) and ShCal13 Southern Hemisphere Curve (Hogg et al., 2013).

Field sample	Lab. sample	Type of sample	Conventional ^{14}C age	Calibrated ^{14}C age
COY004	Beta-263837	Organic matter	19,360 ± 90 BP	22,973 - 23,550 yrs cal BP
COY009	Beta-263838	Organic matter	14,000 ± 70 BP	19,711 - 20,285 yrs cal BP
COY010	Beta-263839	Organic matter	16,630 ± 90 BP	16,612 - 17,193 yrs cal BP
COY012	Beta-263841	Organic matter	32,510 ± 280 BP	35,686 - 37,266 yrs cal BP
COY014	Beta-263840	Organic matter	24,090 ± 140 BP	27,773 - 28,449 yrs cal BP
COY017	Beta-263843	Organic matter	17,080 ± 90 BP	20,268 - 20,825 yrs cal BP
COY021a	Beta-263849	Organic matter	9,870 ± 50 BP	666 - 808 yrs cal BP
COY021b	Beta-263850	Organic matter	9,510 ± 50 BP	446 - 559 yrs cal BP

4.4 Results

4.4.1 Coyhaique River Basin (CRB)

In CRB, glacial valleys characterized by their typical U-shaped cross-section are recognized. The main trough corresponds to Artesa Coyhaique (AC; Figures 4.3a, 4.3c, and Appendix B1). It reached its greatest expression in the vicinity of Coyhaique city and opened the Coyhaique lobe (Appendix Figure B2b). The secondary trough called Artesa Baguales (AB) leads to the first at the Las Bandurrias Bridge, owing to

its name due to the Baguales lobe (Figures 4.3b, 4.3c, Appendix B1 and B2c). Eastward of the joint area of both valleys, the U-shape begins to fade as it moves eastward (Appendix Figures B1, B3a, B3b, B3d, and B3e). However, striations found on its slopes and other morphological features leave no doubt of its glacial origin.

The best exposed glacial cirques are those located on Cerro Pirámide (Appendix Figure B1). They are also recognized in the Cerro Cinchao and Cerro Divisaderos. In Cerro Pirámide, a total of seven glacial cirques were detected. They are oriented southward and eastward, with altitudes ranging between 1,500 and 1,700 m a.s.l., limited to each other by glacial edges. These glacial cirques are characterized by abrupt walls with a flat or slightly wavy bottom, with diameters ranging between 600 and 1,000 m. Both the stepped morphology and the presence of a small lagoon in the main glacial cirque is evidence of the last stage of glacial over-excavation. These glacial cirques currently accumulate snow occasionally, as they are below the line of snow accumulation in the area.

Roches moutonnées are widely distributed along with the CRB, reaching up to the high areas. They are mainly molded on basement rocks, with glacial striations, whose axes vary eastward between W-E and SW-NE (Appendix Figure B1). The dimensions of these features length and width range between 100 and 2,000 m, and between 40 and 500 m, respectively. In general, they present smoothly rounded shapes with low slopes and striations at their western edges. In contrast, at their eastern edges, it has rougher and steeper surfaces. All these features indicate an eastward glacial advance in the western sector of the basin, and southeastward in the central-western sector.

Three fluvial-glacial plains are recognized in the CRB central and eastern zones. These plains are formed by gravels and sands. Pampa El Diablo is the best developed and conserved in the area. It has an SW-NE orientation (Appendix Figures B1 and B3b). The eskers correspond to subglacial channels filled by gravels and irregularly stratified sand that constitute elongated and sinuous ridges with abrupt walls (Appendix Figures B1)

Lateral moraines are located mainly in the CRB north-central zone, between Pedregoso and Las Nieves estuaries (Appendix Figure B1). They correspond to elongated strands, parallel to the valley axis, composed mainly of angular volcanic clasts of the Divisaderos Formation, which make up the walls of the valley in this zone.

Along with the CRB, three sets of frontal moraines are recognized. From east to west are defined as the Coyhaique Alto system, El Diablo system, at both ends of Pampa El Diablo, and El Toro system, in the vicinity of the lagoon of the same name, in Baguales Lagoon and in La Cascada Estuary (Figure 4.4). The three systems are characterized by being transversal to the valley. They are differentiated by the degree of erosion, degree of weathering of their constituent clasts, which in both cases increases eastward, with significant differences between the Coyhaique Alto System and the other two. While there are differences among the Western systems, these are minor compared to the first one.

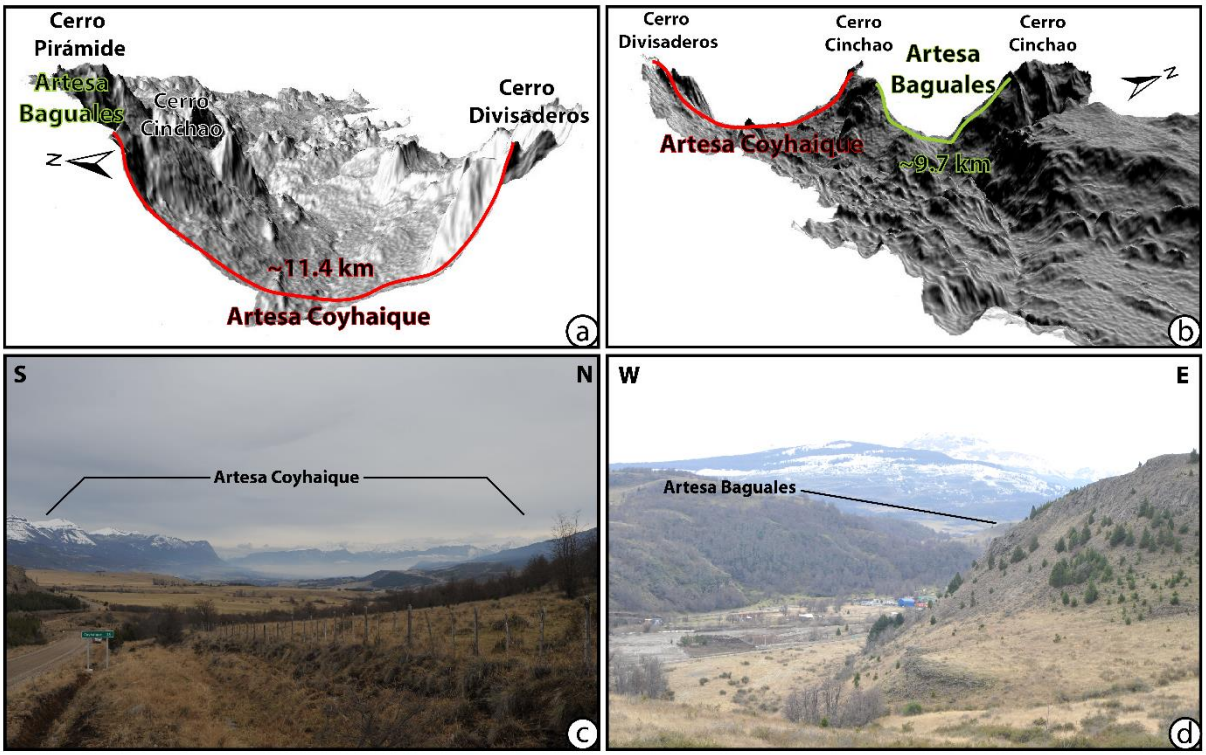

Figure 4.3. (a) 3D-DEM seen from the west and centered in Artesa Coyhaique (AC) zone. (b) 3D DEM is seen from the east showing Artesa Coyhaique (AC) and Artesa Baguales (AB). (c), (d) Photographs of both glacial troughs taken from Las Bandurrias Bridge.

4.4.1.1 Glacial morphostratigraphic units in the CBR

Glacial landforms and sediment deposits exposed in CBR were grouped into four morphostratigraphic systems (drifts). First-order criteria are their geographical location from their frontal moraines. These moraine systems are from east to west: Los Flamencos, Coyhaique Alto, El Diablo, and El Toro (Figure 4.4).

From Los Flamencos System, inside the study area, there is only preserved lodgement till deposits, lateral moraines, and eskers (Appendix Figure B1). The other three systems are formed by i) glacial or till deposits, ii) glaciofluvial and glaciolacustrine deposits, iii) loess deposits, and iv) glacial landforms, such as frontal and lateral moraines, eskers, and roches moutonnées. The sedimentary deposits and geomorphological units of the different systems differ in their stratigraphic relationships and weathering degree (Figure 4.4).

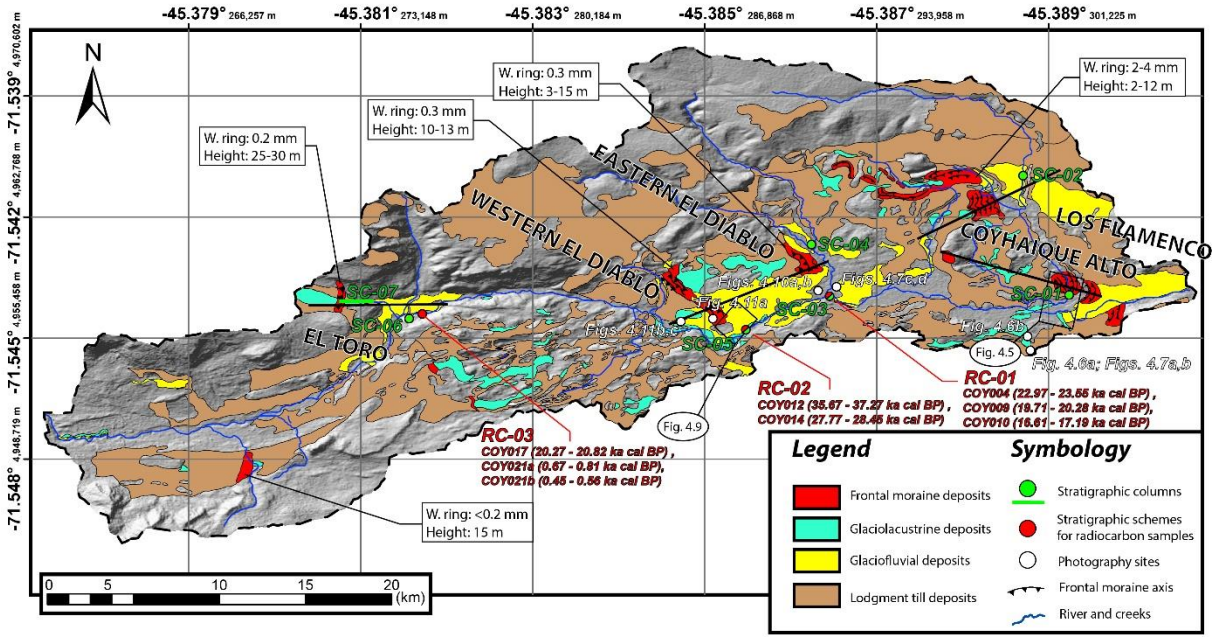

Figure 4.4. Geological map of the Coyhaique River Basin moraine systems using a 30x30 m DEM hillshade (ASTER-GDEM). The deposits that integrate these systems (glacial drifts) are colored, highlighting their depositional environment. From oldest to youngest (east to west): Los Flamencos, Coyhaique Alto, El Diablo (along with their two cord series), and El Toro systems are indicated. Front moraines are shown using red polygons and main axes. White boxes indicate characteristics such as height (GPS and UAV measurements) and weathering rings in volcanic clasts. Data sites are indicated in symbology. Heavy black lines indicate schematic profiles shown in Figures B5, B6, and B7.

A. Coyhaique Alto System

Coyhaique Alto System corresponds to a glacial record set located in the valley central-eastern zone, mainly between Pedregosos and Los Tres Puentes - Casa Piedra estuaries (Figure 4.4). It is composed of till, glaciofluvial, glaciolacustrine, and loess deposits, and landforms as frontal and lateral moraine, glaciofluvial plains, eskers, and kame terraces (Figure B1). It overlays an erosional unconformity pre-Quaternary basement rocks, mainly from Cerro Mirador - Casa Piedra Dome Complex (Ksd), and to a lesser extent, by Divisaderos Formation (Kid) rocks (Figure B5a). It also overlays in erosional unconformity Los Flamencos System deposits and locally underlay El Diablo System deposits. Finally, it is overlayed in conformable or erosional unconformity by post-glacial Holocene deposits.

i. Glacial landforms

Frontal moraines

In the study area, thirty-one frontal moraines associated with this system were recognized (Figures 4.4 and 4.6). These were recognised based on the following characteristics: photogeological mapping of the deposits, generation of stratigraphic columns, degree of erosion, and weathering of their clasts. They are located near Los

Tres Puentes, Casa Piedra, and El Culebra estuaries, ranging between 800 and 950 m a.s.l. These features range between 250 and 2,400 m long, between 8 to 15 m wide, and between 2 and 12 m high.

Moraine crests cose to Casa Piedra and Los Tres Puentes estuaries have N-S strikes and have an arched-geometry with the concave side westward (Figure 4.4 and 4.5). Those close to El Culebra Estuary source range widely between NW-SE and W-E strikes and its concave side faces southwest and also north.

Composed by a till poor in matrix (<30%), polymictic clasts ranging between angular and subrounded shapes (Figures 4.7a and 4.7b). Weathering rings range between 2 to 4 mm. The unit overlays lodgment till deposits of the same system. In some cases, over Cerro Mirador - Casa Piedra Dome Complex (Ksd) rocks (Figure B5a). The spatial arrangement of the successive frontal moraine indicates that at least seven glacier front detention and slightly advances events.

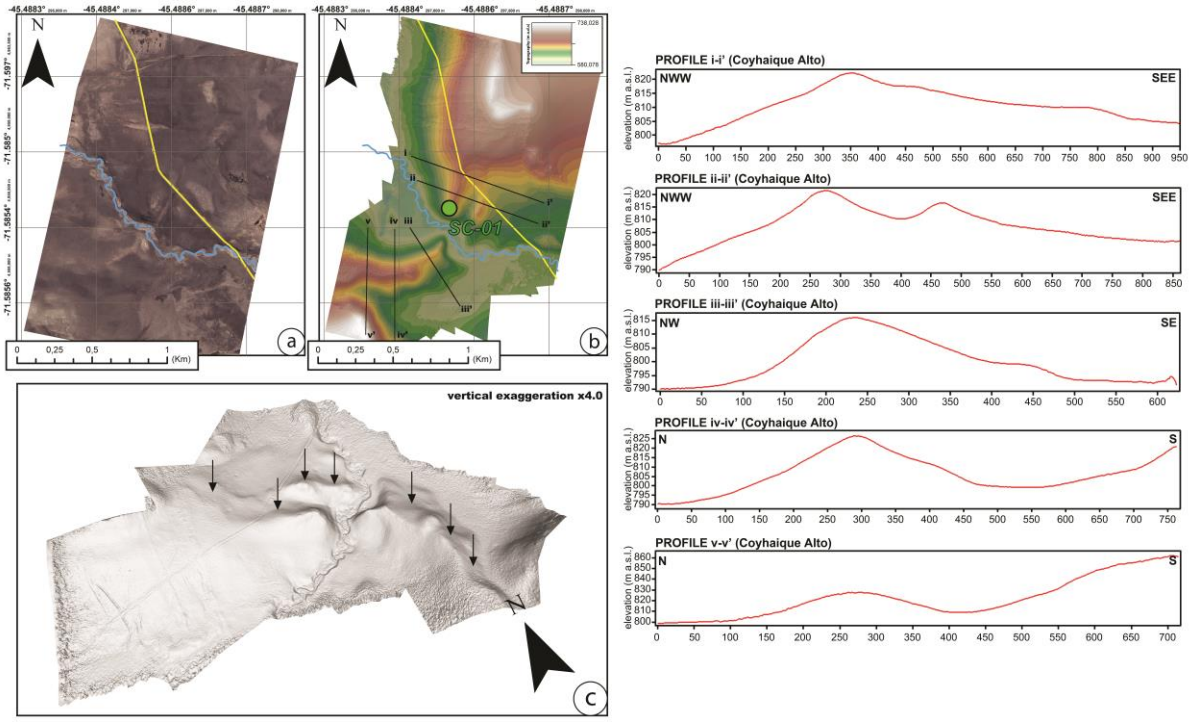

Figure 4.5. (a) Orthophoto mosaic of an area close to Coyhaique River showing Coyhaique Alto frontal moraines. (b) Plan view of the DEM area. A semi-translucent color palette was used alongside a hillshade. Heavy black lines correspond to profiles i-i' to v-v' (upper right). (c) 3D-DEM seen from the southwest. Green dot correspond to SC-01 stratigraphic column.

Lateral moraines

A lateral moraine is preserved, located at 950 m a.s.l., between Las Nieves and El Culebra estuaries at Meseta Boscosa skirts (Appendix Figure B1). The geometry of

this unit is 460 m long, 4 m wide, and 3 m high. The strike of this cord is W-E. It is composed of poorly selected till deposits poor in matrix. Its volcanic clasts are andesitic, dacitic, and rhyolitic in composition. They have brown-yellow 2-3 mm thick weathering rings. This landforms overlay lodgment till deposits of this same system.

Eskers

Thirty-eight glaciofluvial eskers were recognized, from subglacial to englacial environment origin. These landforms were identified by its sedimentological characteristics (grains and structures) and orientation. They are cut, both north and south, by Coyhaique River, westward between Las Nieves and Pedregoso estuaries, and eastward El Culebra and Casa Piedra estuaries, between 750 and 900 m a.s.l. (Appendix Figure B1). Its geometry range between 180 and 2,190 m long, 4 and 10 m wide, and 3 to 12 m high. All overlaying lodgment till deposits, and some partially covered by glaciolacustrine deposits of the same system. Their orientation within the valley ranges widely, from N-S northward in places and W-E southward of the valley. In general, they have sinuous forms. They are composed of medium-sized, poorly selected, solid gravels that range from subangular to subrounded shapes, arranged in solid or flat stratification (rarely cross-laminated) deposits.

Glaciofluvial plains

Two of these units associated with the Coyhaique Alto System were recognized, with a ~30 cm thick loess coverture. These plains were also recognised based on photogeological mapping of the deposits, generation of stratigraphic columns, degree of erosion, and weathering of their clasts The first one exposed eastward Los Tres Puentes Estuary and dissected by Casa Piedra Estuary, between 900 and 950 m a.s.l. (Figure 4.4). Its morphology is flat, with 5.3 km long and 1.5 km wide on average (Appendix Figure B1). Their strike is NW-SE with a slight SE dip. They overlay Los Flamencos System lodgment till deposits, and is partly covered southward by lake deposits (Appendix Figure B5). Erosional channels with NW-SE strikes are preserved. They are composed of poorly selected thick gravels with clasts that reproduce a slight southeast slope.

The second unit is located eastward Casa Piedra estuary at its southern end, until Los Flamencos lagoon, ranging heights between 800 and 850 m a.s.l. (Appendix Figure B3d). It is 4.5 km long and 1 km wide, with a W-E strike (Appendix Figure B1). This glaciofluvial plain overlay Los Flamencos System lodgment till deposits, and at its eastern border, is covered by lacustrine deposits of the homonymous lagoon. The unit is composed of gravels and poorly selected sands (Figures 4.7c and 4.7d). It also preserves some erosional channels, although in smaller quantities than the previous plain. These channels have a 5 m maximum width.

Figure 4.6. Panoramic views. (a) Eastward and (b) northward, respectively. Part of the Coyhaique Alto System frontal moraine is observed. Black arrows indicates moraine crests.

Figure 4.7. (a), (b) Angled and sub-rounded clasts within the till of the on Coyhaique Alto System frontal moraine. (c) Northward view of Coyhaique Alto System glaciofluvial deposits exposed in a natural section of Pedregoso Estuary. (d) Zoom in to Coyhaique Alto System glaciofluvial deposits. Quartz-feldspathic sand layers are observed along with clast-supported gravel.

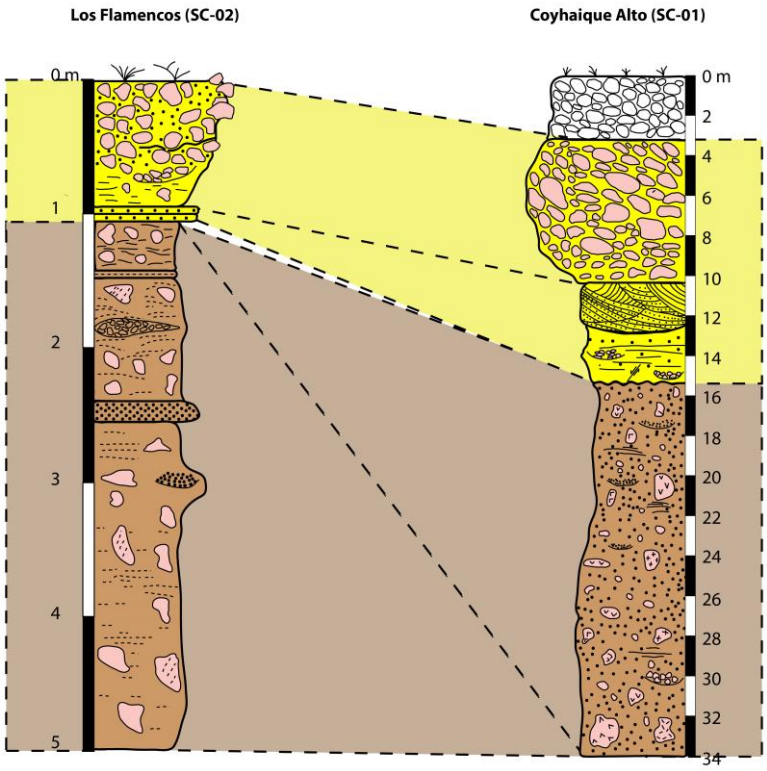

Figure 4.8. Stratigraphic correlation between stratigraphic columns SC-01 and SC-02. Respectibely, they represent part of the Coyhaique Alto System deposits located on Casa Piedra Estuary (eastern bank), and part of the Los Flamencos and Coyhaique Alto systems deposits located on Casa Piedra Estuary (eastern bank).

ii. Stratigraphic column SC-01

In the Hacienda Los Cóndores zone, at the height of 773 m a.s.l., a natural vertical section is exposed on Casa Piedra Estuary eastern shore (Figure 4.4). A 34 m thick sequence (Figure 4.8) with an unknown base starts with a 19 m thick compact and well consolidated diamict unit. Its matrix is 70% silty and has a structure given by small fine sand lenses with thin-flat lamination. Angular blocks are 50 cm maximum diameter (20 cm average).

Its composition is mainly andesitic lavas, andesitic breccias, and tuffs, also granitic and dioritic rocks are common. Some clasts are faceted, and those of volcanic origin have 2 - 4 mm thick weathering rings. Upward this deposit has erosional channels. These facies are interpreted as lodgment till deposits of accumulated till facies zone.

Overlaying in erosional unconformity, there is a 6 m thick sequence of fine-mid quartz-lithic sands, with 2 mm lamination. It has cross-bedding, indicating contributions from west to east. Downward, small normal fault-like structures are observed with the W-E strike and 50 to 70 °S dip. Displacements range between 15 and 20 cm. This sequence is the diamict channels infill. Its depositional environment corresponds to a mid-energy glaciofluvial system, in a supraglacial facies zone.

In non-erosive contact with the latter unit, there is a clast-supported gravel unit. The clasts are 12 cm average diameter, well-selected, with a well-rounded shape, and no imbrication. The matrix corresponds to thick quartz sand. The depositional environment is a high-energy river, forming a fluvial terrace in this zone.

iii. Stratigraphic column SC-02

Southward Veranada Casa Piedra, at 914 m a.s.l., on Casa Piedra Estuary eastern shore (Figure 4.4), the following sequence emerges (Figure 4.8).

Overlaying on erosional unconformity, Los Flamencos System lodgment till deposit, a clast-supported poorly-sorted gravels deposit is found. These clasts have a slight SE imbrication and 30 cm maximum diameter (20 cm average). Clasts range from angular to sub-rounded shapes, with 2.5 - 3.5 mm thick weathering rings (volcanic clasts). Some of them have striations. They were deposited in a high-energy glaciofluvial environment, proglacial facies zone.

B. El Diablo System

El Diablo System is defined as the drift developed in CRB central zone (Figure 4.4). It consists of till, glaciofluvial, glaciolacustrine, loess deposits, and landforms such as frontal moraines and eskers, distributed in a NE-SW elongated strip (Appendix Figure B1).

The deposits overlay pre-Quaternary basement rocks from Ibáñez and Divisaderos (Kid) composed by rhyolitic, dacitic and andesitic volcanic and hypabyssal rocks , and El Toro (Kset) formations composed by basaltic dikes, basalt-andesitic volcanic rocks and pyroclastic breccias, and Cerro Mirador - Casa Piedra Dome Complex (Ksd; Appendix Figure B6) composed by dacitic and rhyolitic rocks. It also overlays Coyhaique Alto System deposits in erosional unconformity and underlays El Toro System deposits. These deposits are partly covered (conformable and unconformable) by Holocene deposits.

i. Glacial landforms

Frontal moraines

Twelve frontal moraine crests grouped into two series are recognized (Figures 4.4 and Appendix B6). The first series is located near Pedregoso Estuary, with five moraines, at heights ranging between 750 and 800 m a.s.l. Its geometry range between

440 and 1,540 m long, 4 and 6 m wide, and 3 and 8 m high. The second series is located 4.5 km further west than the first one, eastward Estero Zanjón Hondo (Figure 4.9), at ~725 m a.s.l. Seven moraines form it with geometry ranging from 250 to 1,560 m long, 6 to 20 m wide, and 8 to 15 m high.

The frontal moraines have NNW-SSE strikes, with arched-shaped geometry and the concave side facing west. They are composed of polymictic till deposits, low in the matrix (<25%), and poorly selected clasts. It is also common to see oversized clasts near the moraine crests (Figures 4.11b and 4.11c).

The first moraine series represent at least four glacial front detentions periods and (or) slight advances. The second one has the best developed (or better preserved) moraines and evidence three glacial front detention periods with slight retreat and advance movements. Even when the first series is older than the second one, weathering rings (0.3 mm) have the same thickness.

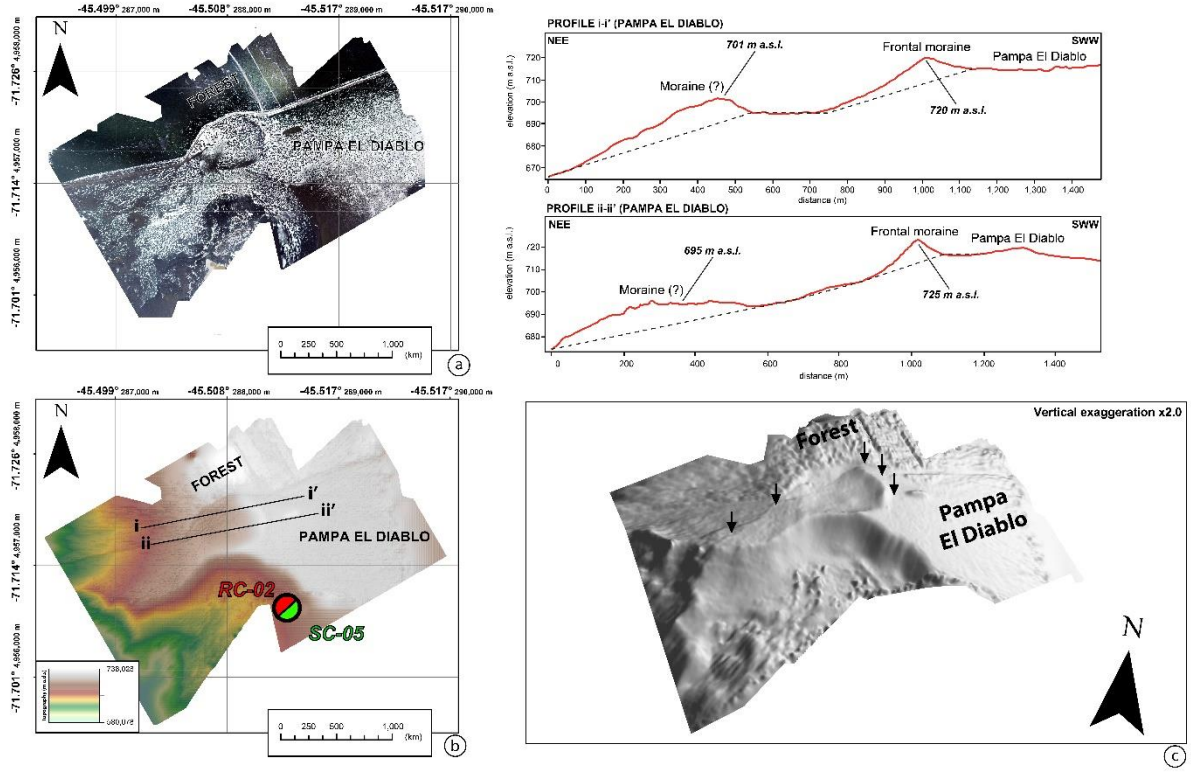

Figure 4.9. (a) Orthophoto mosaic from the Pampa El Diablo area close to Coyhaique River. (b) Plan view of the DEM area. We use a semi-translucent color palette alongside a hillshade. Heavy black lines correspond to profiles i-i 'and ii-ii' (upper right). (c) 3D-DEM seen from the south. Green-Red dot correspond to SC-05 and RC-02 stratigraphic columns.

Eskers

Twenty eskers of subglacial and englacial origin were observed, distributed northward and southward Coyhaique River. Its heights range between 750 and 850 m

a.s.l. Its geometry is slightly sinuous, with SW-NE to E-W strikes. Meanwhile, their lengths range between 600 and 1,300 m (Appendix Figure B1). Eskers are composed of poorly selected polymictic gravels and sands (Figure 4.15). The clasts range from subangular to subrounded shapes.

All recognized eskers are over the lodgment till deposits. Due to their geographical location, we divided them into two groups. The first group between Pedregoso and Zanjón Hondo estuaries. And the second one westward Zanjón Hondo (Appendix Figure B1). In general, the first group has smaller dimensions, 1 to 4 m long, and 2 to 4 m wide. Volcanic clasts have 0.3 m thick weathering rings—the second group range between 3 and 6 m long, and between 3 to 7 m wide. Weathering rings also are common and range between 0.2 and 0.3 mm thick.

Glaciofluvial plain

The glaciofluvial plain assigned to this system, better developed and preserved, is the Pampa El Diablo (Appendix Figure B1). It extends on Coyhaique River northern bank, from Zanjón Hondo Estuary to El Culebra Estuary in the east, between 725 to 800 m a.s.l. (Appendix Figures B3b and B3c). It is 8 km long, and 2 km wide, and SW-NE strikes. It recognizes two levels limited by Pedregoso Estuary that cuts it and partly erodes it. It covers glaciolacustrine deposits assigned to this system and is overlayed by loess and subactual fluvial deposits of Pedregoso Estuary. It is composed of poorly selected gravels and coarse sands (Figure 4.11a) illustrated in SC-03 and SC-05 (Figures 4.12a and 4.12c).

Two other records of this same kind of unit were found and assigned to El Diablo System. One of them is a larger remnant area located at Las Nieves and Pedregoso estuaries confluence, ranging between 750 and 800 m a.s.l. SC-04 illustrates the thickness of the deposits (Figure 4.12b). Its origin is from the first moraine series described. The other record is located southward Pampa El Diablo glaciofluvial plain.

Figure 4.10. (a), (b) Esker close to El Diablo System. It has dense mid-size gravels, highly compacted.

Figure 4.11. (a) Sand fraction, El Diablo System glaciofluvial deposit. (b), (c) Boulders of glacial origin within a till sequence. Close to El Diablo System frontal moraine (second moraine series).

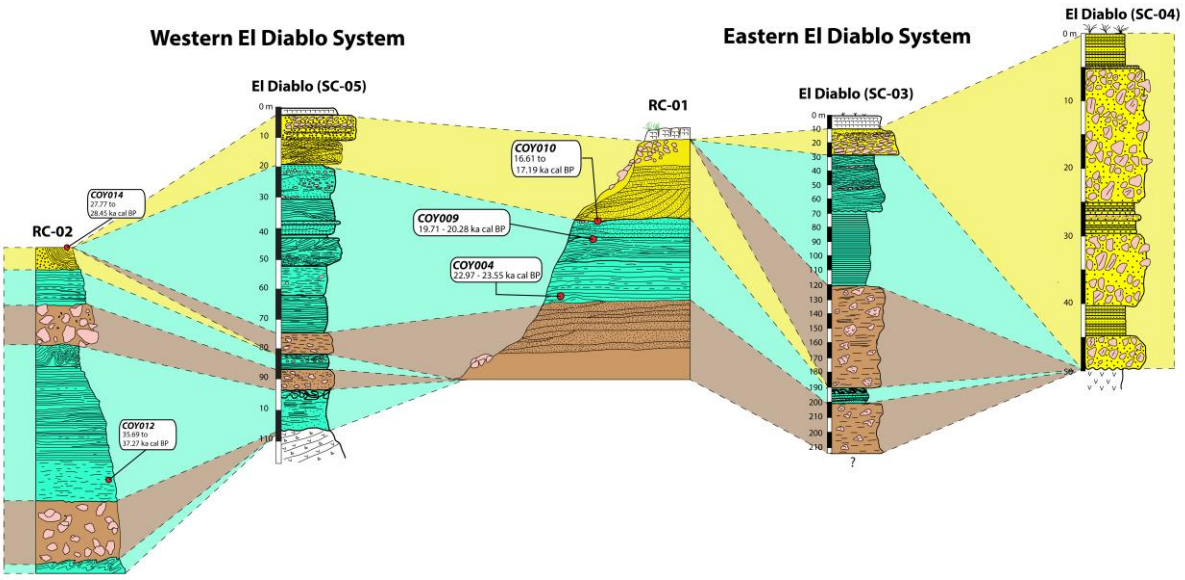

Figure 4.12. Stratigraphic correlation of El Diablo system western and eastern deposits. Figure shows stratigraphic column SC-03(Coyhaique River northern bank); stratigraphic column SC-04 (Las Nieves and Pedregoso estuaries confluence); stratigraphic column SC-05(Coyhaique River northern bank);.schematic stratigraphic column RC-01, it represents the site where samples COY004, COY009, and COY010 were extracted close to Pedregoso Estuary and Coyhaique River confluence; and schematic stratigraphic column RC-02, where COY012 and COY014 were extracted on Coyhaique River northern bank close to Pampa El Diablo.

ii. Stratigraphic column SC-03

This stratigraphic column (Figure 4.12a) is located on Coyhaique River northern bank, eastward Pedregoso Estuary, and Coyhaique River confluence at 716 m a.s.l. (Figure 4.7).

With an unknown base, this column starts with a 3 m thick polymictic diamict. Its matrix comprises laminated and solid silts, mainly quartziferous, with 5 cm average diameter clasts. Volcanic clasts have a 0.6 mm thick weathering rings. These facies were deposited in a lodgment till the environment.

Overlaying in non-erosive contact, there is a ~1 m thick, fine feldspathic sands and varved silts unit. This sands highlight for their light brown color, while silts are dark brown. Upward, sediments have wet-state deformation features (folds-and-thrust like structures). This deposit represents a deep low-energy glaciolacustrine environment without ice-contact.

Covering the previous unit, in erosional-deformational contact, a 7 m thick diamict is exposed. It has an 80% solid silt downward, which becomes more laminated and sandy upward. Clasts are commonly greenish and violet tuffs (75%) and andesitic clasts (25%), with 0.4 mm thick weathering rings. This unit corresponds to a lodgment till deposit.

Overlaying in non-erosional contact, a varied 5 m thick greywackes and silty rocks sequence appears. Each varve is 4 cm thick. The thickest units correspond to 1 mm laminated feldspathic quartz greywackes. Their grain sizes range from very coarse sands downward to very fine upward and range from angular to subrounded shapes. They have a solid silt matrix (upward, 45% - 75%). The silty horizons are well-consolidated and have 5% sand. This sequence was deposited in a glaciolacustrine environment, without ice-contact.

A fine to coarse quartz-feldspathic sand unit overlay the sequence. These sands have 4 mm thick gravel lenses, with cross-bedding. Thus, facies were deposited in shallow glaciolacustrine delta environments, with local variations in flow direction and energy in the system.

Overlying the previous facies, in non-erosional contact, there is a 2 m thick gravels unit. The average clast diameter is 10 cm, with 2 mm thick lamination. The clasts composition is andesitic (40%), tuffs (30%), breccias (20%), and granitoid (10%). Volcanic clast has 0.3 mm thick weathering rings. These facies were deposited in a glaciofluvial system, in which the energy decreases progressively.

Completing this sequence of facies, also in non-erosional contact, there is a volcanic ash deposit connected to a Hudson Volcano event dated in 3,600 years BP correlated using isopach maps (Naranjo & Stern, 1998), close to 1 m thick soil horizon.

iii. Stratigraphic column SC-04

SC-04 (Figure 4.12b) is a 50 m thick stratigraphic column close to Las Nieves and El Pedregoso estuaries confluence, at 760 m a.s.l. (Figure 4.4).

The sequence starts with a 5 m thick polymictic gravels unit overlaying in non-conformity basement rocks. Its poorly-selected clasts are 25 cm maximum diameter (15 cm average). Its shape ranges from subangular to subrounded. Volcanic clasts have 0.4 mm thick weathering rings. The unit is matrix-supported, with coarse to very coarse sands.

In non-erosional contact, 5 m thick quartz-feldspathic greywackes are deposited. The main clasts are mid-size sands, while the matrix (45%) is solid silt. They have a 2 mm thick lamination.

The sequence continues, with a non-erosional contact and 10 m thick polymictic gravels unit with very poor-selection. The unit is matrix-supported and is composed of coarse to very coarse sands. The clast sizes have a 20 cm maximum diameter (10 cm average). Volcanic clasts have 0.4 mm thick weathering rings.

Overlaying, in non-erosional contact, there is a 5 m thick fine to coarse quartz sands unit. The grains are immature and poorly-selected. It has thin-lamination (2 mm), and occasionally fine gravels intercalations.

The latter unit is overlayed by a 20 m thick polymictic gravels unit. These sediments are matrix-supported (60%) and very poorly-selected. In contrast, the main clasts are granitic, tuffs, and breccia fragments in composition. Some of them are striated, and volcanic origin has a ~0.3 mm thick weathering ring.

Upward, in non-erosional contact, a 5 m thick, thin to mid-laminated (~1 mm), quartz-feldspathic greywackes sequence is recognized. The matrix (50%) ranges from mid to thick silt, while sand grains range from subangular to subrounded shapes.

iv. Stratigraphic column SC-05

In the Pampa El Diablo zone, between Cuesta Los Leones and Pedregoso Estuary (Figure 4.4), the following sequence emerges (Figure 4.12c) in Coyhaique River northern bank.

The sequence starts with a 13 m thick laminated fine quartz-feldspathic sands deposit. This unit discordantly overlay Ibáñez Group volcanic rocks (Kid). The deposits present lateral gradation to mix silty facies. Upward, these sediments are folded, probably caused by wet-state deformation. The deposition occurred in mid to deep waters, low to mid-energy glaciolacustrine environment.

It is overlaying the previous unit, in erosional-deformed contact, a 7 m thick well-consolidated diamict. Polymictic clasts dominate its composition with a 5 cm average diameter and a quartz-sand matrix. Meanwhile, volcanic clasts have a 0.4 mm thick weathering rings. It represents a lodgment till the environment, in a till accumulation zone.

Overlying, in non-erosional contact, there is a 2 m thick varved silts and clays deposit, grain-size thickening upward. It continues with 3.5 m thick silts and dropstones facies. Upward, it presents wet-state deformation. The two units were deposited in a deep low-energy glaciolacustrine environment, without ice-contact that evolved to another with ice-contact. Westward, these silty facies grain-size thickening laterally to fine-laminated gravels. It represents high-energy lacustrine facies associated with glaciolacustrine turbidites closer to the glacial front.

The Varved silts unit underlay a 6.5 m thick well-consolidated matrix-supported diamict (5% clasts). The clasts have a 0.3 mm thick weathering rings. The matrix is

gray-brown, silty-clay with a mainly quartziferous composition. It represents a lodgment till the environment, in a till accumulation zone.

The sequence continues with a well-consolidated varved clays and silts unit, in a non-erosional contact. It is 13 m thick and has a thin-lamination (0.5 - 2 mm). Each varve is 2 cm thick. This unit was deposited in a shallow low-energy glaciolacustrine environment, without ice-contact.

In non-erosional contact, overlaying the previous unit, there is a 10 m thick sequence of solid silts with dropstones (5%). It has bioturbed horizons (larvae traces). The unit represents a deep low-energy glaciolacustrine environment with ice-contact.

Subsequently, in non-erosional contact, 2 m thick cross-bedding silts and fine quartz-feldspathic sands unit is shown. Layers indicate an east to west sedimentary contribution direction. We interpreted the unit as a shallow mid-energy glaciolacustrine environment.

In non-erosional contact, there is a ~1 m thick alternation of consolidated solid silts. Upward, it has 18 m thick solid silts facies with fine to very fine quartz sands facies intercalations. Layers have cross-bedding and symmetric ripples. Both facies were deposited in an environment that evolved from deep low-energy to a shallow high-energy glaciolacustrine set.

In gradational contact, we found a 13 m thick sequence formed by fine gravels, mid to thin-laminated greywackes, and solid silts intercalations. The greywackes have planar lamination and silty matrix. The silt alternations are brown, solid, and very consolidated. In contrast, the gravels are 2 cm diameter average. In this unit, fine and coarse quartz-feldspathic greywackes predominate. Sands are poor-selected with grains ranging from angled to sub-rounded shape, and low sphericity.

Overlaying in non-erosional contact the previous unit, a 10 m thick cross-bedding fine to very fine quartz-lithic sands sequence. Layers indicate east-to-west deposition. These facies are interpreted as a mid-energy glaciolacustrine delta environment.

There is a 10 m thick gravels deposit in slight erosional contact, with an upward grain-size thickening. Their clasts range from 1 to 20 cm in diameter. The 20 cm thick polymictic gravels facies present stratification and are clast-supported. The clasts are well-selected and slightly westward imbricated. Volcanic clasts have a 0.3 mm thick weathering rings. Also, some clasts are striated. Sand facies have ~1 mm thick lamination. They are composed of thick quartz-feldspathic sands, with a fine sandy to a solid silty matrix. The matrix is very poorly-selected, and grains range from angled to subangular shapes, with mid-sphericity. The unit represents an upward, increasing energy facies in a glaciofluvial environment.

This stratigraphic column ends with a 2 m thick volcanic ash cover close to a soil horizon. We associate this ashes to a Hudson Volcano eruption dated 3,600 years BP correlated using isopach maps (Naranjo & Stern, 1998).

v. Stratigraphic scheme RC-01

In RC-01 (Figure 4.14a), three samples were taken: COY004, COY009, and COY010. COY004 has organic sediments from the base of a laminated unit composed of clastic varves between 1 and 2 mm thick, and silt varves with 0.5 cm thick average. This unit is equivalent to the SC-05 varved unit. Radiocarbon ages obtained range between 22.97 and 23.55 ka cal BP (Appendix Figure B13).

COY009 has organic sediments from the same unit's roof described above. Radiocarbon ages range between 19.71 and 20.28 ka cal BP (Appendix Figure B13).

COY010 has organic sediments from a laminated unit base with grain-size coarsening upward, ranging from silts to fine sands. The unit could be equivalent to the unit overlying SC-05 varves (Figure 4.12c). It has similar granulometry and internal structure, allowing us to give it a glaciolacustrine origin. Radiocarbon ages range between 16.61 and 17.19 ka cal BP (Appendix Figure B13).

vi. Stratigraphic scheme RC-02

In RC-02 (Figure 4.14b), two samples were taken: COY012 and COY014. COY012 has organic sediments from the center of a thick-laminated silt unit. This unit is below SC-05 (Figure 4.12c). Its facies are interpreted as a glaciolacustrine environment. COY012 radiocarbon ages range between 35.69 and 37.27 ka cal BP (Appendix Figure B14).

COY014 has organic sediments taken from a cross-bedding sand unit, just below the first layer of SC-05. The unit is interpreted as a low to the mid-energy glaciolacustrine environment. COY014 radiocarbon ages range between 27.77 and 28.45 ka cal BP (Appendix Figure B14).

C. El Toro System

El Toro System is defined as the drift composed by till, glaciofluvial, and glaciolacustrine deposits. Landforms are located in west of Coyhaique, close to El Toro lagoon (Figure 4.4).

The deposits of this system overlay, in angular unconformity, Coyhaique Group (Kic) shales, Divisaderos (Kid) and El Toro (Kset) formations volcanic rocks, and also in non-conformity Acid Porphyry (Kspa), Gabro Bandurrias (Ogb), and hypabyssal rocks (Ohb; Appendix Figure B7). The unit, conformable overlay El Diablo System deposits.

i. Glacial landforms of the El Toro System

Frontal moraines

Five frontal moraine assigned to this system were recognized distributed northward and southward Coyhaique River. Three of them, ranging between 700 and 750 m a.s.l., and two more eastward at an average height of 570 m a.s.l. One westward El Toro lagoon, the second one westward Las Perdices lagoon, another one eastward Baguales lagoon, and the two eastern ones, at Cascada Estuary (Figures Appendix B1 and 4.4). All of them constitute natural dams for lakes or palaeolagoons. Examples of these relationships are Baguales lagoon, on the eastern side, and Las Perdices lagoons, on the western edge.

The moraines have N-S strikes. Baguales moraine is the largest with 1,100 m long, 60 m wide, and 30 m high. The remaining ones range between 500 – 1,300 m long, 15 - 35 m wide, and 15 - 25 m high.

The moraines are composed of a low in till matrix (<25%). Its clast composition is polymictic, with 2 m maximum diameter, ranging from very angular to subrounded shapes. Some of these clasts are faceted and striated. Volcanic clasts of the three eastern moraines have a very incipient 0.2 mm thick weathering rings, those of La Cascada Estuary have less than 0.2 mm thick.

The five moraine overlay lodgment till deposits, although the two most western ones overlay Divisadero Formation (Kid) rocks. Baguales lagoon moraine is eroded in its central part by Los Corrales Estuary.

Eskers

Three eskers were recognized southward Coyhaique River. Two of them eastward Colorada slope, and the third one at Cerro Divisaderos feet (Appendix Figure B1). They range between 600 and 650 m a.s.l. They have W-E to NE-SW strikes and overlaying lodgment till deposits of this same system. Its dimensions range between 600 to 2,000 m long, 5 to 12 m wide, and 5 to 15 m high. The eskers are composed of poorly selected polymictic gravels, reaching up to 70 cm in diameter. Clasts are also ranging from subangular to subrounded. Volcanic clasts have 0.2 mm thick weathering rings.

Glaciofluvial plains

The only accumulation of glaciofluvial sediments recognized as a plain assigned to the El Toro System is located 2 km eastward Baguales lagoon. It is about 3 km long, 1 km wide, and has a W-E strike (Appendix Figure B1). It is partially eroded by Los Corrales Estuary and by another estuary that descends from Cerro La Pirámide. It is composed of moderate to poorly selected polymictic gravels.

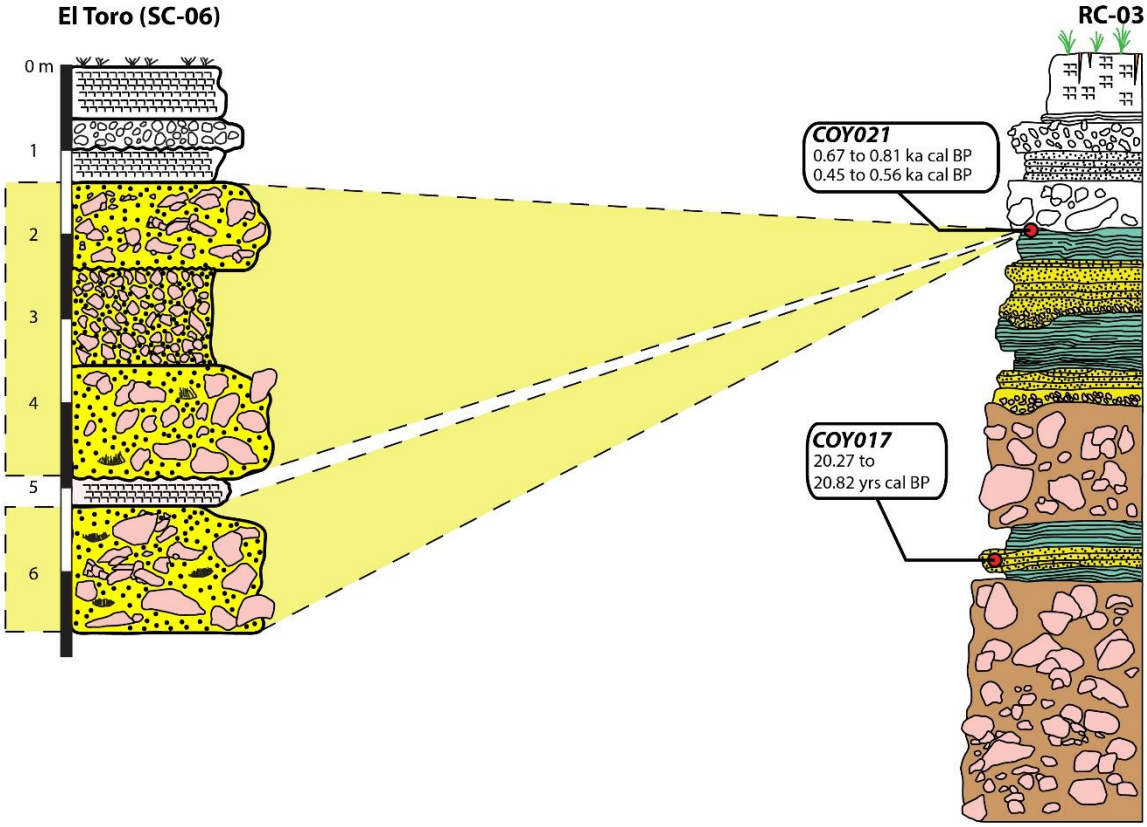

Figure 4.13. Stratigraphic correlation for El Toro System deposits between stratigraphic column SC-06 (after Arqueros, 2004) located in Las Bandurrias, and schematic stratigraphic column RC-03. It represents the site where samples COY017, COY021a, and COY021b were extracted. It is located close to Los Corrales Estuary and Coyhaique River confluence.

ii. Stratigraphic columns SC-06 and SC-07

In Las Bandurrias northern zone (Figure 4.4), on Los Corrales Estuary banks, close to Coyhaique River mouth, at the height of 470 m a.s.l., the sequence SC-06 is located (Figure 4.13a).

This sequence has an unknown base and begins with a 1.5 m thick, coarse polymictic gravels. Poorly-selected coarse sands matrix-supported form it. Its main

clasts are faceted and westward imbricated. They also have a <0.2 mm thick weathering ring. We interpreted it as a proximal high-energy glaciofluvial environment. Upward, in non-erosional contact, there is 0.3 m thick volcanic ash deposit undated, not associated with any known event.In erosional contact, there is another 1.2 m thick matrix-supported gravels deposit. This deposit shares the same characteristics, as previously mentioned. We interpret it as a proximal high-energy glaciofluvial environment. Upward, in non-erosional contact, there is a ~1 m thick fine polymictic gravels deposit. These deposits go from clast-supported to fine gravels matrix-supported. Further, the matrix has finely-laminated sands. We interpret it as a mid-energy distal glaciofluvial environment. It is followed by 1.2 m of thick matrix gravels supported in erosional unconformity. It has few faceted clasts and an eastward imbrication. We interpret it as a proximal high energy fluvioglacial environment. Upward, in non-erosional contact, there is a 0.4 m thick volcanic ash deposit. This horizon is not associated with any known event. An erosional unconformity, there is a ~0.4 m thick clast-supported gravels unit with moderate-selection. These sediments correspond to a mid-energy ancient fluvial environment.

Finally, close to the surface, there is a ~0.5 m thick volcanic ash deposit associated with an incipient soil horizon. This deposit was associated with a Hudson Volcano eruption, dated in 3,600 BP correlated using isopach maps (Naranjo & Stern, 1998).

iii. Stratigraphic scheme RC-03

We took three samples in RC-03 (COY017, COY021a, and COY021b). Sample COY017 corresponds to organic sediments obtained from a medium to fine sands and gravels alternation unit (Figure 4.14c). This level also has silts with root traces, from where the sample was obtained. These layers present the characteristic features previously seen for the same kind of facies. Their relationship with the underlying unit (diamict) allows us to associate it with a glaciolacustrine deposition environment. Radiocarbon ages of COY017 range between 20.27 and 20.82 ka cal BP (Appendix Figure B14).

COY021a and COY021b correspond to carbonized material and organic sediments, respectively. These samples were obtained from the top of a silts package within a gravels (diamicts) and medium sand layers alternation. Silt layers have root remains. Using the same criteria mentioned above, we interpret this level as part of a glaciolacustrine environment. COY021a (b) radiocarbon ages range between 0.67 (0.45) and 0.81 (0.56) ka cal BP (Appendix Figure B14).

4.4.2 Emperador Guillermo and Mañihuales rivers confluence zone

4.4.2.1 Glacial morphostratigraphic units

Glacial landforms and sediment deposits exposed in EMC are scarce. We have detected only one glacial drift located on Emperador Guillermo River northern bank (Figure 4.14a). Of this sediments-set, what stands out with the naked eye is the presence of a tall moraine (Figure 4.14b) attached to the rocky mountain massif that separates both rivers. Westward of the moraine, over the glaciofluvial plain, in a natural section, we build a short stratigraphic column (SC-09; Figure 4.14c)

i. Glacial landforms

Moraine

Only one moraine cord was mapped in this zone and is mostly located in the Emperador Guillermo river northern bank (Figure 4.14a), and partially eroded by it. It has an apparent equant geometry with an average dimension of 856 m long, 714 m wide, and ~50 m high (Figure 4.14b). This moraine is mainly composed of till deposits packed into three layers (Figure 4.15a). The bottom layer is composed of a clast-supported matrix. Its clast composition is polymictic, with 1 m maximum diameter (including the entire gravel size scale), ranging from very angular to subrounded shapes (Figure 4.15d). Some of these clasts are faceted and striated. The second layer is matrix-supported, mostly composed of coarse quartz-feldspathic sands laminated and pebble-sized grains (Figure 4.15c). The clasts (~35%) are polymictic, with a wide range of sizes and shapes, highlighting some <2 m angular clasts close to the roof. Finally, a well oxidized and bioturbed soil horizon is present (Figure 4.15b). This horizon is mainly composed of silt and clay; it also has some gravels close to the downward contact.

Glaciofluvial plain

The only accumulation of glaciofluvial sediments recognized as a plain is the hanging surface close to the EMC confluence (Figure 4.14a). It has a triangular shape, with 2.1, 2.4, and 2.6 km on each side. It is composed of moderate to poorly selected polymictic gravels.

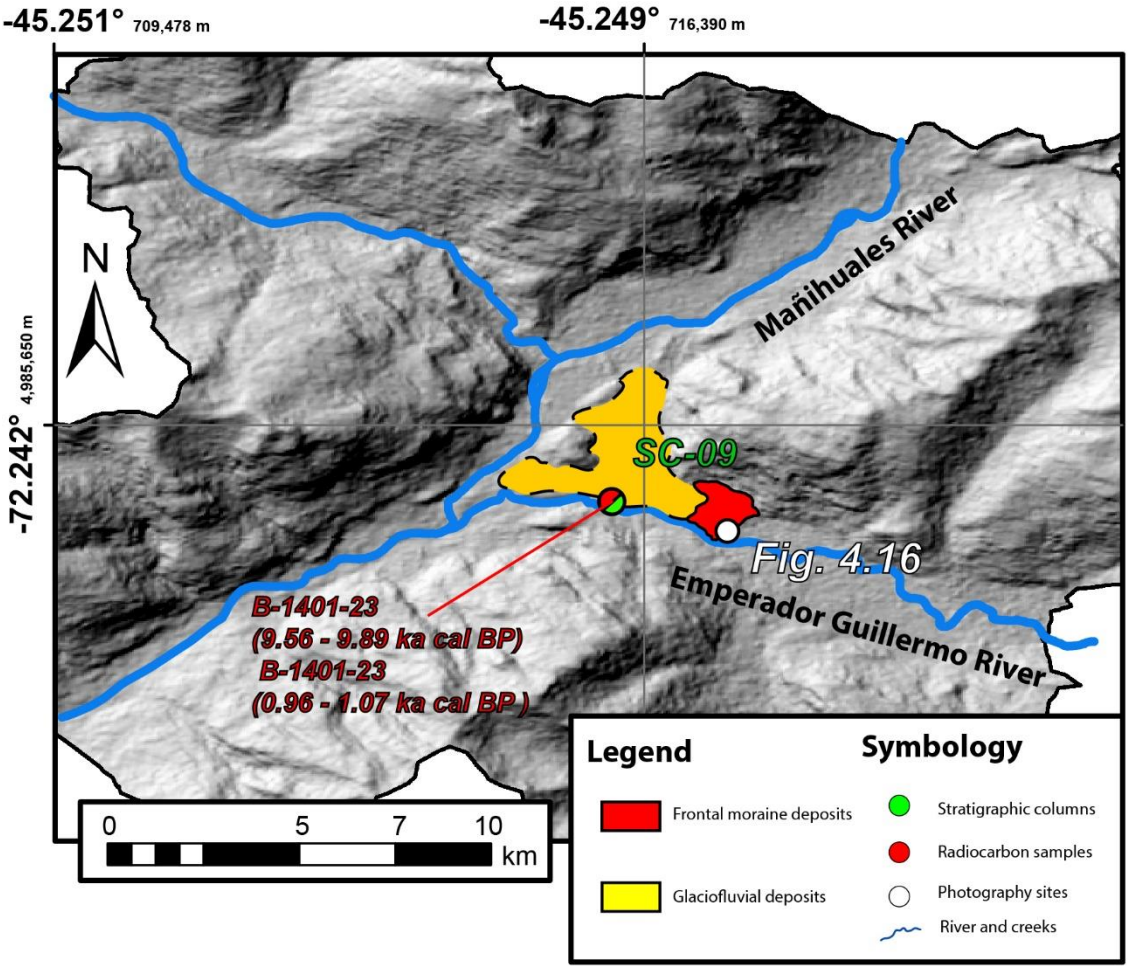

Figure 4.14. Map indicanting landform features and sites in Emperador Guillermo and Mañihuales confluence zone (EMC), using a 30x30 m DEM hillshade (ASTER-GDEM). Heavy black line indicates Profile M-M' position.

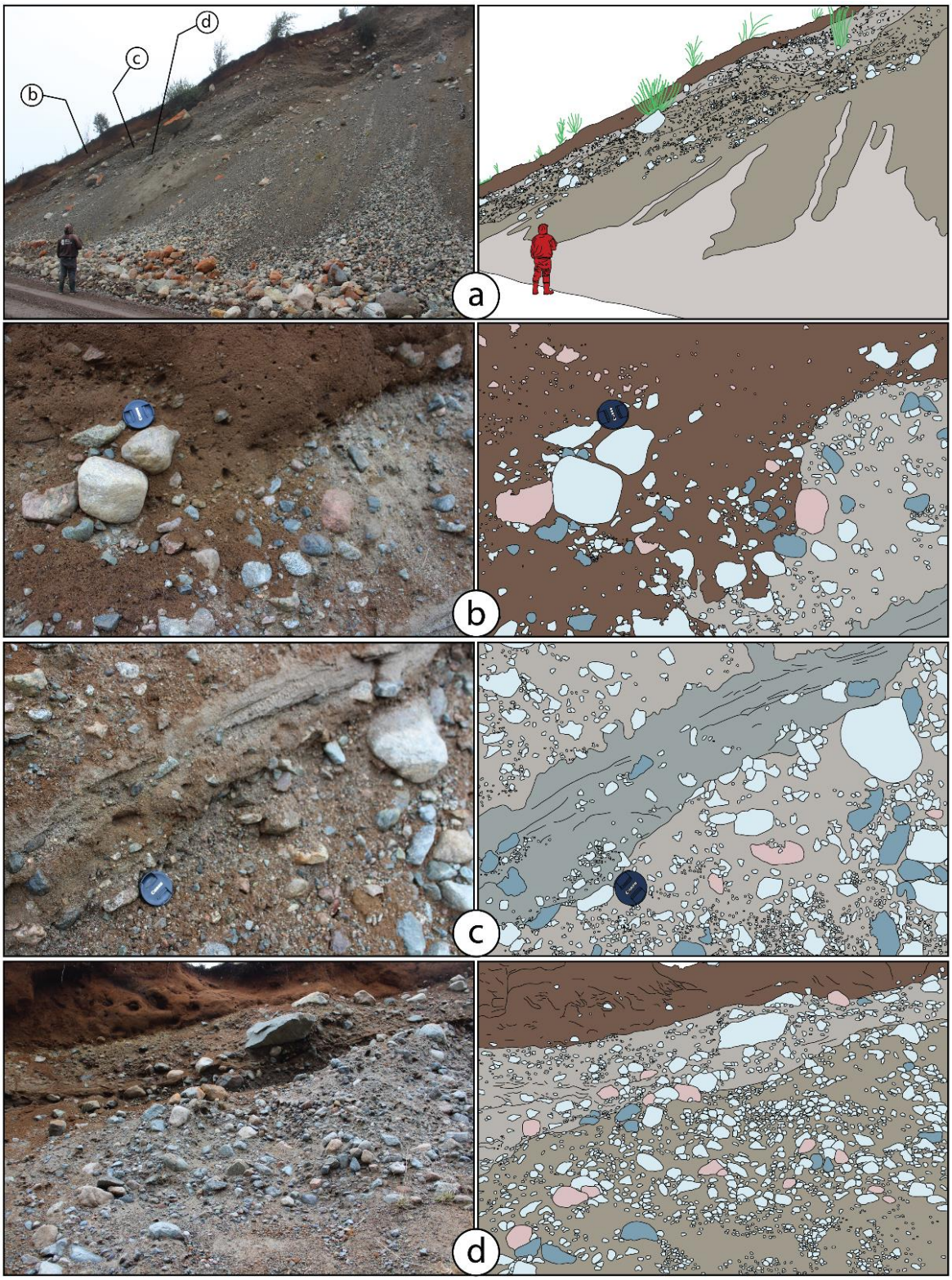

Figure 4.15. (a) Partial view of the frontal moraine observed in Emperador Guillermo River northern bank. Right: photography, Left: Schematic interpretation indicating each layer. (b) Close-up view of the contact between the soil horizon and the underlying moraine layer. Righ: Photo, Left: Scheme that highlights the grain size and shape of the underlying layer. (c) Close-up view of the underlying layer at the soil horizon level. Right: Photo. Left: Scheme showing a sand lens surrounded by the gravel size fraction of the diamict. (d) View centered on the moraine bottom layer. Right: Photo. Left: Scheme highlighting the class-supported nature of this layer.

ii. Stratigraphic column SC-09 and radiocarbon ages

This sequence (Figure 4.16) has an unknown base and begins with a ~2.5 m thick, coarse polymictic gravel. Poorly-selected mid-coarse quartz-feldspathic sands matrix-supported form it. Its main clasts are good-selected and rounded shapes. Present a slight westward imbrication. The sands show cross-lamination. We interpret it as a proximal high-energy upward to a mid-energy glaciofluvial environment. Close to the contact with the next unit, a sample was taken for radiocarbon dating. The sample B-1401-23 gave an age ranging between 9.56 and 9.89 ka cal BP (Appendix Figure B15).

Upward, in non-erosional contact, there is a ~0.8 m thick volcanic ash deposit. We can divide the deposit into two ash layers. The first layer (~0.4 m thick) present grain size coarsening upward, and sometimes downward. The second layer (~0.4 m thick) presents diffuse contact downward, maybe indicating weak erosional conditions. Also, the present grain size coarsening upward. We interpreted these layers as part of the same environment previously described.

Immediately above, in erosional unconformity, there are 0.25 m thick ash deposits dominated by pumice clasts. The abundant presence of wood and coal rest make this deposit a good target for radiocarbon dating. The sample B-1401-24 was taken from this layer and gave an age ranging between 0.96 and 1.07 ka cal BP (Appendix Figure B15).

Finally, covering the sequence, there is a 0.25 m thick ash deposit.

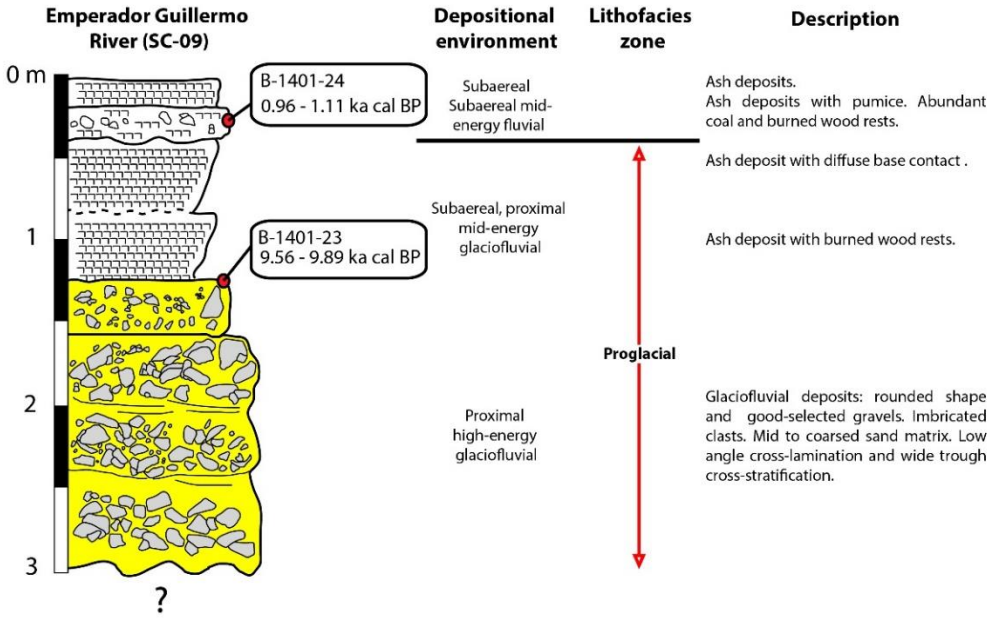

Figure 4.16. Stratigraphic column SC-09. It represents part of this glacial drift on Emperador Guillermo River's northern bank. It also shows the site where samples B-1401-23 and B-1401-24 were extracted.

4.4.3 Lake Riesco zone

4.4.3.1 Glacial morphostratigraphic units

Lake Riesco zone is located 6 km to the south of Puerto Aysén (Figure 4.17a). Glacial landforms and sediment deposits exposed in this area are covered entirely (or at least in free zones) by vegetation (Figure 4.19a). For this reason, we saw ourselves in the task of generating test-pits and clean some road cuts, which led us to detect only glaciolacustrine units. Despite this impediment, the area has conspicuous geomorphic features which we have registered through UAV flights (Figure 4.18), allowing us to broaden our knowledge of this glacial record, which, together with Vargas et al. (2013)'s underwater data and first-order interpretation, gives us a starting point for future work. Below we present the data acquired in this research.

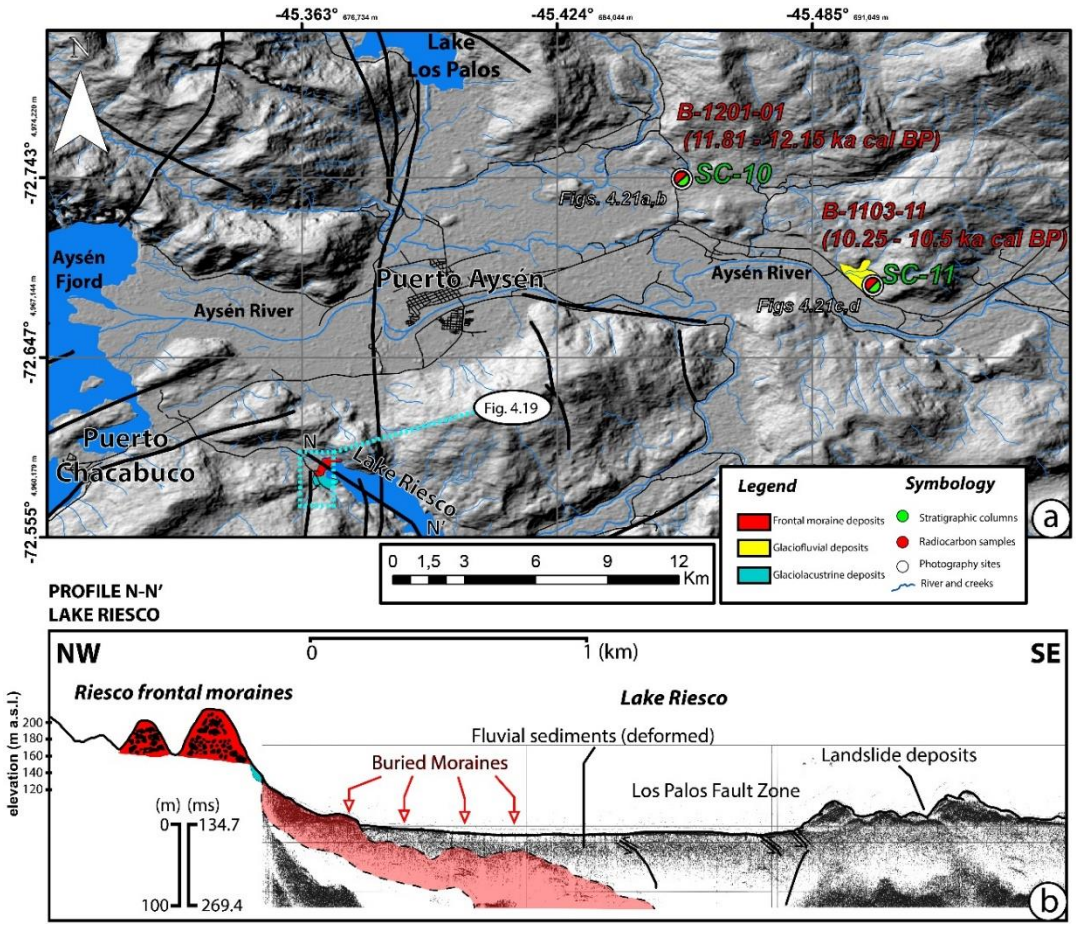

Figure 4.17. (a) Hillshade map indicating landform features and sites in Aysén River Basin and surrounding localities, using a 30x30 m DEM (ASTER-GDEM). The heavy black line indicates Profile N-N' position. Thin black lines indicate roads. Heavy black lines indicate fault zones. The red inset corresponds to a UAV flight zone. (b) Profile M-M' Emperador Guillermo River (sub-bottom cross-section). It shows seismic reflectors interpreted as buried moraine, current lacustrine, and landslide deposits (modified from Vargas et al., 2013).

i. Glacial landforms Lake Riesco

At least four frontal moraine are observed (and interpreted) nearby and within Lake Riesco. One of them and the most conspicuous in the northwestern shore, and the other three inside the lake's sedimentary infill (Figure 4.17b).

Riesco frontal moraine has NNE-SSW general strike, which curves southward, giving it an arched-shaped geometry and the concave side facing east. We make four profiles (i-i', ii-ii', iii-iii' and iv-iv' profiles) perpendicular to the cord axis, approximate equidistant distance, and cover the entire glacial feature representatively. These profiles show that the Riesco frontal moraine's height decreases and thins from north to south, ranging from 42.83 and 31.97 m high, 354.2 to 47.3 m wide.

The other moraine are shown in a sub-bottom profile made parallel to the lake axis (Figure 4.17b). (Vargas et al. 2013). Based on reflectors geometry from seismic facies we interpreted as buried moraine deposits, and the distance between mound-like packages peaks, at least four glacial advances (or retreats) are recorded in the Lake Riesco sedimentary infill.

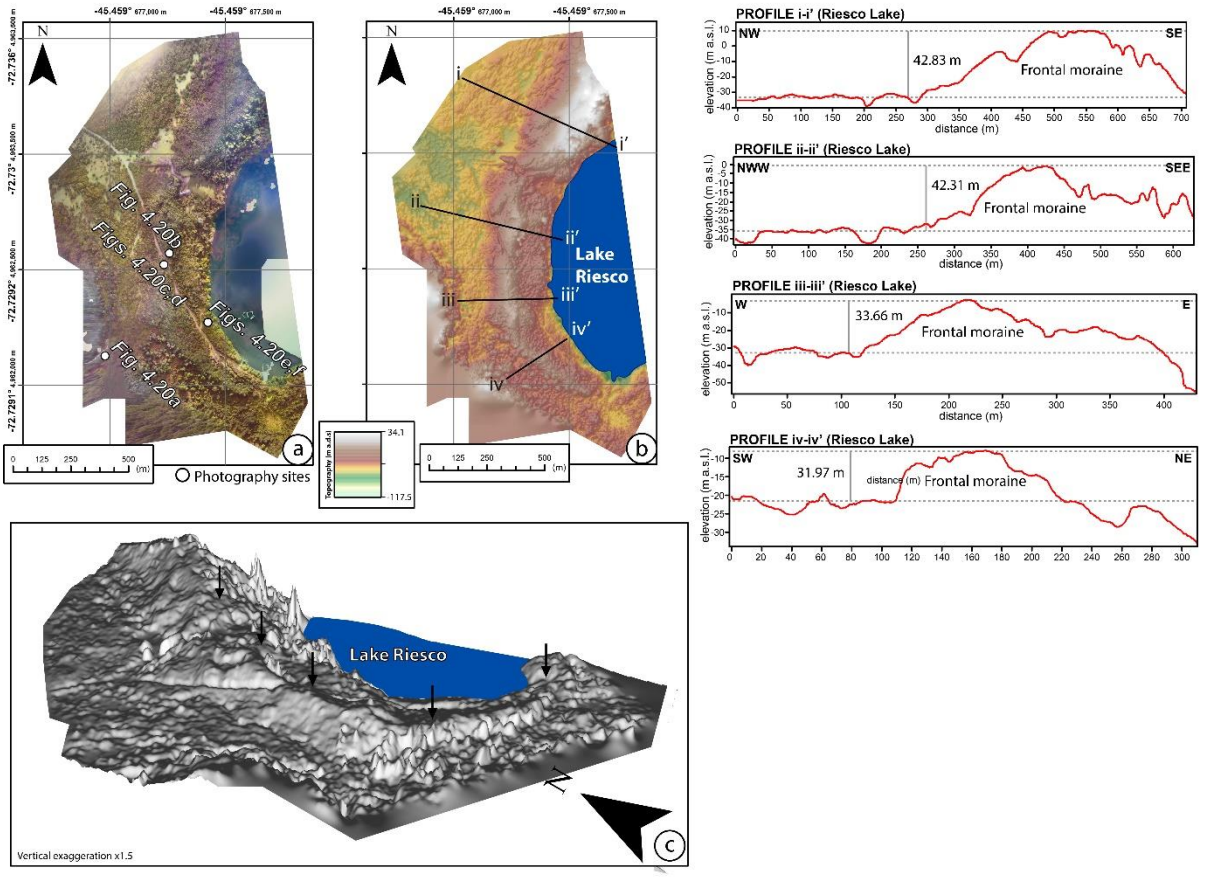

Figure 4.18. (a) Orthophoto mosaic derived from SfM data from Lake Riesco western shore zone. (b) Plan view of the DEM area. A semi-translucent color palette was used alongside a hillshade. Heavy black lines correspond to profiles i-i' to iv-iv' (upper right). (c) 3D-DEM seen from the southwest.

As already stated above, a dense forest jungle's presence prevented us from locating outcrops with a complete glacial sediment sequence. Despite this, the presence of a road cutting part of Riesco frontal moraine facilitated the access to a glaciolacustrine sediment unit. Interestingly, this unit is located close to Riesco frontal moraine eastern edge (Figure 4.18a). These glaciolacustrine sediments are exposed on both sides of the road and in lakeshore vicinity

There is a finely-laminated varved sequence composed by dark and light silts in the area between profiles ii-ii' and iii-iii', which evidences a wet-state deformation (Figures 4.19b, 4.19c, and 4.19d). An intense folding and low angle failure with an apparent vergence towards the SE is observed.

In the zone immediately eastward profile iv-iv', close to the current lakeshore, a natural section is observed where a matrix-supported sedimentary package (Figure 4. 19e) is observed. It is composed of a muddy-sandy dominant portion, with pebble-sized gravels, ranging from sub-rounded to rounded shapes (Figure 4.19f). This deposit is partially rusty due to the presence of a well-developed soil horizon.

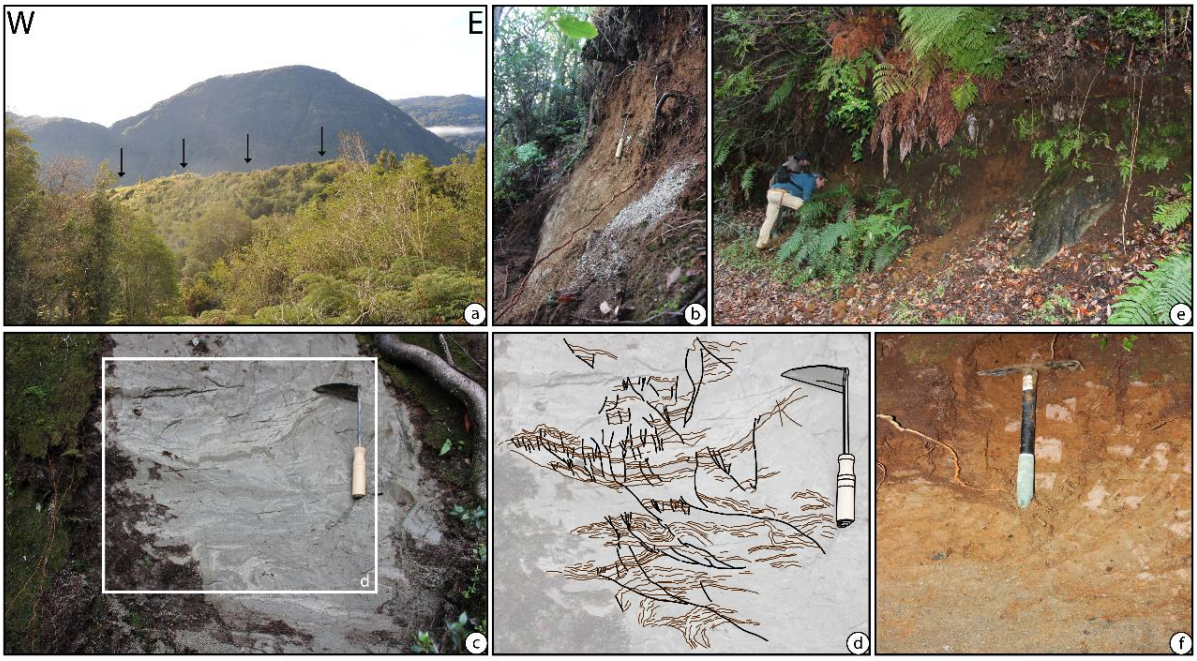

Figure 4.19. (a) View from a southern hill looking to Riesco frontal moraine. Arrows indicate the position of the landform. (b) Road cut (southern view) before being cleaned and verticalized using a nejirigama blade. (c) Road cut (northern view) after being cleaned and verticalized using a nejirigama blade. An alternation of light and dark silts and clays is observed. (d) This layer was exposed to wet-state deformation, which has left folding and folding structures. (e) The natural section is located close to the Lake Riesco western shore. It shows sandy and gravel layers. (f) Close-up view of the natural section showing more details of the sediments.

4.4.4 Aysén River valley zone

4.4.4.1 Glacial morphostratigraphic units

Glacial landforms and sediment deposits exposed in the Aysén River valley (Puerto Aysén and vicinity) are scarce and difficult to locate. This could be mainly due to a substantial control over the valley by more current activity, as fluvial and gravitational processes that obliterate and cover any glacial features trace.

Nevertheless, we were lucky to locate two glacial “outcrops” (Figure 4.17a), thanks to regional aggregates exploitation works. These works leave free faces for our observation. These two study areas are Pangal (Figures 4.20a and 4.20b), 7.7 km to the northeast of Puerto Aysén city, and the East Quarry (Figures 4.20c and 4.20d), located 11.2 km eastward of the city. Our observations were fruitful as we were able to map two stratigraphic columns (SC-10 and SC-11; Figure 4.21) and sampling organic matter for radiocarbon dating.

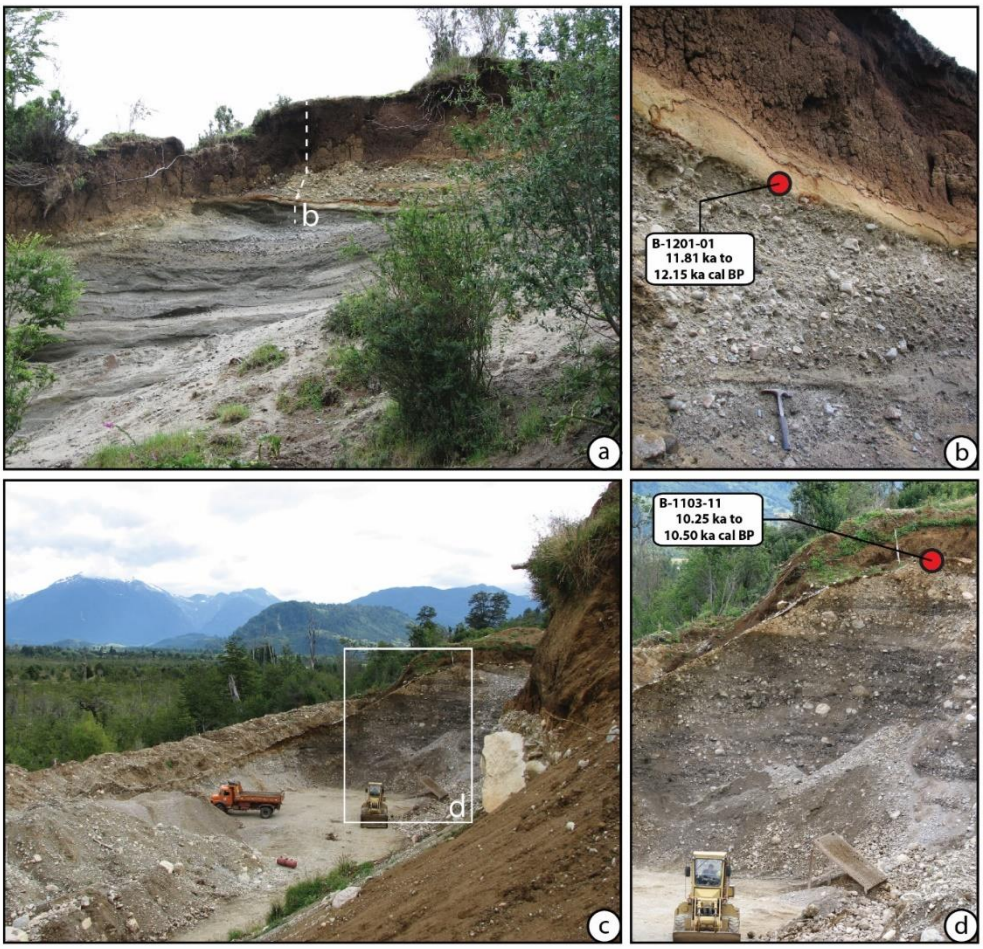

Figure 4.20. (a), (b) Outcrop showing glaciolacustrine and fluvial sediments overlaid by volcanic ash fall deposits, located some kilometers to the northeast from Puerto Aysén in the Pangal locality. Note hammer for scale in b. (c), (d) Outcrop showing glaciolacustrine and fluvial sediments overlaid by volcanic ash fall deposits, located some kilometers eastward Puerto Aysén city, in the East Quarry. Red circles indicate radiocarbon sampling sites with results shown (modified from Vargas et al., 2013).

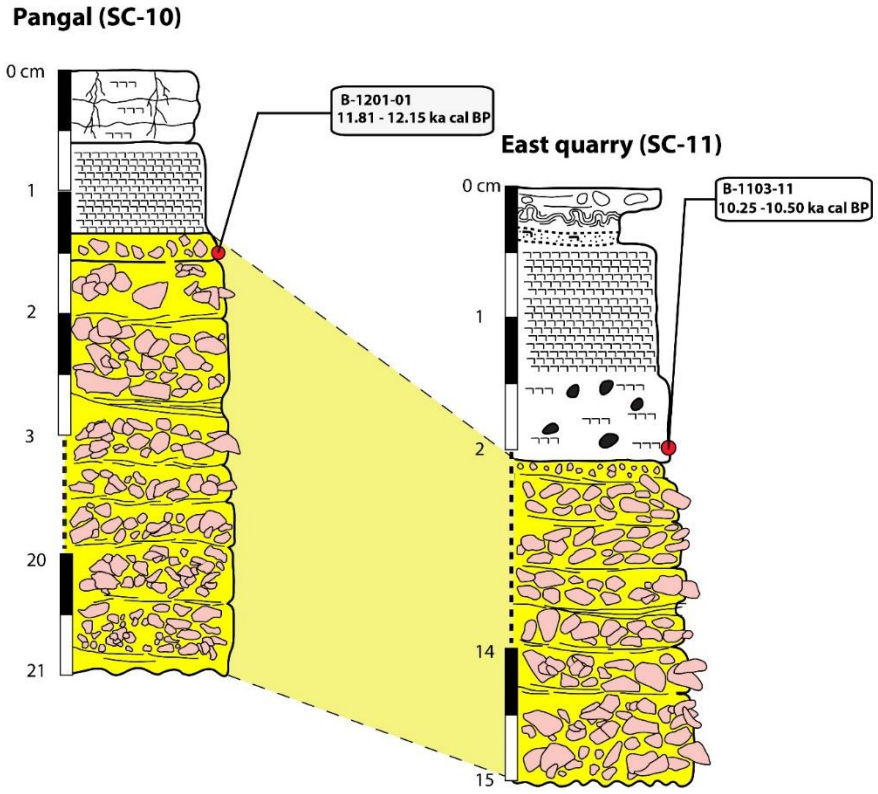

Figure 4.21. Stratigraphic correlation between column SC-10 located close to the Pangal locality (It also shows the site where B-1201-01 was extracted), and column SC-11. It represents a part of the glacial drift located in the East Quarry locality. It also shows the site where B-1103-11 was extracted.

i. Stratigraphic column SC-10 and radiocarbon ages

A 21 cm total thick stratigraphic column is exposed in the Pangal locality near Puerto Aysén (Figure 4.21a). It begins with a ~19.7 cm thick alternation of well-rounded and well-selected clast-supported gravels. These gravel layers present imbricated clasts. Its matrix is composed of mid to coarse sands. Also, the same grain-size sands are arranged in a low-angle cross-bedding, as well in trough cross-bedding. In the last centimeters of these alternations, very close to the overlying sedimentary package, an organic matter sample (B-1201-01) was extracted. It was dated using radiocarbon methods between 11.81 and 12.15 ka cal BP (Appendix Figure B16). We interpreted this deposit as a high-energy proximal glaciofluvial environment.

Overlaying in conformable contact, a ~0.8 cm thick layer of unaltered volcanic ash layer, with a ~0.5 cm thick ash, altered to a soil horizon. The soil horizon segment shows a strong development, through oxidation and argilization of the ashes. Roots penetrate several millimeters into the ground. Coal remains are also common. Thus, we interpreted these layers as a recent volcanic event in a subaerial environment.

ii. Stratigraphic column SC-11 and radiocarbon ages

The East Quarry zone is represented by a 15 cm total thick stratigraphic column (Figure 4.21b). It starts with a 13 cm thick alternation of clast-supported gravels and cross-bedding mid to coarse sands layers. This unit has the same characteristics of the SC-10 bottom unit, but with a radical change in the clast-size close to the overlying unit. We interpreted this deposit as a high-energy proximal glaciofluvial environment.

Overlaying in conformable contact, a ~1.5 cm volcanic ash unit is characterized by upward (and downward) coarsening clast-size alternated layers. Close to the bottom of this unit, wood and coal remains are common. We took an organic matter sample and dated using radiocarbon methods between 10.25 and 10.5 ka cal BP (Appendix Figure B16). We interpreted these units as a mixture of subaerial and mid-energy fluvial environments.

Upward SC-11, we found a thin ash-pumice layer close to a disturbing level, probably related to the quarry exploitation works.

4.4.5 Aysén Fjord zone

To the west of the Aysén River lies Aysén Fjord and here our transact goes from a terrestrial setting to an offshore setting. Immediately westward Puerto Aysén city and Puerto Chacabuco town, the inner-segment of Aysén Fjord is located, an area where research is based on bathymetry and sub-bottom profiles have been carried out (Vargas et al., 2013; Villalobos et al., 2020). Aysén Fjord has an EW to NW-SE strike and corresponds to a typical U-shaped glacier valley. Active branches of the LOFZ were recognized across the fjord, and despite strong erosion rates and sediment supply to the valleys, especially by the Aysén River, which drains the overall Northern Patagonian Andes at this latitude. Geomorphologic markers of Holocene tectonic activity were found on land and at the seafloor, suggesting rapid tectonic rates associated with active structures of this fault system (Vargas et al., 2013).

4.4.5.1 Sub-bottom profile and buried moraines

Using Profile SL-06 from Villalobos et al. (2020), and their interpretation, some seismicfacies suggest the presence of glacial landforms (see Villalobos et al., 2020).

i. Moraine Seismic Unit

This seismic unit is constituted by continuous to semicontinuous irregularly shaped reflectors with moderate to intense acoustic contrast in lateral contact with the Cuervo Ridge, most possibly onlapping this last feature (Villalobos et al., 2020). It

constitutes a multicrested mound with a hummocky internal shape that we interpret as a buried moraine, following the similarities in geometry and semichaotic facies seen in previous seismic surveys in Chilean fjords (e.g., Boyd et al., 2008; Breuer et al., 2013). This glacial deposit appears at ~0.42 s from Cuervo Ridge eastern flank up to the Punta Cola vicinities, covering ~7 km along the inner fjord. The seismic moraine unit ranges at least between ~14 m and ~33 m thick (until the first multiple). The stepped geometry, as evidenced in the sub-bottom profile, is characteristic of push frontal moraines (Villalobos et al., 2020). Furthermore, the deposit's considerable thickness could indicate successive phases of glacial advancements and retreats that contributed to shaping the fjord.

ii. Post-glacial sedimentary infill

The inner Aysén Fjord, which is limited to the west by Cuervo Ridge and associated bathymetric step (Villalobos et al., 2020), is characterized by a well-stratified sedimentary cover that can be interpreted as a postglacial unit overlying the buried moraine exhibiting characteristic wedge architecture to the west. The sedimentary thickness ranges between >300 m, near the Aysén river mouth, to ~109 m, near the Cuervo Ridge (Villalobos et al., 2020). It has a conspicuous west vergent wedge architecture, involving a substantial contribution from the Aysén River during the last deglaciation in Patagonian Andes and the current global sea level high stand after 7 ka (Lambeck et al., 2002). Considering the local observations of glaciofluvial sediments and moraines covered by ash layers with soil horizon made in the other study areas, and in the Aysén River mouth zone (Vargas et al., 2013), it is possible to infer an age close to ~12 ka BP for the last ice sheet retreat in the area (Villalobos et al., 2020), giving a maximum age for the well-stratified sediment unit.

4.5 Discussions

4.5.1 First-order glacial geomorphological domains and depositational environments

The presence of u-shaped valleys, cirques, glacial deposits and other glacial landforms show that icesheets have shaped Cuervo River Basin (CRB), Emperador Guillermo and Mañihuales rivers confluence, Aysén River Basin, Lake Riesco Zone, and Aysén Fjord in all its extent and elevations. In the case of CRB glacial troughs (AC and AB, Figures 4.3 and Appendix B1), the disposition of frontal and lateral moraines, roches moutonnées, as well as the direction of glacial striations marks, eskers, and imbricated clasts in glaciofluvial deposits indicate that glaciers flowed and advanced from west to east.

In CRB westernmost zone, the glacier advance direction was E-W, while eastward, it is verified by a slight field change towards the northeast, probably controlled by inherited paleogeography (Appendix Figure B1). On the other hand, in the study areas located in the main mountain range (EMR, Lake Riesco, and Aysén

basin), imbricated clasts are quite common in glaciofluvial and glaciolacustrine deposits. Another type of indicator of glacier movement is fold-and-thrust like structures (Figures 4.19c and 4.19d) associated with the deformation of fine-grain sediments. Few indicators were found in these sites' outcrops, so statistically, we consider them insufficient for the construction of a vector map. In general, these show directions parallel to the valleys where they are.

To the west (Domain A_1; read Appendix B; after Arqueros, 2004) the u-shape of AC and AB troughs demonstrates a first-order valley glaciers' action. Eastward in the central domain (Domain A_2) these features are lost, and a flat morphology takes place. These drastic changes would be due to the merge of two lobes and an altogether action. Which is linked to the action of glacier(s) during a complete glacial cycle, long term glacial process on the local geology and structures. Towards Chile-Argentina frontier (Domain A_3), this plain morphology is more extensive, probably due to mountain foot glaciers action during glacial phases. First-order features and characteristics as i) low heights watershed divide with Pollux River and Mayo Alto River basins, located southward CRB; ii) the slight change to the northeast, of the glacier advance structures strikes in A_2 and A_3 domains; and iii) the presence of eskers, roches moutonnées, and glacial striations marks in the watershed zone make us propose glaciers' action at the mountains skirts may have occurred during pre-LGM glacial phases. Thus, the last glacier event would have inherited this flat-extended paleotopography in the central zone of the Basin (Domain A_2).

CRB paleoenvironmental evolution during Quaternary glacial phases is summarized in Appendix Figure B8 (after Arqueros, 2004). It represents an integrated stratigraphic record scheme for the four morphostratigraphic systems, the stages interpretated in the basin, glacial paleosurfaces associated with each system, and their equivalent drifts in other basins.

For the sites located to the west, outcrops are scarce. Therefore a clear recognition of the environmental evolution seems to be, for now, difficult. Although the absence of a complete drift system and the scarcity of deposits of glacial origin could indicate that these areas went through high erosion processes, which have obliterated most of the geological evidence of their presence. We are inclined towards this idea because signs of underwater glacial deposits highlight that glacial action was dominant in this area, which allows us to rule out its total absence.

4.5.2 Morphostratigraphic Systems ages and correlation with other glacial systems

CRB frontal moraine systems show an increased erosional degree and increase weathering of their volcanic clasts, eastward (Figure 4.4). In the first-order, we can hypothesize that systems located eastward are necessarily older than the western ones.

Of the four defined morphostratigraphic systems in CRB, only three have frontal moraine in Chilean territory. Coyhaique Alto System presents the most advanced erosional and weathering states based in our description of the geometry of the landforms and major clasts. The other two systems, El Diablo and El Toro are better preserved, and the differences between them are minor. This suggests that they were formed in much later periods, and closer to each other.

El Diablo System is the most extensive glacial record in CRB (Figure 4.4). From the lithofacies analysis (Appendix Figure B18), we obtain five major re-advances (Figure 4.12). The maximum glacier advances with glacial front detention periods are evidenced by the Pedregoso Estuary frontal moraines and by the great thickness of proglacial phases in SC-04 (Figure 4.12). A slight setback with a significant detention period during 23.55 to 17.19 ka cal BP would have given rise to the great Lake El Diablo (SC-05, RC-01, SC-03 in Figure 4.12), dammed by moraines.

To an understanding of the glacial retreat evolution, radiocarbon dating (Table 4.1) was carried out on glaciolacustrine samples. From the lithofacies interpreted as major re-advances, only three ages were obtained (Figures 4.4 and 4.12). From RC-02 stratigraphic column close to the base, the glacial front position's minimum age ranges between 37.27 and 35.69 ka cal BP. Meanwhile, close to the roof, the minimum age ranges between 28.45 and 27.77 ka cal BP. In RC-01 stratigraphic column, which corresponds to the most extensive lake record, three samples have obtained minimum ages between 23.55 to 16.61 ka cal BP.

For its part, in the El Toro System (Figure 4.4), two minimum ages were obtained (Figure 4.12). From RC-03 close to the base the glacial front position's minimum age ranges between 20.82 and 20.27 ka cal BP. This age range that escapes the expected order of younger ages presents a problem within our model's consistency. We propose that: i) said layers corresponding to a sequence of glaciolacustrine and glaciolfluvial deposits could be part of the El Diablo System, therefore representing a local variation of the geometry of the icesheet (an area whose retreat was more accelerated), ii) an overexposed section of El Diablo System due to glacial and river erosion, or iii) the samples used for the analysis of radiocarbon (bulk) present contamination. We are inclined to the first two hypotheses. Close to the roof two closely spaced samples were obtained that range the minimum age between 0.81 and 0.45 ka cal BP. In this case, a significantly abnormal situation occurs. The radiocarbon age range provided by the samples stands out for being very young when considering the position of the glacier front provided by the most current models of the Patagonian Icesheet (Figure 4.22b) (e.g., Hubbard et al., 2005; Davies et al., 2020). Although ages in moraines recognized for the Late Holocene range between 0.5 and 0.2 ka (e.g., Davies & Glasser, 2012; Glasser & Jansson, 2008; Glasser et al., 2008, 2011a), they have been found generally at the edges of glacial valleys, and generally, these moraines have a fresh-looking appearance and are close to glaciers. The case closest to our study area, but still far enough away, corresponds to those located near the Northern Patagonian Icefields and which usually reach ages of 0.2 ka (Davies & Glasser, 2012; Glasser et al., 2011). Considering the descriptions provided of the sampled lithofacies and the regional geological antecedents in the context of glaciations, we are inclined to suggest that the youngest ages could correspond to the fluvial deposits seen upward in RC-03, due this sample was extracted at the limit of both layers.

In the other sites located westward, some glaciofluvial sedimentary packages can be used as markers of glacier movement in the main mountain range. For the EMC site, the minimum ages obtained ranges between 9.89 and 9.56 ka cal BP (Figures 4.14 and 4.16). Further west in the area immediately east of Puerto Aysén city, minimum ages range between 12.15 and 10.25 ka cal BP (Figures 4.17, 4.20, and 4.21).

To generate a correlation at both the local and regional scale of the glacial drift deposits, we have assumed as a framework for comparison and work the time-dependent evolution model proposed by Hubbert et al. (2005) (Figures 4.22 and Appendix B17). Their model explains the fluctuations of the Patagonian Icesheet between 45° and 48° S, and it will allow us to avoid complexities and variations in the behavior of an ice mass associated with its location and assosiation with respect to the axis of the main mountain range and and water bodies. We will focus on making a strictly temporal correlation, considering our radiocarbon samples represent minimum ages and therefore can be improved in future works.

Both, areal extension, stratigraphic, and geochronologically El Diablo System can be correlated with Fénix Moraines, Río Blanco Moraines and in some extent with Menucos Moraine (Figure 4.22b). Considering the great thickness of the morphostratigraphic record of the El Diablo System, the low erosional and weathering degree of in volcanic clasts (Figure 4.4), the fact that their surface constitutes the starting level of postglacial fluvial incision in A_1 and A_2 domains (Arqueros, 2004; Appendix Figures B1, B2 and B3), and mainly their minimum radiocarbon ages (Figures 4.12 and Table 4.1), we suggest a LGM age (~25 – 18 ka BP) for the system.

Appendix Figure B8 and Figure 4.22b represent a summary of our age correlation between El Diablo System and Fénix Moraines, Río Blanco Moraines and Menucos Moraine (Douglass et al., 2006; Hein et al., 2010; Smedley et al., 2016). It is also possible to correlate these systems with Sarmiento Lake frontal moraines I and II (Paine Range) assigned to LGM (Marden & Clapperton, 1995), which dam a lake. Both locations are located eastward Main Mountain Range and southward CRB. Northward CRB, in the Nahuel Huapi Lake area, El Diablo System has an equivalent in Nahuel Huapi Drift II (Flint & Fidalgo, 1964; Rabassa et al., 1987; Clapperton, 1993), that also dam a lake.

Concerning previous studies on the western side of the Andes, mainly the Chilean Lake District, El Diablo and El Toro systems would be equivalent to the Llanquihue II stage, which corresponds to LGM. For Denton et al. (1999), this stage is a ~15,000 years event, from 29.40 to 14.50 ka BP. Using Porter (1981) and Clapperton (1993)'s nomenclature, El Diablo System would be coeval with Llanquihue II, restricted to 28 – 18 ka BP, and El Toro System would be coeval with Llanquihue III. Nevertheless, using our minimum ages, we can observe that the temporary interval covered by El Diablo System is much broader. However, our data are occasionally generating age overlapping, which could be overcome by using more precise methods.

Meanwhile, the fluvioglacial deposits located in Aysén River Basin site can be correlated with the Esmeralda Moraines and Tranquilo Valley (Monte San Lorenzo) moraines. The first group of deposits yielded cosmogenic nuclide ages of 13.4 ka (Figure 4.23b) (Thorndycraft et al., 2019). A series of moraines in the Tranquilo Valley (Monte San Lorenzo) the moraines yield mean ^{10}Be ages of 13.8 ka, 13.3 ka, 13.7 ka, and 12.1 ka (Figure 4.23b) (Sagredo et al., 2018). By 10 ka, the Northern Patagonian Icefield evolved into a series of separate icefields. As glaciers continued to recede during the Holocene, the influence of topography became more important as ice masses. We propose that EMC site glaciofluvial deposits with minimum ages ranging between 9.89 and 9.56 ka cal BP clould represent such glacial context.

It is essential to mention that several moraine deposits in this stretch of the Patagonian Andes have been found underwater (Heusser, 1960; 2002; DaSilva et al., 1997; Fernández et al. 2011. Fernández et al. (2011), in their study of the sedimentary infill of the Golfo Elefantes, dated the sedimentary infill between ~ 11.3 ± 3.0 ka and 4.2 ± 0.3 ka (early – middle Holocene). With this information and with an analysis of reflection seismic images, they determined the absence of ice contact sediments raises for the arcuate terminal moraines (MS Guales I) associated with the Guales Glacier that occurs on the edge of the Gulf of Elefantes. Their data suggest that the moraines were formed before >11.3 ± 3.0 ka (Figure 4.23b), probably in the local LGM's late/waning stages.

Although a hybrid chronology (radiocarbon and stratigraphy relative dating) suitable for paleoenvironmental reconstruction is proposed above, a more detailed chronology based on absolute ages would affirm and refine regional and global correlations. Patagonian steppe vegetation during the LGM in the area (Whitlock et al., 2001) would explain the lack of radiocarbon material. AMS techniques could be applied in recognition of more glaciolacustrine sediments. Another possibility, and the more suitable, is the application of chronology of cosmogenic radionuclides (Marchant et al., 2002; Phillips, 2001), along terraces (Burbank, 2002), or moraine crests (Kaplan et al., 2005; Douglass et al., 2006; Hein et al., 2010; Bertrand et al., 2012; Glasser et al., 2012; 2016).

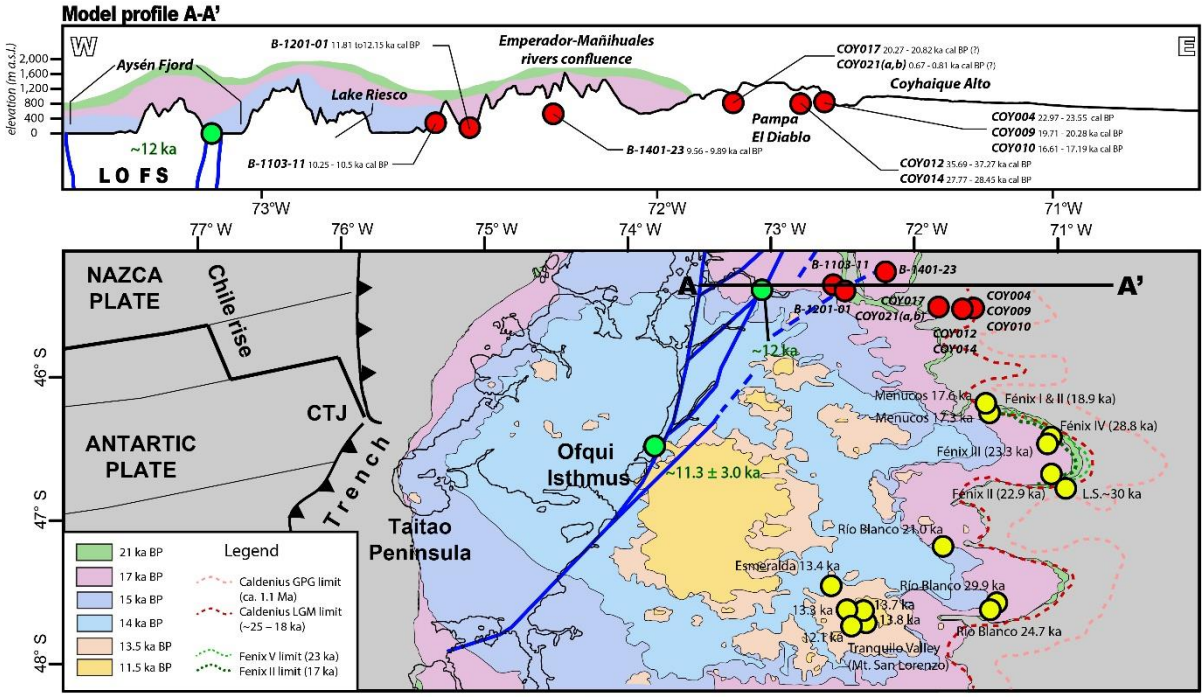

Figure 4.22. Time-dependent model for the fluctuation of the Patagonian Icesheet between 45° and 48° S (Hubbard et al., 2005). It shows an LGM configuration compatible with the available records until that time. Average ice thickness ~1,130 m. Red dots correspond to our radiocarbon ages,yellow dots correspond to correlated drifts (Douglass et al., 2006; Hein et al., 2010; Smedley et al., 2016), and green dots to age estimations for the moraines of respective local area (Fernández et al., 2011; Villalobos et al., 2020). Down-right: Time-slices of ice sheet surface elevation and isostatic adjustment at key snap-shots during deglaciation.

4.5.3 Dating of glacial deposits as a proxy for paleoseismology studies in fjords

Because of their fast sedimentation rates and often long sedimentary records, and broad temporal spectrum related to active faulting (Late Holoce), fjords and glacial channels constitute ideal archives to explore the seismic history of an area. This last characteristic is also a double-edged sword if we consider the technical aspect of obtaining deep sediment samples which, in the case of the fjordland of the Aysén Region, can easily reach depths close to 300 m, a complicated scenario for the implementation of longer sediment cores.

In the Aysén Region, the most conspicuous active tectonic structures in the Andes is the Liquiñe-Ofqui Fault System (Villalobos et al., 2020). The faults cuts several of these fjords (Aysén Fjord, Quitralco Fjord, Puyuhuapi Channel, Elefantes Channel, and Bahía Erasmo Fjord, among others; Figure 4.2) so the development of a methodology to delimit the age of the lower limit of said sedimentary packages has a significant weight in the calculation of estimates of the ages of possible paleo-earthquakes registered in them. It was shown that the Liquiñe-Ofqui Fault System presents complex seismic activity in the branches that are part of its transfer zone (e.g., Punta Cola, Quitralco, Cuervo faults), where in recent times it has triggered the seismic sequence in Aysén Fjord site in 2007 (Agurto et al., 2013; Vargas et al., 2013; Legrand

et al., 2013; Villalobos et al., 2020). Similar events at the Quaternary scale presented in recent works (Wils et al., 2018; Villalobos et al., 2020) point out the record of their paleoseismicity in the sedimentary infill of the fjord. The use of glacial deposits and landforms as a guide for determining effective time windows in which paleo-earthquakes are recorded in the area. This can be achieved using known ages and implemented in a Patagonian Ice Sheet evolution model allowing to know roughly (first-order) when these fjords and channels began their filling process.

In Aysén Fjord, where evidence of paleo-earthquakes was found together with the presence of seismic facies interpreted as moraines, is a key point to prove this idea. Tentative age of at least ~12 ka were assigned to the buried moraine deposits. This age comes from an extrapolation from inland glacial deposits covered by an ash layer (Vargas et al., 2013), and are consistent with estimates of >11.7 ka for the filling of other channels such as Elefantes Channel (Fernández et al., 2011). Using the evolution model for the Patagonian Ice Sheet of the last 21 ka from Hubbard et al. (2005) as a guide together with our radiocarbon ages, and also the newest chronologies at a regional scale, we observe minimal differences in the glacial position fronts (Figure 4.23). The concordance with our data would imply that Aysén Fjord exposed to sedimentation since 15 ka (Figure 4.23b).

These results are first order, and studies based on more accurate dating methods are necessary (cosmogenic nuclides on the lodgment till deposits or frontal moraines) and the implementation of a model that uses new data as previous ones. Despite the above, it gives us a reasonable window of time that will allow us to better characterize the degree of activity of the Liquiñe-Ofqui Fault System during postglacial times.

4.6 Conclusions

In this work, we have presented the first transect (~45.5° S) through the three geomorphological domains (fjordland, main mountain range, pampa zone) of the Aysén Region, southern Chile. This transect covered five study sites from east to west corresponding to the Coyhaique River Basin, Emperor Guillermo and Mañihuales rivers confluence, Aysén River Basin, Lake Riesco zone, and Aysén Fjord. Within these sites, we recognized a set of geomorphological features (landforms) and deposits that allowed us to build 13 stratigraphic columns to describe, characterize, and interpretate lithofacies of glacial origin.

In Coyhaique River Basin (pampa zone), we grouped the recognized glacial deposits and landforms into four morphostrarigraphic systems, which result from multiple advances, setbacks, and arrests of the Glaciers during the Quaternary. These systems are: Los Flamencos, Coyhaique Alto, El Diablo, and El Toro systems. Los Flamencos System is located further west in the pampa area and is found both in Chile but mainly in Argentina. This drift of probable Lower Pleistocene age, and was correlated by Arqueros (2004) with the Ricardo Rojas Drift (Alto Mayo River), Telken Drift (General Carrera - Buenos Aires Lake). Coyhaique Alto system located in the

central-eastern zone was correlated by Arqueros (2004) with Mayo River Drift (Alto Mayo River), Moreno Drift (General Carrera - Buenos Aires Lake). For El Diablo System, we have recognized six sub-stages (El Diablo I to El Diablo VI) in the basin's central area. Five glaciolacustrine samples were dated using radiocarbon method, which allowed us to determine minimum ages that vary between 37.27 ka cal BP and 16.61 ka cal BP, giving this drift an association to the LGM. Based on a chronological criterion, we correlate the El Diablo System with the Fénix Moraines (Fénix I to Fénix V; ~ 30.0 ka to 18.9 ka), Río Blanco Moraines (29.9 ka to 21.0 ka), and the series of younger moraines from Menucos Moiraine (17.6 ka to 17.3 ka). For its part, El Toro System located in the western part of the basin consists of four sub-stages (El Toro I to El Toro IV). We took three samples of glaciolacustrine origin for radiocarbon analysis. These gave ages, which we have considered as anomalies (20.27 to 20.82 ka cal BP, and 0.67 to 0.71 ka cal BP), probably associated with contamination by root presence. We tentatively give a post-last ice age to these deposits.

To the west, in the main mountain range, the Emperador Guillermo and Mañihuales rivers confluence site is located. Here landforms were identified as terminal moraines and also fluvioglacial deposits were observed in the stratigraphic column. A fluvioglacial layer was sampled for radiocarbon dating with minimum ages of 9.89 to 9.56 ka cal BP. Our interpretation for this sector based on evolution models from the Patagonian Ice Sheet is that these deposits were associated to the remnants of ice bodies' relics that, after 10 ka, formed separate icesheets. Further west is the Aysén River Basin, where two exposed stratigraphic columns were made on the flanks of the mountain whose deposits have been interpreted as glaciofluvial. They were dated with the radiocarbon method giving minimum ages ranging between 12.15 and 10.25 ka cal BP. We have correlated these deposits and landforms with a series of moraines in the Tranquilo Valley (13.8 ka to 12.1 ka) and the Esmeralda Moraine (13.4 ka).

This transect also incorporates two sites that contain evidence of submerged glacial landforms. In the Lake Riesco zone, these correspond to the continuation of the four frontal moraines observed on the northwest shore of the lake. Inland to the west of Puerto Aysén and Puerto Chacabuco cities, in Aysén Fjord, another landform interpreted as a frontal moraine was observed near Cuervo Ridge. The buried moraines are shown in sub-bottom profiles. The first group are shown parallel to the axis. Based on reflectors geometry from seismic facies we interpreted at least four glacial advances (or retreats) are recorded in the Lake Riesco sedimentary infill.

Finally, we evaluate the possibility of using dated glacial landforms as a new way to determine the time interval of the postglacial sedimentary infill of fjords and channels in the Aysén Region. The methodology can be improved by using/generating an evolution model of the Patagonian Ice Sheet's advances and retreats by incorporating a more robust input of data close to the area of interest, which has begun to develop through the making of our transect. As a first-order result, we can determine that in the Aysén Fjord area, the sedimentary fill has a minimum age of 15 ka based on this principle, which provides a study framework for the paleo-earthquake record analysis.

Chapter 5: Discussions

As a final section of this thesis, some points that were not directly addressed in the two main chapters will be discussed. It is essential to establish that the discussion's aim is not to achieve a definitive solution to the problem of the link between climate, erosion rates, tectonics, and uplift for the study area, or to propose whether Wedge Model (steady-state flow or quasi-steady-state) is the most indicated. Rather, it will be considered whether active faults study and the paleoseismological record within the sedimentary infill of the Patagonian Fjordland can be used as a new proxy to help us understand the long-scale processes such as Andean orogenesis during Quaternary, and mostly, what the Liquiñe-Ofqui Fault System current contribution to the morphology of the Patagonian Andes.

5.1 The 2007-AYSS and surface rupture along the active branches of LOFS

In this thesis including the literature review in Chapter 2, and the case studies presented in Chapters 3, I presented evidence that shows that the 2007-AYSS was characterized by shallow earthquakes at depths no greater than 10 km in the upper crust, with the main events close to 6 - 8 km deep. Along with this, at first glance and once applied a relocation method (e.g. Agurto et al., 2013; Mora et al., 2010), earthquakes presented a random distribution on a plat view. Considering the structures (faults and lineaments; Vargas et al., 2013) recognized in the study area and its surroundings, my approach was to perform a first-order 4D seismotectonic model (Figure 3.9). In the context of this complex geometric setting my model was capable to associate each event detected to a closest fault in the sector. In particular, three branches of the LOFS stand out: the Punta Cola, Quitralco, and Río Cuervo faults, which present a strong presence in features of the sector both on the surface and disturbing the sedimentary infill of the Aysén Fjord. Besides, all three show the highest degree of activity during the first stage of the sequence, particulary during April 2007, which is arbitrarily defined until the main event M_w 6.2 and the loss of the recording equipment. Punta Cola Fault plays a more important role due to the presence of an NW cluster characterized by shallow depths (1.8–3.7 km, green circles and envelope in Figures 3.9a and 4.9e), located near the area where the surface rupture is observed. It is important to emphasize that seismicity during the first phase of the seismic sequence was characterized by having a shallow activity (mainly the first ~ 5 km) and with a trend of seismic clusters getting closer and closer to this until the occurrence of the events. M_w 6.1 and M_w 6.2 (Figure 3.9). After this, there is a period where the seismic activity advances towards the north (Figure 3.9a) and becomes increasingly deep (Figure 9f) and difficult to associate with any structure with surface features.

Held et al. (2016), in their work carried out in the northern segment of the Liquiñe-Ofqui Fault System (near Villarica Volcano), present results based on resistivity profiles. The profiles were oriented perpendicular to fault zones for both the Liquiñe-Ofqui Fault System and other structures. The data obtained ranged in depth from the mid-crust to the near-surface. Held et al. (2016) observed the phenomenon of mid-crust conductors (Jones 1992; Jiracek, 1995), which is observed worldwide concentrated in the vicinity of faults. Examples of fault zones where this phenomenon

was recorded correspond to North and East Anatolian Fault Systems (Türkoğlu et al. 2015), reaching depths below 10 km. In San Andreas Fault, both in the Parkfield segment where it reaches very shallow depths ranging 2-3 km (Unsworth et al. 1997; Becken et al., 2008) and the Carrizo segment where it reaches depths of the mid-crust (Mackie et al. 1997; Unsworth et al. 1999; Bedrosian 2002). Examples of fault zones with compressive kinematics also present this phenomenon, allowing identifying the brittle-ductile transition zone's location, as in Wannamaker et al. (2002) for the Alpine Fault in the Southern Alps in New Zealand.

Held et al. (2016), based on their results and assuming mean values for the crust heat flux (130–170 mW m^{-2}; Hamza & Muñoz, 1996), the thermal conductivity of 2.8 W m^{-1} K^{-1}, and a radioactive heat production of 5 μWm^{-3}, they calculated temperatures exceeding the critical temperature for the brittle-ductile transition (250–500 °C; Sibson 1977; Ivanov & Ivanov, 1994) at a depth of 10 km. This value is consistent with both our observations (Villalobos et al., 2020) and for works observed in the northern section of the Liquiñe-Ofqui Fault System (Bohm et al. 2002; Lange et al. 2008). Finally, this is also consistent with the observations made by Thomson (2002) using geobarometers and fission tracks dating in apatite, giving depths for this transition zone between> 7 to 14 km for a time window of ca. 9 Ma

The three structures already named, the Punta Cola, Quitralco, and Río Cuervo faults, are a significant focus of study interest from a seismic hazard perspective. Here I focused primarily on the Punta Cola and Quitralco faults due to their conspicuous record within the sedimentary infill. Surface and subsurface submarine rupture from the 2007 M_w 6.2 dextral strike slip earthquake was directly interpreted from the observation of deformed strata in seismic profiles using a geophysical approach (Figures 3.4 – 3.6). These features also could be the resultfrom a) an earthquake with full seafloor rupture; b) an earthquake with subsurface rupture; and c) no rupture but was covered by submarine landsliding thar make it look like a rupture. In the end it was decided that the first scenario with greater slip along the northern segment of PCF, evidenced by a well-developed fault zone reaching up to the seafloor surface in the northern profiles (Figures 3.8a and 3.8b), with respect to the southern profile (Figure 3.6). A local subsidence occurred associated to a relaxation lapse generated in the transpressive structure, overimposed by submarine landsliding phenomena (i.e., Kodaira et al., 2012). This would has produced a local rotation of blocks driving an apparent amplification of the vertical offset along the escarpments, with secondary normal faulting at shallow depths.

Seismic profiles SL-05 and SL-06 (Figures 3.4 and 3.5) clearly show sediment layers disrupted by a Quitralco Fault, where a 650 m long escarpment is visible (Figure 3.3b), with a bathymetric change of ~2 m (Figure 3.3d). This escarpment is parallel to the fault trace projected into the Aysén Fjord, proposed by Vargas et al. (2013). In opposition to the statement of Wils et al. (2018), which interprets this feature as a fault scarp associated with QF actual rupture, I suggest that this escarpment does not correspond to a 2007 event fault scarp but rather to an ancient fault scarp draped by the younger sedimentary infill because the profiles SL-05 and SL-06 show the fault tip between ~17.9 and 14.6 m b.s.f. (Appendix Figures A9 and A10). With this it is proposed that the M_w 6.1 dextral-normal event that occurred during the 2007-AYSS

along the Quitralco Fault, with a partial rupture, not reaching the seafloor at the Aysén Fjord.

Meanwhile, the Río Cuervo Fault is a highly potential structure for generating a new mid to high earthquake magnitude. No surface rupture features can be associated with the 2007-AYSS along the Río Cuervo Fault according to my observations in the seismic profile data (Appendix Figures A9 and A10). Because of both the lack evidence for full ruptures (i.e., to the seafloor surface) along the Río Cuervo and also Quitralco faults in 2007 combined with the strong evidence for recurrence of strong ground motions here in the past 12 kyr as revealed from buried landslides deposits in Aysén Fjord sediments, these faults should be considered important sources of seismic hazard and require further analysis to better understand the recurrence of events and potential hazard associated with these structures.

The problem increases in complexity when taking into consideration the complex geometry of the structures in the fjord area and surroundings could generate several scenarios of earthquake events. This point born from the perspective of paleoearthquake models, and when considered from a seismic hazard perspective, it becomes more valuable. In this work, I make a call for attention and propose the generation of faulting models that consider different scenarios and how these could affect the local population. The 2007-AYSS has opened an opportunity to study seismogenic faults in Chile, where the correct detection of the current expression (Holocene) should be the seeds of future work.

Finally, in order to evaluate the seismogenic capacity of the active faults studied in this thesis, I used the empirical equations of Shaw & Suppe (1996) to link the magnitude of an earthquake (M, in moment magnitude) with a Recurrence Interval (RI, in years) and the Long-Term Slip Rate (LTS, in meters per year). This equation is made based on the empirical equation by Wells & Coppersmith (1994) that links the magnitude of an earthquake (in moment magnitude) and Average Coseismic Displacement (in meters). A table with attributes summarizes the observations and interpretations for each fault (Table 5.1). We will consider as characteristic earthquakes the events M_w 6.1 and M_w 6.2 for the Punta Cola and Río Cuervo faults, respectively, and RI values of 1,100 and 1,500 years (Villalobos et al., 2020) for both faults.

Table 5.1. The table summarizes the geometric features, seismogenic and paleoseismological characteristics of the faults studied in the Aysén Fjord area and its surroundings.

Structure	Length (km)	Down dip position (km)	Attitude of fault	Kinematic	Rupture area (km^2)	Recurrence interval (RI) (years)	Magnitude (Mw)	Magnitude (M_{max})
Punta Cola Fault	15 - 20	10	NS /80-85°W	RLR	200	1,100 - 1,500	6.2	6.4
Quitralco Fault	~70	10	NE-SW/80-90°W	RLN	700	1,100 - 1,500	6.1	6.8
Río Cuervo Fault	~100	10	NS /60-90°W	RLR	1,000	1,100 - 1,500	-----	7.0

As previously suggested, the Shaw & Suppe (1996) equation calculates/estimates the parameters mentioned above, knowing two of these. It can

also be represented through a two-dimensional graph that simplifies said relationships and generates a direct relationship with the rupture area (Appendix Figure A17). As Wells & Coppersmith (1994) equations, these depend on two constants (a & b), which are the result of empirical data fits (regressions) and which vary depending on the fault kinematics evaluated. In these cases, I use the adjustments for strike-slip faults (a_{ss}: -6.32; b_{ss}: 0.9) and the general one (a_{all}: -4.8; b_{all}: 0.69). The results obtained for the fault slip rate at a geological time scale (LTS) in this evaluation are shown in Table 5.2, highlighting mainly those for RI values of 1,100 years and with a_{all} and b_{all} that use the highest data accuracy, values recommended in the literature for this type of evaluation (Shaw & Suppe, 1996).

Table 5.2. The table shows the parameters and results obtained for two faults (Quitralco and Punta Cola faults) studied in this thesis using Shaw & Suppe (1996) equation. Regression values are for strike-slip faults and all kinematics.

Structure	M	RI_1(years)	RI_2(years)	a_{all}	b_{all}	a_{ss}	b_{ss}	LTS_{all-1}(mm/yr)	LTS_{all-2}(mm/yr)	LTS_{ss-1}(mm/yr)	LTS_{ss-2}(mm/yr)
Punta Cola Fault	6.2	1,100	1,500	-4.8	0.69	-6.32	0.9	0,539	0,396	0,434	0,318
Quitralco Fault	6.1	1,100	1,500	-4.8	0.69	-6.32	0.9	0,503	0,369	0,396	0,291

To evaluate the case of total ruptures of the lengths of the traces of the three faults studied, the relationship between the total rupture areas given a depth of 10 km was used. The latter assuming that the structures being strike-slip faults in-depth where they will verticalize at shallow depths of the crust. The results are shown in Table 5.3, highlighting the earthquake magnitude for the Río Cuervo Fault and their slip rates.

Table 5.3. The table shows the parameters and results obtained for the thre faults (Río Cuervo, Quitralco and Punta Cola faults) studied in this thesis using Shaw & Suppe (1996) equation. Regression values are for all kinematics. Earthquake Maximum Magnitude correspond to the entire theorical rupture area for each fault.

Structure	M_{max}	RI_1(years)	RI_2(years)	a_{all}	b_{all}	LTS_{all-1}(mm/yr)	LTS_{all-2}(mm/yr)
Punta Cola Fault	6.4	1,100	1,500	-4.8	0.69	0,619	0,454
Quitralco Fault	6.8	1,100	1,500	-4.8	0.69	0,816	0,598
Río Cuervo Fault	7.0	1,100	1,500	-4.8	0.69	0,937	0,687

5.2 Post-glacial activity on the LOFS and Ice-sheet retreat after the LGM

The sedimentary infill of the inner fjord is dominated in the seismic profiles by well-stratified flat laminar facies (PLU) (Figure 3.8b). Within this infill, in the deepest part of it, I interpret the presence of moraine sediments based on the detection of seismic facies with similar geometric characteristics and impedances (multicrested mound with a hummocky internal shape) seen in both fjords and lakes of Patagonia and the rest of the world (e.g., Boyd et al., 2008; Breuer et al., 2013, Fernández et al., 2017). In its entirety, the internal fjord infill has a wedge architecture thinning to the

west in PLU, which implies a substantial contribution from the Aysén River during the last deglaciation in the Patagonian Andes from 12 ka to 7 ka and the current global sea level high stand after 7 ka (Lambeck et al., 2002). The last point is relevant to our sedimentary rates estimations and hence our recurrence calculations.

Based on ages of tephras in fluvioglacial sediments and moraines around ~ 12 ka (Vargas et al., 2013) and the new maps of glacial landforms and glacial deposits together with their ages, it is possible to infer a retreat of the glaciers within that time range, which gives a maximum age to the PLU laminated sedimentary infill. Also, considering that no glaciofluvial-deformed sediment can be observed in the sedimentary infill of the Aysén Fjord from seismic imagery, it is suggested that most of the sedimentary column is postglacial in origin (Villalobos et al., 2020). Seismic facies interpreted as moraine banks (MU) are visible at ~200 m depth in the profiles. By assuming a minimum age of ~12,000 yr for the top of the MU (Figure 3.4), it is possible to infer a postglacial age for the entire stratified sediment forming the PLU overlaying the MU (Figure 3.4). The new data support my first inference providing a stronger support to the hypothesis with respect to the previous interpretation of Wils et al. (2018), who assigned an age of ~18–20 kyr for the reflectors located at ~55 m b.s.f., within the PLU, based on the overinterpreted extrapolation of sedimentation rates from surface sediment core.

Using a ~ 21 m long sediment core extracted in a pre-2007 campaign, it was possible to identify the sedimentary level that defines the change from a transgressive (when sea level rises) to a progradational sedimentation phase (when a river delta growth farther out into the sea over time). Lambeck et al. (2002, 2014) proposed this change in sedimentation rates between ~ 6 and ~ 7 ka. This ages comes from observed records restricted to ~6–7 ka, when far-field sea-level change was slow enough for the microatoll development to be able tokeep up with change.

By considering average sedimentation rates from the PLU (~25 mm/yr, between 12 and 6 kyr Cal BP; Villalobos et al., 2020), representing the transgressive phase of the sedimentary infill of the inner Aysén Fjord, I speculate that the last seven paleolandslides, with a similar sedimentary imprint that resulted from earthquakes nucleated along active faults in the area, similar to the M_w 6.2 during the 2007-AYSS. Evidence show that landslides related to the 1960 M_w 9.5 Valdivia earthquake have been superficial, restricted to soil and of relatively small volume (Wright & Mella, 1963) while landslides related to the 2007 M_w 6.2 Aysén earthquake several tens of million m^3 large deep seated and in bedrock (Oppikofer et al., 2012).

All the data previously exposed allows us to propose in the form of a first-order model that the deep seated landslides that enter Aysén Fjord should only be from large, local ruptures and not from the subduction zone (i.e., 1960-style events). From the first-order estimation model the seven paleoevents occurred close to ~8.31 ka BP to ~7.11 ka BP (MDU-07), ~6.84 ka BP to ~6.24 ka BP (MDU-06), ~5.58 ka BP to ~4.67 ka BP (MDU-05), ~4.35 ka BP (MDU-04), ~3.58 ka BP (MDU-03), ~2.65 ka BP (MDU-02), and ~1.34 ka BP (MDU-01). If the assumptions about sedimentation rates and timing are correct, these events occurred approximately every ~1.1–1.5 Ma in the Holocene epoch (Appendix Figure A12).

An interesting point to evaluate for future research is the effect of the ice sheet's load on the LOFS and its retreat. Hubbard et al. (2005), in their model, proposes thicknesses of the ice layer that vary in its central part between 1.5 to 2 km (were my study are is located), with edges close to 600 m. Assuming that 2 km of the load is equivalent to 20 MPa, which is equivalent to between 10 to 25% of the lithostatic load in the seismogenic zone of a fault (80 - 250 MPa), it affects seismic activity is expected. This load on the faults affects their velocity (slip rate) but never taking it to an inactive state, so removing this load could increase this parameter, which would also affect the magnitude of the earthquakes produced by the fault system, as well as their recurrence. This effect would be reflected by a slight decrease in accumulated and released energy over time, together with decreasing recurrence rates.

5.3 Sedimentary and geomorphological imprinting as a tool to detect tectonic processes

Orogens and their uplift tend to adjust to long-term average climatic conditions (millions of years). In contrast, factors such as erosional rates and sediment flow at scales of 10^2-10^3 years are strongly influenced by high-frequency climatic variations and seismic activity (Dadson et al., 2003). As a final section of this thesis, some points that were not directly addressed in the two main chapters will be discussed. It is essential to establish that the discussion's aim is not to achieve a definitive solution to the problem of the link between climate, erosion rates, tectonics, and uplift for the study area, or to propose whether Wedge Model (steady-state flow or quasi-steady-state) is the most indicated. Rather, it will be considered whether active faults study and the paleoseismological record within the sedimentary infill of the Patagonian Fjordland can be used as a new proxy to help us understand the long-scale processes such as Andean orogenesis during Quaternary, and mostly, what the Liquiñe-Ofqui Fault System current contribution to the morphology of the Patagonian Andes.

The link between climate change and tectonic forces generates permanent rock alterations that are reflected through rock uplift (Hilley & Strecker, 2004; Whipple & Meade, 2004; Roe et al., 2006). The most accepted models for the orogens behaviors in long periods of glaciation and exposure to extensive ice sheets (Brozović et al., 1997; Small & Anderson, 1998; Whipple et al., 1999; Brocklehurst & Whipple, 2002; Thomson, 2002; Thomson et al., 2010) have put into question the previous ideas that gave greater preponderance to climatic phenomena (Molnar & England, 1990) that trigger high erosional rates and also to the isostatic rebound factor to explain the increase in elevation relief through positive feedback, leaving aside the tectonics factor. It is worth re-emphasizing that even so, climate change has tremendous potential to alter rock deformation patterns and rates, with a possible increase in uplift rates (Brozović et al., 1997; Small & Anderson, 1998; Whipple et al., 1999; Brocklehurst & Whipple, 2002).

Glacial periods with a wide temporal and spatial distribution have taken place in the Southern Andes (e.g., Singer et al., 2004; Douglass & Bockheim, 2006; Kaplan et al., 2004; Smedley et al., 2016; Hein et al., 2010). In the North Patagonian Andes

sector, there is strong evidence of this process from ~7 to ~5 Ma (Mercer et al., 1982; Ton-That et al., 1999). A recent study by Willett et al. (2020) based on ages (U-Th) / He in apatites for granitic boulders suggests systematic changes in mountain-scale erosion rates over a ~ 6 Ma response to glacial conditions in a mid-latitude mountain range. In the first stage, a slow erosion is observed before ~ 6 Ma ago, followed by a two- to threefold increase in the spatially averaged erosion rate of the source region after the onset of alpine glaciations and a 15-fold increase. This transition is followed by a pronounced decrease in erosion rates over the past ~ 3 Ma. This period of time was theoretically predicted using response models for orogens under climate change and tectonics 1.5 to 5.5 Ma (Tomkin & Roe, 2007).

As Thomson et al. (2010) and Whipple (2009) demonstrate, the validity of any model has great difficulties due to the complex link between climate change, erosion, and tectonics. The previous factors worsen by not being able to recognize unsightly evidence (geomorphic features) in the field to constrain orogenic stages. Thomson et al. (2010), through their fission track studies in apatites, demonstrated the existence of erosional rate changes, where an acceleration began ~7 Ma ago, which coincides with the beginning of the development of glaciation in the area.

Another well-known reaction to climate cooling is the decrease in tectonic activity in the fold-and-thrust systems located on the eastern flank of the Patagonian Andes, which began during the same time interval (Thomson, 2002). It is proposed that the crustal shortening was delimited to a much-limited area of the Southern Andes, where tectonic activity ended up restricted mainly to the Liquiñe-Ofqui Fault System through its transpressive kinematics since ~ 7 Ma (Thomson, 2002).

Thomson et al. (2010) stated that the geometry, both in width and height, of the Patagonian Andes, is characterized by an erosive imprint. The Andes in the zone were mainly sharpened by the ice sheet rather than active structures, which is noticeable on its western flank by minimum ages close to the ELA position, using three fission-track profiles. These same authors also interpret the lack of faulting between ~47° S and ~49° S. While, northward of this fringe, the calculated erosion rates indicate the prolonged activity of the Liquiñe-Ofqui Fault System, being a factor important in the destruction of the Andean orogen through the reduction of both width and height. Regarding the previous point raised by Thomson et al. (2010), it is better to understand this lack of structures as an absence of evidence or documentation.

Whipple & Meade (2006) propose that for an asymmetric orogenic wedge, like the Patagonian Andes, the mass balance associated with sediment recycling (which includes parameters such as the evolution of the relief, uplift rates, and erosion) is expressed as the response time of a mountain range given by an erosional coefficient which will change (a) much more quickly to an increase in erosion efficiency, followed by (b) slightly less rapid response to a change in accretionary flow, and ultimately it will be (c) much slower to a decrease in erosion efficiency.

It is essential to consider that the balance between climate, topography, erosional rates, and tectonics can vary during the evolution of mountain ranges,

therefore, constraining different time windows associated to an erosive-sedimentary more or less constant behavior is important for the calculation of slip rates for these faults in the long term time-scale. So, variations over time will directly influence the calculation of any of the variants of interest, whether tectonic or geomorphic, so it will always be necessary to have parameters such as erosion and sedimentation rates temporarily constrained. Estimations in the Transgressive Phase, the sedimentation rates are comparable to current rates in similar glacier settings (e.g., Morehead, 2001; Syvitski & Shaw, 1995). It ranges in the fjord between ~ 8.3 and ~ 19.1 mm/yr (average of ~ 13.3 mm/yr) (Villalobos et al., 2020) for a time window between 17.3 ka (Glasser et al., 2012; Hein et al., 2010; Sugden et al. al., 2005) and 6 ka Cal BP (~7–6 kyr BP; Lambeck et al., 2002, 2014). The Progressive Phase rates range between 1.9 mm/yr (Salamanca & Jara, 2003) - 3.0 mm/yr (Van Daele et al., 2013). These values are considered medium-low sedimentation rates for fjords and inlets (Syvitski et al., 1987) but high sedimentation rates concerning tectonics. Along the Quitralco Fault, growth strata are observed near the surface, indicating a higher slip rate than the last thousands of years' deposition rates. Despite the difficulties in calculating slip-rates, Punta Cola Fault shows remarkable reflectors offsets size (Appendix Figures A12e and A12f) and allows us to propose that slip rates on this fault should also be more significant than the sedimentation rates in fjords since the last deglaciation.

Using depth-converted seismic profiles to assess vertical accumulated offsets caused by Punta Cola and Quitralco faults, using up to 28 reflectors, covering almost the entire postglacial sedimentary infill. As expected, the offset increases with depth and within the curves, and offset peaks escape this general tendency, as can be observed from the comparison of reflectors' position versus the vertical offset for each fault analyzed, and the accumulated offsets curves (Appendix Figures A12h and A12i). Considering that Punta Cola Fault activity during the 2007 Aysén Seismic Sequence generated submarine rupture associated with a medium magnitude earthquake (M_w 6.2) and other structures were activated at depth as well. It is possible to interpret the occurrence of peaks within the vertical separation curves of stratigraphic horizons as surface ruptures associated with paleo-earthquakes (Appendix Figure A12). This evidence complements well the deposits within the postglacial infill interpreted as paleo-landslides associated with events similar to the 2007-earthquake.

It is very likely that within the sedimentary record of the Aysén Fjord and the entire Patagonian Fjordland represents an essential source of information that would clarify how these factors influenced the Southern Andes orogenesis during the Late Quaternary (Pleistocene-Holocene). For this reason, an understanding of the sedimentary flow changes by calculating more bracket sedimentation rates within depositional phases is necessary as in the work carried out by Fernández et al (2011) in the area of Elefantes Gulf, as well as carrying out calculations and estimates of glacial erosion rates (Fernández et al., 2016). To solve this problem sediment cores covering most of the fjord's post-glacial deposition history is one approach. Given the depth of the fjords and channels shown in this work, strategies that maximize data recovery are necessary. The search for condensed sections is proposed together with extensive seismic imagery (and, if possible 3D seismic) that help extrapolate values laterally. At present, it is already established that based on climatic fluctuations within the Quaternary, so it is impossible to think that the orogenic wedge has been in a steady-state (Willett et al., 2020). Thus these data would be a significant contribution

within the field of orogenic modeling in its final stages of glaciation and especially post-glacial.

The detection of active faulting within the sedimentary infill and especially past earthquakes record help us to confirm seismic activity in the Liquiñe-Ofqui Fault System, through the presence of evidence of dislocations of the postglacial sedimentary fill where it is possible to distinguish different degrees of development of the damage areas, together with evidence of rupture on the surface, in addition to the presence of seismic facies interpreted as evidence of paleo-earthquakes similar to the one experienced during 2007. It also generates more questions as: a) how long this activity has been present?; b) how the load generated by the ice sheets has affected the tectonic activity of this fault system?; c) how the load generated by the ice has affected this activity?. New approaches are necessary to answer these questions, such as modeling that considers both active tectonic and geomorphological factors that use as input erosion, sedimentation and slip rates values, where the degree of influence of glacial processes on these factors is put into evaluation. These new studies must have both a regional and individual scale. Thomson et al. (2010) stated that the contribution to the construction (or destruction) of the orogen by the Liquiñe-Ofqui Fault System is limited to the north of 45° S. Based on current evidence, this point could be controversial, taking into account the mainly transpressive kinematics dominant in the NS branches, whose individual lengths, geometry as a whole, and seismogenic potential seem to be important—added to the fact that the area between 45° and 50° S (where is located the study area) is characterized by an increase in the maximum non-volcanic heights and the average heights of the Patagonian Andes, well above the LGM and current ELA. Alternatively, these elevation values could be associated with the presence of the slab window in the area associated with the triple junction, or with a combination of both phenomena named here.

As a conclusion/proposal I think that the tectonic factor could have played an essential role during the interglaciation periods and especially during the Late Quaternary. Due to climatological and geological conditions, any geomorphological evidence directly associated with faulting processes has likely been obliterated. This effect generated by the obliteration of evidence of paleo-earthquakes could generate an overestimation of the length of the recurrence periods, which in turn would imply an underestimation of the seismic hazard for a given section of the Liquiñe-Ofqui Fault System. In other words, this would imply a disadvantage in characterizing the Liquiñe Ofqui Fault System's degree of activity since the lack of a continuous record on land and underwater would denounce any attempt to calculate significant importance parameters, such as recurrence and the rate of fault slip. I propose to continue with a methodology similar to that carried out in this thesis with the primary objective of detecting and characterizing the traces of the Liquiñe-Ofqui Fault System for each fjord and channel within the currently known limit for the main guidelines that define this crustal structure. In addition to the detection of shallow paleo-earthquake deposits such as paleoturbidites and deep ones as paleo-mass removal deposits, a delimitation of sediment deposition/accumulation speeds obtained directly by sediment cores or indirectly through geometric estimates, and not forgetting a more robust model for the positioning of the Patagonian Icesheet that brackets the period to be evaluated, it would be possible to obtain input values for a physical orogenic model that links tectonic activity and glacier development on a regional scale.

Chapter 6: Conclusions and recommendations

Conclusions

The results presented in this thesis provide new insights on the interplay between the longest Andean crustal structures, the ~1,200 km long parallel margin strike-slip fault Liquiñe-Ofqui Fault System, its earthquake activity, the Late Quaternary climate changes, and the current orogenic processes. In particular, this thesis contributes to understanding better the role of this large-scale active fault system on the geomorphic imprinting (topographic features) during glacial and postglacial times.

This study focuses between ~45° and ~45.5° S of the Southern Andes: through a W-E transect (~45.5° S) where the fjordland, main mountain range, and pampa zone morphological domains were analyzed.

My research presented here focuses on the active branches of the Liquiñe-Ofqui Fault System and its records. In Chapter 4, a combined methodology was used to map seafloor morphology derived from multibeam sonar data, plus fjord basin stratigraphy from subseafloor seismic profiles. I also used the local seismicity recorded for the duration of the entire event known as the 2007 Aysén Seismic Sequence. This multidisciplinary and synergistic approach allows us for a more comprehensive assessment of structures from within the faults than using any of these methods in isolation. The seismic imagery performed in the inner part of the Aysén Fjord reveals that this fault has been active al least during postglacial times. Surface rupture features related to both the 2007 Aysén Seismic Sequence and I interpretated that in other paleo-events are standard. Seismic imagery also show the complex geometry of some structures as Punta Cola and Río Cuervo faults, both with a positive flower geometry, but much more developed in Punta Cola Fault. Meanwhile, Quitralco Fault present a subvertical geometry slithly inclined to the west in seismic lines thus highlighting its nature of normal fault. SL-05 and SL-07 profiles show a dip orientation change, where to the north it slopes to the west, while southward it is inclined to the east. This emphasize its strike-slip nature (Sylverster, 1988). Paleoearthquake sedimentary records are widely present in the fjord's sedimentary infill. Its general characterists are similar to the sedimentary deformation imprinting leave by the main earthquake in 2007 (Mw 6.3).

Also in Chapter 4, I started to approach to the problem related to the age of the seismic activity of the LOFS. Using the same techniques already referred to above allowed the identification of moraine deposits buried in the fjord, similar in geometric features to those found both west and east of the main mountain range and other fjords, channels, and Patagonia lakes. Using some seismic reflectors close to the crest of this deposit allowed me to estimate sedimentation rates. A first-order recurrence evaluation was done for events with similar ground acceleration capacities generated for nearby faults. It has become clear by previous studies the complexity of this segment of the Liquiñe-Ofqui Fault System. Here this feature is emphasized and

presented as an essential factor of seismic hazard assessment. Using geological and seismological data, this complexity is represented in a 4D seismotectonic model. To build it, it was necessary to project the faults geometries in deep-reaching depths where the brittle-ductile transition appears to be located in the study area. To achieve that goal, I plotted all the hypocenters in a 3D environment and the fault traces recognized in the Aysén Fjord and surrounded areas. After this, it was possible to associate each seismicity cluster with the three main structures recognized in the submarine sedimentary infill. Furthermore, the existence of other structures involved in this event is not ruled out either, but so far, it is difficult to determine based on strong geological evidence. The use of this type of model presents a straightforward way to understand the activation history of different structures in a tectonically complex area, as well as an opportunity for future modeling of rupture processes and, above all, the generation of seismic hazard models for crust faults. I conclude that similar events in their destructive capacity, and even greater ones, are within the seismogenic capacity of these faults. From my observations I propose that north-south striking faults, with dextral-reverse kinematics, are the most reliable in seismic hazard sources in the area. From the 4D and 3D seismotectonic and geometric model, both at crustal scale, this can be understood from the fault plane proposed dimensions and the limited activity shown by earthquake distribution in terms of area (volume), which generated the effects already known.

From the results obtained in my first research in the sedimentary infill of the Aysén Fjord, I infer that Liquiñe-Ofqui has been active during postglacial times. These results are partially consistent with what was observed by Wils et al. (2018) only for Quitralco Fault. One of the second research aims was to bracket the time-lapse represented by the postglacial sedimentary infill (addressed in both Chapters 4 and 5). Finding evidence that provides us with a time framework for these geological processes has implications, both for the study of the seismic activity of the fault system, because it allows the correct estimation of the recurrence of earthquakes, avoiding underestimations of the seismic-hazard of these structures; and for the understanding of the paleoclimatic conditions under the climatic cycles that occur in the Patagonian Andes and how could affect in the orogenic processes, which, in the second instance, could help to refine calculations of sedimentation rates within the fjords. I detected frontal and lateral moraines, as other glacial features, using remote sensing techniques (i.e., Satellite, aerial, and UAV/drone imagery) that were validated in the field through field characterisation. Specifically, UAV allowed me to detect highly eroded moraines, impossible to detect with conventional imagery and distinguish different frontal moraine stages in more detail. Seven glacial drift (moraine system) were detected in the Coyhaique River Basin. Besides this, using a stratigraphic approach to distinguish each glacial facies, it was possible to interpret most of the glacial drift following the model of Sugden & Jhon (1976). Glacial stages were defined, and glaciolacustrine (outwash) facies were used as targets for radiocarbon dating. Eight samples were taken spanning between 37.27 and 0.67 cal ka BP. The results demonstrate a broad and complex history of glacier evolution between the main Andes mountain range and the pampa zone, which could be further explored by making models of glacial advance and retreat outside the focus of this thesis. On a regional scale and only considering roughly the location of the moraines and glacial deposits identified in this research, it is observed and confirmed that the retreat of the glaciers has a concentric flow direction directed to the current location of the closest ice fields in this of the Andes (Campos de Hielo Norte). Other authors have already proposed through regional topographic studies (e.g., Hulton et al., 2002). For its part, the evidence of morphological features

directly associated with the displacement of ice bodies is scarce, and it focuses mainly on the pampas sector (Coyhaique River Basin), showing a general W-E strike direction, with some shivering degree at a detailed scale, from which the ice masses flow can be interpreted through a more little getaway and associate them directly with ancient accumulation areas (lobes) such as Artesa Coyhaique and Artesa Baguales. Said landforms (eskers and moutonnées), although not dated, can be associated and limited by the position and ages of the drift deposits (here moraine systems); Coyhaique Alto System (22.97 – 17.19 ka cal BP), El Diablo System (37.27 – 27.77 ka cal BP), and El Toro System (20.82 - 0.45 ka cal BP).

Westward, in the main mountain range domain, only one drift was located in the Emperador Guillermo – Mañihuales rives confluence. Using two radiocarbon samples gave ages between 9.89 and 0.96 cal ka BP. In the Lake Riesco zone, it was possible to identify one well preserved frontal moraine using UAV and interpret a buried moraine using seismic imagery on the lake itself. Evidence of glacial facies was challenging to found, but glaciotectonized outwash deposits are the common expression. Samples from these layers will be dated shortly. Two nearby sites located northward, in the domain of the Aysén River Basin, were described. Although they cannot be associated with a moraine system, glaciolacustrine/fluvial facies were detected with radiocarbon ages between 12.15 and 10.25 ka cal BP.

Finally, by tying the submarine and terrestrial data, I identified the glacial limits on both sides of the North Patagonian Andes. In an ~300 km long W-E transect (~45.5° S), I study seven zones to constrain the locations where frontal moraines or another linked glacial deposits could help to understand the retreat of the Patagonian Icesheet. It is important to note that this transect corresponds to the first of its kind carried out in these latitudes and provides new insights. With this new data, I could correlate with previous works further northwest (Lake Chilean District) and southeast (Buenos Aires and Pueyrredón lakes), using a guide map for the physical-geometric model Late-Quaternary Patagonian Ice sheet.

Based on the data presented and analysed in this thesis, I propose that the climatic-tectonic connection within the North Patagonian Andes is reflected in the interaction between the estimated sedimentation rates and the same action of the faults cutting the sediment column of Aysén fiord. Thus, once the glacial retreat in the final phases of the LGM caused a reduction of the ice load (and associted glacial-isostatic rebound) on the LOFS, which then perhaps led to the increase in the activity of the faults in this area. Said seismogenic activity seems to be necessary, which is reflected within the sedimentary package. When considering the sedimentation rates expected for Transgressive Phases, those associated to the glacier retreat, of the order of two orders of magnitude (e.g., ~ 13 mm/yr), which are higher in contrast with current rates (1.9 – 3.0 mm/yr) (e.g., Morehead, 2001; Syvitski & Shaw, 1995), which dominated until ~ 6 to ~ 7 ka ago (Lamebeck et al., 2002; 2014). Recent slip rate data by De Pascale et al. (2021), suggest that the main fault within the LOFS is slipping between 11.6–24.6 mm/yr, which would then suggest that major earthquakes happen here to accommodate this motion. These same observations, i.e. a potential acceleration of rates and potential moment release could be extrapolated to all the fjords, lakes, and channels of southern Chile, and the objective of future research will be to refine and increase observations and calculations that support this hypothesis.

Recommendations

Some recommendations already pointed out within this text are the following.

1. The detection of active faulting within the fjordland sedimentary infill must be a priority. Dislocations of the postglacial sedimentary is expected, and the distinction of different degrees of development of the damage areas, together with evidence of surface rupture will help to elucidate degree of activity since the lack of a continuous record on land. I propose to continue with a similar (or even improved) methodology shown in this thesis with the primary objective of detecting and characterizing the traces of the Liquiñe-Ofqui Fault System for each fjord and channel within the currently known limit for the main guidelines that define this crustal structure.

2. Detection of shallow paleo-earthquake deposits such as paleoturbidites and deep ones as paleo-mass removal deposits is also a critical point to confirm seismic activity along Liquiñe-Ofqui Fault System. Such information must be accompanied with sediment deposition/accumulation rates obtained directly by sediment cores or indirectly through geometric estimates. Searching for condensed sections is highly recommended.

3. A more robust model for the positioning of the Patagonian Icesheet that brackets the period to be evaluated must be made. This model could function as the base to obtain input values for a more complex physical orogenic model to links tectonic activity and glacier development on a regional scale. Following this idea, the effect of the ice sheet's load on the LOFS and its retreat must be considered. Faults can be affected in their velocity (slip rate) by this loads but never reaching it to an inactive state, so removing glacial ice increase this parameter, and therefore the magnitude of the earthquakes produced, as well as their recurrence.

4. As it was demonstrated in this thesis, active faulting behaviour in the Liquiñe-Ofqui Fault System is complex. This nature must be considered in the future generation of faulting models and seismic hazard scenarios that have implications for the local population.

Bibliography

Ackert, R. P., Becker, R. A., Singer, B. S., Kurz, M. D., Caffee, M. W., & Mickelson, D. M. (2008). Patagonian glacier response during the Late Glacial–Holocene transition. Science, 321(5887), 392-395. https://doi.org/10.1126/science.1157215

Adriasola, A. C., & Stöckhert, B. (2008). Cooling histories and deformation of plutonic rocks along the Liquiñe-Ofqui Fault Zone, Southern Chile (41°–42°15'S). Andean Geology, 35(1), 39–61. https://doi.org/10.4067/S071602082008000100002

Aguirre-Urreta, M. B., & Ramos, V. A. (1981). Crustáceos decápodos del Cretácico inferior de la Cuenca Austral, provincia de Santa Cruz, Argentina. Comité Sudamericano del Jurásico y Cretácico: Cuencas sedimentarias del Jurásico y Cretácico de América del Sur, 2, 599-623.

Agurto, H., Rietbrock, A., Barrientos, S., Bataille, K., & Legrand, D. (2012). Seismo-tectonic structure of the Aysén Region, Southern Chile, inferred from the 2007 M w= 6.2 Aysén earthquake sequence. Geophysical Journal International, 190(1), 116-130. https://doi.org/10.1111/j.1365-246X.2012.05507.x

Agurto-Detzel, H., Rietbrock, A., Bataille, K., Miller, M., Iwamori, H., & Priestley, K. (2014). Seismicity distribution in the vicinity of the Chile Triple Junction, Aysén Region, southern Chile. Journal of South American Earth Sciences, 51, 1-11. https://doi.org/10.1016/j.jsames.2013.12.011

Ahumada, R., & Rudolph, A. (2004). Trace metals and other constitutive components in two sediment cores from a remote glacier-fed estuarine lagoon in southern Chile. Estuarine, Coastal and Shelf Science, 59(2), 231-236. https://doi.org/10.1016/j.ecss.2003.08.012

Alparone, S., & Gambino, S. (2003). High precision locations of multiplets on south-eastern flank of Mt. Etna (Italy): Reconstruction of fault plane geometry. Physics of the Earth and Planetary Interiors, 135(4), 281–289. https://doi.org/10.1016/S0031-9201(03)00048-7

Ambraseys, N., & Jackson, J. (1984). Seismic movements (pp. 353-380). Surrey University Press, Surrey, UK.

Anastasopoulos, I., Gazetas, G., Bransby, M. F., Davies, M. C. R., & El Nahas, A. (2007). Fault rupture propagation through sand: finite-element analysis and validation through centrifuge experiments. Journal of Geotechnical and Geoenvironmental Engineering, 133(8), 943-958. https://doi.org/10.1061/(ASCE)1090-0241(2007)133:8(943)

Andersen, B., Denton, G. H., & Lowell, T. V. (1999). Glacial geomorphologic maps of Llanquihue drift in the area of the southern Lake District, Chile. Geografiska Annaler: Series A, Physical Geography, 81(2), 155-166. https://doi.org/10.1111/1468-0459.00056

Anderson, J. G., Wesnousky, S. G., & Stirling, M. W. (1996). Earthquake size as a function of fault slip rate. Bulletin of the Seismological Society of America, 86(3), 683-690.

Angermann, D., Klotz, J., & Reigber, C. (1999). Space-geodetic estimation of the Nazca-South America Euler vector. Earth and Planetary Science Letters, 171(3), 329-334. https://doi.org/10.1016/S0012-821X(99)00173-9

Antevs, E. (1928). The last glaciation: with special reference to the ice retreat in northeastern North America (No. 17). American geographical society.

Aniya, M. (1988). Glacier inventory for the Northern Patagonia Icefield, Chile, and variations 1944/45 to 1985/86. Arctic and Alpine Research, 20(2), 179-187. https://doi.org/10.1080/00040851.1988.12002663

Aniya, M., Sato, H., Naruse, R., Skvarca, P, & Casassa, G. (1996). The use of satellite and airborne imagery to inventory outlet glaciers of the Southern Patagonia Icefield, South America. Photogrammetric Engineering and Remote Sensing, 62(12), 1361-1369. https://doi.org/0099-1112I96I6212-1361$3.00/0

Araneda, A., Torrejón, F., Aguayo, M., Torres, L., Cruces, F., Cisternas, M., & Urrutia, R. (2007). Historical records of San Rafael glacier advances (North Patagonian Icefield): another clue to'Little Ice Age'timing in southern Chile?. The Holocene, 17(7), 987-998. https://doi.org/10.1177/0959683607082414

Aravena, J. C., & Luckman, B. H. (2009). Spatio-temporal rainfall patterns in southern South America. International Journal of Climatology: A Journal of the Royal Meteorological Society, 29(14), 2106-2120. https://doi.org/10.1002/joc.1761

Araya-Vergara, J. F. (1997). Geomorphological profiles of the fjords and longitudinal depression of North Patagonia. Cienc. Tecnol. Mar, 20, 3-22.

Araya-Vergara, J. F. (2011). Submarine failures in the bottom of the Aysén fjord, Northern Patagonia, Chile. Geographical Research — Santiago, Chile, 43, 17–34.

Arenas, M., Naranjo, J., Clavero, J., & Lara, L. (2008). Earth quake-induced landslides: susceptibility mapping for crisis management. In Congreso Geológico Argentino (No. 17, p. 255).

Armijo, R., Pondard, N., Meyer, B., Uçarkus, G., de Lépinay, B. M., Malavieille, J., et al. (2005). Submarine fault scarps in the Sea of Marmara pull-apart (North Anatolian Fault): Implications for seismic hazard in Istanbul. Geochemistry, Geophysics, Geosystems, 6,Q06009. https://doi.org/10.1029/2004GC000896

Arqueros, C.R. (2004). Evolución glacial de la hoya del río Coyhaique: Una aproximación a partir del análisis geomorfológico y morfoestratigráfico. Tesis de Magíster (Inédito), Universidad de Chile, Departamento de Geología, 114 p

Arrowsmith, J. R. (2006). Active tectonics, tectonic geomorphology, and fault system dynamics: How geoinformatics can help. Special Papers-Geological Society Of America, 397, 131. https://doi.org/10.1130/2006.2397(09)

Atwater, B. F., Carson, B., Griggs, G. B., Johnson, H. P., & Salmi, M. S. (2014). Rethinking turbidite paleoseismology along the Cascadia subduction zone. Geology, 42, 827–830. https://doi.org/10.1130/G35902.1

Auer, V., & Goldthwait-Väänänen, H. (1956). The Pleistocene of Fuego-Patagonia: The Ice and Interglacial Ages/by Väinö Auer;[transl. from the Fin. Helen Goldthwait-Väänänen]. Suomalainen tiedeakatemia.

Bangs, N. L., & Cande, S. C. (1997). Episodic development of a convergent margin inferred from structures and processes along the southern Chile margin. Tectonics, 16(3), 489–503. https://doi.org/10.1029/97TC00494

Barnes, P. M. (2009). Postglacial (after 20 ka) dextral slip rate of the offshore Alpine fault, New Zealand. Geology, 37, 3–6. https://doi.org/10.1130/G24764A.1

Barnes, P. M., & Pondard, N. (2010). Derivation of direct on-fault submarine paleoearthquake records from high-resolution seismic reflection profiles: Wairau Fault, New Zealand. Geochemistry, Geophysics, Geosystems, 11(11). https://doi.org/10.1029/2010GC003254

Barnes, P. M., Bostock, H. C., Neil, H. L., Strachan, L. J., & Gosling, M. (2013). A 2300-year paleoearthquake record of the Southern Alpine Fault and Fiordland Subduction Zone, New Zealand, based on stacked turbidites. Bulletin of the Seismological Society of America, 103, 2424–2446. https://doi.org/10.1785/0120120314

Barnes, P. M., Sutherland, R., & Delteil, J. (2005). Strike-slip structure and sedimentary basins of the southern Alpine Fault, Fiordland, New Zealand. Geological Society of America Bulletin, 117, 411. https://doi.org/10.1130/b25458.1

Barrientos, S. E., & Acevedo-Aránguiz, P. S. (1992). Seismological aspects of the 1988–1989 Lonquimay (Chile) volcanic eruption. Journal of Volcanology and Geothermal Research, 53, 73–87. https://doi.org/10.1016/0377-0273(92)90075-O

Barrientos, S. E., & Ward, S. N. (1990). The 1960 Chile earthquake: inversion for slip distribution from surface deformation. Geophysical Journal International, 103(3), 589-598. https://doi.org/10.1111/j.1365-246X.1990.tb05673.x

Barrientos, S., Bataille, K., Aranda, C., Legrand, D., Baez, J. C., Agurto, H., et al. (2007). Complex sequence of earthquakes in Fiorland, Southern Chile. Paper presented at Geosur 2007, International Geological Congress on the Southern Hemisphere, Santiago, Chile.

Bartholomew, D. S. (1984). Geology and geochemistry of the Patagonian batholith (45°; 46° S), Chile, (Doctoral dissertation). Retrieved from Ethos (https://ethos.bl.uk/OrderDetails.do?uin=uk.bl.ethos.304782). Location: University of Leiceter.

Beavan, J., Motagh, M., Fielding, E. J., Donnelly, N., & Collett, D. (2012). Fault slip models of the 2010–2011 Canterbury, New Zealand, earthquakes from geodetic data and observations of postseismic ground deformation. New Zealand Journal of Geology and Geophysics, 55, 207–221. https://doi.org/10.1080/00288306.2012.697472

Beck, C., Mercier de Lépinay, B., Schneider, J. L., Cremer, M., Çağatay, N., Wendenbaum, E., et al. (2007). Late Quaternary co-seismic sedimentation in the Sea of Marmara's deep basins. Sedimentary Geology, 199, 65–89. https://doi.org/10.1016/j.sedgeo.2005.12.031

Beck, C., Reyss, J.-L., Leclerc, F., Moreno, E., Feuillet, N., Barrier, L., Beauducel, F., Boudon, G., Clément, V., Deplus, C., Gallou, N., Lebrun, J.-F., Le Friant, A., Nercessian, A., Paterne, M., Pichot, T., and Vidal, C. (2012). Identification of deep subaqueous co-seismic scarps through specific coeval sedimentation in Lesser Antilles: implication for seismic hazard. Nat. Hazards Earth Syst. Sci., 12, 1755–1767. https://doi.org/10.5194/nhess-12-1755-2012

Beck Jr, M. E. (1988). Analysis of Late Jurassic-Recent paleomagnetic data from active plate margins of South America. Journal of South American Earth Sciences, 1(1), 39-52. https://doi.org/10.1016/0895-9811(88)90014-4

Beck Jr, M. E., Rojas, C., & Cembrano, J. (1993). On the nature of buttressing in margin-parallel strike-slip fault systems. Geology, 21(8), 755-758. https://doi.org/10.1130/0091-7613(1993)021<0755:OTNOBI>2.3.CO;2

Beck, S., Barrientos, S., Kausel, E., & Reyes, M. (1998). Source characteristics of historic earthquakes along the central Chile subduction Askew et Alzone. Journal of South American Earth Sciences, 11(2), 115-129. https://doi.org/10.1016/S0895-9811(98)00005-4

Becken, M., Ritter, O., & Burkhardt, H. (2008). Mode separation of magnetotelluric responses in three-dimensional environments. Geophysical Journal International, 172(1), 67-86. https://doi.org/10.1111/j.1365-246X.2007.03612.x

Bedrosian, P. A., Unsworth, M. J., & Egbert, G. (2002). Magnetotelluric imaging of the creeping segment of the San Andreas Fault near Hollister. Geophysical Research Letters, 29(11), 1-1. https://doi.org/10.1029/2001GL014119

Belknap, D. F., & Shipp, R. C. (1991). Seismic stratigraphy of glacial marine units, Maine inner shelf. In J. B. Anderson, & G. M. Ashley (Eds.), Glacial marine sedimentation; paleoclimatic significance (Vol. 261, 1st ed., pp. 137–157). Boulder, CO: Geological Society of America. https://doi.org/10.1130/SPE261-p137

Bellier, O., & Sébrier, M. (1994). Relationship between tectonism and volcanism along the Great Sumatran fault zone deduced by SPOT image analyses. Tectonophysics, 233, 215–231. https://doi.org/10.1016/0040-1951(94)90242-9

Beltramone, C. (1991). Estratigrafia glacial del valle de Rio Mayo, provincia de Chubut, Argentina. In Congreso geologico chileno. 6 (pp. 58-61).

Bendle, J. M., Thorndycraft, V. R., & Palmer, A. P. (2017). The glacial geomorphology of the Lago Buenos Aires and Lago Pueyrredón ice lobes of central Patagonia. Journal of Maps, 13(2), 654-673. https://doi.org/10.1080/17445647.2017.1351908

Bertrand, S., Hughen, K., Lamy, F., Stuut, J. B., Torejon, F., & Lange, C. (2012). Precipitation as the main driver of Neoglacial fluctuations of Gualas glacier, Northern Patagonian Icefield. Climate of the Past, 8, 1-16. https://doi.org/10.5194/cp-8-1-2012

Besana, G. M., & Ando, M. (2005). The central Philippine fault zone: Location of great earthquakes, slow events and creep activity. Earth, planets and space, 57(10), 987-994. https://doi.org/10.1186/BF03351877

Biggs, J., Robinson, D. P., & Dixon, T. H. (2009). The 2007 Pisco, Peru, earthquake (M 8.0): seismology and geodesy. Geophysical Journal International, 176(3), 657-669. https://doi.org/10.1111/j.1365-246X.2008.03990.x

Blaauw, M., Heuvelink, G. B., Mauquoy, D., van der Plicht, J., & van Geel, B. (2003). A numerical approach to 14C wiggle-match dating of organic deposits: best fits and confidence intervals. Quaternary Science Reviews, 22(14), 1485-1500. https://doi.org/10.1016/S0277-3791(03)00086-6

Blaauw, M., Van Geel, B., Mauquoy, D., & Van Der Plicht, J. (2004). Carbon-14 wiggle-match dating of peat deposits: advantages and limitations. Journal of Quaternary Science, 19(2), 177-181. https://doi.org/10.1002/jqs.810

Boex, J., Fogwill, C., Harrison, S., Glasser, N. F., Hein, A., Schnabel, C., & Xu, S. (2013). Rapid thinning of the late Pleistocene Patagonian Ice Sheet followed migration of the Southern Westerlies. Scientific Reports, 3, 2118. https://doi.org/10.1038/srep02118

Bohm, M., Lüth, S., Echtler, H., Asch, G., Bataille, K., Bruhn, C., ... & Wigger, P. (2002). The Southern Andes between 36 and 40 S latitude: seismicity and average seismic velocities. Tectonophysics, 356(4), 275-289. https://doi.org/10.1016/S0040-1951(02)00399-2

Bonilla, B. M. P. MG, 1970, Surface faulting and related effects, Chap. 3 in Wiegel, RL, ed. Earthquake Engineering: Englewood Cliffs,.. NJ, Prentice-Hall, 47-74.

Bonilla, M. G., Mark, R. K., & Lienkaemper, J. J. (1984). Statistical relations among earthquake magnitude, surface rupture length, and surface fault displacement. Bulletin of the Seismological Society of America, 74(6), 2379-2411.

Borgel, R. (1970). Geomorfología de las regiones australes de Chile. Revista Geológica de Chile, 21, 135-140. http://bibliotecadigital.ciren.cl/handle/123456789/22031

Boyd, B. L., Anderson, J. B., Wellner, J. S., & Fernández, R. A. (2008). The sedimentary record of glacial retreat, Marinelli Fjord, Patagonia: Regional correlations and climate ties. Marine Geology, 255, 165–178. https://doi.org/10.1016/j.margeo.2008.09.001

Bowman, S. (1990). Radiocarbon dating (Vol. 1). Univ of California Press.

Bray, J. D., Seed, R. B., Cluff, L. S., & Seed, H. B. (1994). Earthquake fault rupture propagation through soil. Journal of Geotechnical Engineering, 120(3), 543-561. https://doi.org/10.1061/(ASCE)0733-9410(1994)120:3(543)

Breuer, S., Kilian, R., Schörner, D., Weinrebe, W., Behrmann, J., & Baeza, O. (2013). Glacial and tectonic control on fjord morphology and sediment deposition in the Magellan region (53° S), Chile. Marine Geology, 346, 31-46. https://doi.org/10.1016/j.margeo.2013.07.015

Brocklehurst, S. H., & Whipple, K. X. (2002). Glacial erosion and relief production in the Eastern Sierra Nevada, California. Geomorphology, 42(1-2), 1-24. https://doi.org/10.1016/S0169-555X(01)00069-1

Brozović, N., Burbank, D. W., & Meigs, A. J. (1997). Climatic limits on landscape development in the northwestern Himalaya. Science, 276(5312), 571-574. https://doi.org/10.1126/science.276.5312.571

Burbank, D. W. (2002). Rates of erosion and their implications for exhumation. Mineralogical Magazine, 66(1), 25-52. https://doi.org/10.1180/0026461026610014

Caldenius, C. C. Z. (1932). Las Glaciaciones Cuaternarias en la Patagonia y Tierra del Fuego: Una investigación regional, estratigráfica y geocronológica.—Una comparación con la escala geocronológica sueca. Geografiska Annaler, 14(1-2), 1-164.

Cameron, W. M., & Pritchard, D. W. (1963). Estuaries In: MN Hill (editor): The Sea John Wiley and Sons. New York, 2, 306-324.

Campos, J., Hatzfeld, D., Madariaga, R., Lopez, G., Kausel, E., Zollo, A., ... & Lyon-Caen, H. (2002). A seismological study of the 1835 seismic gap in south-central Chile. Physics of the Earth and Planetary Interiors, 132(1-3), 177-195. https://doi.org/10.1016/S0031-9201(02)00051-1

Cande, S. C., & Leslie, R. B. (1986). Late Cenozoic tectonics of the southern Chile trench. Journal of Geophysical Research: Solid Earth, 91(B1), 471-496. https://doi.org/10.1029/JB091iB01p00471

Cande, S.C., Leslie, R.B., Parra, J.C., & Hobart, M. (1987). Interaction between Chile ridge and Chile trench: Geophysical and geothermal evidence. Journal of Geophysical Research, 92, 495–520. https://doi.org/10.1029/JB092iB01p00495

Castagnoli, G., & Lal, D. (1980). Solar modulation effects in terrestrial production of carbon-14. Radiocarbon, 22(2), 133-158. https://doi.org/10.1017/S0033822200009413

Cattaneo, A., Babonneau, N., Ratzov, G., Dan-Unterseh, G., Yelles, K., Bracène, R., Mercier de Lépinay, B., Boudiaf, A., and Déverchère, J. (2012). Searching for the seafloor signature of the 21 May 2003 Boumerdès earthquake offshore central Algeria, Nat. Hazards Earth Syst. Sci., 12, 2159–2172, https://doi.org/10.5194/nhess-12-2159-2012

Cembrano J., & Hervé F. (1993). The Liquine Ofqui fault zone: a major cenozoic strike slip duplex in the Southern Andes. In Andean geodynamics: extended abstracts. Paris: ORSTOM, 175-178. (Colloques et Séminaires). Géodynamique Andine, Symposium International, 2, Oxford (GBR), 1993/09/21-23. ISBN 2-7099-1154-X

Cembrano, J., & Moreno, H. (1994). Geometría y naturaleza contrastante del volcanismo Cuaternario entre los 38° S y 46° S. Dominios compresionales y tensionales en un régimen transcurrente. In Congreso Geológico Chileno (Vol. 7, pp. 240-244).

Cembrano, J., & Lara, L. (2009). The link between volcanism and tectonics in the southern volcanic zone of the Chilean Andes: a review. Tectonophysics, 471(1-2), 96-113. https://doi.org/10.1016/j.tecto.2009.02.038

Cembrano, J., Hervé, F., & Lavenu, A. (1996a). The Liquiñe Ofqui fault zone: a long-lived intra-arc fault system in southern Chile. Tectonophysics, 259(1-3), 55-66. https://doi.org/10.1016/0040-1951(95)00066-6

Cembrano J., Schermer E., Lavenu, A., Hervé F., Barrientos S., McClelland B., & Arancibia G. (1996b). Nature and timing of Cenozoic intra-arc deformation, southern Chile. In Andean geodynamics: extended abstracts. Paris : ORSTOM, 311-314. (Colloques et Séminaires). ISAG 96: Symposium International sur la Géodynamique Andine, 3, Saint-Malo (FRA), 1996/09/17-19. ISBN 2-7099-1332-1

Cembrano, J., Lavenu, A., Arancibia, G., López, G., & Sanhueza, A. (1999). Crustal-scale pop-up structure at the southern Andes plate boundary zone: A kinematic response to Pliocene transpression. Paris (FRA); Göttingen: IRD; Georg August Universität, 1999, p. 151-154.

Cembrano, J., Schermer, E., Lavenu, A., & Sanhueza, A. (2000). Contrasting nature of deformation along an intra-arc shear zone, the Liquiñe–Ofqui fault zone, southern Chilean Andes. Tectonophysics, 319(2), 129-149. https://doi.org/10.1016/S0040-1951(99)00321-2

Cembrano, J., Lavenu, A., Reynolds, P., Arancibia, G., López, G., & Sanhueza, A. (2002). Late Cenozoic transpressional ductile deformation north of the Nazca–South America–Antarctica triple junction. Tectonophysics, 354(3-4), 289-314. https://doi.org/10.1016/S0040-1951(02)00388-8

Cembrano, J., Lara, L., Lavenu, A., & Hervé, F. (2007a, October). Long-term and short-term kinematic history of the Liquiñe Ofqui fault zone, southern Chile: a review and implications for geologic hazard assessment. In Proceedings Geological Society of América Annual Meeting.

Cembrano, J., Lavenu, A., Yañez, G., Riquelme, R., García, M., González, G., & Hérail, G. (2007b). Neotectonics. The geology of Chile, 231-261.

Chandler, B. M., Evans, D. J., Roberts, D. H., Ewertowski, M., & Clayton, A. I. (2016). Glacial geomorphology of the Skálafellsjökull foreland, Iceland: A case study of 'annual' moraines. Journal of Maps, 12(5), 904-916. https://doi.org/10.1080/17445647.2015.1096216

Chinn, D. S., & Isacks, B. L. (1983). Accurate source depths and focal mechanisms of shallow earthquakes in western South America and in the New Hebrides island arc. Tectonics, 2(6), 529-563. https://doi.org/10.1029/TC002i006p00529

Chinnery, M. A. (1969). Earthquake magnitude and source parameters. Bulletin of the Seismological Society of America, 59(5), 1969-1982.

Christen, J. A., & Litton, C. D. (1995). A Bayesian approach to wiggle-matching. Journal of Archaeological Science, 22(6), 719-725. https://doi.org/10.1016/0305-4403(95)90002-0

Cifuentes, I. L. (1989). The 1960 Chilean earthquakes. Journal of Geophysical Research: Solid Earth, 94(B1), 665-680. https://doi.org/10.1029/JB094iB01p00665

Cifuentes, I. L., & Silver, P. G. (1989). Low-frequency source characteristics of the great 1960 Chilean earthquake. Journal of Geophysical Research: Solid Earth, 94(B1), 643-663. https://doi.org/10.1029/JB094iB01p00643

Cisternas, M., Atwater, B. F., Torrejón, F., Sawai, Y., Machuca, G., Lagos, M., ... & Husni, M. (2005). Predecessors of the giant 1960 Chile earthquake. Nature, 437(7057), 404-407. https://doi.org/10.1038/nature03943

Cisternas, M., Garrett, E., Wesson, R., Dura, T., & Ely, L. L. (2017a). Unusual geologic evidence of coeval seismic shaking and tsunamis shows variability in earthquake size and recurrence in the area of the giant 1960 Chile earthquake. Marine Geology, 385, 101-113.

Cisternas, M., Carvajal, M., Wesson, R., Ely, L. L., & Gorigoitia, N. (2017b). Exploring the Historical Earthquakes Preceding the Giant 1960 Chile Earthquake in a Time-Dependent Seismogenic Zone Exploring the Historical Earthquakes Preceding the Giant 1960 Chile Earthquake. Bulletin of the Seismological Society of America, 107(6), 2664-2675.

Clapperton, C. M. (1990). Quaternary glaciations in the Southern Hemisphere: an overview. Quaternary Science Reviews, 9(2-3), 299-304. https://doi.org/10.1016/0277-3791(90)90024-5

Clapperton, C. M. (1993). Nature of environmental changes in South America at the Last Glacial Maximum. Palaeogeography, palaeoclimatology, palaeoecology, 101(3-4), 189-208. https://doi.org/10.1016/0031-0182(93)90012-8

Clapperton, C. M. (1994). The quaternary glaciation of Chile: a review. Revista Chilena de Historia Natural, 67(4), 369-383.

Cole Jr, D. A., & Lade, P. V. (1984). Influence zones in alluvium over dip-slip faults. Journal of Geotechnical Engineering, 110(5), 599-615. https://doi.org/10.1061/(ASCE)0733-9410(1984)110:5(599)

Comte, D., & Pardo, M. (1991). Reappraisal of great historical earthquakes in the northern Chile and southern Peru seismic gaps. Natural hazards, 4(1), 23-44. https://doi.org/10.1007/BF00126557

Comte, D., Gallego, A., Russo, R., Mocanu, V., Murdie, R., & VanDecar, J. (2007). The Aysen (Southern Chile) 2007 seismic swarm: volcanic or tectonic origin?. AGUSM, 2007, S43C-04.

Cormier, M. H., Seeber, L., McHugh, C. M. G., Polonia, A., Çagatay, N., Emre, Ö., et al. (2006). North Anatolian Fault in the Gulf of Izmit (Turkey): Rapid vertical motion in response to minor bends of a nonvertical continental transform. Journal of Geophysical Research, 111, B04102. https://doi.org/10.1029/2005JB003633

Covacevich, V., De la Cruz, R., & Suárez, M. (1994). Primer hallazgo de fauna del Berriasiano inferior (Neocomiano) en la Formación Ibanez, Region XI, Aisén. In Congreso Geológico Chileno (No. 7, pp. 425-429).

Dadson, S. J., Hovius, N., Chen, H., Dade, W. B., Hsieh, M. L., Willett, S. D., ... & Lague, D. (2003). Links between erosion, runoff variability and seismicity in the Taiwan orogen. Nature, 426(6967), 648-651. https://doi.org/10.1038/nature02150

Das, S., & Scholz, C. H. (1983). Why large earthquakes do not nucleate at shallow depths. Nature, 305(5935), 621–623. https://doi.org/10.1038/305621a0

DaSilva, J. L., Anderson, J. B., & Stravers, J. (1997). Seismic facies changes along a nearly continuous 24 latitudinal transect: The fjords of Chile and the northern Antarctic Peninsula. Marine Geology, 143, 103–123. https://doi.org/10.1016/S0025-3227(97)00092-3

Davies, B. J., Glasser, N. F. (2012). Accelerating shrinkage of Patagonian glaciers from the Little Ice Age (similar to AD 1870) to 2011. Journal of Glaciology, 58 (212), 1063-1084. https://doi.org/10.3189/2012JoG12J026

Davies, B. J., Darvill, C. M., Lovell, H., Bendle, J. M., Dowdeswell, J. A., Fabel, D., ... & Thorndycraft, V. R. (2020). The evolution of the Patagonian Ice Sheet from 35 ka to the present day (PATICE). Earth-Science Reviews, 103152. https://doi.org/10.1016/j.earscirev.2020.103152

DeMets, C., Gordon, R. G., & Argus, D. F. (2010). Geologically current plate motions. Geophysical Journal International, 181(1), 1-80. https://doi.org/10.1111/j.1365-246X.2009.04491.x

De la Cruz, R. (2004). Geología del área oriental de las hojas Cochrane y Villa O'Higgins: región Aisén del general Carlos Ibáñez del Campo. Servicio nacional de Geología y Minería.

De Pascale, G. P., & Langridge, R. M. (2012). New on-fault evidence for a great earthquake in A.D. 1717, central alpine fault, New Zealand. Geology, 40, 791–794. https://doi.org/10.1130/G33363.1

De Pascale, G.P., Froude, M., Penna, I. et al. (2021). Liquiñe-Ofqui's fast slipping intra-volcanic arc crustal faulting above the subducted Chile Ridge. Sci Rep 11, 7069. https://doi.org/10.1038/s41598-021-86413-w

De Porras, M. E., Maldonado, A., Abarzúa, A. M., Cárdenas, M. L., Francois, J. P., Martel-Cea, A., ... & Reyes, O. (2012). Postglacial vegetation, fire and climate dynamics at Central Chilean Patagonia (Lake Shaman, 44 S). Quaternary Science Reviews, 50, 71-85. https://doi.org/10.1016/j.quascirev.2012.06.015

De Porras, M. E., Maldonado, A., Quintana, F. A., Martel Cea, A., Reyes, O., & Méndez Melgar, C. (2014). Environmental and climatic changes in central Chilean Patagonia since the late Glacial (Mallín El Embudo, 44° S). https://doi.org/10.5194/cp-10-1063-2014

De Saint Blanquat, M., Tikoff, B., Teyssier, C., & Vigneresse, J. L. (1998). Transpressional kinematics and magmatic arcs. Geological Society, London, Special Publications, 135, 327–340. https://doi.org/10.1144/GSL.SP.1998.135.01.21

Denton, G. H., Lowell, T. V., Heusser, C. J., Schlüchter, C., Andersen, B. G., Heusser, L. E., ... & Marchant, D. R. (1999). Geomorphology, stratigraphy, and radiocarbon chronology of Llanquihue Drift in the area of the Southern Lake District, Seno Reloncaví, and Isla Grande de Chiloé, Chile. Geografiska Annaler: Series A, Physical Geography, 81(2), 167-229. https://doi.org/10.1111/1468-0459.00057

Dewey, J. F., & Lamb, S. H. (1992). Active tectonics of the Andes. Tectonophysics, 205(1-3), 79-95. https://doi.org/10.1016/0040-1951(92)90419-7

Diemer, J. A., Forsythe, R. D., Engelhardt, D., & Porter, C. (1997). An Early Cretaceous forearc basin in the Golfo de Penas region, southern Chile. Journal of the Geological Society, 154(6), 925-928. https://doi.org/10.1144/gsjgs.154.6.0925

Douglass, D. C., Bockheim, J. G. (2006). Soil-forming rates and processes on Quaternary moraines near Lago Buenos Aires, Argentina. Quaternary Research, 65(2), 293-307. https://doi.org/10.1016/j.yqres.2005.08.027

Douglass, D. C., Bockheim, J. G., Singer, B. S., Kaplan, M. R., & Mickelson, D. (2001, November). One million years of soil development in Patagonia: preliminary results from Lago Buenos Aires, Argentina (46° S). In Annual Meeting of the Geological Society of America, November 5–8, 2001, Boston, Massachusetts, Paper No. 106-0.

Douglass, D. C., Kaplan, M. R., Singer, B. S., & Mickelson, D. M. (2002). A low gradient outlet glacier of the Patagonian Ice Cap at Lago Buenos Aires: Argentina, during the Last Glacial Maximum. Geological Society of America, Abstracts whit Programs, 34(s6).

Douglass, D. C., Singer, B. S., Kaplan, M. R., Mickelson, D. M., & Caffee, M. W. (2006). Cosmogenic nuclide surface exposure dating of boulders on last-glacial and late-glacial moraines, Lago Buenos Aires, Argentina: interpretive strategies and paleoclimate implications. Quaternary Geochronology, 1(1), 43-58. https://doi.org/10.1016/j.quageo.2006.06.001

Dowdeswell, J. A., & Vásquez, M. (2013). Submarine landforms in the fjords of southern Chile: implications for glacimarine processes and sedimentation in a mild glacier-influenced environment. Quaternary Science Reviews, 64, 1-19. https://doi.org/10.1016/j.quascirev.2012.12.003

Dowdeswell, J. A., Dowdeswell, E. K., Rodrigo, C., & Diaz, J. (2016). Assemblage of glacial and related landforms in the fjords of southern Chile. Geological Society, London, Memoirs, 46(1), 131-134. https://doi.org/10.1144/M46.139

Dowrick, D. J., & Rhoades, D. A. (2004). Relations between earthquake magnitude and fault rupture dimensions: How regionally variable are they?. Bulletin of the Seismological Society of America, 94(3), 776-788. https://doi.org/10.1785/0120030151

Duda, S. J. (1963). Strain release in the circum-Pacific belt, Chile: 1960. Journal of Geophysical Research, 68(19), 5531-5544. https://doi.org/10.1029/JZ068i019p05531

Dunbar, P. K., Lockridge, P. A., & Whiteside, L. S. (1992). Catalog of Significant Earthquakes, 2150 BC-1991 AD: Including Quantitative Casualties and Damage. US Department of Commerce, National Oceanic and Atmospheric

Administration, Environmental Data and Information Service, National Geophysical Data Center.

Dziewonski, A. M., Ekström, G., Woodhouse, J. H., & Zwart, G. (1990). Centroid-moment tensor solutions for April-June 1989. Physics of the earth and planetary interiors, 60, 243-253. https://doi.org/10.1016/0031-9201(90)90265-Y

Dziewonski, A. M., Ekström, G., & Salganik, M. P. (1995). Centroid-moment tensor solutions for October–December 1994. Physics of the Earth and Planetary Interiors, 91(4), 187-201. https://doi.org/10.1016/0031-9201(95)03081-7

Dziewonski, A. M., Ekström, G., & Maternovskaya, N. N. (1999). Centroid-moment tensor solutions for July–September, 1998. Physics of the earth and planetary interiors, 114(3-4), 99-107. https://doi.org/10.1016/S0031-9201(99)00057-6

D'Orazio, M., Innocenti, F., Manetti, P., Tamponi, M., Tonarini, S., González-Ferrán, O., ... & Omarini, R. (2003). The Quaternary calc-alkaline volcanism of the Patagonian Andes close to the Chile triple junction: geochemistry and petrogenesis of volcanic rocks from the Cay and Maca volcanoes (~ 45 S, Chile). Journal of South American Earth Sciences, 16(4), 219-242. https://doi.org/10.1016/S0895-9811(03)00063-4

Edwards, M. (1986). Glacial environments. Sedimentary environments and facies, 445-470.

Ely, J. C., Graham, C., Barr, I. D., Rea, B. R., Spagnolo, M., & Evans, J. (2017). Using UAV acquired photography and structure from motion techniques for studying glacier landforms: application to the glacial flutes at Isfallsglaciären. Earth Surface Processes and Landforms, 42(6), 877-888. https://doi.org/10.1002/esp.4044

Erlenkeuser, H., & Berger, R. (1979). A thermal diffusion plant for radiocarbon isotope enrichment from natural samples. In Radiocarbon Dating: Proceedings of the Ninth International Conference, Los Angeles and La Jolla, 1976 (p. 216). Univ of California Press.

Escartín, J., Leclerc, F., Olive, J. A., Mevel, C., Cannat, M., Petersen, S., ... & Bonnemains, D. (2016). First direct observation of coseismic slip and seafloor rupture along a submarine normal fault and implications for fault slip history. Earth and Planetary Science Letters, 450, 96-107. https://doi.org/10.1016/j.epsl.2016.06.024

Espinoza, W., & Fuenzalida, P. (1971). Geología de las Hojas Isla Rivero, Puerto Aysén y Balmaceda entre los paralelos 45 y 46 de latitud sur. Instituto de Investigaciones Geológicas Convenio Instituto CORFO Aysén, 50.

Evans, D. J., Ewertowski, M., Jamieson, S. S., & Orton, C. (2016). Surficial geology and geomorphology of the Kumtor Gold Mine, Kyrgyzstan: human impacts on mountain glacier landsystems. Journal of Maps, 12(5), 757-769. https://doi.org/10.1080/17445647.2015.1071720

Eyles, N., Eyles, C. H., & Miall, A. D. (1983). Lithofacies types and vertical profile models; an alternative approach to the description and environmental interpretation of glacial diamict and diamictite sequences. Sedimentology, 30(3), 393-410. https://doi.org/10.1111/j.1365-3091.1983.tb00679.x

Farías, M., Vargas, G., Tassara, A., Carretier, S., Baize, S., Melnick, D., & Bataille, K. (2010). Land-level changes produced by the Mw 8.8 2010 Chilean earthquake. Science, 329(5994), 916-916. https://doi.org/10.1126/science.1192094

Fernández, R., Anderson, J., Bertrand, S., & Wellner, J. (2012). Gualas Glacier sedimentary record of climate and environmental change, Golfo Elefantes, Western Patagonia (46.5 S). The Holocene, 22(4), 451-463. https://doi.org/10.1177/0959683611425545

Fernández, R., Gulick, S., Rodrigo, C., Domack, E., & Leventer, A. (2017). Seismic stratigraphy and glacial cycles in the inland passages of the Magallanes región of Chile, southernmost South America. Marine Geology, 386, 19-31. https://doi.org/10.1016/j.margeo.2017.02.006

Feruglio, E. (1944). Estudios geologicos y glaciologicos en la region del Lago Argentino (Patagonia):(Expedición Alberto M. De Agostini 1930-31) (Vol. 37, No. 1).

Feruglio, E. (1949). Descripción geológica de la Patagonia (Vol. 3). Casa Editora" Coni".

Folguera, A., Ramos, V. A., Hermanns, R. L., & Naranjo, J. (2004). Neotectonics in the foothills of the southernmost central Andes (37–38 S): Evidence of strike-slip displacement along the Antiñir-Copahue fault zone. Tectonics, 23(5). https://doi.org/10.1029/2003TC00153

Fonstad, M. A., Dietrich, J. T., Courville, B. C., Jensen, J. L., & Carbonneau, P. E. (2013). Topographic structure from motion: a new development in

photogrammetric measurement. Earth surface processes and Landforms, 38(4), 421-430. https://doi.org/10.1002/esp.3366

Forsythe, R., & Nelson, E. (1985). Geological manifestations of ridge collision: Evidence from the Golfo de Penas-Taitao Basin, southern Chile. Tectonics, 4(5), 477-495. https://doi.org/10.1029/TC004i005p00477

Forsythe, R. & Prior, D.J. (1992). Cenozoic continental geology of South America and its relations to the evolution of the Chile Triple Junction. In Proceedings of the Ocean Drilling Program, Initial Reports (Vol. 141, pp. 23-31). Ocean Drilling Program.

Forsythe, R. D., Nelson, E. P., Carr, M. J., Kaeding, M. E., Herve, M., Mpodozis, C., ... & Harambour, S. (1986). Pliocene near-trench magmatism in southern Chile: A possible manifestation of ridge collision. Geology, 14(1), 23-27. https://doi.org/10.1130/0091-7613(1986)14<23:PNMISC>2.0.CO;2

Friedman, G. M., & Sanders, J. E. (1978). Principles of sedimentology. Wiley.

Fletcher, J. M., Teran, O. J., Rockwell, T. K., Oskin, M. E., Hudnut, K. W., Mueller, K. J., et al. (2014). Assembly of a large earthquake from a complex fault system: Surface rupture kinematics of the 4 April 2010 El Mayor-Cucapah (Mexico) Mw 7.2 earthquake. Geosphere, 10, 797–827. https://doi.org/10.1130/ges00933.1

Flint, R. F., & Fidalgo, F. (1964). Glacial geology of the East flank of the Argentine Andes between Latitude 39 10′ S. and Latitude 41 20′ S. Geological Society of America Bulletin, 75(4), 335-352. https://doi.org/10.1130/0016-7606(1964)75[335:GGOTEF]2.0.CO;2

Flint, R. F., & Fidalgo, F. (1969). Glacial drift in the eastern Argentine Andes between latitude 41 10'S. and latitude 43 10'S. Geological Society of America Bulletin, 80(6), 1043-1052. https://doi.org/10.1130/0016-7606(1969)80[1043:GDITEA]2.0.CO;2

Garreaud, R., Lopez, P., Minvielle, M., & Rojas, M. (2013). Large-scale control on the Patagonian climate. Journal of Climate, 26(1), 215-230. https://doi.org/10.1175/JCLI-D-12-00001.1

Geersen, J., Völker, D., Behrmann, J. H., Kläschen, D., Weinrebe, W., Krastel, S., & Reichert, C. (2013). Seismic rupture during the 1960 Great Chile and the 2010 Maule earthquakes limited by a giant Pleistocene submarine slope failure. Terra Nova, 25(6), 472-477. https://doi.org/10.1111/ter.12060

Geller, R. J. (1976). Scaling relations for earthquake source parameters and magnitudes. Bulletin of the Seismological Society of America, 66(5), 1501-1523.

Geyh, M. A. (1965). Proportional counter equipment for sample dating with ages exceeding 60,000 yr BP without enrichment. In Proceedings of Radiocarbon and Tritium Dating (pp. 29-36). Pulman Washington.

Gilbert, G. K. (1884). A theory of the earthquakes of the Great Basin, with a practical application: American Journal of Science, Third Series, v.

Glasser, N. F., & Jansson, K. N. (2005). Fast-flowing outlet glaciers of the last glacial maximum Patagonian Icefield. Quaternary Research, 63(2), 206-211. https://doi.org/10.1016/j.yqres.2004.11.002

Glasser, N. F., Jansson, K. N., Harrison, S., & Kleman, J. (2008). The glacial geomorphology and Pleistocene history of South America between 38 S and 56 S. Quaternary Science Reviews, 27(3-4), 365-390. https://doi.org/10.1016/j.quascirev.2007.11.011

Glasser, N. F., Harrison, S., Jansson, K. N., Anderson, K., & Cowley, A. (2011). Global sea-level contribution from the Patagonian Icefields since the Little Ice Age maximum. Nature Geoscience, 4(5), 303-307. https://doi.org/10.1038/ngeo1122

Glasser, N. F., Harrison, S., Schnabel, C., Fabel, D., & Jansson, K. N. (2012). Younger Dryas and early Holocene age glacier advances in Patagonia. Quaternary Science Reviews, 58, 7–17. https://doi.org/10.1016/j.quascirev.2012.10.011

Glodny, J., Echtler, H., Collao, S., Ardiles, M., Burón, P., & Figueroa, O. (2008). Differential late paleozoic active margin evolution in south-central chile (37 s–40 s)–the lanalhue fault zone. Journal of South American Earth Sciences, 26(4), 397-411. https://doi.org/10.1016/j.jsames.2008.06.001

Goldfinger, C., Morey, A. E., Black, B., Beeson, J., Nelson, C. H., & Patton, J. (2013). Spatially limited mud turbidites on the Cascadia margin: Segmented earthquake ruptures? Natural Hazards and Earth System Sciences, 13, 2109–2146. https://doi.org/10.5194/nhess-13-2109-2013

Goldfinger, C., Nelson, C. H., Johnson, J. E., & Shipboard Scientific Party. (2003). Holocene earthquake records from the Cascadia subduction zone and northern San Andreas fault based on precise dating of offshore turbidites. Annual Review of Earth and Planetary Sciences, 31(1), 555-577. https://doi.org/10.1146/annurev.earth.31.100901.141246

Gorring, M. L., Kay, S. M., Zeitler, P. K., Ramos, V. A., Rubiolo, D., Fernandez, M. I., & Panza, J. L. (1997). Neogene Patagonian plateau lavas: continental magmas associated with ridge collision at the Chile Triple Junction. Tectonics, 16(1), 1-17. https://doi.org/10.1029/96TC03368

Gràcia, E., Dañobeitia, J. J., Terrinha, P., Blondel, P., Jacobs, C., & Fernandez, M. (2003). High-resolution imaging of active faults in the SW Iberian margin from the hits marine geophysical survey.

Gràcia, E., Pallas, R., Soto, J. I., Comas, M., Moreno, X., Masana, E., ... & Danobeitia, J. (2006). Active faulting offshore SE Spain (Alboran Sea): Implications for earthquake hazard assessment in the Southern Iberian Margin. Earth and Planetary Science Letters, 241(3-4), 734-749. https://doi.org/10.1016/j.epsl.2005.11.009

Gràcia, E., Bartolomé, R., Lo Iacono, C., Moreno, X., Perea, H., Martínez-Loriente, S., ... & Dañobeitia, J. J. (2012). Active strike-slip faults offshore the South Iberian Margin (Alboran Sea and Gulf of Cadiz): Implications for submarine paleoseismology.

Gràcia, E., Lamarche, G., Nelson, H., & Pantosti, D. (2013). Preface: marine and lake paleoseismology. Natural Hazards and Earth System Sciences, 13(12), 3469-3478. https://doi:10.5194/nhess-13-3469-2013

Grootes, P. M., Mook, W. G., Vogel, J. C., de Vries, A. E., Haring, A., & Kistemaker, J. (1975). Enrichment of radiocarbon for dating samples up to 75,000 years. Zeitschrift für Naturforschung A, 30(1), 1-14. https://doi.org/10.1515/zna-1975-0102

GUC (2007). Informe de últimos sismos con magnitud igual o superior a 3.0. Universidad de Chile. Santiago, Chile: Servicio Sismológico Nacional. http://ssn.dgf.uchile.cl/

Gut, B. (2008). Trees in Patagonia. Springer Science & Business Media.

Guzmán, D., & Silva, N. (2002). Physical and chemical characterization and water masses of the southern channels of Chile between Boca del Guafo and Golfo Elefantes (Cimar Fiordo 4 Cruise). Ciencia y Tecnología del Mar, 25(2), 45-76.

Haberland, C., Rietbrock, A., Lange, D., Bataille, K., & Hofmann, S. (2006). Interaction between forearc and oceanic plate at the south-central Chilean margin as seen in local seismic data. Geophysical Research Letters, 33, L23302. https://doi.org/10.1029/2006GL028189

Haberle, S. G., & Bennett, K. D. (2004). Postglacial formation and dynamics of North Patagonian rainforest in the Chonos Archipelago, Southern Chile. Quaternary Science Reviews, 23(23-24), 2433-2452. https://doi.org/10.1016/j.quascirev.2004.03.001

Hackney, C., & Clayton, A. (2015). Unmanned Aerial Vehicles (UAVs) and Their Application in Geomorphic Mapping. Geomorphological Techniques. Bristish Society for Geomporlogy. http://eprints.soton.ac.uk/id/eprint/376639

Hackney, R. I., Echtler, H. P., Franz, G., Götze, H. J., Lucassen, F., Marchenko, D., ... & Tassara, A. (2006). The segmented overriding plate and coupling at the south-central Chilean margin (36–42 S). In The Andes (pp. 355-374). Springer, Berlin, Heidelberg. https://doi.org/10.1007/978-3-540-48684-8_17

Held, S., Schill, E., Pavez, M., Díaz, D., Munoz, G., Morata, D., & Kohl, T. (2016). Resistivity distribution from mid-crustal conductor to near-surface across the 1200 km long Liquiñe-Ofqui Fault System, southern Chile. Geophysical Journal International, 207(3), 1387-1400. https://doi.org/10.1093/gji/ggw338

Haller, M., & Lapido, O. (1980). El Mesozoico de la Cordillera Patagónica Central. Revista de la Asociación Geológica Argentina, 35(2), 230-247.

Hamling, I. J., Hreinsdóttir, S., Clark, K., Elliott, J., Liang, C., Fielding, E., et al. (2017). Complex multifault rupture during the 2016 Mw 7.8 Kaikōura earthquake, New Zealand. Science, 356, eaam7194. https://doi.org/10.1126/science.aam7194

Hardebeck, J. L. (2013). Geometry and earthquake potential of the shoreline fault, Central California. Bulletin of the Seismological Society of America, 103, 447–462. https://doi.org/10.1785/0120120175

Harwin, S., & Lucieer, A. (2012). Assessing the accuracy of georeferenced point clouds produced via multi-view stereopsis from unmanned aerial vehicle (UAV) imagery. Remote Sensing, 4(6), 1573-1599. https://doi.org/10.3390/rs4061573

Hauser, A. (1991). Hans Steffen, precursor del concepto falla liquine-ofqui. Andean Geology, 18(2), 177-179. http://dx.doi.org/10.5027/andgeoV18n2-a07

Healy, D., Yielding, G., & Kusznir, N. (2004). Fracture prediction for the 1980 El Asnam, Algeria earthquake via elastic dislocation modeling. Tectonics, 23, 1–21. https://doi.org/10.1029/2003TC001575

Hedges, R. E. M., Ho, P., & Moore, C. B. (1980). Enrichment of carbon-14 by selective laser photolysis of formaldehyde. Applied physics, 23(1), 25-32. https://doi.org/10.1007/BF00899566

Heim, A. (1940). Geological Observations in the Patagonian Cordillera:(preliminary Report). Birkhaeuser.

Hein, A. S., Hulton, N. R., Dunai, T. J., Schnabel, C., Kaplan, M. R., Naylor, M., & Xu, S. (2009). Middle Pleistocene glaciation in Patagonia dated by cosmogenic-nuclide measurements on outwash gravels. Earth and Planetary Science Letters, 286(1-2), 184-197. https://doi.org/10.1016/j.epsl.2009.06.026

Hein, A. S., Hulton, N. R., Dunai, T. J., Sugden, D. E., Kaplan, M. R., & Xu, S. (2010). The chronology of the Last Glacial Maximum and deglacial events in central Argentine Patagonia. Quaternary Science Reviews, 29, 1212–1227. https://doi.org/10.1016/j.quascirev.2010.01.020

Hepp, C., Thiermann, H., & Ramírez, C. (1996). Praderas en la zona austral: XI Región (Aysén). Praderas para Chile. Instituto de Investigaciones Agropecuarias, Santiago.

Herron, E.M., Cande, S.C., & Hall, B.R. (1981). An active spreading center collides with a subduction zone: A geophysical survey of the Chile Margin triple junction. In L.V.D. Kulm, J. Dymond, E.J. Dasch, D.M. Hussong, R. Roderick (Eds.), Nazca Plate: Crustal Formation and Andean Convergence. Geological Society of America Memoir.

Hervé, M. (1976). Estudio geologico de la falla Liquine-Reloncavi en el area de Liquine: antecedentes de un movimiento transcurrente (Provincia de Valdivia). Actas Congr. Geol. Chil, 1, B39-B56.

Hervé, F., & Thiele, R. (1987). Estado de conocimiento de las megafallas en Chile y su significado tectónico. Comun. Univ. Chile, 38, 67-91.

Hervé, F. (1994). The southern Andes between 39 and 44 S latitude: The geological signature of a transpressive tectonic regime related to a magmatic arc. In Tectonics of the Southern Central Andes (pp. 243-248). Springer, Berlin, Heidelberg. https://doi.org/10.1007/978-3-642-77353-2_17

Heusser, C. J. (1960). Late-Pleistocene environments of the Laguna de San Rafael area, Chile. Geographical Review, 50(4), 555-577. https://doi.org/10.2307/212310

Heusser, C. J. (1990). Chilotan piedmont glacier in the southern Andes during the last glacial maximum. Andean Geology, 17, 3–18. https://doi.org/10.5027/andgeoV17n1-a01

Heusser, C. J. (2002). On glaciation of the southern Andes with special reference to the Península de Taitao and adjacent Andean cordillera (~ 46° 30′ s). Journal of South American Earth Sciences, 15(5), 577-589. https://doi.org/10.1016/S0895-9811(02)00076-7

Hilley, G. E., & Strecker, M. R. (2004). Steady state erosion of critical Coulomb wedges with applications to Taiwan and the Himalaya. Journal of Geophysical Research: Solid Earth, 109(B1). https://doi.org/10.1029/2002JB002284

Hollin, J. T., Schilling, D. H., Denton, G. H., & Hughes, T. J. (1981). The last great ice sheets. Late Wisconsin-Weichselian mountain glaciers and small ice caps, pp-179.

Hogg, A.G., Higham, T.F.G., Lowe, D.J., Palmer, J.G., Reimer, P.J. & Newnham, R.M. (2002). A wiggle-match date for Polynesian settlement of New Zealand. Antiquity, 77(295), 116-125.

Hogg, A. G., Hua, Q., Blackwell, P. G., Niu, M., Buck, C. E., Guilderson, T. P., ... & Zimmerman, S. R. (2013). SHCal13 Southern Hemisphere calibration, 0–50,000 years cal BP. Radiocarbon, 55(4), 1889-1903. https://doi.org/10.2458/azu_js_rc.55.16783

HRV (2007). Harvard Seismology (USA), Centroid Moment Tensor (CMT) Catalog [WWW Document]. URL www.globalcmt.org

Hu, Y., Wang, K., He, J., Klotz, J., & Khazaradze, G. (2004). Three-dimensional viscoelastic finite element model for postseismic deformation of the great 1960 Chile earthquake. Journal of Geophysical Research: Solid Earth, 109(B12). https://doi.org/10.1029/2004JB003163

Hubbard, A., Hein, A. S., Kaplan, M. R., Hulton, N. R., & Glasser, N. (2005). A modelling reconstruction of the last glacial maximum ice sheet and its deglaciation in the vicinity of the Northern Patagonian Icefield, South America.

Geografiska Annaler: Series A, Physical Geography, 87(2), 375-391. https://doi.org/10.1111/j.0435-3676.2005.00264.x

Hugenholtz, C. H., Whitehead, K., Brown, O. W., Barchyn, T. E., Moorman, B. J., LeClair, A., ... & Hamilton, T. (2013). Geomorphological mapping with a small unmanned aircraft system (sUAS): Feature detection and accuracy assessment of a photogrammetrically-derived digital terrain model. Geomorphology, 194, 16-24. https://doi.org/10.1016/j.geomorph.2013.03.023

Hulton, N. R., Purves, R. S., McCulloch, R. D., Sugden, D. E., & Bentley, M. J. (2002). The last glacial maximum and deglaciation in southern South America. Quaternary Science Reviews, 21(1-3), 233-241. https://doi.org/10.1016/S0277-3791(01)00103-2

Isozaki, Y., Aoki, K., Nakama, T., & Yanai, S. (2010). New insight into a subduction-related orogen: A reappraisal of the geotectonic framework and evolution of the Japanese Islands. Gondwana Research, 18(1), 82-105. https://doi.org/10.1016/j.gr.2010.02.015

Jara, J., & Melnick, D. (2009). Tasa de deformación dextral holocena de la Falla Liquiñe-Ofqui en la localidad de Liquiñe. Santiago, 22, S9_037.

Jiracek, G. R. (1995). Geoelectromagnetics charges on. Reviews of Geophysics, 33(S1), 169-176. https://doi.org/10.1029/95RG00548

Jones, A. G. (1992). Electrical conductivity of the continental lower crust. Continental lower crust, 81-143.

Kanamori, H. (1995). The Kobe (Hyogo-ken Nanbu), Japan, earthquake of January 16, 1995. Seismological Research Letters, 66(2), 6-10. https://doi.org/10.1785/gssrl.66.2.6

Kanamori, H., & Anderson, D. L. (1975). Theoretical basis of some empirical relations in seismology. Bulletin of the seismological society of America, 65(5), 1073-1095.

Kanamori, H., & Cipar, J. J. (1974). Focal process of the great Chilean earthquake May 22, 1960. Physics of the Earth and Planetary Interiors, 9(2), 128-136. https://doi.org/10.1016/0031-9201(74)90029-6

Kanamori, H., & Rivera, L. (2017). An M w= 7.7 slow earthquake in 1960 near the Aysén Fjord region, Chile. Geophysical Journal International, 211(1), 93-106. https://doi.org/10.1093/gji/ggx292

Kaplan, M. R., Singer, B. S., Douglass, D. C., Ackert Jr, R. P., & Caffee, M. W. (2001, November). The Last Two Glacial Maxima Recorded In Middle Latitude Argentina. In Gsa Annual Meeting, November 5-8, 2001.

Kaplan, M. R., Ackert, R. P., Singer, B. S., Douglass, D. C., & Kurz, M. D. (2004). Cosmogenic nuclide chronology of millennial-scale glacial advances during O-isotope stage 2 in Patagonia. GSA Bulletin, 116(3-4), 308-321. https://doi.org/10.1130/B25178.1

Kaplan, M. R., Douglass, D. C., Singer, B. S., Ackert, R. P., & Caffee, M. W. (2005). Cosmogenic nuclide chronology of pre-last glacial maximum moraines at Lago Buenos Aires, 46 S, Argentina. Quaternary Research, 63(3), 301-315. https://doi.org/10.1016/j.yqres.2004.12.003

Kendrick, E., Bevis, M., Smalley Jr, R., Brooks, B., Vargas, R. B., Laurıa, E., & Fortes, L. P. S. (2003). The Nazca–South America Euler vector and its rate of change. Journal of South American Earth Sciences, 16(2), 125-131. https://doi.org/10.1016/S0895-9811(03)00028-2

Khazaradze, G., Wang, K., Klotz, J., Hu, Y., & He, J. (2002). Prolonged post-seismic deformation of the 1960 great Chile earthquake and implications for mantle rheology. Geophysical Research Letters, 29(22), 7-1. https://doi.org/10.1029/2002GL015986

Kilb, D., Gomberg, J., & Bodin, P. (2002). Aftershock triggering by complete Coulomb stress changes. Journal of Geophysical Research, 107(B4), 2060. https://doi.org/10.1029/2001JB000202

Klotz, J., Khazaradze, G., Angermann, D., Reigber, C., Perdomo, R., & Cifuentes, O. (2001). Earthquake cycle dominates contemporary crustal deformation in Central and Southern Andes. Earth and Planetary Science Letters, 193(3-4), 437-446. https://doi.org/10.1016/S0012-821X(01)00532-5

Kodaira, S., No, T., Nakamura, Y., Fujiwara, T., Kaiho, Y., Miura, S., et al. (2012). Coseismic fault rupture at the trench axis during the 2011 Tohoku-oki earthquake. Nature Geoscience, 5, 646–650. https://doi.org/10.1038/ngeo1547

Kotô, B. (1893). On the cause of the great earthquake in central Japan, 1891. J. Sci. Coll. Imp. Univ., 5, 295-353.

Lagabrielle, Y., Suárez, M., Rossello, E. A., Hérail, G., Martinod, J., Régnier, M., & de la Cruz, R. (2004). Neogene to Quaternary tectonic evolution of the Patagonian Andes at the latitude of the Chile Triple Junction. Tectonophysics, 385(1-4), 211-241. https://doi.org/10.1016/j.tecto.2004.04.023

Lahsen, A. (1966). Geología de la región continental de Aysén. Inst Invest Recursos Nat, Corfo, 20, 1-20.

Lamarche, G., Barnes, P. M., & Bull, J. M. (2006). Faulting and extension rate over the last 20,000 years in the offshore Whakatane Graben, New Zealand continental shelf. Tectonics, 25(4). https://doi.org/10.1029/2005TC001886

Lambeck, K., Esat, T. M., & Potter, E. K. (2002). Links between climate and sea levels for the past three million years. Nature, 419(6903), 199–206. https://doi.org/10.1038/nature01089

Lambeck, K., Rouby, H., Purcell, A., Sun, Y., & Sambridge, M. (2014). Sea level and global ice volumes from the Last Glacial Maximum to the Holocene. Proceedings of the National Academy of Sciences, 111, 15,296–15,303. https://doi.org/10.1073/pnas.1411762111

Lange, D., Cembrano, J., Rietbrock, A., Haberland, C., Dahm, T., & Bataille, K. (2008). First seismic record for intra-arc strike-slip tectonics along the Liquiñe-Ofqui fault zone at the obliquely convergent plate margin of the southern Andes. Tectonophysics, 455, 14–24. https://doi.org/10.1016/j.tecto.2008.04.014

Lapido, O. R., Beltramone, C., & Haller, M. J. (1990). Glacial deposits on the Patagonian cordillera at latitude 43° 30′ S. In Quaternary of South America & Antarctic Peninsula (Vol. 6). AA Balkema Publishers Rotterdam.

Lara, L. E., Cembrano, J., & Lavenu, A. (2008). Quaternary vertical displacement along the Liquiñe-Ofqui Fault Zone: Differential uplift and coeval volcanism in the southern Andes?. International Geology Review, 50(11), 975-993. https://doi.org/10.2747/0020-6814.50.11.975

Lara, L. E., & Folguera, A. (2006). The Pliocene to Quaternary narrowing of the Southern Andean volcanic arc between 37° and 41° S latitude. Special papers - Geological Society of America, 407, 299.

Lara, L.E., Díaz-Naveas, J., & Arroyo-Suárez, E. (2009). Volcanes Submarinos del Fiordo Aysén: Antecedentes morfoestructurales basados en batimetría de alta resolución. Paper presented at XII Congreso Geológico Chileno, Santiago, Chile.

Lastras, G., Amblas, D., Calafat, A. M., Canals, M., Frigola, J., Hermanns, R. L., et al. (2013). Landslides cause tsunami waves: Insights from Aysén Fjord, Chile. Eos Transactions American Geophysical Union, 94, 297–298. https://doi.org/10.1002/2013EO340002

Lavenu, A., & Cembrano, J. (1999). Compressional- and transpressional-stress pattern for Pliocene and Quaternary brittle deformation in fore arc and intra-arc zones (Andes of Central and Southern Chile). Journal of Structural Geology, 21, 1669–1691. https://doi.org/10.1016/S0191-8141(99)00111-X

Lawson, A. C., & Reid, H. F. (1908). The California Earthquake of April 18, 1906: Report of the State Earthquake Investigation Commission.. (No. 87). Carnegie institution of Washington.

Lay, T., Ammon, C. J., Kanamori, H., Koper, K. D., Sufri, O., & Hutko, A. R. (2010). Teleseismic inversion for rupture process of the 27 February 2010 Chile (Mw 8.8) earthquake. Geophysical Research Letters, 37(13). https://doi.org/10.1029/2010GL043379

Legrand, D., Barrientos, S., Bataille, K., Cembrano, J., & Pavez, A. (2011). The fluid-driven tectonic swarm of Aysen Fjord, Chile (2007) associated with two earthquakes (Mw=6.1 and Mw=6.2) within the Liquiñe-Ofqui Fault Zone. Continental Shelf Research, 31, 154–161. https://doi.org/10.1016/j.csr.2010.05.008

Lingenfelter, R. E. (1963). Production of carbon 14 by cosmic-ray neutrons. Reviews of Geophysics, 1(1), 35-55. https://doi.org/10.1029/RG001i001p00035

Lomnitz, C. (1970). Major earthquakes and tsunamis in Chile during the period 1535 to 1955. Geologische Rundschau, 59(3), 938-960. https://doi.org/10.1007/BF02042278

Lomnitz, C. (2004). Major earthquakes of Chile: a historical survey, 1535-1960. Seismological Research Letters, 75(3), 368-378. https://doi.org/10.1785/gssrl.75.3.368

Lumley, S. H., & Switsur, R. (1993). Late quaternary chronology of the Taitao Peninsula, southern Chile. Journal of Quaternary Science, 8(2), 161-165. https://doi.org/10.1002/jqs.3390080208

Mackie, R. L., Livelybrooks, D. W., Madden, T. R., & Larsen, J. C. (1997). A magnetotelluric investigation of the San Andreas fault at Carrizo Plain, California. Geophysical Research Letters, 24(15), 1847-1850. https://doi.org/10.1029/97GL01604

Madariaga, R., Métois, M., Vigny, C., & Campos, J. (2010). Central Chile finally breaks. Science, 328(5975), 181-182. https://doi.org/10.1126/science.1189197

Maksymowicz, A., Contreras-Reyes, E., Grevemeyer, I., & Flueh, E. R. (2012). Structure and geodynamics of the post-collision zone between the Nazca–Antarctic spreading center and South America. Earth and Planetary Science Letters, 345-348, 27–37. https://doi.org/10.1016/j.epsl.2012.06.023

Manighetti, I., Campillo, M., Bouley, S., & Cotton, F. (2007). Earthquake scaling, fault segmentation, and structural maturity. Earth and Planetary Science Letters, 253(3-4), 429-438. https://doi.org/10.1016/j.epsl.2006.11.004

Marchant, D. R., Lewis, A. R., Phillips, W. M., Moore, E. J., Souchez, R. A., Denton, G. H., ... & Landis, G. P. (2002). Formation of patterned ground and sublimation till over Miocene glacier ice in Beacon Valley, southern Victoria Land, Antarctica. Geological Society of America Bulletin, 114(6), 718-730. https://doi.org/10.1130/0016-7606(2002)114<0718:FOPGAS>2.0.CO;2

Marden, C. J., & Clapperton, C. M. (1995). Fluctuations of the South Patagonian Ice-field during the last glaciation and the Holocene. Journal of Quaternary Science, 10(3), 197-209. https://doi.org/10.1002/jqs.3390100302

Mason, D. B. (1996). Earthquake magnitude potential of the Intermountain seismic belt, USA, from surface-parameter scaling of late Quaternary faults. Bulletin of the Seismological Society of America, 86(5), 1487-1506.

McHugh, C. M. G., Seeber, L., Cormier, M. H., Dutton, J., Cagatay, N., Polonia, A., et al. (2006). Submarine earthquake geology along the North Anatolia Fault in the Marmara Sea, Turkey: A model for transform basin sedimentation. Earth and Planetary Science Letters, 248, 661–684. https://doi.org/10.1016/j.epsl.2006.05.038

McCalpin, J. P. (Ed.) (2009). Paleoseismology, International Geophysics Series (Vol. 95, 2nd ed., 629p.). San Diego, CA: Academic Press.

.

McCalpin, J. P., & Nelson, A. R. (2009). Introduction to paleoseismology. International Geophysics, 95, 1-27.

McCarthy, A. J., & Elders, C. F. (1997). Cenozoic deformation in Sumatra: oblique subduction and the development of the Sumatran Fault System. Geological Society, London, Special Publications, 126(1), 355-363. https://doi.org/10.1144/GSL.SP.1997.126.01.21

McCulloch, R. D., Bentley, M. J., Purves, R. S., Hulton, N. R., Sugden, D. E., & Clapperton, C. M. (2000). Climatic inferences from glacial and palaeoecological evidence at the last glacial termination, southern South America. Journal of Quaternary Science: Published for the Quaternary Research Association, 15(4), 409-417. https://doi.org/10.1002/1099-1417(200005)15:4<409::AID-JQS539>3.0.CO;2-%23

Meghraoui, M., Philip, H., Albarede, F., & Cisternas, A. (1988). Paleoseismicity, trench investigations through the trace of the 1980 El Asnam thrust fault: Evidence for paleoseismicity. Bulletin of the Seismological Society of America, 70, 979–999.

Melnick, D., & Echtler, H. P. (2006). Inversion of forearc basins in south-central Chile caused by rapid glacial age trench fill. Geology, 34(9), 709-712. https://doi.org/10.1130/G22440.1

Melnick, D., Bookhagen, B., Echtler, H. P., & Strecker, M. R. (2006). Coastal deformation and great subduction earthquakes, Isla Santa María, Chile (37 S). Geological Society of America Bulletin, 118(11-12), 1463-1480. https://doi.org/10.1130/B25865.1

Melnick, D., Bookhagen, B., Strecker, M. R., & Echtler, H. P. (2009). Segmentation of megathrust rupture zones from fore-arc deformation patterns over hundreds to millions of years, Arauco peninsula, Chile. Journal of Geophysical Research: Solid Earth, 114(B1). https://doi.org/10.1029/2008JB005788

Melnick, D., Sanchez, M., Echtler, H., Bataille, K., & Pineda, V. (2003). Geología estructural de la Isla Mocha, centro-sur de Chile (38° 30'S, 74° W): Implicancias en la tectónica regional. In 10° Congreso Geologico Chileno (Concepción, Chile 2003).

Mercer, J. H. (1983). Cenozoic glaciation in the Southern Hemisphere. Annual Review of Earth and Planetary Sciences, 11(1), 99-132. https://doi.org/10.1146/annurev.ea.11.050183.000531

Métois, M., Socquet, A., & Vigny, C. (2012). Interseismic coupling, segmentation and mechanical behavior of the central Chile subduction zone. Journal of Geophysical Research: Solid Earth, 117(B3). https://doi.org/10.1029/2011JB008736

Miall, A. D. (1977). Lithofacies types and vertical profile models in braided river deposits: a summary.

Micheletti, N., Chandler, J. H., & Lane, S. N. (2015). Investigating the geomorphological potential of freely available and accessible structure-from-motion photogrammetry using a smartphone. Earth Surface Processes and Landforms, 40(4), 473-486. https://doi.org/10.1002/esp.3648

Miller, J.M.G. (1996). Glacial Environments. In: Sedimentary Environments and Facies (ed. Reading, H.G.), editorial Blackwell Scientific Publications, p. 454-667.

Miller, A. (1976). The climate of Chile. World survey of climatology, 12, 113-145.

Moernaut, J., Van Daele, M., Fontijn, K., Heirman, K., Kempf, P., Pino, M., ... & De Batist, M. (2018). Larger earthquakes recur more periodically: New insights in the megathrust earthquake cycle from lacustrine turbidite records in south-central Chile. Earth and Planetary Science Letters, 481, 9-19.

Moernaut, J., Van Daele, M., Fontijn, K., Heirman, K., Kempf, P., Pino, M., ... & De Batist, M. (2018). Larger earthquakes recur more periodically: New insights in the megathrust earthquake cycle from lacustrine turbidite records in south-central Chile. Earth and Planetary Science Letters, 481, 9-19.

Montade, V., Nebout, N. C., Kissel, C., Haberle, S. G., Siani, G., & Michel, E. (2013). Vegetation and climate changes during the last 22,000 yr from a marine core near Taitao Peninsula, southern Chile. Palaeogeography, Palaeoclimatology, Palaeoecology, 369, 335-348. https://doi.org/10.1016/j.palaeo.2012.11.001

Mora, C., Comte, D., Russo, R., Gallego, A., & Mocanu, V. (2010). Aysén seismic swarm (January 2007) in southern Chile: Analysis using joint hypocenter determination. Journal of seismology, 14(4), 683-691. https://doi.org/10.1007/s10950-010-9190-y

Morehead, M. (2001). The link between abrupt climate change and basin stratigraphy: A numerical approach. Global and Planetary Change, 28, 107–127. https://doi.org/10.1016/S0921-8181(00)00068-0

Moreno, H., & Naranjo, J. (2003). Mapa de peligros del volcán Llaima, Región de la Araucanía. In Carta Geológica de Chile, Serie Geología Ambiental 7, (scale 1:75,000). Chile: Santiago: Servicio Nacional de Geología y Minería.

Moreno, M. S., Klotz, J., Melnick, D., Echtler, H., & Bataille, K. (2008). Active faulting and heterogeneous deformation across a megathrust segment boundary from GPS data, south central Chile (36–39 S). Geochemistry, Geophysics, Geosystems, 9(12). https://doi.org/10.1029/2008GC002198

Moreno, M. S., Bolte, J., Klotz, J., & Melnick, D. (2009). Impact of megathrust geometry on inversion of coseismic slip from geodetic data: Application to the 1960 Chile earthquake. Geophysical Research Letters, 36(16). https://doi.org/10.1029/2009GL039276

Moreno, M., Rosenau, M., & Oncken, O. (2010). 2010 Maule earthquake slip correlates with pre-seismic locking of Andean subduction zone. Nature, 467(7312), 198-202. https://doi.org/10.1038/nature09349

Moreno, M., Melnick, D., Rosenau, M., Bolte, J., Klotz, J., Echtler, H., ... & Oncken, O. (2011). Heterogeneous plate locking in the South–Central Chile subduction zone: Building up the next great earthquake. Earth and Planetary Science Letters, 305(3-4), 413-424. https://doi.org/10.1016/j.epsl.2011.03.025

Moreno, M., Melnick, D., Rosenau, M., Baez, J., Klotz, J., Oncken, O., ... & Socquet, A. (2012). Toward understanding tectonic control on the Mw 8.8 2010 Maule Chile earthquake. Earth and Planetary Science Letters, 321, 152-165. https://doi.org/10.1016/j.epsl.2012.01.006

Moreno, H., & Naranjo, J. A. (2003). Mapa de Peligros del Volcán Llaima, región de La Araucanía. Servicio Nacional de Geología y Minería. Carta Geológica de Chile, Serie Geología Ambiental, (7).

Molnar, P., & England, P. (1990). Late Cenozoic uplift of mountain ranges and global climate change: chicken or egg?. Nature, 346(6279), 29-34. https://doi.org/10.1038/346029a0

Morehead, M. (2001). The link between abrupt climate change and basin stratigraphy: A numerical approach. Global and Planetary Change, 28, 107–127. https://doi.org/10.1016/S0921-8181(00)00068-0

Mörner, N. A., & Sylwan, C. (1989). Magnetostratigraphy of the Patagonian moraine sequence at Lago Buenos Aires. Journal of South American Earth Sciences, 2(4), 385-389. https://doi.org/10.1016/0895-9811(89)90016-3

Muraoka, H., Takahashi, M., Sundhoro, H., Dwipa, S., Soeda, Y., Momita, M., Shimada, K. (2010). Geothermal systems constrained by the Sumatran fault and its pull-apart basins in Sumatra, western Indonesia. Paper presented at 2010 Proceedings World Geothermal Congress, Bali, Indonesia.

Murdie, R. E., Prior, D. J., Styles, P., Flint, S. S., Pearce, R. G., & Agar, S. M. (1993). Seismic responses to ridge-transform subduction: Chile triple junction. Geology, 21(12), 1095-1098. https://doi.org/10.1130/0091-7613(1993)021<1095:SRTRTS>2.3.CO;2

Nakamura, K. (1977). Volcanoes as possible indicators of tectonic stress orientation—principle and proposal. Journal of Volcanology and Geothermal Research, 2(1), 1-16. https://doi.org/10.1016/0377-0273(77)90012-9

Nakanishi, T., Takemura, K., Okada, A., Morino, M., Hayashida, A., Nakamura, M., ... & Hirose, M. (2004). Identification of multiple faulting events of the Median Tectonic Line active fault system in the Tokushima Plain, Japan, based on close-interval radiocarbon dating. Nuclear Instruments and Methods in Physics Research Section B: Beam Interactions with Materials and Atoms, 223, 573-578. https://doi.org/10.1016/j.nimb.2004.04.106

Naranjo, J. A., & Stern, C. R. (1998). Holocene explosive activity of Hudson Volcano, southern Andes. Bulletin of Volcanology, 59(4), 291-306. https://doi.org/10.1007/s004450050193

Naranjo, J. A., & Stern, C. R. (2004). Holocene tephrochronology of the southernmost part (42 30'-45 S) of the Andean Southern Volcanic Zone. Revista geológica de Chile, 31(2), 224-240. http://dx.doi.org/10.4067/S0716-02082004000200003

Naranjo, J. A., Arenas, M., Clavero, J., & Muñoz, O. (2009). Mass movement-induced tsunamis: Main effects during the Patagonian Fjordland seismic crisis in Aisén (45° 25′S), Chile. Andean Geology, 36, 137–145. https://doi.org/10.5027/andgeoV36n1-a11

Naranjo, J.A.; Clavero, J.; Arenas, M.; Lara, L.; Moreno, M. (2007). Efectos de la crisis sísmica de Aisén 2007. In Congreso Nacional, No. 28 y Congreso Internacional de Geografía, No. 13. Universidad de Chile, Facultad de Arquitectura, Urbanismo y Geografía, Resúmenes: 116 p. Santiago.

Natawidjaja, D. H., & Triyoso, W. (2007). The Sumatran fault zone—From source to hazard. Journal of Earthquake and Tsunami, 1(01), 21-47. https://doi.org/10.1142/S1793431107000031

Nelson, C. H., Gutiérrez Pastor, J., Goldfinger, C., & Escutia, C. (2012). Great earthquakes along the Western United States continental margin: Implications for hazards, stratigraphy and turbidite lithology. Natural Hazards and Earth System Sciences, 12, 3191–3208. https://doi.org/10.5194/nhess-12-3191-2012

Niemeyer, H. (1975). Geología de la región comprendida entre el Lago General Carrera y el río Chacabuco, Provincia de Aisén, Chile. Memoria de Título (Inédito), Universidad de Chile, Departamento de Geología.

Niemeyer, H., Skármeta, J., Fuenzalida, R., & Espinosa, W. (1984). Hojas Península de Taitao y Puerto Aisén: Región de Aisén del General Carlos Ibañez del Campo: Carta Geológica de Chile 1: 500.000. Servicio Nacional de Geología y Minería.

Nikonov, A. A. (1977). Holocene and contemporary movements of the earth's crust.

Nishenko, S. P. (1985). Seismic potential for large and great interplate earthquakes along the Chilean and southern Peruvian margins of South America: a quantitative reappraisal. Journal of Geophysical Research: Solid Earth, 90(B5), 3589-3615. https://doi.org/10.1029/JB090iB05p03589

Nordenskjöld, O. (1898). Från Eldslandet: skildringar från den Svenska expeditionen till Magellansländerna, 1895-97. PA Norstedt.

Nostro, C., Chiaraluce, L., Cocco, M., Baumont, D., & Scotti, O. (2005). Coulomb stress changes caused by repeated normal faulting earthquakes during the 1997 Umbria-Marche (central Italy) seismic sequence. Journal of Geophysical Research, 110, B05S20. https://doi.org/10.1029/2004JB003386

Ojeda, J., Ruiz, S., DelCampo, F., Pasten, C., Otarola, C., & Silva, R. (2017, December). Stochastic strong motion generation using slip model of 21 and 22 May 1960 mega-thrust earthquakes in the main cities of Central-South Chile. In 2017 AGU Fall Meeting. AGU.

Oppikofer, T., Hermanns, R. L., Redfield, T. F., Sepúlveda, S. A., Duhart, P., & Bascuñan, I. (2012). Morphologic description of the Punta Cola rock avalanche and associated minor rockslides caused by the 21 April 2007 Aysén earthquake (Patagonia, southern Chile). Revista de la Asociación Geológica Argentina, 69, 339–353.

Pankhurst, R. J., Weaver, S. D., Hervé, F., & Larrondo, P. (1999). Mesozoic-Cenozoic evolution of the North Patagonian batholith in Aysen, southern Chile. Journal of the Geological Society, 156(4), 673-694. https://doi.org/10.1144/gsjgs.156.4.0673

Parada, M. A., López-Escobar, L., Oliveros, V., Fuentes, F., Morata, D., Calderón, M., ... & Figueroa, O. (2007). Andean magmatism. In The geology of Chile (pp. 115-146).

Pardo-Casas, F., & Molnar, P. (1987). Relative motion of the Nazca (Farallon) and South American plates since Late Cretaceous time. Tectonics, 6(3), 233-248. https://doi.org/10.1029/TC006i003p00233

Pérez-Flores, P., Cembrano, J., Sánchez-Alfaro, P., Veloso, E., Arancibia, G., & Roquer, T. (2016). Tectonics, magmatism and paleo-fluid distribution in a strike-slip setting: Insights from the northern termination of the Liquiñe–Ofqui fault System, Chile. Tectonophysics, 680, 192-210. https://doi.org/10.1016/j.tecto.2016.05.016

Pavez, A.; Sepúlveda, S.A.; Aguilera, R. 2007. Remote sensing analysis of landslides and coastal changes after the 2007 Aysén Mw 6.2 earthquake. In Geosur 2007: 120 p. Santiago.

Phillips, W. M. (2001). A review of cosmogenic nuclide surface exposure dating: new challenges for Scottish geomorphology. Scottish Geographical Journal, 117(1), 1-15. https://doi.org/10.1080/00369220118737107

Pickard, G. L. (1971). Some physical oceanographic features of inlets of Chile. Journal of the Fisheries Board of Canada, 28(8), 1077-1106. https://doi.org/10.1139/f71-163

Pinto, L. A., & Bonert, C. (2005). Origen y distribución espacial de hidrocarburos alifáticos en sedimentos de seno Aysén y canal Moraleda, Chile Austral. Ciencia y Tecnología del Mar, 28(1), 35-44.

Plafker, G., & Savage, J. C. (1970). Mechanism of the Chilean earthquakes of May 21 and 22, 1960. Geological Society of America Bulletin, 81(4), 1001-1030. https://doi.org/10.1130/0016-7606(1970)81(1001:MOTCEO)2.0.CO;2

Pondard, N., & Barnes, P. M. (2010). Structure and paleoearthquake records of active submarine faults, Cook Strait, New Zealand: Implications for fault interactions,

stress loading, and seismic hazard. Journal of Geophysical Research: Solid Earth, 115(B12). https://doi.org/10.1029/2010JB007781

Porter, S. C. (1981). Pleistocene glaciation in the southern Lake District of Chile. Quaternary Research, 16(3), 263-292. https://doi.org/10.1016/0033-5894(81)90013-2

Pouderoux, H., Lamarche, G., & Proust, J. N. (2012). Building an 18 000-year-long paleo-earthquake record from detailed deep-sea turbidite characterisation in Poverty Bay, New Zealand. Natural Hazards and Earth System Sciences, 12, 2077–2101. https://doi.org/10.5194/nhess-12-2077-2012

Quensel, P. D. (1910). On the influence of the ice age on the continental watershed of Patagonia. Bulletin Geological Institute of the University of Upsala, 9, 60-92.

Quinteros, J., & Sobolev, S. V. (2013). Why has the Nazca plate slowed since the Neogene?. Geology, 41(1), 31-34. https://doi.org/10.1130/G33497.1

Rabassa, J. (2008). Late cenozoic glaciations in Patagonia and Tierra del Fuego. Developments in quaternary sciences, 11, 151-204. https://doi.org/10.1016/S1571-0866(07)10008-7

Rabassa, J., & Evenson, E. (1987). Edad pre-pleistocena superior de la glaciación El Condor, Valle del rio Malleo, Neuquen. In Congreso Geológico Argentino. 10 (pp. 217-219).

Rabassa, J., & Clapperton, C. M. (1990). Quaternary glaciations of the southern Andes. Quaternary Science Reviews, 9(2-3), 153-174. https://doi.org/10.1016/0277-3791(90)90016-4

Rabassa, J., Coronato, A., & Martinez, O. (2011). Late Cenozoic glaciations in Patagonia and Tierra del Fuego: an updated review. Biological Journal of the Linnean Society, 103(2), 316-335. https://doi.org/10.1111/j.1095-8312.2011.01681.x

Ramos, V. A., & Kay, S. M. (1992). Southern Patagonian plateau basalts and deformation: backarc testimony of ridge collisions. Tectonophysics, 205(1-3), 261-282. https://doi.org/10.1016/0040-1951(92)90430-E

Ramsey, C. B. (1995). Radiocarbon calibration and analysis of stratigraphy: the OxCal program. Radiocarbon, 37(2), 425-430. https://doi.org/10.1017/S0033822200030903

Ramsey, C. B. (1997). Probability and dating. Radiocarbon, 40(1), 461-474. https://doi.org/10.1017/S0033822200018348

Ramsey, C. B., van der Plicht, J., & Weninger, B. (2001). 'Wiggle matching'radiocarbon dates. Radiocarbon, 43(2A), 381-389. https://doi.org/10.1017/S0033822200038248

Rebolledo, L., Lange, C. B., Figueroa, D., Pantoja, S.,Muñoz, P., & Castro, R. (2005). 20th century fluctuations in the abundance of siliceous microorganisms preserved in the sediments of the Puyuhuapi Channel (44° S), Chile. Revista chilena de historia natural, 78(3), 469-488. http://dx.doi.org/10.4067/S0716-078X2005000300009.

Reid, H. F. (1910). The California earthquake of April 18, 1906. Report of the state earthquake investigation commission, 2, 16-18.

Rimando, R. E., & Rimando, J. M. (2020). Morphotectonic Kinematic Indicators along the Vigan-Aggao Fault: The Western Deformation Front of the Philippine Fault Zone in Northern Luzon, the Philippines. Geosciences, 10(2), 83. https://doi.org/10.3390/geosciences10020083

Rippin, D. M., Pomfret, A., & King, N. (2015). High resolution mapping of supra-glacial drainage pathways reveals link between micro-channel drainage density, surface roughness and surface reflectance. Earth Surface Processes and Landforms, 40(10), 1279-1290. https://doi.org/10.1002/esp.3719

Rivera, A., Benham, T., Casassa, G., Bamber, J., & Dowdeswell, J. A. (2007). Ice elevation and areal changes of glaciers from the Northern Patagonia Icefield, Chile. Global and Planetary Change, 59(1-4), 126-137. https://doi.org/10.1016/j.gloplacha.2006.11.037

Rivera, A., Casassa, G., Acuna, C., & Lange, H. (2000). Variaciones recientes de glaciares en Chile. Investigaciones geográficas, (34), pp. 29. https://www.jstor.org/stable/40996718

Rockwell, T. K., & Ben-Zion, Y. (2007). High localization of primary slip zones in large earthquakes from paleoseismic trenches: Observations and implications for earthquake physics. Journal of Geophysical Research, 112, B10304. https://doi.org/10.1029/2006JB004764

Rodrigo, C. (2008). Submarine topography in the Chilean North Patagonian channels. progress in the oceanographic knowledge of Chilean inner waters, from Puerto Montt to Cape Horn. Comité Oceanográfico Nacional-Pontificia Universidad Católica de Valparaíso, Valparaíso, 19-23.

Roe, G. H., Stolar, D. B., & Willett, S. D. (2006). Response of a steady-state critical wedge orogen to changes in climate and tectonic forcing. Special Papers-Geological Society of America, 398, 227.

Rojas, N. (2002). Distribución de materia orgánica, carbono y nitrógeno, y diagénesis temprana en sedimentos de la zona de canales australes entre los golfos Corcovado y Elefantes, Chile. Undergraduate Thesis, Universidad Católica de Valparaıso, Valparaıso, Chile.

Rojas, C., Beck Jr, M. E., Burmester, R. F., Cembrano, J., & Hervé, F. (1994). Paleomagnetism of the Mid-Tertiary Ayacara Formation, southern Chile: counterclockwise rotation in a dextral shear zone. Journal of South American Earth Sciences, 7(1), 45-56. https://doi.org/10.1016/0895-9811(94)90033-7

Romero, G.A., (1983), Geología del sector Alto Palena–Puerto Ramirez. Chiloe continental (Diploma thesis): Santiago, Departamento de Geologı´a, Universidad de Chile.

Rose, J. (1991). Subaerial modification of glacier bedforms immediately following ice wastage. https://doi.org/10.1080/00291959108552267

Rosenau, M., Melnick, D., & Echtler, H. (2006). Kinematic constraints on intra-arc shear and strain partitioning in the southern Andes between 38 S and 42 S latitude. Tectonics, 25(4). https://doi.org/10.1029/2005TC001943

Roth, W. H., Scott, R. F., & Austin, I. (1981). Centrifuge modeling of fault propagation through alluvial soils. Geophysical Research Letters, 8(6), 561-564. http://dx.doi.org/10.1029/GL008i006p00561

Rothé, J. P. (1969). The Seismicity of the Earty, 1953-1965: La Séismicité Du Globe 1953, 1965. Unesco.

Ruegg, J. C., Rudloff, A., Vigny, C., Madariaga, R., De Chabalier, J. B., Campos, J., ... & Dimitrov, D. (2009). Interseismic strain accumulation measured by GPS in the seismic gap between Constitución and Concepción in Chile. Physics of the Earth and Planetary Interiors, 175(1-2), 78-85. https://doi.org/10.1016/j.pepi.2008.02.015

Ruiz, S., & Madariaga, R. (2018). Historical and recent large megathrust earthquakes in Chile. Tectonophysics, 733, 37-56. https://doi.org/10.1016/j.tecto.2018.01.015

Ruiz, S., Moreno, M., Melnick, D., Del Campo, F., Poli, P., Baez, J. C., ... & Madariaga, R. (2017). Reawakening of large earthquakes in south central Chile: The 2016 Mw 7.6 Chiloé event. Geophysical Research Letters, 44(13), 6633-6640. https://doi.org/10.1002/2017GL074133

Russo, R. M., Gallego, A., Comte, D., Mocanu, V. I., Murdie, R. E., Mora, C., & VanDecar, J. C. (2011). Triggered seismic activity in the Liquiñe-Ofqui fault zone, southern Chile, during the 2007 Aysen seismic swarm. Geophysical Journal International, 184(3), 1317-1326. https://doi.org/10.1111/j.1365-246X.2010.04908.x

Ryan, J. C., Hubbard, A. L., Todd, J., Carr, J. R., Box, J. E., Christoffersen, P., ... & Snooke, N. (2014). Repeat UAV photogrammetry to assess calving front dynamics at a large outlet glacier draining the Greenland Ice Sheet. The Cryosphere Discuss, 8(2), 2243-2275. https://doi.org/10.5194/tcd-8-2243-2014

Sagredo, E. A., Kaplan, M. R., Araya, P. S., Lowell, T. V., Aravena, J. C., Moreno, P. I., ... & Schaefer, J. M. (2018). Trans-pacific glacial response to the Antarctic Cold Reversal in the southern mid-latitudes. Quaternary Science Reviews, 188, 160-166. https://doi.org/10.1016/j.quascirev.2018.01.011

Salamanca, M. A., & Jara, B. (2003). Distribución y acumulación de plomo (Pb y 210Pb) en sedimentos de los fiordos de la XI región. Revista Ciencia y Tecnología del Mar, 26, 61–71.

Sato, H., Kato, N., Abe, S., Van Horne, A., & Takeda, T. (2015). Reactivation of an old plate interface as a strike-slip fault in a slip-partitioned system: Median Tectonic Line, SW Japan. Tectonophysics, 644, 58-67. https://doi.org/10.1016/j.tecto.2014.12.020

Schnellmann, M., Anselmetti, F. S., Giardini, D., & McKenzie, J. A. (2005). Mass movement-induced fold-and-thrust belt structures in unconsolidated sediments in Lake Lucerne (Switzerland). Sedimentology, 52, 271–289. https://doi.org/10.1111/j.1365-3091.2004.00694.x

Scholz, C. H. (1982a). Scaling laws for large earthquakes: consequences for physical models. Bulletin of the Seismological Society of America, 72(1), 1-14.

Scholz, C. H. (1982b). Scaling relations for strong ground motion in large earthquakes. Bulletin of the Seismological Society of America, 72(6A), 1903-1909.

Scholz, C. H. (1988). The brittle-plastic transition and the depth of seismic faulting. Geologische Rundschau, 77(1), 319–328. https://doi.org/10.1007/BF01848693

Scharer, K. M., Weldon, R. J., Fumal, T. E., & Biasi, G. P. (2007). Paleoearthquakes on the southern San Andreas fault, Wrightwood, California, 3000 to 1500 BC: A new method for evaluating paleoseismic evidence and earthquake horizons. Bulletin of the Seismological Society of America, 97(4), 1054-1093. https://doi.org/10.1785/0120060137

Sepúlveda, S. A., & Serey, A. (2009). Tsunamigenic, earthquake-triggered rock slope failures during the April 21, 2007 Aisén earthquake, southern Chile (45.5 S). Andean Geology, 36, 131–136. https://doi.org/10.4067/S0718-71062009000100010

Sepúlveda, J., Pantoja, S., Hughen, K., Lange, C., Gonzalez, F., Muñoz, P., ... & Rossel, P. (2005). Fluctuations in export productivity over the last century from sediments of a southern Chilean fjord (44 S). Estuarine, Coastal and Shelf Science, 65(3), 587-600. https://doi.org/10.1016/j.ecss.2005.07.005

Sepúlveda, S.A.; Serey, A.; Pavez, A.; Barrientos, S.; Lara, M. (2008a). Analysis of earthquake-induced landslides during the 2007 Aysén Fjord seismic swarm, Chilean Patagonia (45.5ºS). In International Geological Congress, No. 33. Proceedings, paper GHZ04203L. Oslo.

Sepúlveda, S.A.; Serey, A.; Lara, M.; Rebolledo, S. (2008b). Deslizamientos cosísmicos asociados al terremoto del fi ordo aysén de 2007, sur de Chile. In Congreso Geológico Argentino, No. 17, Actas 1: 316-317. Salvador de Jujuy.

Sepúlveda, S. A., Serey, A., Lara, M., Pavez, A., & Rebolledo, S. (2010). Landslides induced by the April 2007 Aysén Fjord earthquake, Chilean Patagonia. Landslides, 7, 483–492. https://doi.org/10.1007/s10346-010-0203-2

Shaw, B. E., & Scholz, C. H. (2001). Slip-length scaling in large earthquakes: Observations and theory and implications for earthquake physics. Geophysical Research Letters, 28(15), 2995-2998. https://doi.org/10.1029/2000GL012762

Shaw, J. H., & Suppe, J. (1996). Earthquake hazards of active blind-thrust faults under the central Los Angeles basin, California. Journal of Geophysical Research: Solid Earth, 101(B4), 8623-8642. https://doi.org/10.1029/95JB03453

Siani, G., Colin, C., Michel, E., Carel, M., Richter, T., Kissel, C., & Dewilde, F. (2010). Late Glacial to Holocene terrigenous sediment record in the Northern Patagonian margin: Paleoclimate implications. Palaeogeography, Palaeoclimatology, Palaeoecology, 297(1), 26-36. https://doi.org/10.1016/j.palaeo.2010.07.011

Sieh, K. E. (1981). A review of geological evidence for recurrence times of large earthquakes (No. 4, pp. 181-207). Washington, DC: American Geophysical Union.

Sievers, H. A. (2008). Water masses and circulation in austral Chilean channels and fjords. Progress in the oceanographic knowledge of Chilean interior waters, from Puerto Montt to Cape Horn, 53-58.

Silva, N. (2008). Physical and chemical characteristics of the surface sediments in the austral Chilean channels and fjords. Progress in the oceanographic knowledge of Chilean interior waters, from Puerto Montt to Cape Horn, 69-75.

Silva, N., & Guzmán, D. (2006). Condiciones oceanográficas físicas y químicas, entre boca del Guafo y fiordo Aysén (Crucero Cimar 7 Fiordos). Ciencia y Tecnología del Mar, 29(1), 25-44.

Silva, N., & Prego, R. (2002). Carbon and nitrogen spatial segregation and stoichiometry in the surface sediments of southern Chilean inlets (41–56° S). estuarine, Coastal and shelf science, 55(5), 763-775. https://doi.org/10.1006/ecss.2001.0938

Silva, N., Sievers, H. A., & Prado, R. 1995. Características oceanográficas y una proposición de circulación para algunos canales australes de Chile entre 41º20'S y 46º40'S. Rev. Biol. Mar., Valparaíso, 30, 207-254.

Singer, B. S., Ackert Jr, R. P., & Guillou, H. (2004). 40Ar/39Ar and K-Ar chronology of Pleistocene glaciations in Patagonia. Geological Society of America Bulletin, 116(3-4), 434-450 https://doi.org/10.1130/B25177.1

Skármeta, J., Charrier, R. (1976). Geologia del sector fronterizo de aysen entre los 45o y 46o de latitud sur, chile.

Skármeta, J. (1978). Geologia de la region continental de Aysen entre el Lago General Carrera y la Cordillera Castillo: Carta Geologica de Chile. Esc, 1(250.000).

Slemmons, D. B. (1977). State-of-the-art for assessing earthquake hazards in the United States. Report, 6, 73-1.

Small, E. E., & Anderson, R. S. (1998). Pleistocene relief production in Laramide mountain ranges, western United States. Geology, 26(2), 123-126. https://doi.org/10.1130/0091-7613(1998)026<0123:PRPILM>2.3.CO;2

Smedile, A., De Martini, P. M., & Pantosti, D. (2012). Combining inland and offshore paleotsunamis evidence: The Augusta Bay (eastern Sicily, Italy) case study. Natural Hazards and Earth System Sciences, 12, 2557–2567. https://doi.org/10.5194/nhess-12-2557-2012

Smedley, R. K., Glasser, N. F., & Duller, G. A. T. (2016). Luminescence dating of glacial advances at Lago Buenos Aires (~ 46 S), Patagonia. Quaternary Science Reviews, 134, 59-73. https://doi.org/10.1016/j.quascirev.2015.12.010

Solonenko, V. P. (1973). Paleoseismogeology. Izv. Akad. Nauk SSSR, Fiz. Zem, (9), 3-16.

Somoza, R. (1998). Updated azca (Farallon)—South America relative motions during the last 40 My: implications for mountain building in the central Andean region. Journal of South American Earth Sciences, 11(3), 211-215. https://doi.org/10.1016/S0895-9811(98)00012-1

Sparkes, R., Tilmann, F., Hovius, N., & Hillier, J. (2010). Subducted seafloor relief stops rupture in South American great earthquakes: Implications for rupture behaviour in the 2010 Maule, Chile earthquake. Earth and Planetary Science Letters, 298(1-2), 89-94. https://doi.org/10.1016/j.epsl.2010.07.029

Steffen, H. (1944). Patagonia occidental. Las cordilleras patagónicas y sus regiones circundantes. Ediciones de la Universidad de Chile, Vol. 1, 333 p. Santiago.

Stern, C. R. (2004). Active Andean volcanism: its geologic and tectonic setting. Revista geológica de Chile, 31(2), 161-206. http://dx.doi.org/10.4067/S0716-02082004000200001

Stern C., Moreno H., López-Escobar L., Clavero J., Lara L., Naranjo J., Parada M. and Skewes M. (2007) Chilean volcanoes. In The geology of Chile (eds T. Moreno and W. Gibbons). Geological Society of London, Bath, pp. 147–178.

Steinberg, D. M. (1983). Bayesian Models for Response Surfaces of Uncertain Functional Form (No. MRC-TSR-2474). Wisconsin Univ-Madison Mathematics Research Center.

Stirling, M., Rhoades, D., & Berryman, K. (2002). Comparison of earthquake scaling relations derived from data of the instrumental and preinstrumental era. Bulletin of the Seismological Society of America, 92(2), 812-830. https://doi.org/10.1785/0120000221

Stirling, M. W., Litchfield, N. J., Villamor, P., van Dissen, R. J., Nicol, A., Pettinga, J., et al. (2017). The Mw7.8 2016 Kaikōura earthquake: Surface fault rupture and seismic hazard context. Bulletin of the New Zealand Society for Earthquakes Engineering, 50, 73–84. https://doi.org/10.5459/bnzsee.50.2.73-84

Stirling, M., McVerry, G., Gerstenberger, M., Litchfield, N., Van Dissen, R., Berryman, K., ... & Lamarche, G. (2012). National seismic hazard model for New Zealand: 2010 update. Bulletin of the Seismological Society of America, 102(4), 1514-1542. https://doi.org/10.1785/0120110170

Strub P. T., Mesias J. M., Montecino V., Ruttlant J. & Salinas S. (1998). Coastal ocean circulation off Western South America. In The Global Coastal Ocean. Regional Studies and Syntheses (eds. A. R. Robinson and K. H. Brink). Wiley, New York, pp. 273–315.

Stuiver, M., Heusser, C. J., & Yang, I. C. (1978). North American glacial history extended to 75,000 years ago. Science, 200(4337), 16-21. https://doi.org/10.1126/science.200.4337.16

Stuiver, M., Robinson, S. W., Yang, I. C., Berger, R., & Suess, H. E. (1979). ^{14}C dating to 60,000 years BP with proportional counters. In Radiocarbon dating (pp. 202-215). University of California Press Berkeley.

Stuiver, M., Reimer, P. J., & Reimer, R. W. (2018). CALIB 7.1. 2017. URL: http://calib.org (accessed: 10.02. 2020).

Sugden, D. E., & John, B. S. (1976). Glaciers and landscape: a geomorphological approach. E. Arnold.

Sugden, D. E., Bentley, M. J., Fogwill, C. J., Hulton, N. R. J., McCulloch, R. D., & Purves, R. S. (2005). Late-glacial glacier events in southernmost South America: A blend of “northern” and “southern” hemispheric climatic signals? Geografiska Annaler: Series A. Physical Geography, 87, 273–288. https://doi.org/10.1111/j.0435-3676.2005.00259.x

Sunal, G., & Erturaç, M. K. (2012). Estimation of the pre-North Anatolian Fault Zone pseudo-paleo-topography: A key to determining the cumulative offset of major post-collisional strike-slip faults. Geomorphology, 159-160, 125–141. https://doi.org/10.1016/j.geomorph.2012.03.013

Sylvester, A. G. (1988). Strike-slip faults. Geological Society of America Bulletin, 100, 1666–1703. https://doi.org/10.1130/0016-7606(1988)100<1666:SSF>2.3.CO;2

Syvitski, J. P. M., & Shaw, J. (1995). Chapter 5 Sedimentology and Geomorphology of Fjords. pp. 113–178. https://doi.org/10.1016/S0070-4571(05)80025-1

Syvitski, J. P. M., Burrell, D. C., & Skei, J. M. (1987). . J. P. M. Syvitski D. C. Burrell & J. M. Skei In Fjords; Processes and products, First(X). –215). , . New York: Springer-Verlag. https://doi.org/10.1007/978-1-4612-4632-9

Tebbens, S. F., & Cande, S. C. (1997). Southeast Pacific tectonic evolution from early Oligocene to present. Journal of Geophysical Research: Solid Earth, 102(B6), 12061-12084. https://doi.org/10.1029/96JB02582

Tebbens, S. F., Cande, S. C., Kovacs, L., Parra, J. C., LaBrecque, J. L., & Vergara, H. (1997). The Chile ridge: A tectonic framework. Journal of Geophysical Research: Solid Earth, 102(B6), 12035-12059. https://doi.org/10.1029/96JB02581

Thomson, S. N. (2002). Late Cenozoic geomorphic and tectonic evolution of the Patagonian Andes between latitudes 42 S and 46 S: An appraisal based on fission-track results from the transpressional intra-arc Liquiñe-Ofqui fault zone. Geological Society of America Bulletin, 114(9), 1159-1173. https://doi.org/10.1130/0016-7606(2002)114<1159:LCGATE>2.0.CO;2

Thomson, S. N., Brandon, M. T., Reiners, P. W., Zattin, M., Isaacson, P. J., & Balestrieri, M. L. (2010). Thermochronologic evidence for orogen-parallel variability in wedge kinematics during extending convergent orogenesis of the northern Apennines, Italy. Bulletin, 122(7-8), 1160-1179. https://doi.org/10.1130/B26573.1

Thomson, S. N., Brandon, M. T., Tomkin, J. H., Reiners, P. W., Vásquez, C., & Wilson, N. J. (2010). Glaciation as a destructive and constructive control on mountain building. Nature, 467(7313), 313-317. https://doi.org/10.1038/nature09365

Thorndycraft, V. R., Bendle, J. M., Benito, G., Davies, B. J., Sancho, C., Palmer, A. P., ... & Martin, J. R. (2019). Glacial lake evolution and Atlantic-Pacific drainage reversals during deglaciation of the Patagonian Ice Sheet. Quaternary Science Reviews, 203, 102-127. https://doi.org/10.1016/j.quascirev.2018.10.036

Thornburg, T. M., & Kulm, L. D. (1987). Sedimentation in the Chile Trench: Depositional morphologies, lithofacies, and stratigraphy. Geological Society of America Bulletin, 98(1), 33–52. https://doi.org/10.1130/0016-7606(1987)98<33:SITCTD>2.0.CO;2

Tocher, D. (1958). Earthquake energy and ground breakage. Bulletin of the Seismological Society of America, 48(2), 147-153.

Tomkin, J. H., & Roe, G. H. (2007). Climate and tectonic controls on glaciated critical-taper orogens. Earth and Planetary Science Letters, 262(3-4), 385-397. https://doi.org/10.1016/j.epsl.2007.07.040

Ton-That, T., Singer, B., Mörner, N. A., & Rabassa, J. (1999). Datación de lavas basálticas por 40Ar/39Ar y geología glacial de la región del lago Buenos Aires, provincia de Santa Cruz, Argentina. Revista de la Asociación Geológica Argentina, 54(4), 333-352.

Ton-That, T., Singer, B.S., Mörner, N.A., Rabassa, J. (2000). Datación por el método 40Ar-39Ar de lavas basálticas y geología del Cenozoico superior en la región del Lago Buenos Aires, provincia de Santa Cruz, Argentina. Revista de la Asociación Geológica Argentina, vol. 54, p. 333-352. http://dx.doi.org/10.4067/S0716-02082000000200004

Tong, X., Sandwell, D., Luttrell, K., Brooks, B., Bevis, M., Shimada, M., ... & Blanco, M. (2010). The 2010 Maule, Chile earthquake: Downdip rupture limit revealed by space geodesy. Geophysical Research Letters, 37(24). https://doi.org/10.1029/2010GL045805

Townend, J., & Zoback, M. D. (2006). Stress, strain, and mountain building in central Japan. Journal of Geophysical Research: Solid Earth, 111(B3). https://doi.org/10.1029/2005JB003759

Tsutsumi, H., Okada, A., Nakata, T., Ando, M., & Tsukuda, T. (1991). Timing and displacement of Holocene faulting on the Median Tectonic Line in central Shikoku, southwest Japan. Journal of Structural Geology, 13(2), 227-233. https://doi.org/10.1016/0191-8141(91)90069-U

Türkoğlu, E., Unsworth, M., Bulut, F., & Çağlar, İ. (2015). Crustal structure of the North Anatolian and East Anatolian Fault Systems from magnetotelluric data. Physics of the Earth and Planetary Interiors, 241, 1-14. https://doi.org/10.1016/j.pepi.2015.01.003

Turner, K. J., McCulloch, R. D., and Purves, R. S. (2001). Deglaciation of the late glacial central Patagonian icesheet. Earth Surface Processes. In "A global meeting of the Geological Society of America and the Geological Society of London", Edinburgh.

Unsworth, M., Egbert, G., & Booker, J. (1999). High-resolution electromagnetic imaging of the San Andreas fault in central California. Journal of Geophysical Research: Solid Earth, 104(B1), 1131-1150. https://doi.org/10.1029/98JB01755

Unsworth, M. J., Malin, P. E., Egbert, G. D., & Booker, J. R. (1997). Internal structure of the San Andreas fault at Parkfield, California. Geology, 25(4), 359-362. https://doi.org/10.1130/0091-7613(1997)025<0359:ISOTSA>2.3.CO;2

Utsu, T. (2002). A list of deadly earthquakes in the world: 1500–2000. In International Geophysics (Vol. 81, pp. 691-cp1). Academic Press.

Vakov, A. V. (1996). Relationships between earthquake magnitude, source geometry and slip mechanism. Tectonophysics, 261(1-3), 97-113. https://doi.org/10.1016/0040-1951(96)82672-2

Van Daele, M., Versteeg, W., Pino, M., Urrutia, R., & De Batist, M. (2013). Widespread deformation of basin-plain sediments in Aysén fjord (Chile) due to impact by earthquake-triggered, onshore-generated mass movements. Marine Geology, 337, 67-79. https://doi.org/10.1016/j.margeo.2013.01.006

Van der Plicht, J. (1993). The Groningen radiocarbon calibration program. Radiocarbon, 35(1), 231-237.

Vandekerkhove, E. (2014). The volcanic ash soils of Northern Chilean Patagonia (44–48 S): Distribution, weathering and influence on river chemistry. Universiteit Gent, Faculteit Wetenschappen: Gent.

Vandekerkhove, E., Bertrand, S., Reid, B., Bartels, A., & Charlier, B. (2016). Sources of dissolved silica to the fjords of northern Patagonia (44–48 S): the importance of volcanic ash soil distribution and weathering. Earth Surface Processes and Landforms, 41(4), 499-512. https://doi.org/10.1002/esp.3840

Vargas, G., Farias, M., Carretier, S., Tassara, A., Baize, S., & Melnick, D. (2011). Coastal uplift and tsunami effects associated to the 2010 M_w 8.8 Maule earthquake in Central Chile. Andean Geology, 38, 219–238. https://doi.org/10.5027/andgeoV38n1-a12

Vargas, G., Klinger, Y., Rockwell, T. K., Forman, S. L., Rebolledo, S., Baize, S., et al. (2014). Probing large intraplate earthquakes at the west flank of the Andes. Geology, 42, 1083–1086. https://doi.org/10.1130/G35741.1

Vargas, G., Rebolledo, S., Sepúlveda, S. A., Lahsen, A., Thiele, R., Townley, B., ... & Lara, M. (2013). Submarine earthquake rupture, active faulting and volcanism along the major Liquiñe-Ofqui Fault Zone and implications for seismic hazard assessment in the Patagonian Andes. Andean Geology, 40(1), 141-171. https://doi.org/10.5027/andgeoV40n1-a07

Vigny, C., Socquet, A., Peyrat, S., Ruegg, J. C., Métois, M., Madariaga, R., ... & Carrizo, D. (2011). The 2010 Mw 8.8 Maule megathrust earthquake of central Chile, monitored by GPS. Science, 332(6036), 1417-1421. https://doi.org/10.1126/science.1204132

Villagrán, C. (1988). Expansion of Magellanic Moorland during the late Pleistocene: Palynological evidence from northern Isla de Chiloé, Chile. Quaternary Research, 30(3), 304-314. https://doi.org/10.1016/0033-5894(88)90006-3

Villalobos, A., Easton, G., Maksymowicz, A., Ruiz, S., Lastras, G., De Pascale, G. P., & Agurto-Detzel, H. (2020). Active Faulting, Submarine Surface Rupture, and Seismic Migration Along the Liquiñe-Ofqui Fault System, Patagonian Andes. Journal of Geophysical Research: Solid Earth, 125(9), e2020JB019946. https://doi.org/10.1029/2020JB019946

Wallace, R. E. (1981). Active faults, paleoseismology, and earthquake hazards in the western United States. Earthquake prediction: An international review, 4, 209–216. https://doi.org/10.1029/ME004p0209

Wan, Y. G., Shen, Z. K., Wang, M., Zhang, Z. S., Gan, W. J., Wang, Q. L., et al. (2008). Coseismic slip distribution of the 2001 Kunlun mountain pass west earthquake constrained using GPS and InSAR data. Chinese Journal of Geophysics-Chinese Edition, 51, 753–764. https://doi.org/10.1002/cjg2.1268

Wang, K., Hu, Y., Bevis, M., Kendrick, E., Smalley Jr, R., Vargas, R. B., & Lauría, E. (2007). Crustal motion in the zone of the 1960 Chile earthquake: Detangling earthquake-cycle deformation and forearc-sliver translation. Geochemistry, Geophysics, Geosystems, 8(10). https://doi.org/10.1029/2007GC001721

Wannamaker, P. E., Jiracek, G. R., Stodt, J. A., Caldwell, T. G., Gonzalez, V. M., McKnight, J. D., & Porter, A. D. (2002). Fluid generation and pathways beneath an active compressional orogen, the New Zealand Southern Alps, inferred from magnetotelluric data. Journal of Geophysical Research: Solid Earth, 107(B6), ETG-6. https://doi.org/10.1029/2001JB000186

Wells, D. L., & Coppersmith, K. J. (1994). New empirical relationships among magnitude, rupture length, rupture width, rupture area, and surface displacement. Bulletin of the seismological Society of America, 84(4), 974-1002.

Wesnousky, S. G. (1986). Earthquakes, Quaternary faults, and seismic hazard in California. Journal of Geophysical Research: Solid Earth, 91(B12), 12587-12631. https://doi.org/10.1029/JB091iB12p12587

Wesnousky, S. G. (2008). Displacement and geometrical characteristics of earthquake surface ruptures: Issues and implications for seismic-hazard analysis and the process of earthquake rupture. Bulletin of the Seismological Society of America, 98(4), 1609-1632. https://doi.org/10.1785/0120070111

Wesnousky, S. G., Scholz, C. H., Shimazaki, K., & Matsuda, T. (1984). Integration of geological and seismological data for the analysis of seismic hazard: A case study of Japan. Bulletin of the Seismological Society of America, 74(2), 687-708.

Westoby, M. J., Brasington, J., Glasser, N. F., Hambrey, M. J., & Reynolds, J. M. (2012). 'Structure-from-Motion'photogrammetry: A low-cost, effective tool for geoscience applications. Geomorphology, 179, 300-314. https://doi.org/10.1016/j.geomorph.2012.08.021

Whipple, K. X., Kirby, E., & Brocklehurst, S. H. (1999). Geomorphic limits to climate-induced increases in topographic relief. Nature, 401(6748), 39-43. https://doi.org/10.1038/43375

Whipple, K. X. (2009). The influence of climate on the tectonic evolution of mountain belts. Nature geoscience, 2(2), 97-104. https://doi.org/10.1038/ngeo413

Whipple, K. X., & Meade, B. J. (2004). Controls on the strength of coupling among climate, erosion, and deformation in two-sided, frictional orogenic wedges at steady state. Journal of Geophysical Research: Earth Surface, 109(F1). https://doi.org/10.1029/2003JF000019

Whitlock, C., Bartlein, P. J., Markgraf, V., & Ashworth, A. C. (2001). The midlatitudes of North and South America during the Last Glacial Maximum and early Holocene: similar paleoclimatic sequences despite differing large-scale controls. In Interhemispheric climate linkages (pp. 391-416). Academic Press.

Willett, C. D., Ma, K. F., Brandon, M. T., Hourigan, J. K., Christeleit, E. C., & Shuster, D. L. (2020). Transient glacial incision in the Patagonian Andes from~ 6 Ma to present. Science advances, 6(7), eaay1641. https://doi.org/10.1126/sciadv.aay1641

Wils, K. (2016). Reconstruction of the seismic history of Aysén fjord (South Chile) by means of seismic stratigraphy and sediment-core analysis.

Wils, K., Van Daele, M., Lastras, G., Kissel, C., Lamy, F., & Siani, G. (2018). Holocene event record of Aysén Fjord (Chilean Patagonia): An interplay of volcanic eruptions and crustal and megathrust earthquakes. Journal of Geophysical Research: Solid Earth, 123, 324–343. https://doi.org/10.1002/2017JB014573

Wright, C., & Mella, A. (1963). Modifications to the soil pattern of South-Central Chile resulting from seismic and associated phenomena during the period May to August 1960. Bulletin of the Seismological Society of America, 53(6), 1367–1402.

Yamaguchi, N., & Yamazaki, F. (2001). Estimation of strong motion distribution in the 1995 Kobe earthquake based on building damage data. Earthquake engineering & structural dynamics, 30(6), 787-801. https://doi.org/10.1002/eqe.33

Yeats, R. S., Sieh, K. E., & Allen, C. R. (1997). The geology of earthquakes. USA: Oxford University Press.

Zachos, J., Pagani, M., Sloan, L., Thomas, E., & Billups, K. (2001). Trends, rhythms, and aberrations in global climate 65 Ma to present. Science, 292(5517), 686-693. https://doi.org/10.1126/science.1059412

Appendix A

Text A1: Introduction

This supporting information provides some of the figures seen in the main article (seismic reflection profiles) with the vertical scale transformed to distance (m). Also provides extra figures where some points of the discussion are summarized.

A general overview of the kind of files:

- Information of the data obtained from the seismic reflection and bathymetry data. Where was collected or created.
- Any known error associated to the data, and other uncertainties.
- Tables with measurements and calculations made on the geophysical data.

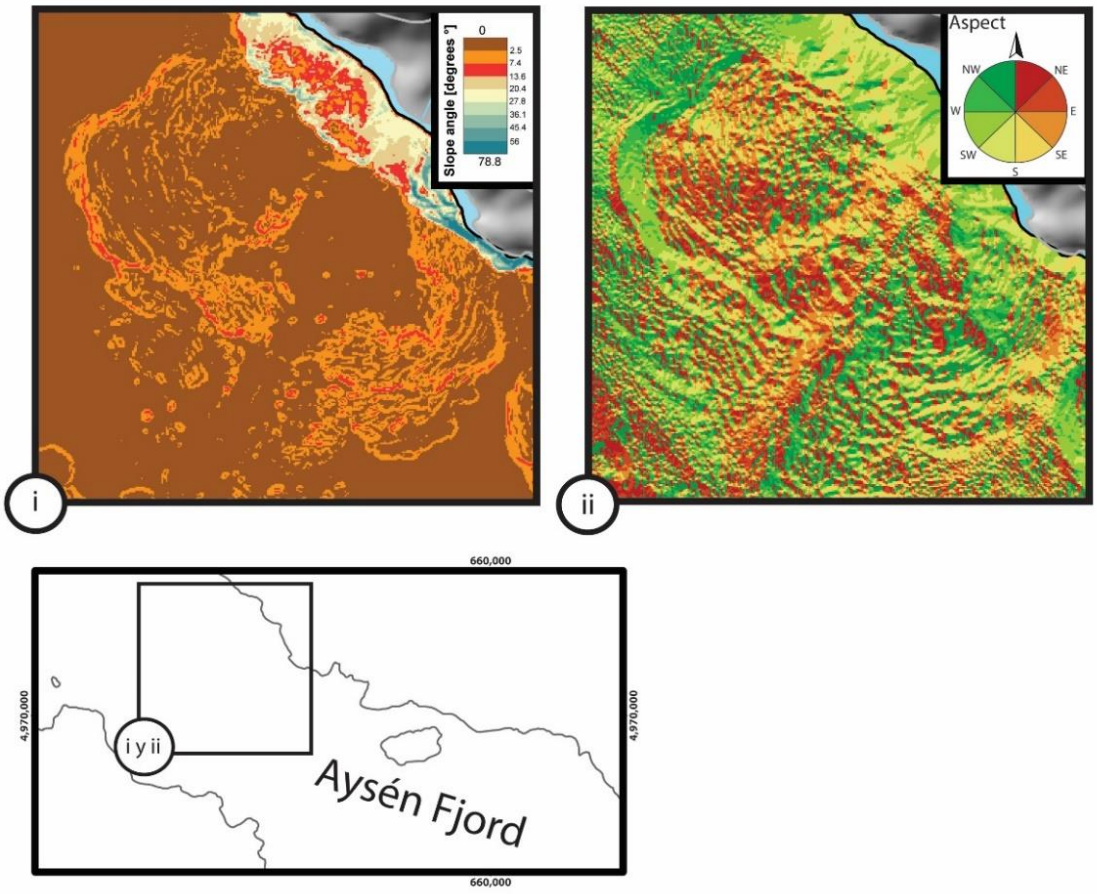

Figure A1. Geomorphological analysis of Punta Cola Bulge. (i) Slope map. (ii) Aspect map. Mini map shows inset location.

P-wave velocity in Aysén Fjord

We decided to use a P-wave velocity (V_P) = 2,000 m/s for migration from time (TWT) to distance (m) because it corresponds to an average value for shallow marine sediments located in the trench of the Nazca beneath the South American plates along Central-Southern Chile (e.g., Maksymowicz et al., 2012). These sediments have been classified as fluvial and glaciomarine in origin (e.g., Thornburg & Kulm, 1987; Bangs & Cande, 1997).
In addition:

Slow values for P-wave velocities in sediments from fjord-type environments

P-wave values (V_P) ~1,500 m/s are widely and normally used in research conducted in environments where glaciomarine sediments are abundant, such as in channels and fjords (e.g. Breuer et al., 2013, Fernández et al., 2011; St-Onge et al., 2012). The use of this standard velocity value is often justified by theory. Empirical velocity-porosity sediment relationships such as those proposed by Erickson & Jarrard (1998), relate V_P, fractional porosity and other empirical constants (Equation A1 and Figure A2).

$$V_p = 0.739 + 0.552\phi + 0.305/[(\phi+.13)^2 + 0.0725] + 0.61(v_{sh}-1.123)x[X_1-abs(X_1)],$$

$$\text{where } X_2=\tanh[20(\phi-0.39)].$$

Equation A1. Empirical equation determined by *Erickson and Jarrard* [1998] where $\mathbf{V_P}$ is expressed by a function controlled by fractional porosity ($\mathbf{\Phi}$), fine fraction of sediments (shale fraction, $\mathbf{v_{sh}}$), and a consolidation history.

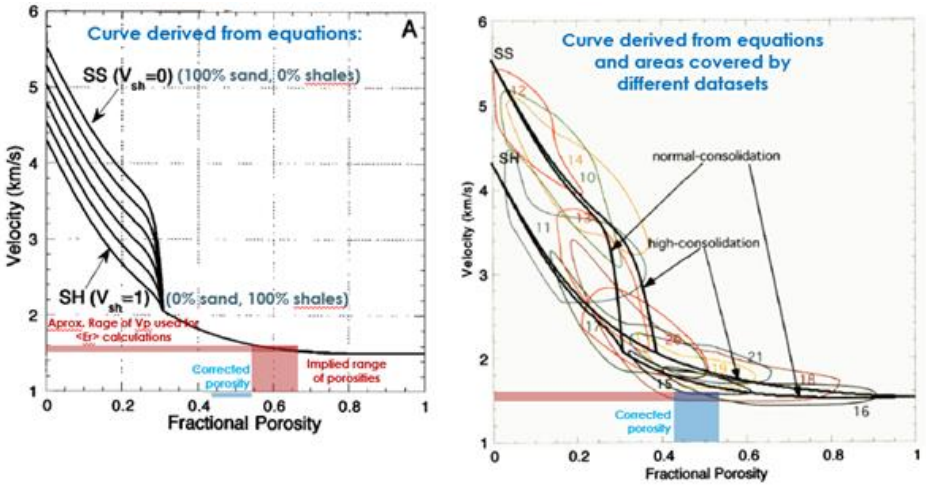

Figure A2. Left) Curve function derived from Empirical Eq. (A1) for sediments and siliciclastic rocks. The range of porosity normally used for glaciomarine sediments is indicated. (Right) Different curves derived from databases are observed.

The use of V_P value ~1,500 m/s is justified in the shallower part of the sedimentary infill of a basin dominated by muddy grain size fraction (green arrow in Figure A3 and Table A1). This approach does not adjust to our study area, to support an appropiate time-distance interpretation of our seismic reflection data, because:

1. The total sedimentary column exceeds 300 m, so it is acceptable to wait for an important sediment compaction. Changes in porosity and density would vary the P wave velocity, increasing this value usually used. Recent research from fjords associated with the Marinelli Glacier at Darwin Mountain Range in the Southern Patagonian Andes, have worked with this approach, by applying a depth-dependly sediment compaction model (Fernández et al., 2011; Figure A4).

2. The observation of our seismic profiles at the first order gives information suggesting that the sedimentary infill in the Aysen fjord is not uniform. The distinction of seismic facies allows the identification of at least three sedimentary units (MU: *Moraine Unit*, PLU: *Parallel Laminated Unit*, MDU: *Mass Deformed Units*). The oldest and deepest has been interpreted as a moraine.

   In the literature, glacial moraines have been characterized with "high" velocities (see Table A1). As an example of the application of this range of speeds, in the work of Stoker & Holmes (1991), in the case of moraines, the authors propose a value of V_P = 1,800 m/s. The overlying sedimentary infill in the Aysén fjord can be differentiated into two units (PLUT and PLUP, which are interpreted as postglacial in age).

3. The section interpreted in the seismic profiles as a postglacial sedimentary infill (PLU) is characterized by the presence of high contrast acoustic impedance changes, from which we interpret reflectors with high amplitude associated with sediments with high density-changes (Veeken, 2006). According our interpretation, this section -of postglacial sedimentary infill- represents a period with high input of dominantly coarse grain size fraction sediments (sand-gravel). The lower section of PLUT that ends approximately at the first 0.5 s is characterized by reflectors of great amplitude with a greater spacing between them, with respect to the overlying sediments. This package could corresponds to deposits associated with the first stages of the glacial retreat at this portion of the Aysén fjord, driving high sedimentation rates and the deposition of coarse grain size fraction sediments. Overlying this last package in the seismic images, an intercalation of packages with different amplitude, lateral continuity and impedance change can be observed within the PLUT, which could be associated to different periods of transport with more or less sediment discharge from rivers, as well as to volcanic and tectonic events.

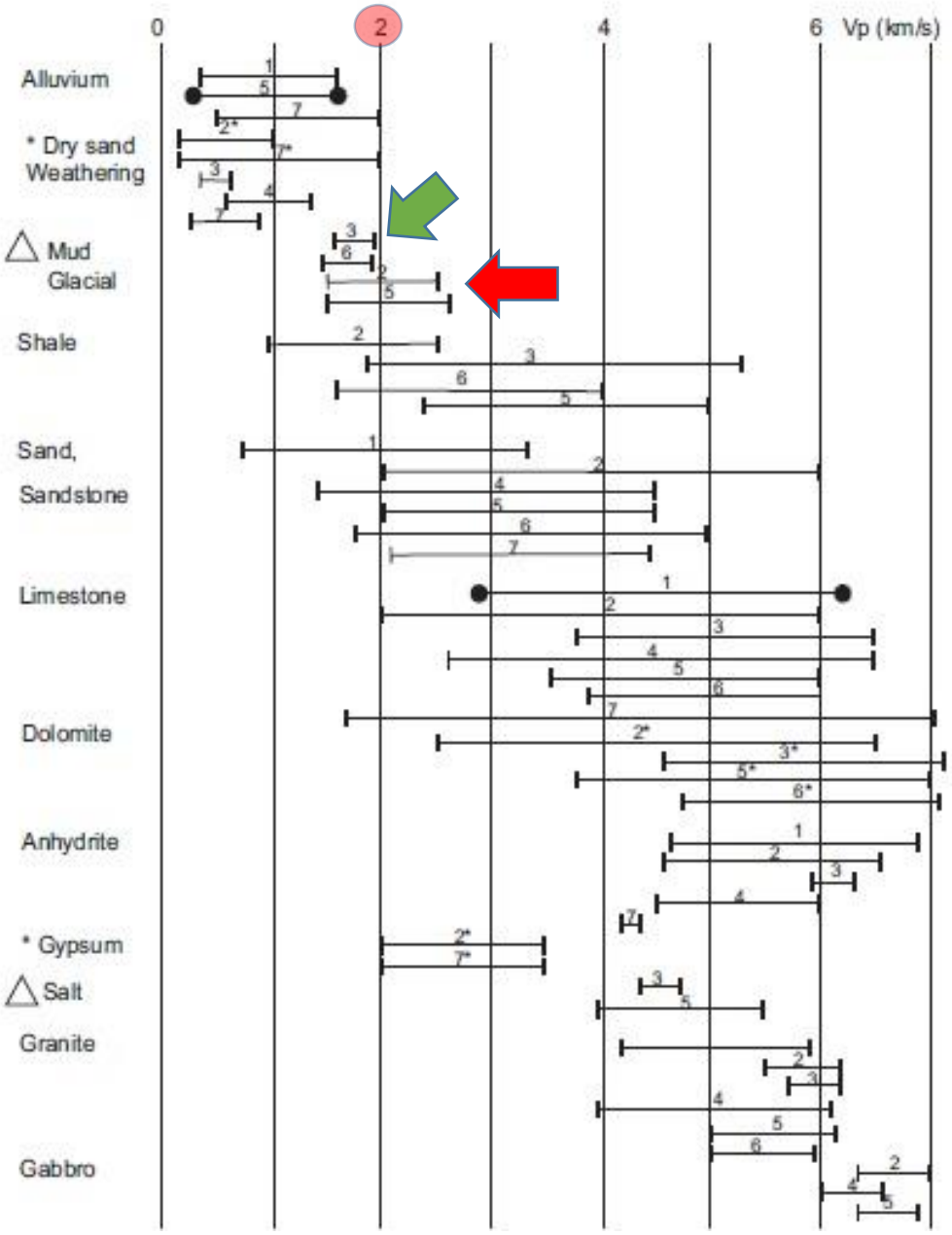

Figure A3. P wave velocities for sediments and common rocks (***Zhaou, 2014***). This figure has been compiled from data based on many investigations. Green arrow indicates the range of velocities for mud type sediments, red arrow indicates the range for glacial sediments.

Based on the arguments previously exposed and considering that most of the sedimentary infill would be of glacial origin (moraine and outwash in addition to fluvial sediments), we decided to use a V_P = 2,000 m/s (see Figure A3, red arrow).

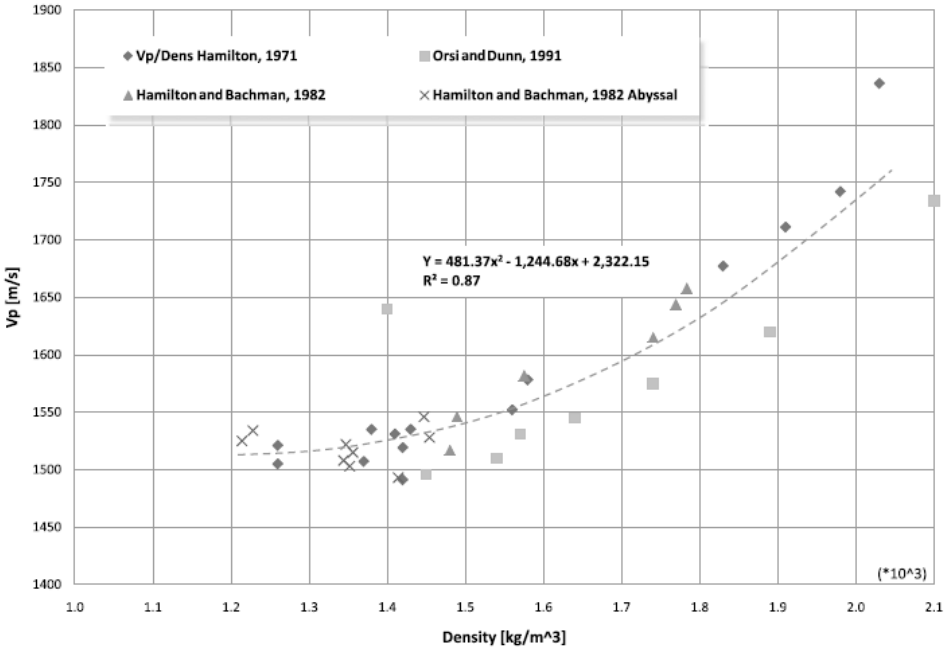

Figure A4. P-wave velocities related to density values from muddy marine sediments based on the data recovered by several authors (*see legend*). These data also correspond to a wide range of densities. Model proposed by ***Fernández et al.*** **(2011)*.***

Table A1. Geomorphological analysis of Punta Cola Bulge. (i) Slope map. (ii) Aspect map. Mini map shows inset location.

TYPE OF MATERIAL	VELOCITY
Water	1490 m/s
Glacimarine muds	1500-1800 m/s
Glacial moraine	1600-2700 m/s
Limestone	3500-6500 m/s
Granite	4600-7000 m/s

Calculation of errors

Once chosen a P-wave velocity of 2,000 m/s, we migrated the seismic profiles to convert time in distance, by considering an error associated to the receiver-emitter geometric arrangement. This equation links the velocities within water and sediments, the thickness of the sedimentary infill, and the emitter-receiver distance. We evaluated three cases for P-wave velocities: 1,800, 2,000 and 2,300 m/s.

Figure A5 shows the results where a maximum error of ~33 cm in the case of V_P = 2,300 m/s, can be observed between ~ 120 and 163 m depth, under the sea bottom. This error does not significantly affect our inferences of sedimentation rates or sedimentary package-thickness estimations.

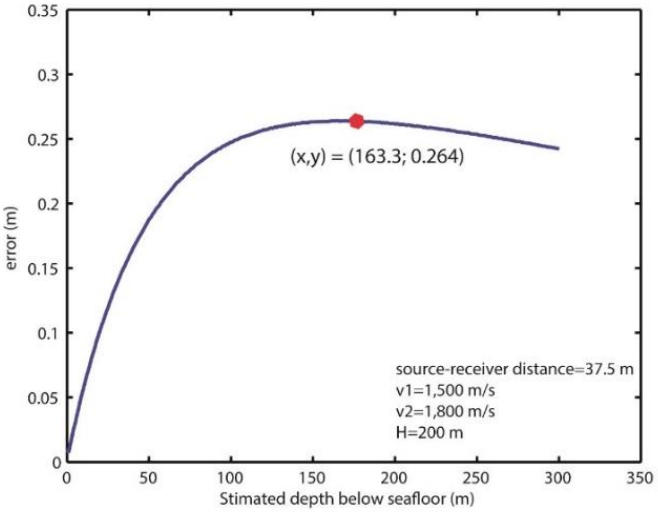

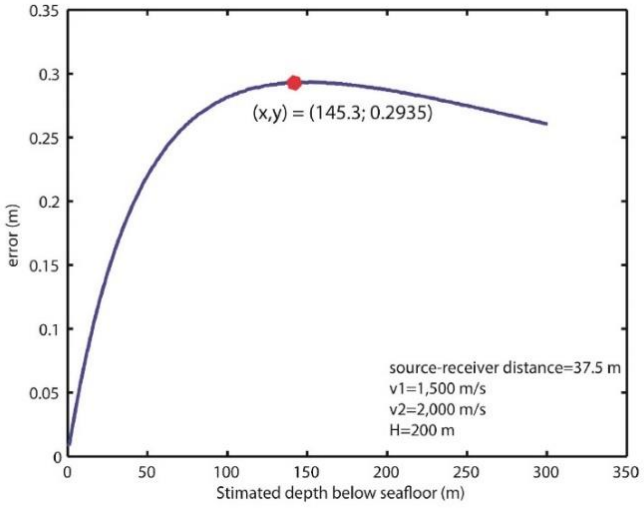

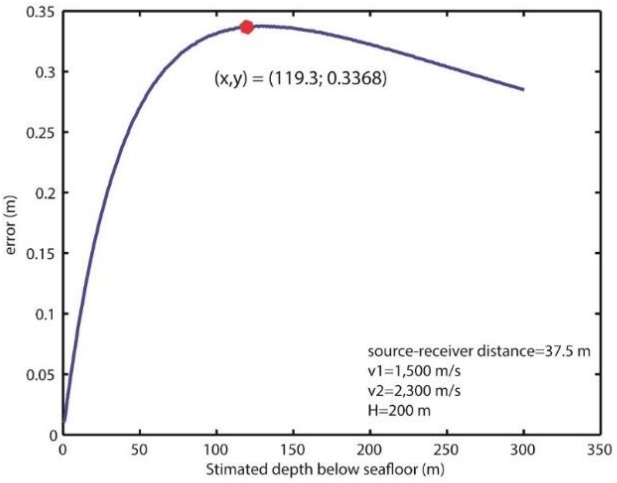

Figure A5. Error curves associated with the geometric arrangement as a function of the thickness of the sedimentary infill. Three V_P values were used: 1,800, 2,000 and 2,300 m/s.

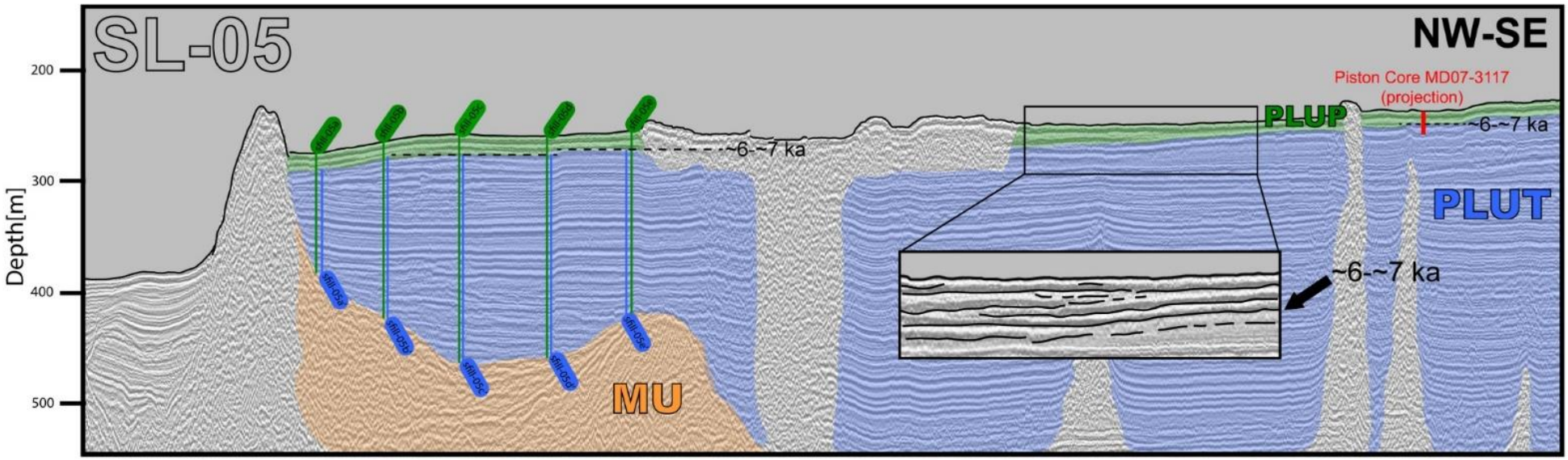

Figure A6. Seismic reflection profile (SL-05) migrated to distance [m] using V_P= 2,000 m/s, showing the measurement sites in the Parallel Laminated Unit (PLU) above the Moraine Bank Unit (MU, orange). PLU (post-glacial sedimentary infill) contains two sub-units: a lower one corresponding to a transgressive phase (PLUT, blue) and overlying strata corresponding to the progradational phase (PLUP, green). Green measurement sites (sfill-05-nn) correspond to the total of the sedimentary column. Blue measurement sites (sfill-05-nn') correspond to a partial sedimentary column limited by the ~6-~ 7 kyrs (found in Piston Core MD07-3117) when the sea level stabilized in the area during the early to mid-Holocene (Lambeck et al., 2002; 2014). Inset (i) shows a top-lap inside the sedimentary infill that matches with the sea level stabilization limit.

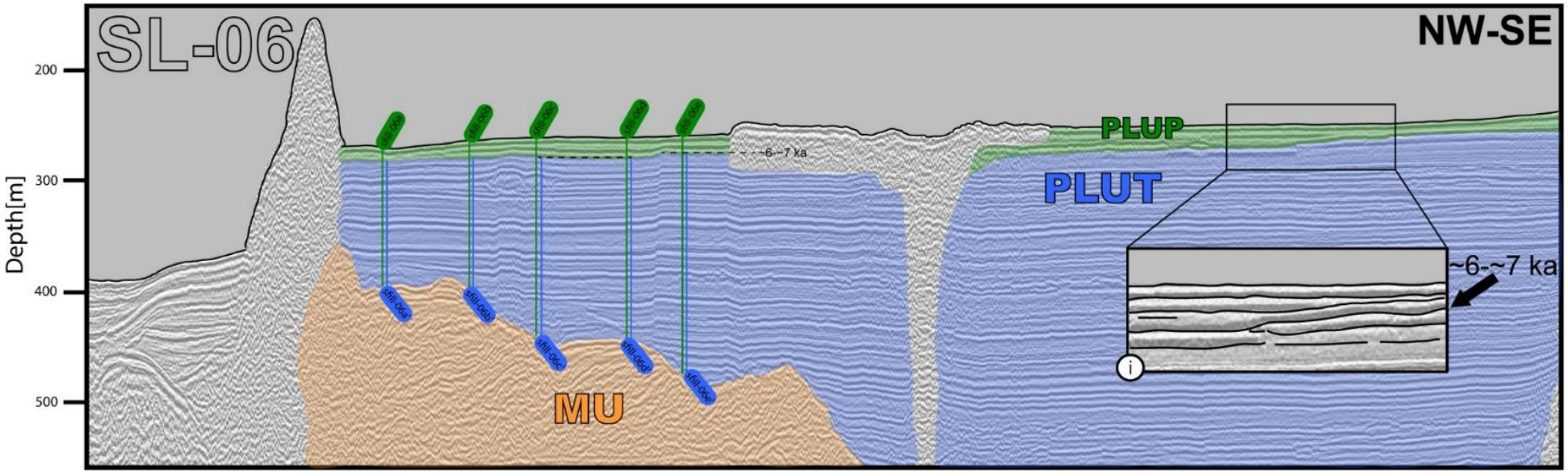

Figure A7. Seismic reflection profile (SL-06), showing the measurement sites in the Parallel Laminated Unit (PLU) above the Moraine Bank Unit (MU, orange). Green measurement sites (sfill-06-nn) correspond to the total of the sedimentary column. Blue measurement sites (sfill-06-nn') correspond to a partial sedimentary column limited by the ~6-~7 kyrs (Lambeck et al., 2002; 2014). Inset (i) shows a top-lap inside the sedimentary infill that matches with the sea level stabilization limit.

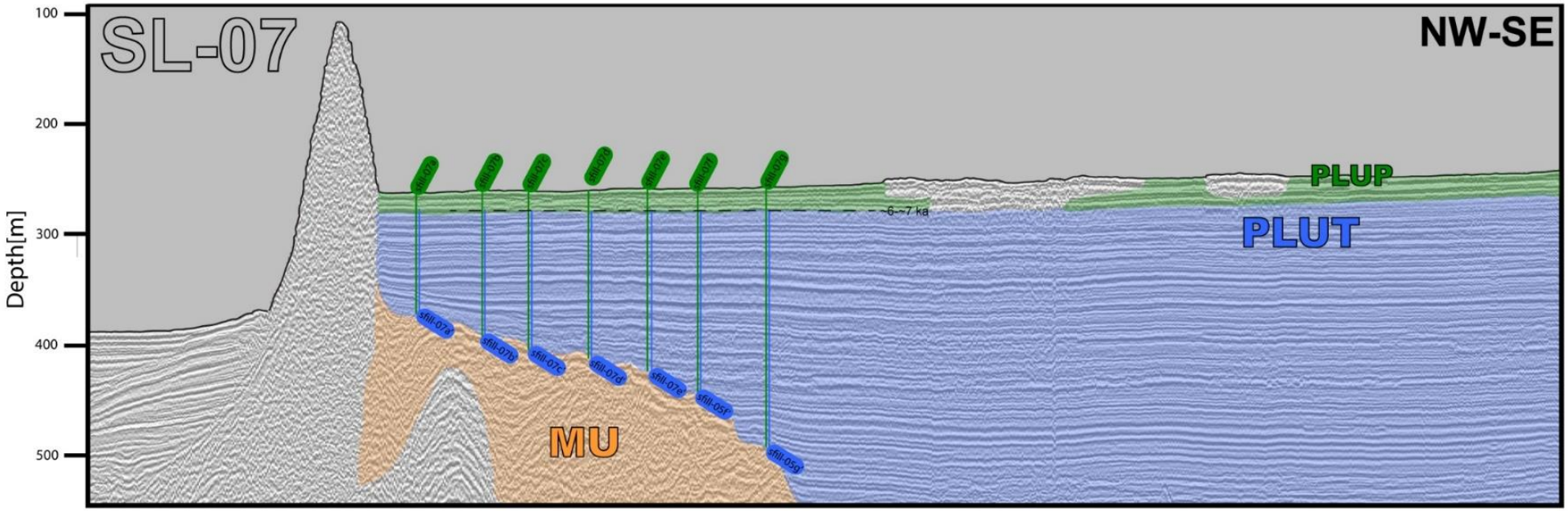

Figure A8. Seismic reflection profile (SL-06), showing the measurement sites in the Parallel Laminated Unit (PLU) above the Moraine Bank Unit (MU, orange). Green measurement sites (sfill-06-nn) correspond to the total of the sedimentary column. Blue measurement sites (sfill-06-nn') correspond to a partial sedimentary column limited by the ~6-~7 kyrs (Lambeck, 2002; 2014).

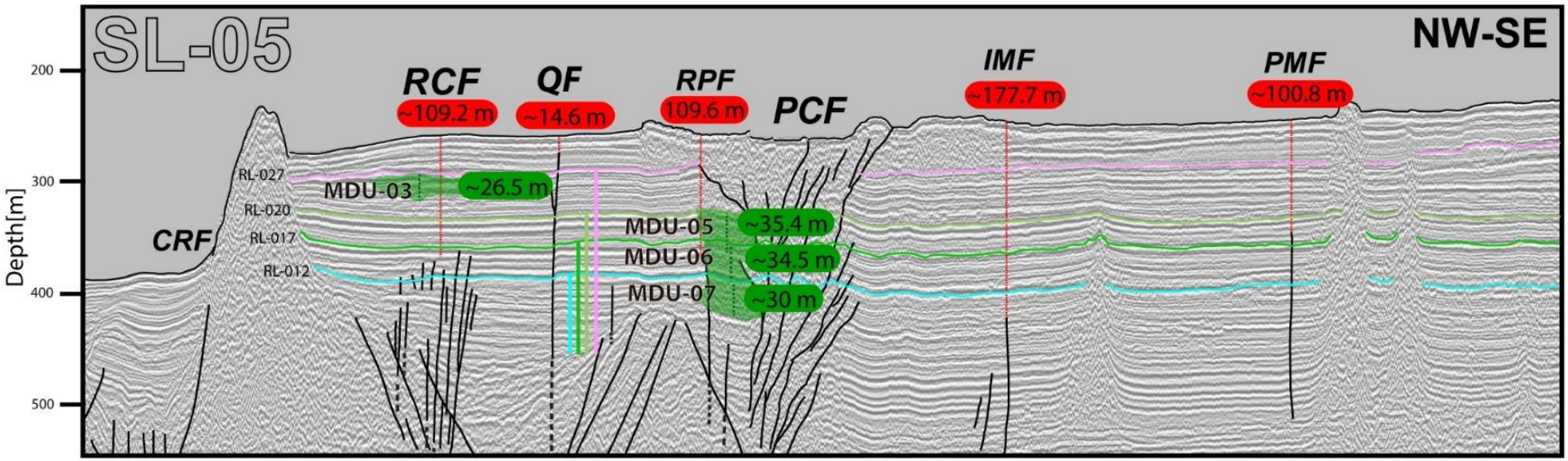

Figure A9. Seismic reflection profile (SL-05) migrated to distance [m] using V_P: 2,000 m/s, showing the distances from the seafloor to the tip faults observed in the Aysén fjord (red labels). Mass Deformed Units (MDU) are highlighted in green, its thickness is shown in green labels. Reflectors (R-012, R-017, R-020 and R-027) interpreted as paleo-seafloor (MDU's upper limit) are shown.

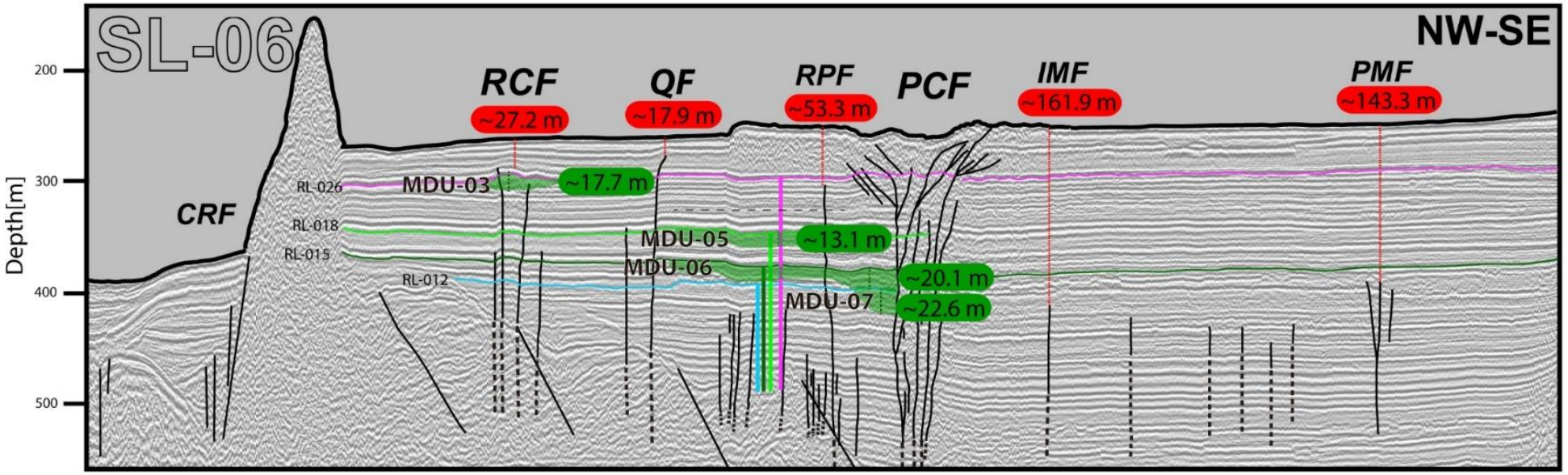

Figure A10. Seismic reflection profile (SL-06) migrated to distance [m] using V_P: 2,000 m/s, showing the distances from the seafloor to the tip faults observed in the Aysén fjord (red labels). Mass Deformed Units (MDU) are highlighted in green, and corresponding thicknesses are shown in green labels. Reflectors (R-012, R-015, R-018 and R-026) interpreted as paleo-seafloor (MDU's upper limit) are shown.

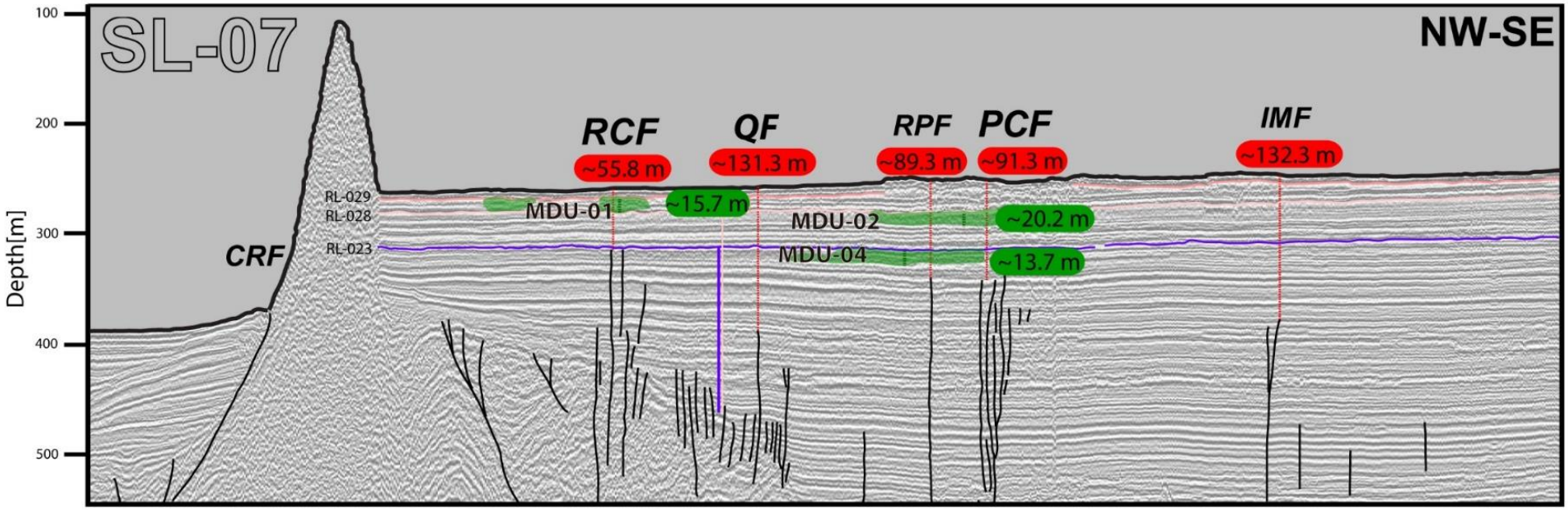

Figure A11. Seismic reflection profile (SL-07) migrated to distance [m] using V_P: 2,000 m/s, showing the distances from the seafloor to the tip faults observed in the Aysén fjord (red labels). Mass Deformed Units (MDU) are highlighted in green, and corresponding thicknesses are shown in green labels.

Measurement site	Infill thickness [m]	Measurement site	pre-6-7 kyrs Infill thickness [m]	Sedimentation rates [m/yr]
sfill-05a	109.0	sfill-05a'	93.9	0.016
sfill-05b	160.6	sfill-05b'	147.2	0.025
sfill-05c	206.3	sfill-05c'	189.0	0.031
sfill-05d	201.5	sfill-05d'	184.8	0.031
sfill-05e	167.2	sfill-05e'	149.5	0.025

Table A2. Measurement results using SL-05. Thickness of sedimentary infill are expressed in meters and sedimentation rates are in meters per year. First considering a constant deposition of the entire sedimentary column, until ~6 kyrs.

Measurement site	Infill thickness [m]	Measurement site	pre-0.4 s Infill thickness [m]	Sedimentation rates [m/yr]
sfill-06a	126.5	sfill-06a'	114.7	0.019
sfill-06b	134.5	sfill-06b'	119.3	0.020
sfill-06c	181.0	sfill-06c'	164.7	0.027
sfill-06d	183.9	sfill-06d'	166.6	0.028
sfill-06e	217.1	sfill-06e'	202.1	0.034

Table A3. Measurement results using SL-06. Thickness of sedimentary infill are expressed in meters and sedimentation rates are in meters per year. First considering a constant deposition of the entire sedimentary column, until ~6 kyrs.

Measurement site	Infill thickness [m]	Measurement site	pre-0.4 s Infill thickness [m]	Sedimentation rates [m/yr]
sfill-07a	111.5	sfill-07a'	95.7	0.016
sfill-07b	134.4	sfill-07b'	117.2	0.020
sfill-07c	145.6	sfill-07c'	127.6	0.021
sfill-07d	153.8	sfill-07d'	134.8	0.022
sfill-07e	166.5	sfill-07e'	146.0	0.024
sfill-07f	188.1	sfill-07f'	168.1	0.028
sfill-07g	237.0	sfill-07g'	216.7	0.036

Table A4. Measurement results using SL-07. Thickness of sedimentary infill are expressed in meters and sedimentation rates are in meters per year. First considering a constant deposition of the entire sedimentary column, until ~6 kyrs.

	Sed. rates [mm/yr]
Using 12 kyrs as MU's top age and 6 kyrs as upper limit	
SL-05	25.48
SL-06	25.58
SL-07	23.96
Average sed. rate	25.00
Using 12 kyrs as MU's top age and 7 kyrs as upper limit	
SL-05	30.57
SL-06	30.69
SL-07	28.75
Average sed. rate	30.01
Using 17.3 Kyr as MU's top age and 6 kyrs as upper limit	
SL-05	13.53
SL-06	13.58
SL-07	12.72
Average sed. rate	13.28
Using 17.3 Kyr as MU's top age and 7 kyrs as upper limit	
SL-05	14.84
SL-06	14.90
SL-07	13.96
Average sed. rate	14.57

Table A5. Sedimentation rates estimated for four possible scenarios from the last glacial maximum to the current sea level stabilization in Aysén fjord. These scenarios are based on C^{14} ages obtained by Vargas et al. (2013) from local moraines (Aysén fjord's proximities); late-glacial glacier advancements in southernmost South America (Patagonian Andes; Sugden et al., 2005; Hein et al., 2010; Glasse et al., 2012); and the sea level stabilization during the early to mid-Holocene (Lambeck et al., 2002; 2014).

Text A2. Reflectors offsets correlation with Buried MDU

By studying the relative position of fault markers in stratigraphic sequences, it is common to observe an increase in their separation further from the fault tip. In active faults, this feature is attributed to coseismic and postseismic slip distribution. Faults that cut Quaternary sediment have important implications, since as layers become older, a greater number of seismic events have displaced it. This principle considers the concept of accumulated offset, and it is often used along normal faults in postglacial sediment due to its potential to identify an accumulated displacement history across multiple seismic cycles (e.g., Bull et al., 2006; Barnes & Pondard, 2010; Pondard & Barnes, 2010). Optimal conditions established by Barnes & Pondard (2010) for carrying out these studies are that the sedimentation rate exceeds vertical displacement rates along a fault for extended time periods covering multiple seismic cycles and that active faulting can generate surface ruptures. This produces a tectonic depression filled with sediment during the aseismic phase, which preserves fault scarps between successive ruptures.

In the Aysén fjord, the modern sedimentation rate is estimated as being between ~1.9 and ~3.0 m/ka (Salamanca & Jara, 2003; Van Daele et al., 2013), which are considered medium-low sedimentation rates for fjords and inlets (Syvitski et al., 1987) but high sedimentation rates with respect to tectonics. On the Quitralco Fault (QF),

growth strata are observed near the surface, indicating a slip rate higher than the deposition rates at least for the last thousands of years (Figures A12b and A12c).

Although Punta Cola Fault (PCF) corresponds to a dextral-inverse fault, the remarkable reflectors offsets size (Figures A12e and A12f) allows us to propose that slip rates on this fault are also greater than the depositional rates since the last deglaciation.

We used depth-converted seismic profiles to assess vertical accumulated offsets caused by PCF and QF, using up to 28 reflectors, covering almost the entire postglacial sedimentary infill. As expected, the offset increases with depth and within the curves, and offset peaks escape this general tendency, as can be observed from the comparison of reflectors' position versus the vertical offset for each fault analyzed, and the accumulated offsets curves. (Figures A12h and A12i).

Considering that PCF activity during 2007-AYSS generated surface submarine rupture associated with a medium magnitude earthquake (M_w 6.2), and that other structures were activated at depth as well, it is possible to interpret the occurrence of peaks within the vertical separation curves of stratigraphic horizons as surface ruptures associated with paleo-earthquakes (Figure A12).

We propose that buried MDUs were formed in the same way as MDU-00 (i.e., the 2007 submarine rockslides). The hypothesis is based on the geometry, the presence of thrust structures, and mainly in their thickness, due to the relationship between larger vertical and horizontal distances from the source, higher impact velocities, and the energy transfer that results in clear seabed deformation (*Van Daele et al., 2013*). Considering the upper limit of buried MDU as paleo-seafloors (Figures A9, A10 and A11), these sedimentary wedges are approximately coeval with the offset-peaks and represent additional evidence for paleoearthquakes with similar characteristics to the 2007 M_w 6.2 event (Figures A12h and A12i).

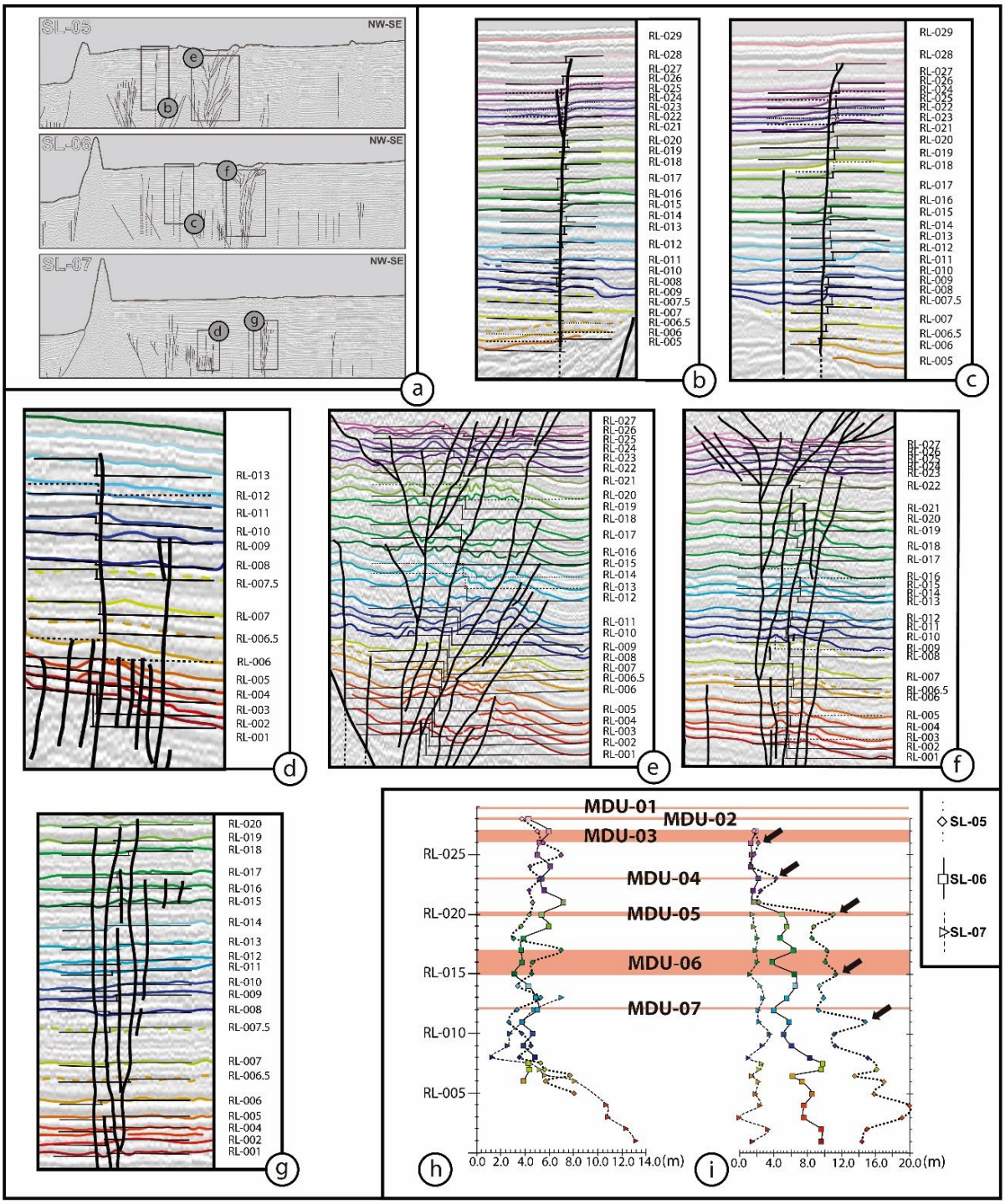

Figure A12. Detail of the displaced reflectors for the Punta Cola fault and Quitralco fault in the SL-05, SL-06 and SL-07 seismic profiles. Migration to distance using a velocity of 2.000 m/s. (a) The figure shows the insets for the calculation for each fault and its vertical offsets. (b) QF in SL-05. (c) QF in SL-06. (d) QF in SL-07. (e) PCF in SL-05. (f) PCF in SL-06. (g) PCF in SL-07. (h) and (i) offset vs. reflector position graph showing QF and PCF (respectively) accumulated offset for each seismic profile. MRDUs top reflector positions (red stripes). Offsets peaks, which we correlate to the horizon events associated with MRDUs top reflector.

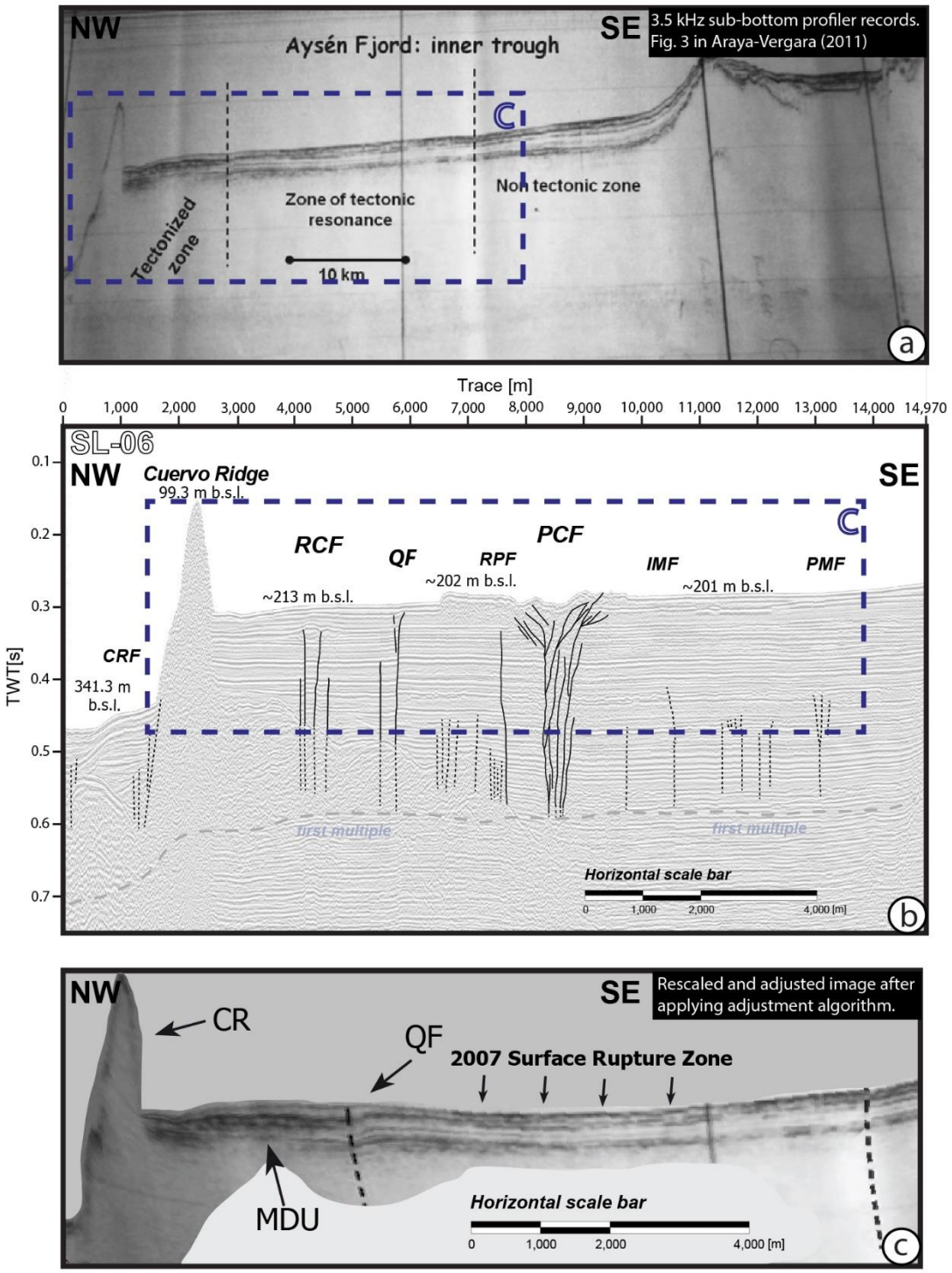

Figure A13. Seismic reflection profile (inner-fjord segment), subparallel to our seismic lines. (a) The original 1995 seismic profile form CIMAR-01 survey (from Araya-Vergara, 2011) (b) Our SL-06 profile works as a reference framework. Segmented inset indicates the segment that we compared. Our interpreted structures were also added as reference points. (c) Part is the post-processed image. QF: Quitralco Fault; MDU: Mass Deformed Unit; CR: Cuervo Ridge.

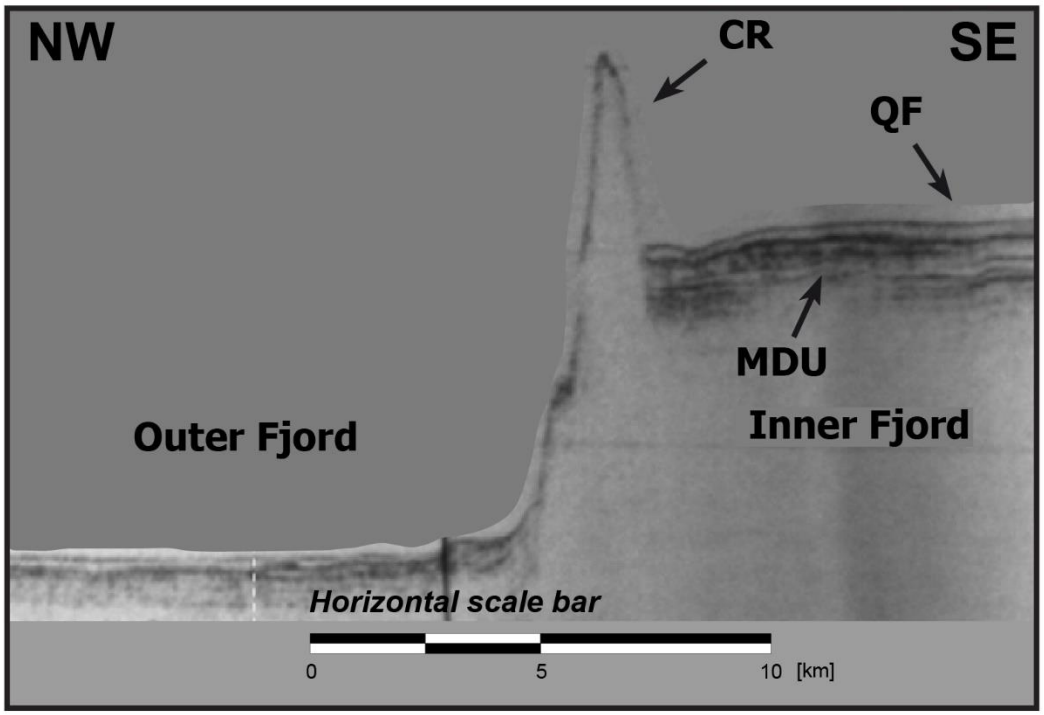

Figure A14. Seismic reflection profile (western segment), subparallel to our seismic lines (modified from Araya-Vergara, 2011). QF: Quitralco Fault; MDU: Mass Deformed Unit; CR: Cuervo Ridge.

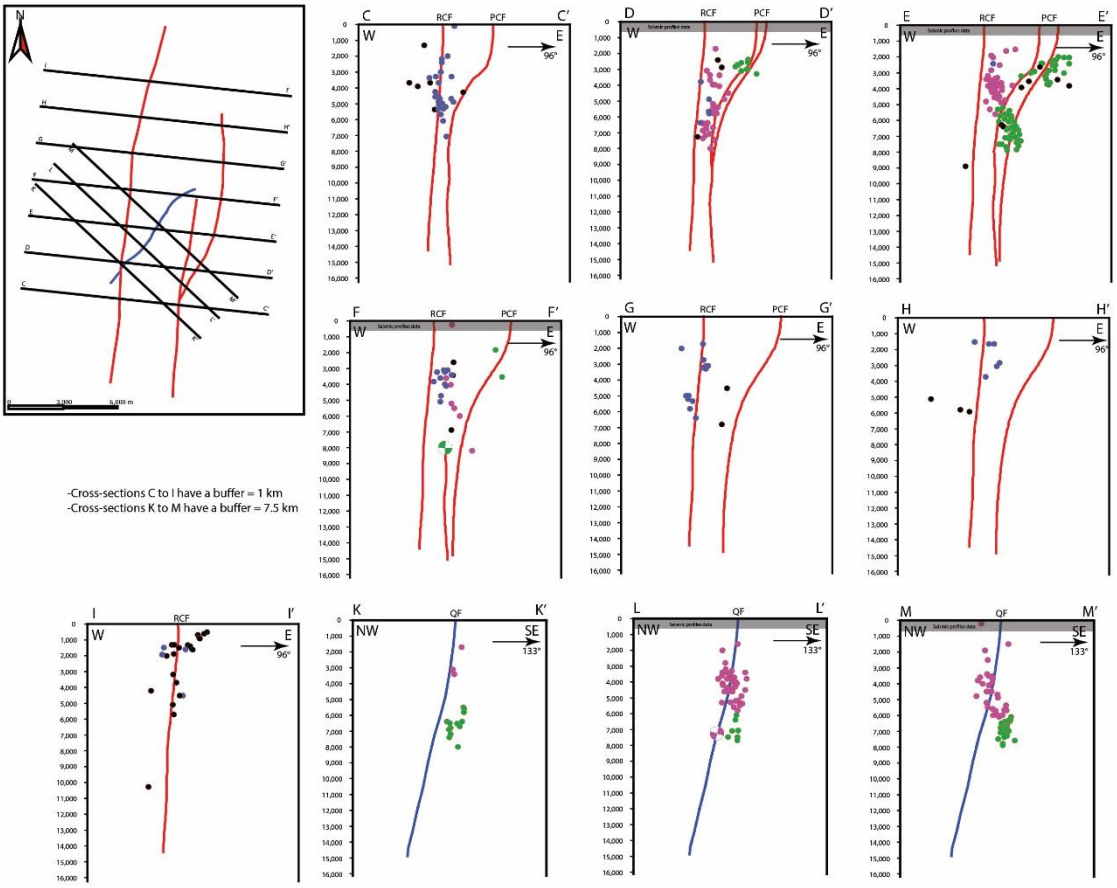

Figure A15. Cross sections used in the construction of the 3d geometric model of the Liquiñe-Ofqui Fault System in the Aysén Fjord. Vertical scale is in meters.

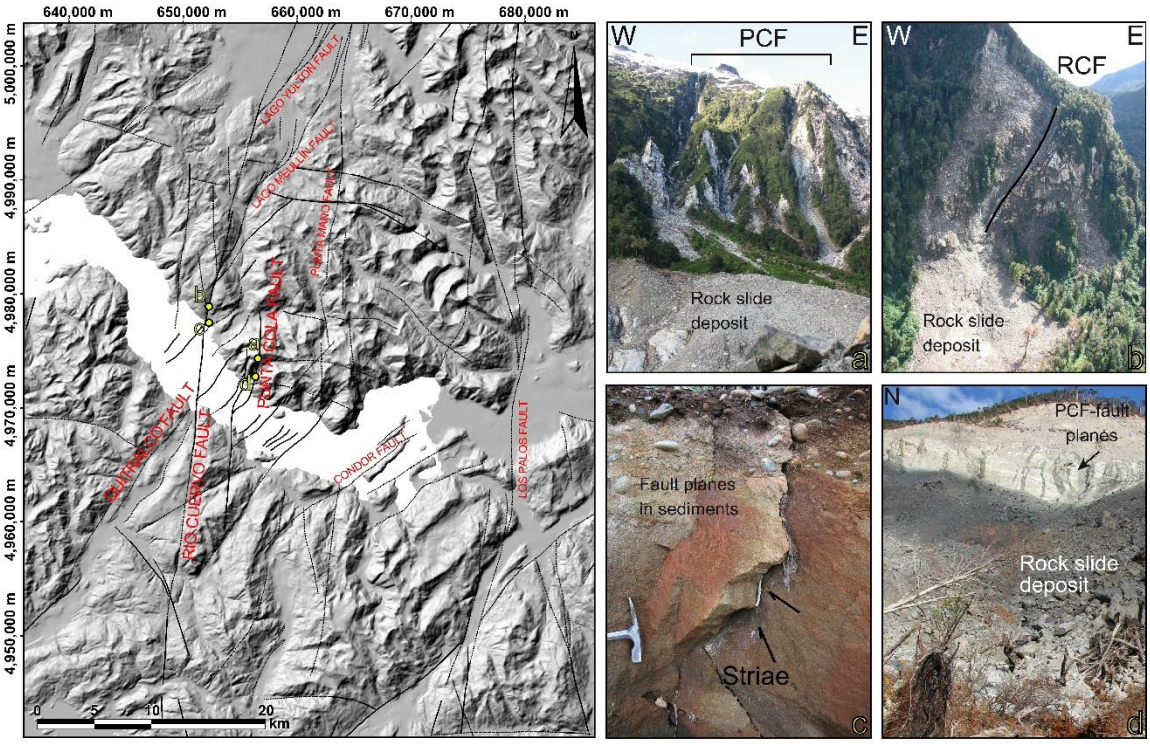

Figure A16. Left: Tectonic map showing fault traces, interpreted from the observation of aerial photographs, satellite images, topographic and bathymetric data, sub-bottom profile data and field recognition [modified from Vargas et al., 2013]. The main structures are Río Cuervo Fault and Punta Cola Fault. This faults are interpreted as the main branch of the Liquiñe-Ofqui Fault System in the area. Punta Mano Fault, Los Palos Fault, Lago Meullín Fault, Lago Yulton Fault, and Río Cóndor Faul are equivalent to Río Mañihuales Fault (Thomson, 2002; Cembrano et al., 2002), Quitralco Fault (Cembrano et al., 1996a, 2002; Thompson, 2002), and Río Blanco Fault. Yellow points indicate the location of four photos highlighting recent activity in the faults investigated in this work [from Vargas et al., 2013]. (a), (d) Punta Cola Fault. (b), (c) Rio Cuervo Fault

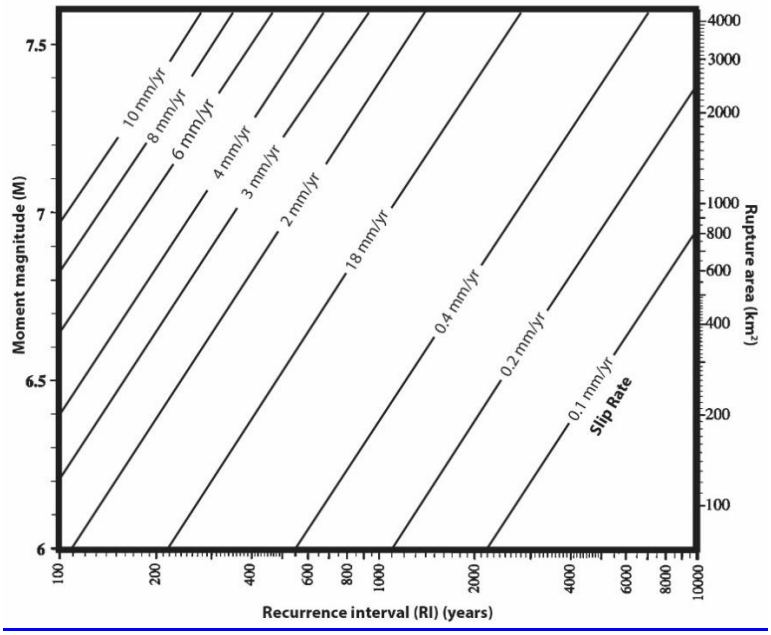

Figure A17. Plot of relations between fault parameters (area and slip rate) and potential earthquake characteristics (magnitude, repea time). From Shaw & Suppe (1996).

Appendix B

Coyhaique River talweg and geomorphological domains

In CRB, three geomorphological domains are distinguished which were defined based on the following criteria: i) topographic profile and slope variations in Coyhaique River talweg line (Figure B2a), ii) transverse and longitudinal topographic profiles to the valley (Figures B2b to B2d, Figure B3), iii) geological and geomorphological maps (Figures B1 and 4.4). This allows us to observe notable differences in at least three aspects: the Coyhaique River, the morphology of the valley, and the glacial surfaces (S_n) areal extension.

Although S_n surfaces were recognized from these transversal profiles, they were legitimized by showing lateral continuity between profiles (Figure B1). They are at different heights with different preservation states. In addition, we present evidence of glacial erosion (roches moutonnées and glacial striations) and glacial deposition (lodgment till and fluvioglacial deposits). The average height of each Sn surfaces is shown in Table B1.

The Coyhaique River runs ~64 km along its talweg line (Figures B1 and B2a). From its river mouth in Simpson River to the eastern basin border, the river raises its elevation from 250 to 750 m a.s.l., with slopes that generally do not exceed 5°. Throughout this profile, three geomorphological domains were defined: A_1, A_2, and A_3.

Domain A_1

This domain extends between Simpson River mouth to the west and Las Bandurrias Bridge to the east. It is characterized by a few slope breaks along the talweg line, which raises its height eastward from 250 to 400 m a.s.l., on a ~18 km length. Both Artesa Coyhaique (AC) and Artesa Baguales (AB) have a well-developed U-shape in cross-section (Figure B2b and B2c).

In AC, three glacial surfaces are recognized, which are S_9, S_8, and S_7, from younger to older. They are characterized by heights between 350 and 360 m a.s.l., 460 - 500 m a.s.l. and 570 - 600 m a.s.l., respectively. The glacial origin of these surfaces is recognized from the presence of roches moutonnées and lodgment till deposits.

An older S_6 surface works as AB valley floor, with a 700 m a.s.l. average height. Other less obvious surfaces may correspond to older incision are at higher elevations in both glacial troughs. In the area close to Coyhaique River mouth on Simpson River, there is a fluvial terrace (Tf_1) at the height of 400 m a.s.l. (Figure 4.3b), which is evidence for a ~150 m recent Coyhaique River incision.

Domain A_2

It is defined between Bandurrias Bridge and the western Pampa El Diablo border (Figure B2a). In this domain, the river bed raises its elevation from 400 to 700 m a.s.l., on a ~20 km length. The most relevant feature of this talweg profile is the general slope change, evidenced in the eastern domain limit by a knickpoint (KP), and located at the western Pampa El Diablo border.

Indeed, eastward KP within domain A_3, the general slope profile is smoother than in the other two domains. This point shows the zone where upstream-down cutting is maximum, constituting an imbalance in the profile. Along with this, in this domain of the talweg line profile presents many breaks slope, suggesting a stepped morphology (Figure B2a). Although these changes could be generated by the interpolation used in the topographic terrain model (an artifact), their presence is supported by field observation. This domain of the Coyhaique river valley is broad and does not have a characteristic U-shaped cross-section shape.

The valley's southern flank, which corresponds to the watershed divide with Pollux River Basin, is made up of low peaks that do not exceed 1,000 m a.s.l., and gradually decrease their height eastward. S_6 and S_5 surfaces reach a maximum areal extent in this zone (Figure B1). On these surfaces rest most of the lagoons of this basin. S_6 surface is at the same height as KP and is where the general river profile acquires a steeper slope. Other relevant surfaces are S_4 and S_3, located at 850-870 m a.s.l. and 950-1,000 m a.s.l., respectively. Other older surfaces are at higher heights (S_2, S_1, S_0; Table B1).

One of the most relevant features in this domain is the strong river incision relative to S_4. The incision increases progressively westward, from a few tens of meters in the western Pampa El Diablo (Figure B3b) to 250 m in Las Bandurrias zone (Figure B2d).

The fluvial origin of this incision is evidenced by the V-shape valley cross-section (Figures B2d and B3a). Furthermore, the Coyhaique River erosional nature has left little presence of modern river deposits.

Domain A_3

It is defined between the western Pampa El Diablo boundary and the eastern CRB boundary, on Chile-Argentina Border. The talweg profile generally presents a smooth slope, with no breaks or abrupt changes (Figure B2a). Its height ranges between 700 to 725 m a.s.l., in a 20 km length. In this domain, the valley is wide and does not have a U-shaped cross-section (Figures B3b, B3c, and B3d). The watershed divide with Alto Mayo River is formed by gentle hills at 800 m a.s.l. with few peaks that exceed 1,000 m a.s.l.

S_6 and S_5 surfaces predominate up to Coyhaique Alto zone, with heights of 700 m a.s.l. and 750 - 775 m a.s.l., respectively. S_4 surface is distributed throughout the domain with heights ranging between 830 - 870 m a.s.l. Eastward of Coyhaique Alto S_3 is exposed, with heights ranging between 950 and 1,000 m a.s.l. The northern valley flank has the oldest surfaces (S_2, S_1, and S_0), ranging between 1,100 and 1,280 m a.s.l. on Meseta Boscosa.

Domain A_3 has no river incision, and the river bed is observed on the S_6 surface more eastward (Figures B3b, B3c, and B3d).

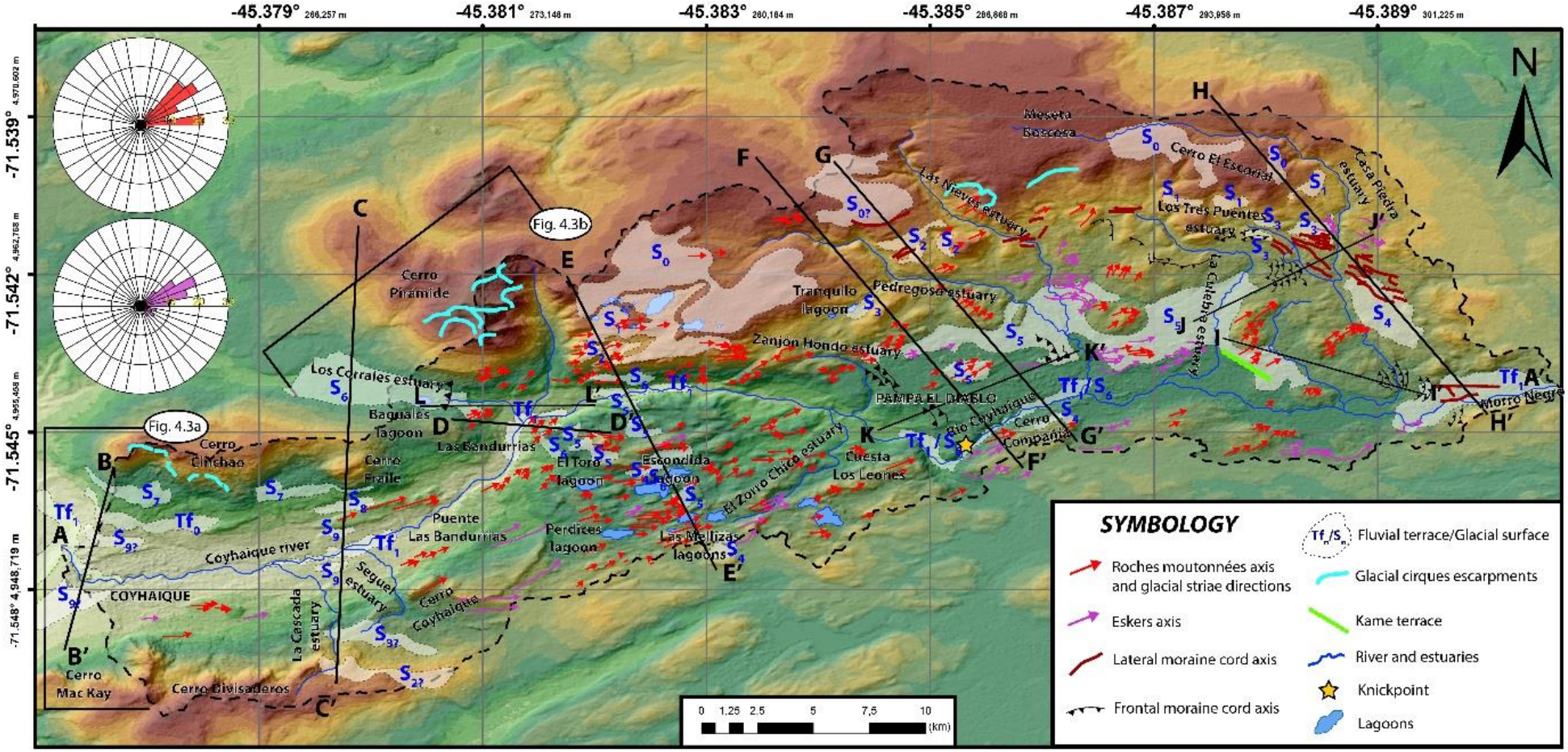

Figure B1. Geomorphological map of Coyhaique River Basin using a 30x30 m DEM (ASTER-GDEM). AA' to HH' are parallel and cross-section profiles used for the definition of the valley domains definition (A1, A2, and A3), and also for the hanging and cut glacial and river surfaces. Other important glacial landforms are indicated, such as glacial troughs, cirques, frontal and lateral moraine, and kame terraces. In particular, we present Rosetta diagrams for linear elements measured in this study area: Eskers (violet arrows) and Roche moutonnées (red arrows). After Arqueros (2004).

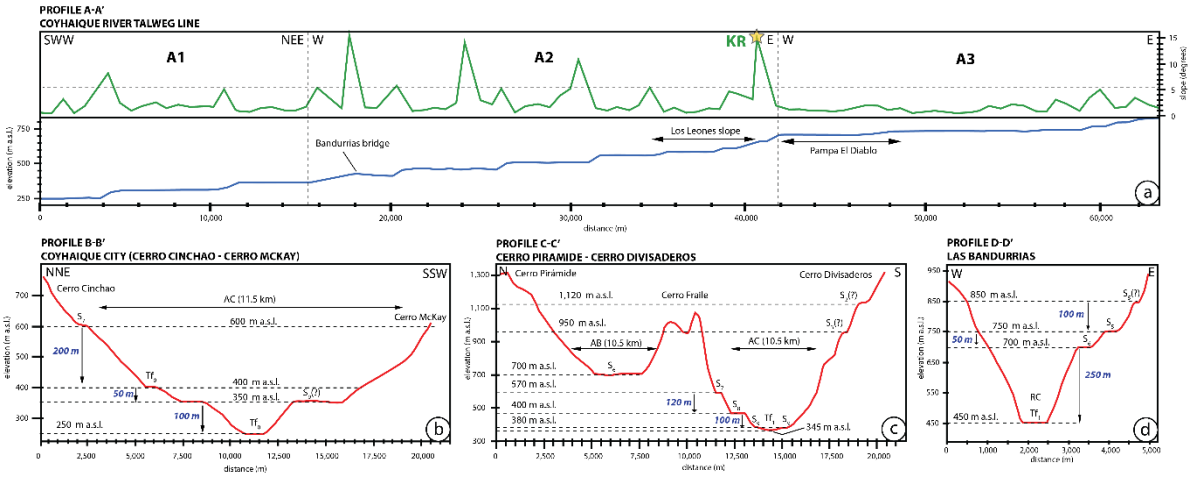

Figure B2. (a) Profile A-A ', Coyhaique River talweg line. This profile shows two lines. The green line shows slope variations within the topographic profile (blue line). We defined three geomorphological domains: A_1, A_2, and A_3. The only considerable break is KP (knickpoint, yellow star), highlighting the river slope change between A_1 and A_2. Other breaks could be model artifacts. (b) Profile B-B' (cross-section), Coyhaique city (Cerro Cinchao - Cerro McKay). S_0, S_1: on till deposits. (c) Profile C-C' (cross-section) Cerro Pirámide - Cerro Divisaderos. S_0, S_1: on Roche moutannées, lodgment till deposits, Kic, and Ohb rocks. S_2 and S3: on background till. (d) Profile D-D' (cross-section) Las Bandurrias. S_3, S_5: on Roche moutannées. S_4: on lodgment till deposits. After Arqueros (2004).

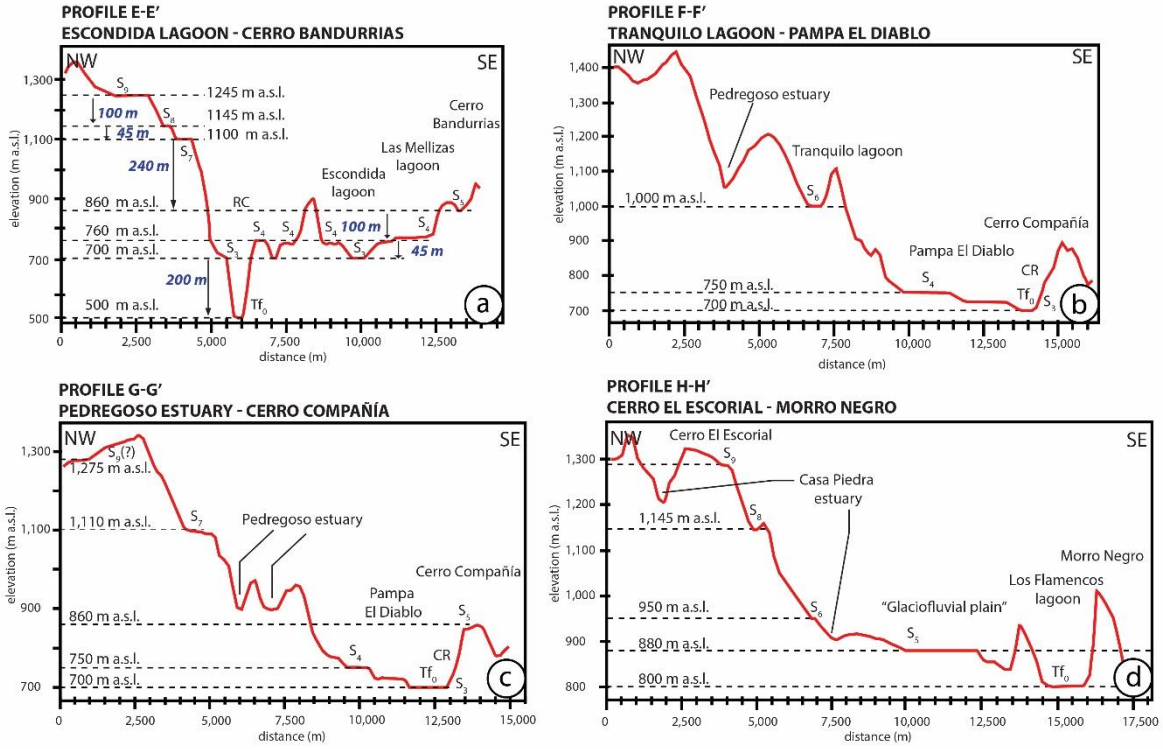

Figure B3. (a) Profile E-E' (cross-section) Escondida lagoon - Cerro Bandurrias. S_3, S_7, S_8: on granite stocks, lacustrine deposits, roche moutannées. S_4: on roche moutannées and logment till deposits. S_9: on stocks and lodgment till deposits. (b) Profile F-F' (cross-section) Tranquilo lagoon - Pampa El Diablo. S_3, S_4: on roche moutannées and lodgment till deposits. S6: on lodgment till deposits. (c) Profile G-G' (cross-section) Pedregoso Estuary - Cerro Compañía. S_3: on glaciofluvial and lodgment till deposits. S_4, S_7, S_9: on roche moutannées and lodgment till deposits. S_5: on roche moutannées. (d) Profile H-H' (cross-section) Cerro El Escorial - Morro Negro. S_5: glaciofluvial plain. S_6, S_9: on lodgment till deposits. S_8: on lodgment till deposits and Ksd rocks. Tf_0: current channel; Tf_1: abandoned fluvial terrace; AB: Artesa Baguales; AC: Artesa Coyhaique; CR: Coyhaique River. After Arqueros (2004).

Table B1. Height for glacial surfaces. In profiles transverse to the Coyhaique River Talweg (Profile A-A').

Profile	Distance from the mouth (km)	Tf_1	Tf_0	S_9	S_8	S_7	S_6	S_5	S_4	S_3	S_2	S_1	S_0
B-B′	2.1	250	400	350		600							
C-C′	12.6	345		360	460	570	700			950	1,120		
D-D′	22.3	450					700	750	850				
E-E′	27.4	500					700	760	860		1,110	1,145	1,245
F-F′	41.6	700					700	750		1,000			
G-G′	44.4	700					700	750	860		1,100		1,275
H-H′	62.0	800							880	950		1,145	1,290

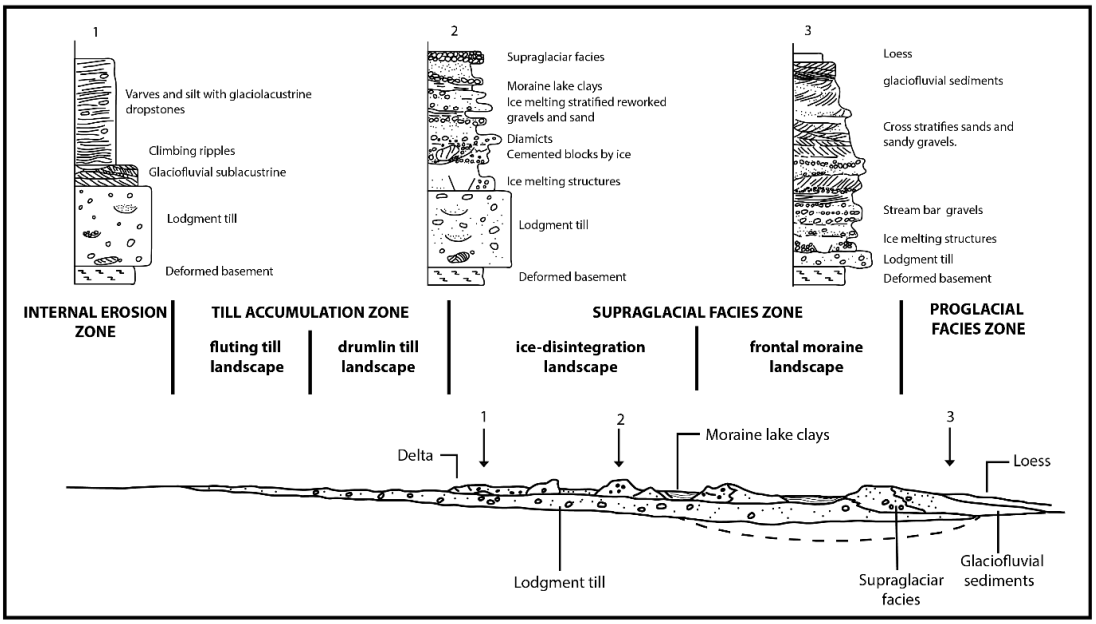

Figure B4. Zonational model showing a general terrestrial glacial landscape and deposited facies. Thegeneral schematic columns that can be deposited in each zone are observed. These deposits can have a thickness that ranges between 5 and 50 m (after Sugden & Jhon, 1976)

Los Flamencos System

Los Flamencos System is defined as a drift located at the eastern CRB border. It is represented by lodgment till deposits and landforms as lateral moraines and eskers. It is exposed eastward Casa Piedra - Los Tres Puentes estuaries and, to a lesser extent, northward Las Culebras Estuary springs (Figure 4.4).

The deposits associated with this system are in a disconformity contact over basement rocks associated with Cerro Mirador - Casa Piedra Dome Complex (Ksd, Figure 4.2) and underlie in erosive contact with Coyhaique Alto System deposits. In some zones, it is covered, in a concordance or an erosive contact, by Quaternary sediments.

i. Glacial landforms

Lateral moraines

Seven lateral moraine are recognized Cerro Las Tetas - Punta Del Monte skirts, northward El Culebra Estuary source, and between this and Las Nieves Estuary (Figure B1). These moraines are at heights ranging between 1,000 and 1,100 m a.s.l., with a W-E strike. They have between 500 and 920 m long, between 4 and 10 m wide, and between 3 and 5 m high. They consist of till with angular rhyolitic-dacitic clasts, with poor matrix of sands and silt (15 - 25%). Clasts have a 10 mm thick brown-yellow weathering rings. This unit overlays lodgment till deposits of the same system.

Eskers

They consist of six glaciofluvial eskers located westward Cerro La Leona, between 950 and 1,000 m a.s.l. (Figure B1). They have a length ranging between 300 and 750 m, 3 and 5 m wide, and a height that does not exceed 5 m. The strikes vary NW-SE. They are composed of polymictic glaciofluvial gravel deposits, from subangular to subrounded clasts, with a coarse sand matrix. The clasts have 8 - 10 mm weathering rings.

ii. Stratigraphic column SC-02

Southward Veranada Casa Piedra, on the eastern bank of the same named estuary at the height of 914 m a.s.l., the sequence described below emerges (Figures 4.4, B5b, and 4.8b).

With an unknown base, a 4.2 m thick diamict is observed. The matrix is composed of fine silt to fine quartz sands. Most of the matrix has no structure, except in some sections where thin lamination is observed. Upward the matrix portion decreases, and clasts become more sub-rounded. This diamict is polymictic and includes andesitic clasts, tuffs, and granitoid. Still, the clasts are mainly angular and range between 25 and 30%. Some of them are striated and have an 8 - 12 mm weathering ring. The diamict is composed of a sandy gravel matrix leness, sand leness, and another of coarse sand with fine sand matrix, both solid and poorly selected. In

addition, 1 to 20 mm thick laminated fine sand intercalations is observed in clear contact with the diamict.

These sediments were deposited in situ in subglacial or englacial channels. Minor lenticular accumulations of varved silts, probably deposited in subglacial lagoons, are also observed. All these facies were deposited in a lodgment till the environment in a till accumulation zone (Figure B2b).

Upward, Coyhaique Alto System glaciofluvial gravels are present.

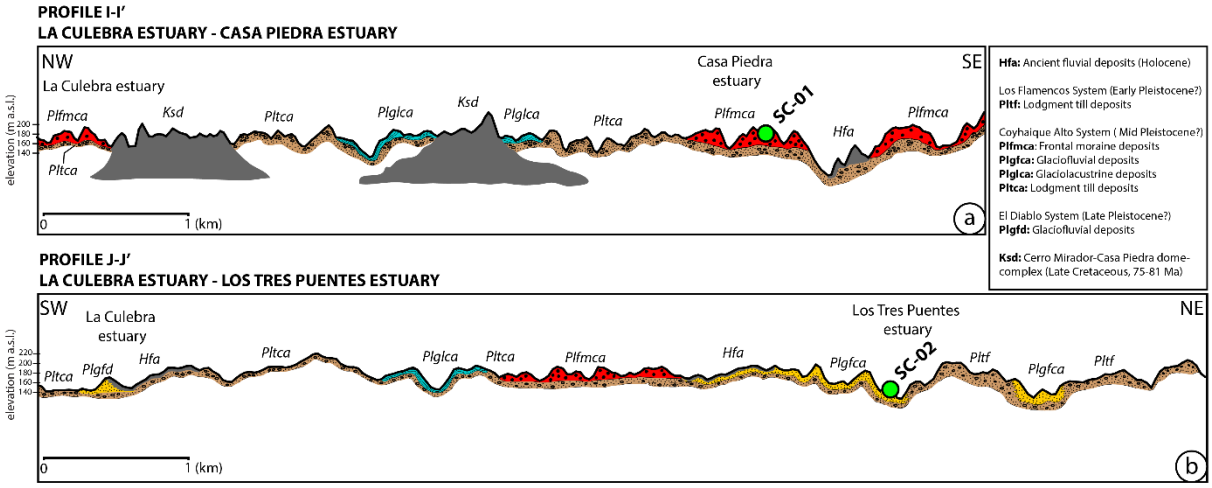

Figure B5. (a) Profile I-I' La Culebra Estuary - Casa Piedra Estuary (schematic cross-section). It shows the deposits and other units' arrangement, and the SC-01 site. (b) Profile J-J' La Culebra Estuary - Los Tres Puentes Estuary (schematic cross-section). It shows the deposits and other units' arrangement, and the SC-02 site.

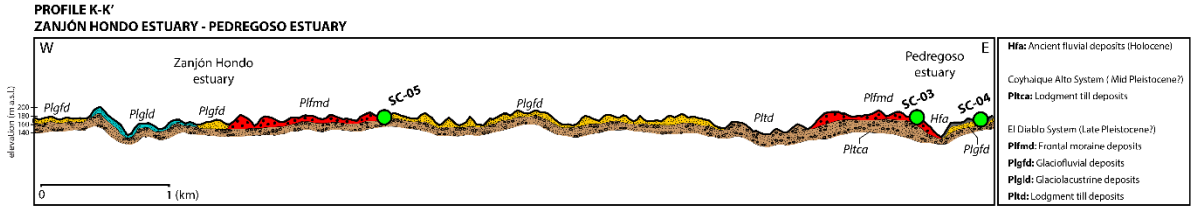

Figure B6. Profile K-K' Zanjón Hondo Estuary - Pedregoso Estuary (schematic cross-section). It shows the deposits and other units' arrangement, and SC-03, SC-04, and SC-05 sites.

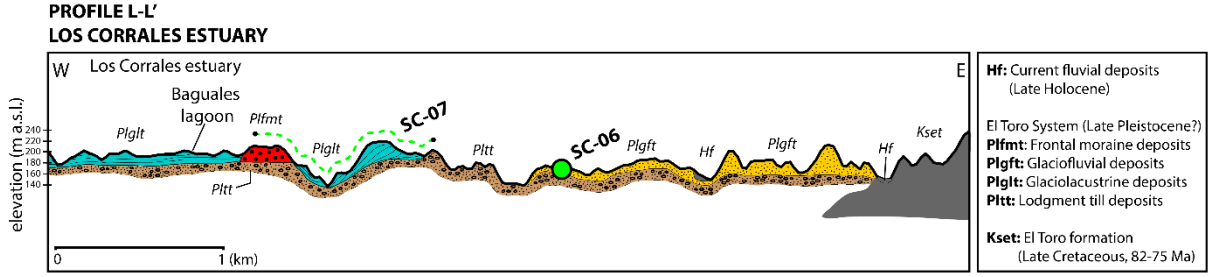

Figure B7. Profile L-L' Los Corrales Estuary (schematic cross-section). It shows the deposits and other units' arrangements and SC-06 and SC-07 sites.

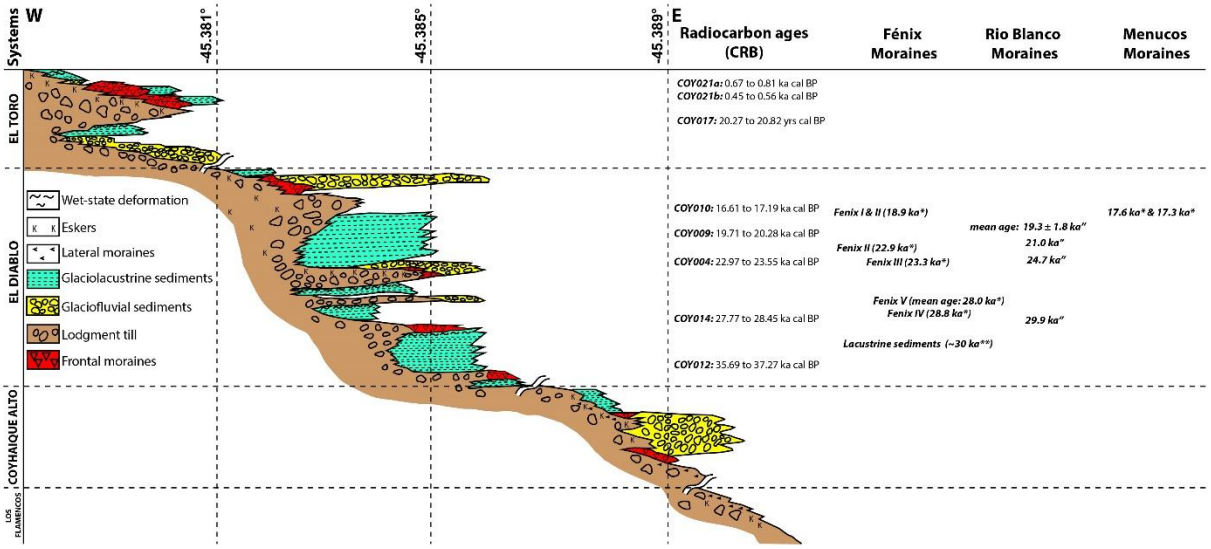

Figure B8. Integrated stratigraphic diagram. It shows the moraine systems in Coyhaique River Basin. Their different types of facies, and morphological units are shown. Environmental evolution during the glacial phasesrecognized is shown. Radiocarbon ages for El Diablo and El Toro systems are contrasted and correlated with chronologically equivalent drifts (Fénix, Río Blanco and Menucos moraines). Douglass et al., (2006) are indicated using a (*); Hein et al., (2010) using a (''); and Smedley et al., (2016) using (**).

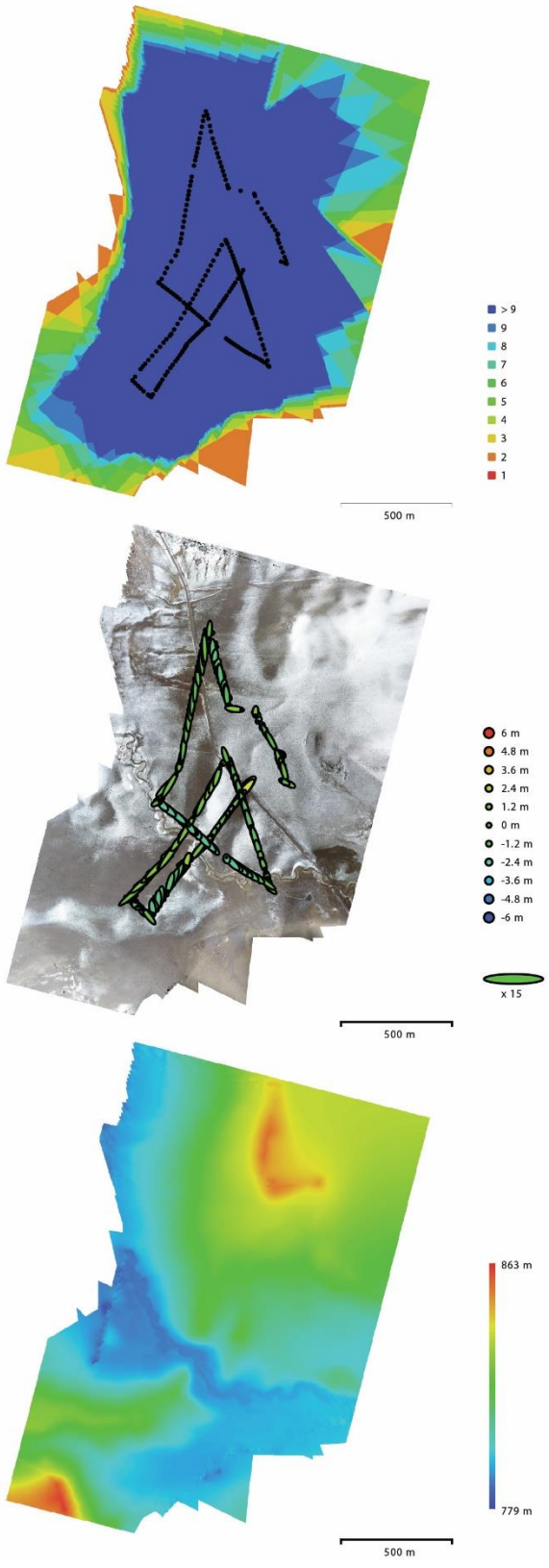

Figure B9. (a) Camera locations and image overlap in the Coyhaique Alto Zone (close to Coyhaique River). Number of images: 281; flying altitude: 314 m; ground resolution: 12.2 cm/pix; coverage area: 2.62 km²; camera stations: 281; tie points: 68,519; projections: 800,662; reprojection error: 1.1 pix. (b) Camera locations and error estimates. Z error is represented by ellipse color. X, Y errors are represented by ellipse shape. Estimated camera locations are marked with a black dot. (c) Reconstructed digital elevation model. Resolution: 48.6 cm/pix; point density: 4.23 points/m².

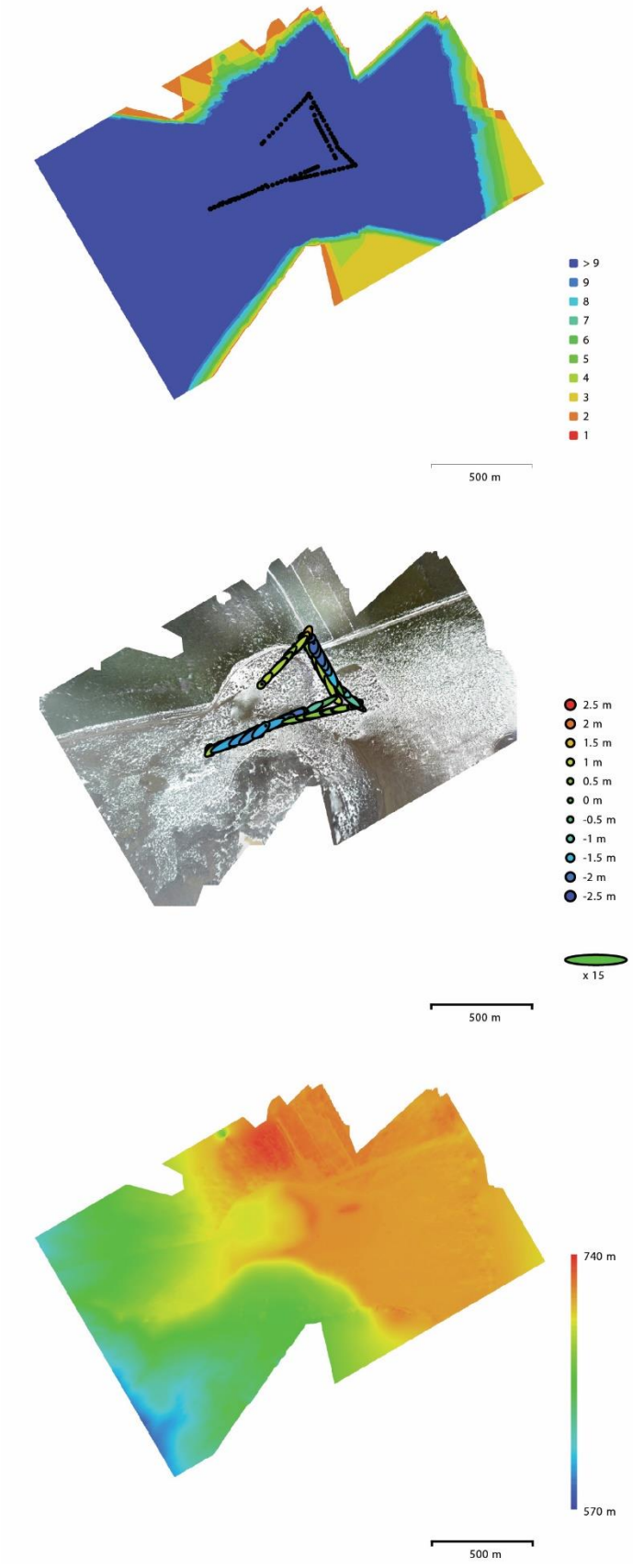

Figure B10. (a) Camera locations and image overlap in the Pampa El Diablo zone. Number of images: 141; flying altitude: 383 m; ground resolution: 14.8 cm/pix; coverage area: 2.56 km²; camera stations: 140; tie points: 34,664; projections: 459,315; reprojection error: 1.08 pix. (b) Camera locations and error estimates. Z error is represented by ellipse color. X, Y errors are represented by ellipse shape. Estimated camera locations are marked with a black dot. (c) Reconstructed digital elevation model. Resolution: 1.18 m/pix; point density: 0.714 points/m².

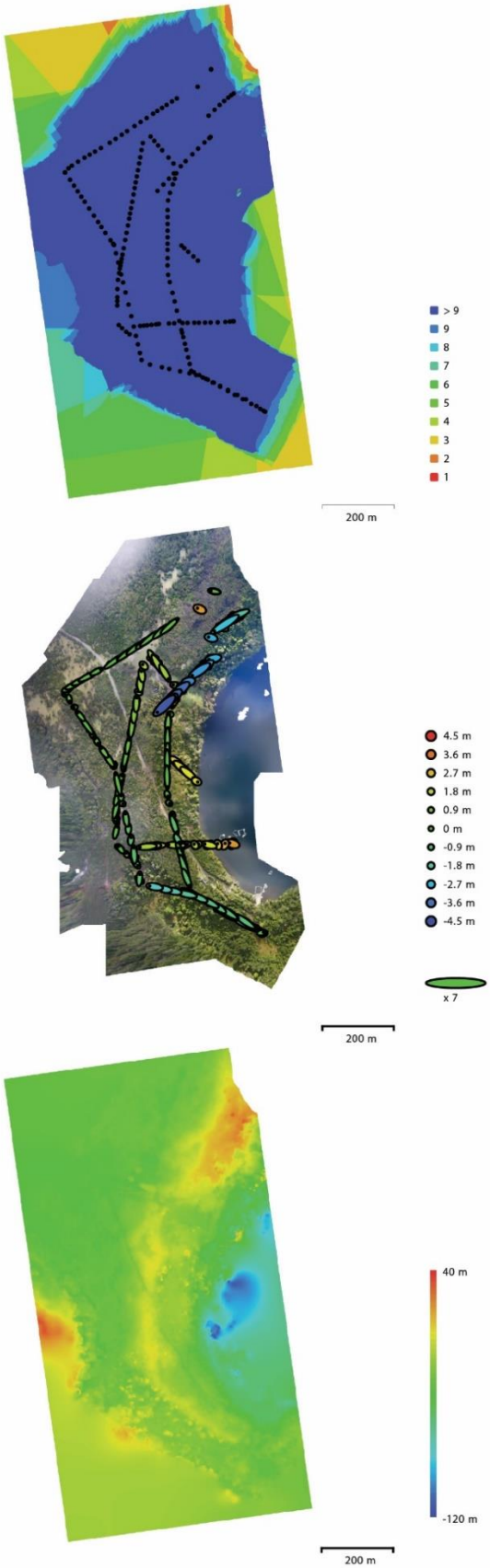

Figure B11. (a) Camera locations and image overlap in the Lake Riesco zone. Number of images: 192; flying altitude: 183 m; ground resolution: 6.95 cm/pix; coverage area: 0.896 km²; camera stations: 192; tie points: 144,086; projections: 656,424; reprojection error: 1.19 pix. (b) Camera locations and error estimates. Z error is represented by ellipse color. X, Y errors are represented by ellipse shape. Estimated camera locations are marked with a black dot. (c) Reconstructed digital elevation model. Resolution: 55.6 cm/pix; point density: 3.24 points/m².

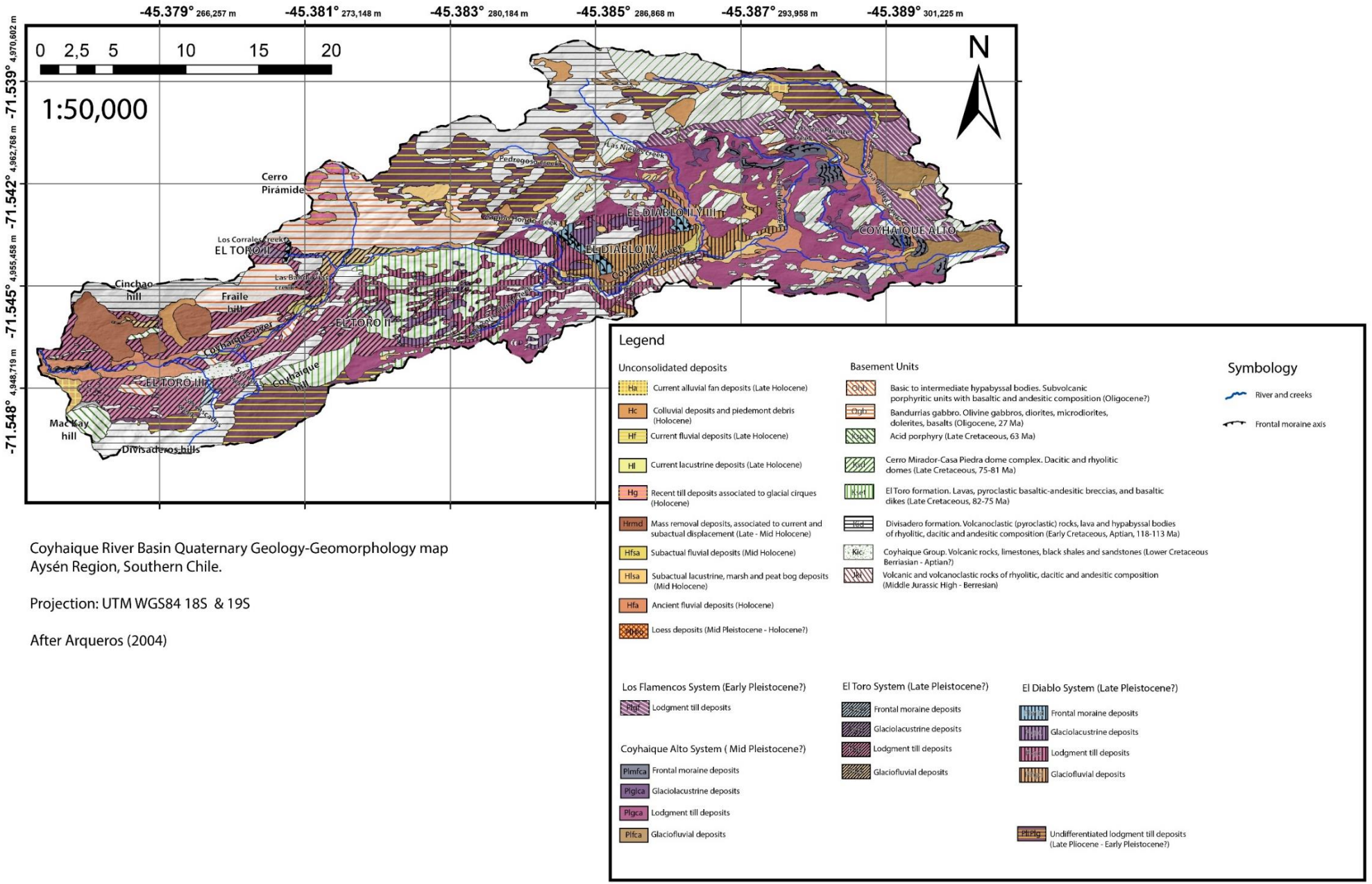

Figure B12. Coyhaique River Basin Quaternary geological-geomorphological map. (After Arqueros, 2004).

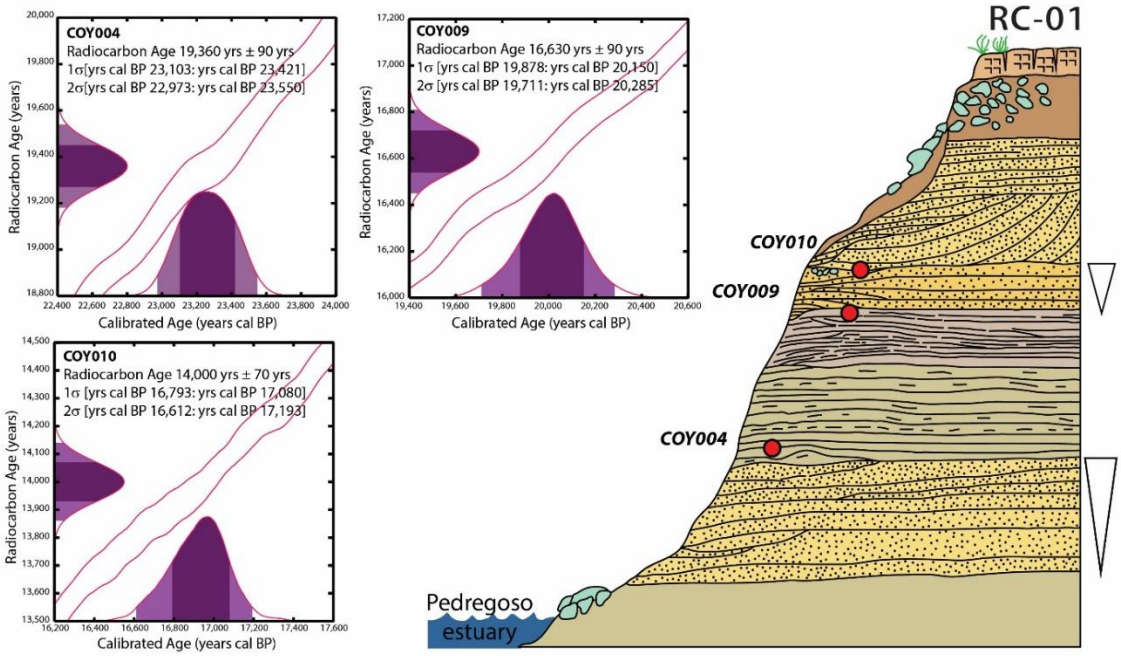

Figure B13. Schematic stratigraphic column RC-01. It represent the site where samples COY004, COY009, and COY010 were extracted. It is located close to Pedregoso Estuary and Coyhaique River confluence. Three graphs indicating the radiocarbon ages calibration for each sample are shown.

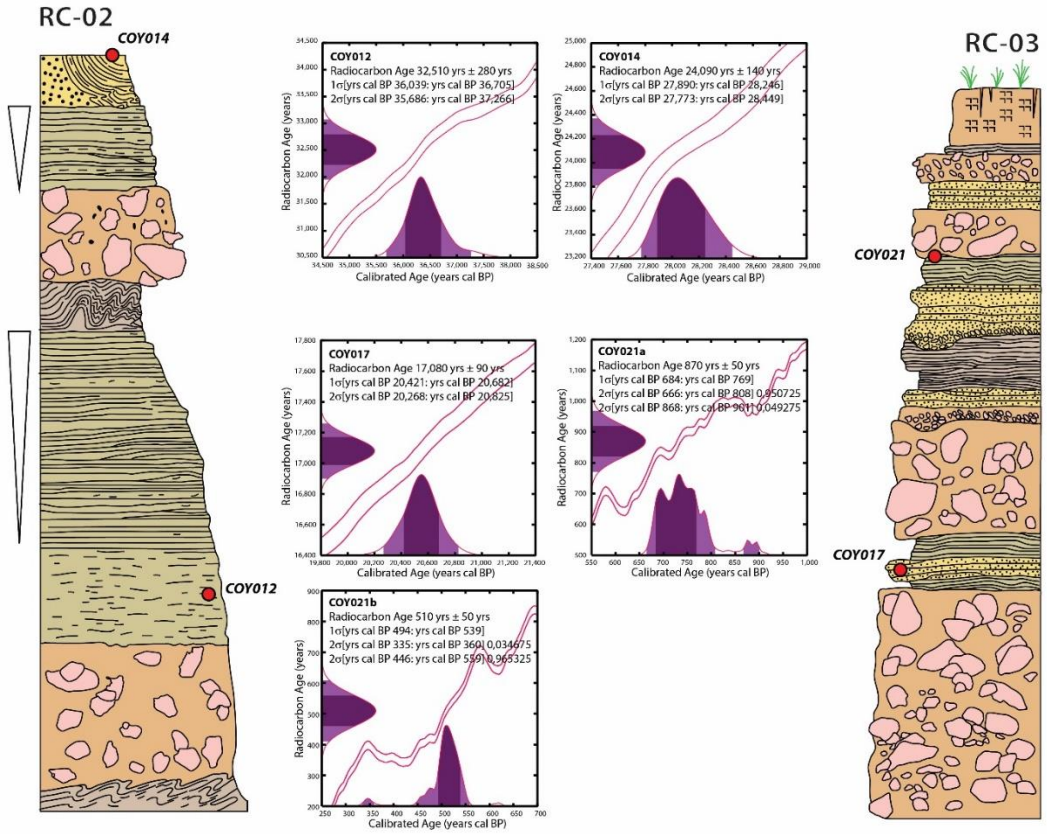

Figure B14. (a) Schematic stratigraphic column RC-02. It represent the site where samples COY012, and COY014 were extracted. It is located on Coyhaique River northern bank close to Pampa El Diablo. Two graphs indicating the radiocarbon ages calibration for each sample are shown. (b) Schematic stratigraphic column RC-03. It represent the site where samples COY017, COY021a, and COY021b were extracted. It is located close to Los Corrales Estuary and Coyhaique River confluence. Three graphs indicating the radiocarbon ages calibration for each sample are shown.

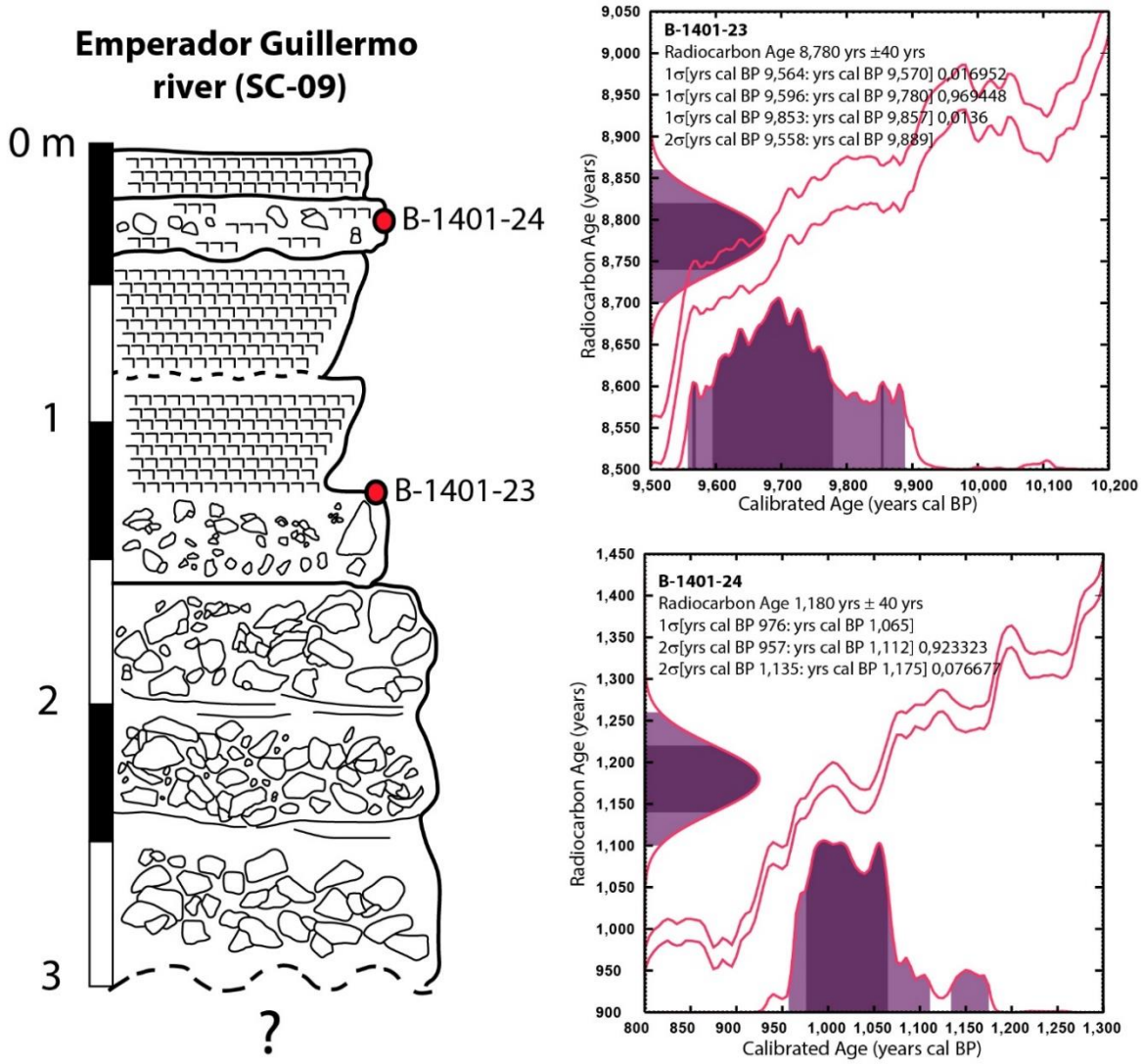

Figure B15. Stratigraphic column SC-09. It represents part of this glacial drift. It is located on Emperador Guillermo northern bank. It also shows the site where samples B-1401-23 and B-1401-24 were extracted. Two graphs indicating the radiocarbon ages calibration for each sample are shown.

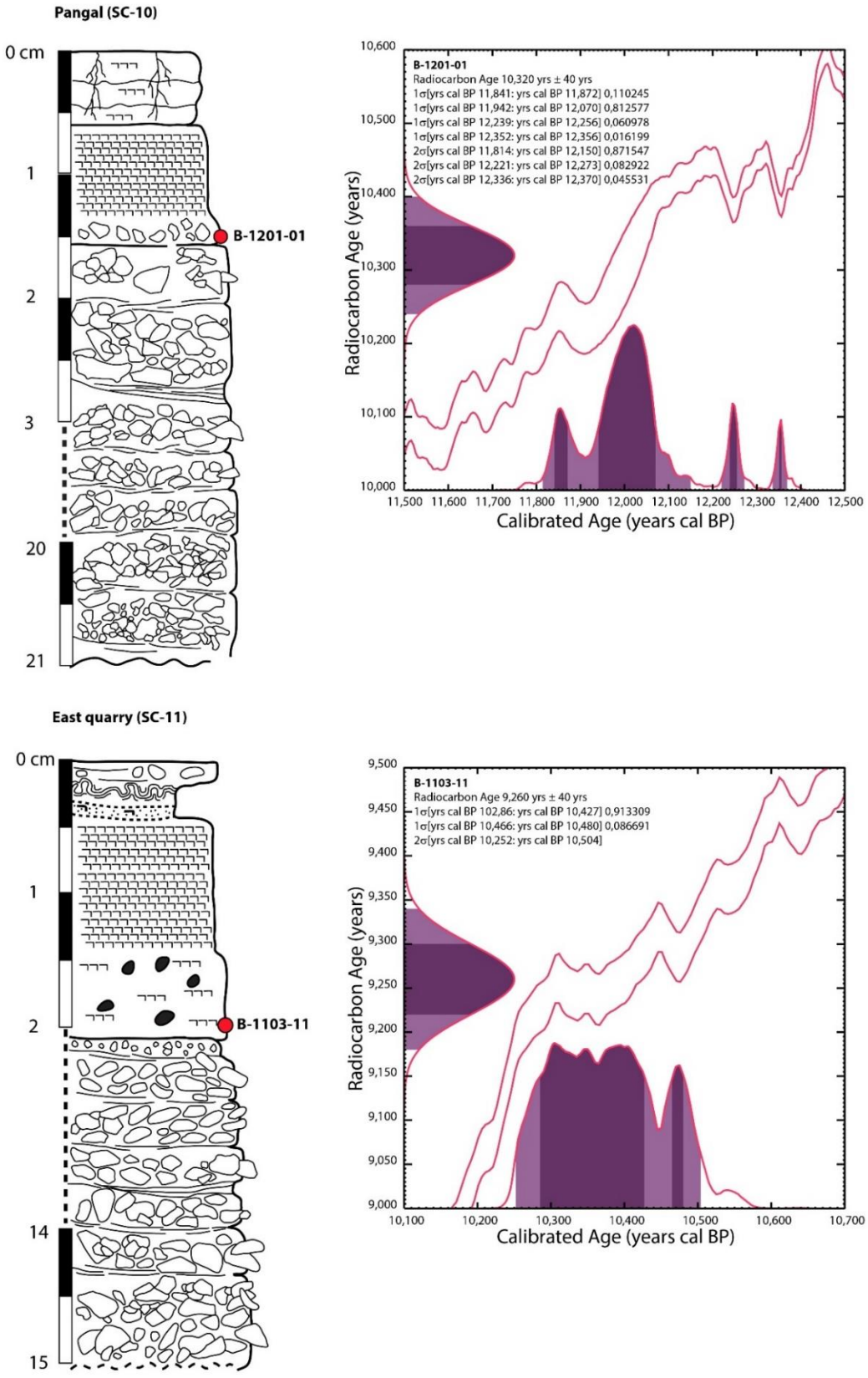

Figure B16. (a) Stratigraphic column SC-10. It represents part of a glacial drift. It is located close to the Pangal locality. It also shows the site where B-1201-01 was extracted. Graph indicates the radiocarbon ages calibration. (b) Stratigraphic column SC-11. It represents part of a glacial drift. It is located on the East Quarry locality. It also shows the site where B-1103-11 was extracted. Graph indicates the radiocarbon ages calibration.

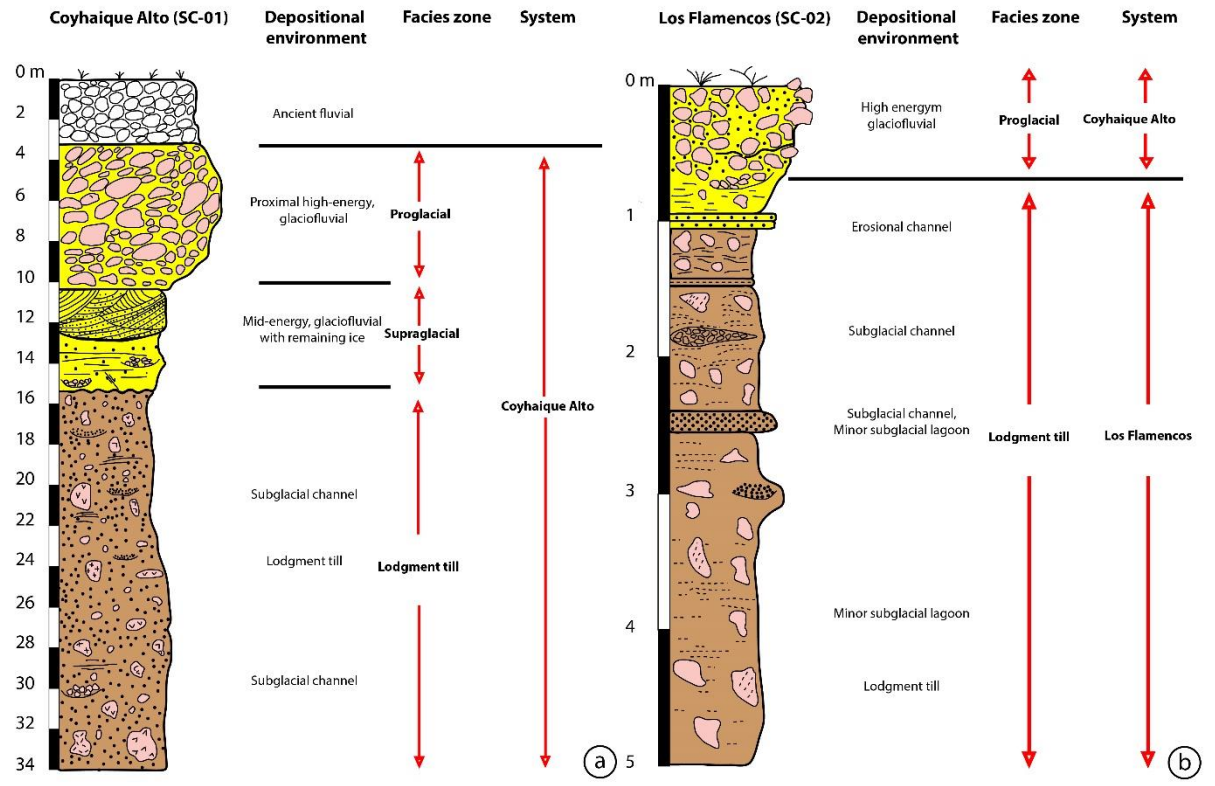

Figure B17. (a) Stratigraphic column SC-01. It represents part of the Coyhaique Alto System deposits. It is located on Casa Piedra Estuary, eastern bank. (b) Stratigraphic column SC-02. It represents part of the Los Flamencos and Coyhaique Alto systems deposits. It is located on Casa Piedra Estuary, eastern bank.

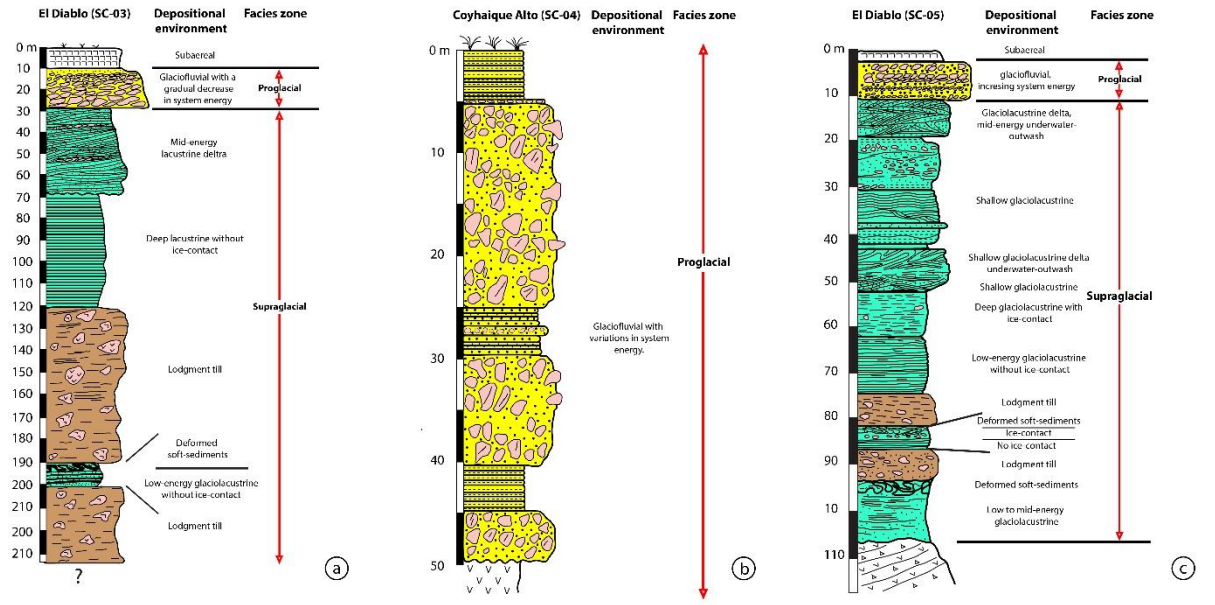

Figure B18. (a) Stratigraphic column SC-03. It represents part of El Diablo System deposits on the Coyhaique River northern bank. (b) Stratigraphic column SC-04. It represents part of El Diablo System deposits on Las Nieves and Pedregoso estuaries confluence. (c) Stratigraphic column SC-05. It represents part of El Diablo System deposits on the Coyhaique River northern bank.

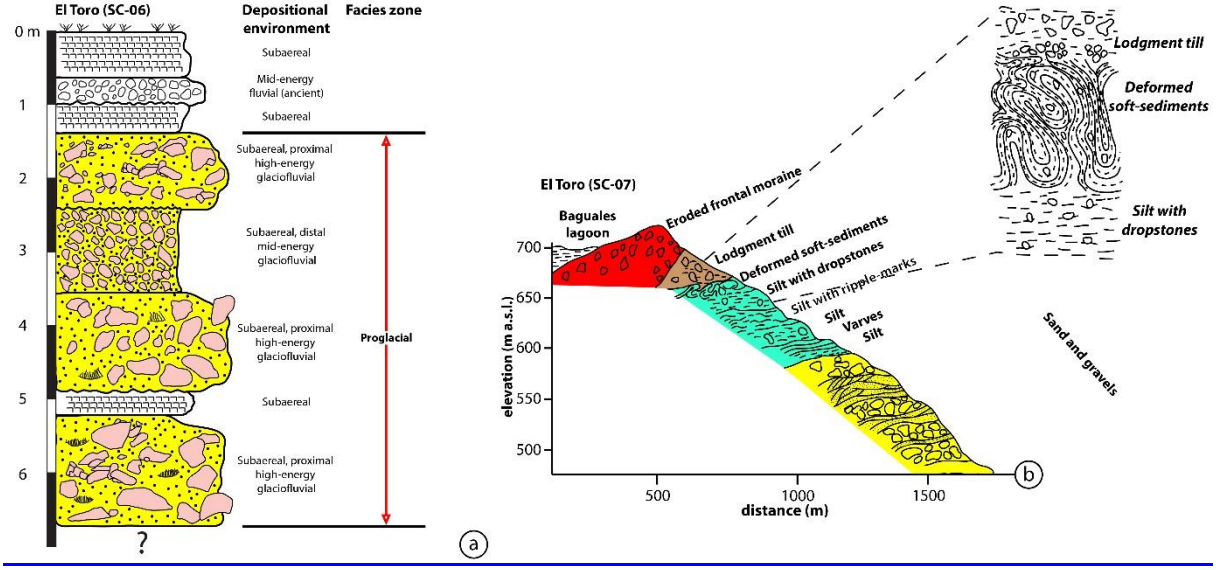

Figure B19. (a) Stratigraphic column SC-06. It represents part of El Toro System deposits located in Las Bandurrias. (b) Schematic stratigraphic profile SC-04. It represents part of El Toro System deposits close to the frontal moraine in Los Corrales Estuary.

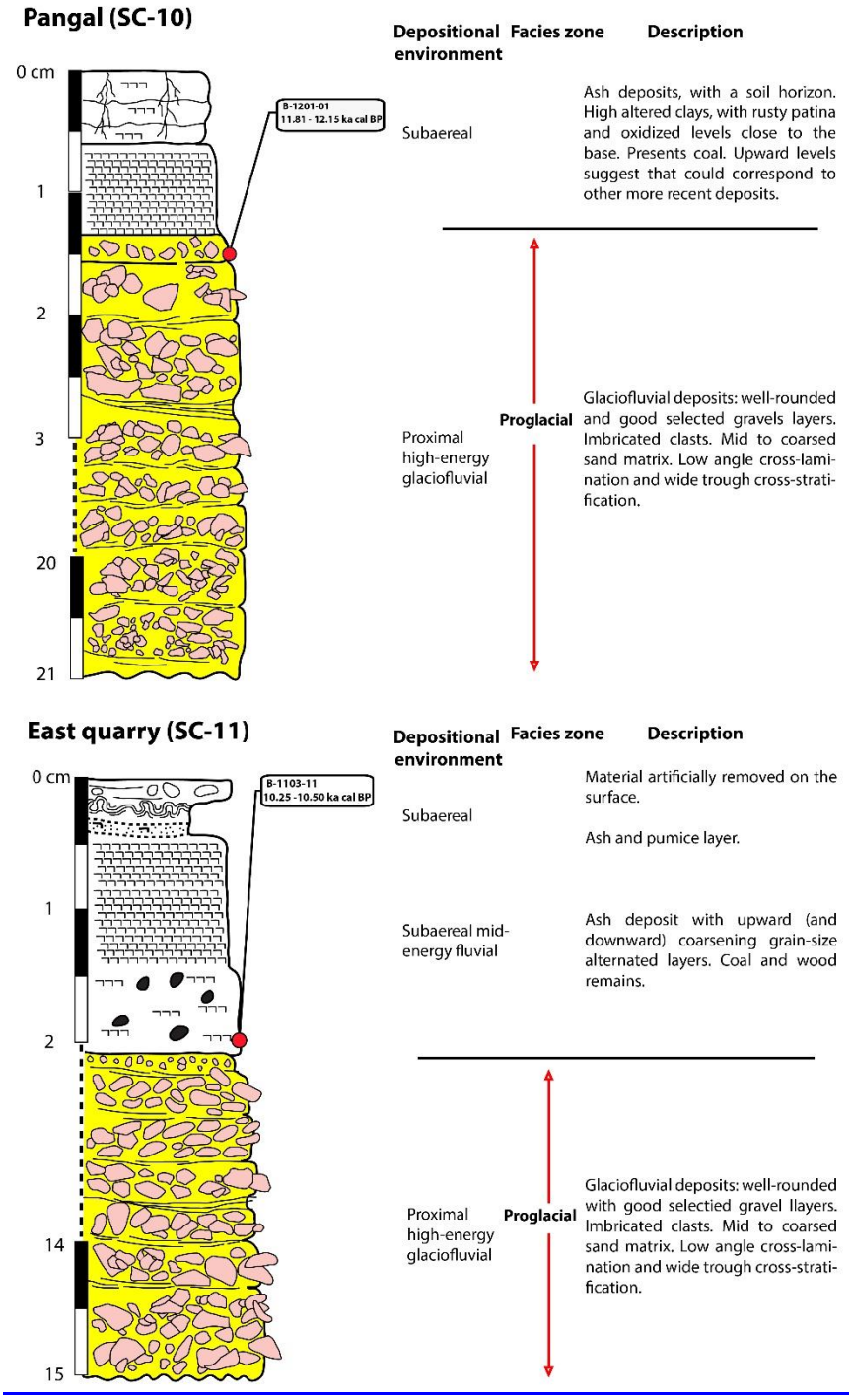

Figure B20. (a) Stratigraphic column SC-10. It represents a part of the glacial drift located close to the Pangal locality. It also shows the site where B-1201-01 was extracted. (b) Stratigraphic column SC-11. It represents a part of the glacial drift located in the East Quarry locality. It also shows the site where B-1103-11 was extracted.

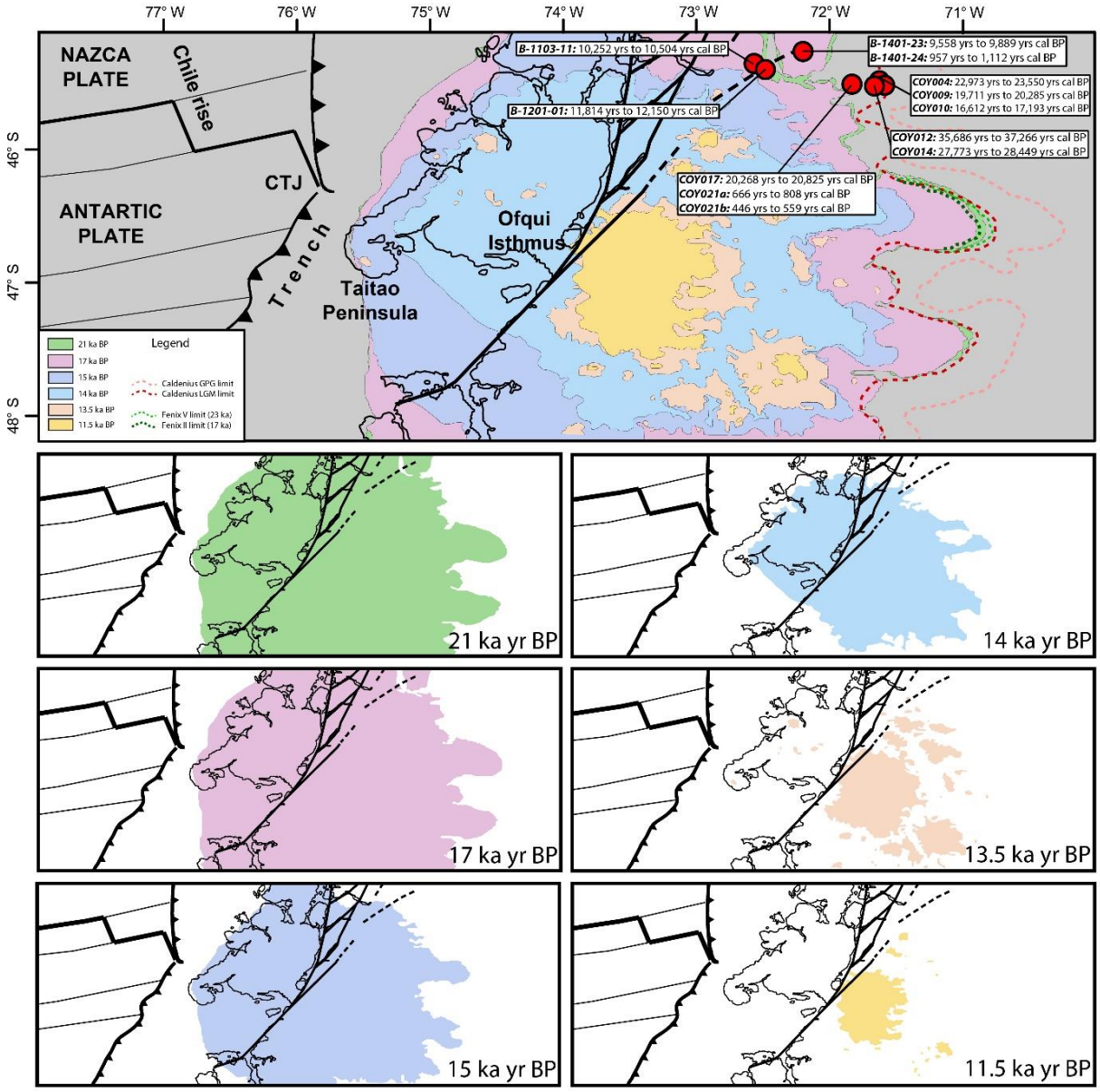

Figure B21. Time dependent model for the fluctuation of the Patagonian Icesheet between 45° and 48° S (Hubbard et al., 2005). It shows a LGM configuration compatible with the abalible records until that times. Average ice thickness ~1,130 m. Red dots correspond to our radiocarbon ages. Down-right: Time-slices of ice sheet surface elevation and isostatic adjustment at key snap-shots during deglaciation.

Publications and Abstracts resulting from this Dissertation

Publications

Villalobos, A., Easton, G., Maksymowicz, A., Ruiz, S., Lastras, G., De Pascale, G. P., & Agurto-Detzel, H. (2020). Active Faulting, Submarine Surface Rupture, and Seismic Migration Along the Liquiñe-Ofqui Fault System, Patagonian Andes. Journal of Geophysical Research: Solid Earth, 125(9). https://doi.org/10.1029/2020JB019946

Villalobos, A.; Arqueros, R.; Vargas-Easton, G.; De Pascale, G. (*to be submitted*). "Glacial Quaternary geology of the Patagonian Andes across the Coyhaique-Puerto Aysén transect constrains neotectonics and paleoseismological observations along the Liquiñe-Ofqui Fault Zone". *Quaternary Science Reviews.*

Conference abstracts

Villalobos-Claramunt, A., Vargas, G., Maksymowicz, A., & Lastras, G. (2015). "Evidencias paleosismológicas del origen cortical de la Crisis Sísmica del año 2007 en la región de Aysén". In *Congreso Geológico Chileno, No. 14*

Presentations in congresses and workshops

10th PATA Days 2020. International Congress of paleosismology, archeosismology and active tectonics that will take place in Hornitos, Antofagasta Region, Chile, between November 8th and 12th.

XV Chilean Geological Congress. It was held in Concepción city between November 13rd and 23rd, 2018. This activity was organized by the Geologisy College and the Chilean Geological Society.

8th PATA Days 2017. It corresponds to an international congress of paleosismology, archeosismology and active tectonics held in the Marlborough Province in New Zealand between November 13rd and 16th.

7th PATA DAYS 2016. It corresponds to an international congress of paleosismology, archeosismology and active tectonics held in Crestone town in Colorado State, United States of America, between May 29th and June 4th, 2016.

ATECSUD-2016. It corresponds to a symposium of South American tectonics held in the Santiago de Chile city between November 14th and 16th, 2016 in the Faculty of Physical Sciences and Mathematics (FCFM) of the University of Chile.

INQUA thematic school, Morphotectonic and Paleoseismology. It corresponded to a workshop in the University of Buenos Aires carried out by Dr. Carlos Costa between 16 and 19 August 2016.

XIV Chilean Geological Congress. It was held in La Serena city between October 4th and 8th, 2015. This activity was organized by the Geologists College and the Chilean Geological Society.

Deform-2015 thematic school, was an international (European) workshop held in Barcelonette town, France, in the Southern Alps, between February 7th and 13rd, 2015. Organized by PhDs in geosciences and experts in neotectonics and paleoseismology Yann Klinger and Jean-Mathieu. Sponsored by the Institut de Physique du Globe de Paris (IPGP), Laboratoire Géoazur (GEOAZUR), Center National d'etudes spatiales (CNES), among others.

Workshop Inventory of Hazardous Structures of South America, organized by the SARA Project (South American Risk Assessment), Santiago city, Chile, from November 17th to 20th.

Publications and Abstracts resulting from side –projects

Publications

Villalobos, *A.; Rodrigo, C.;* De Pascale, G. (*in prep.*). *"*Pockmarks in Chilean Patagonia: structural associations with Liquiñe Ofqui Fault System in Quitralco Fjord*". Geo-Marine letters.*

De Pascale, G.P., Froude, M., Penna, I. et al. (2021) Liquiñe-Ofqui's fast slipping intra-volcanic arc crustal faulting above the subducted Chile Ridge. Sci Rep 11, 7069. https://doi.org/10.1038/s41598-021-86413-w

Vargas-Easton, G.; González-Alfaro, J.; Villalobos, A.; Álvarez, G.; Escobar, M.; Sepúlveda, B; León, T. (*to be submitted*) "Coastal impact of the Mw: 8.3 Illapel megathrust and prehistoric tsunamis in central-northern Chile".

Leyton, F., Gonzalez-Alfaro, J., Villalobos, A., Ruiz, S. and Vargas, G. (*to be submitted*). "Seismic Hazard in Chile". *Seismological Research Letters*.

Fuentes, M.; Riquelme, S.; Hayes, G.; Medina, M.; Melgar, D.; Vargas, G., ... & Villalobos, A. (2017). “A study of the 2015 M w 8.3 Illapel earthquake and tsunami: Numerical and analytical approaches”. *In The Chile-2015 (Illapel) Earthquake and Tsunami (pp. 255-266). Birkhäuser, Cham.*

Fuentes, M.; Riquelme, S.; Hayes, G.; Medina, M.; Melgar, D.; Vargas, G., ... & Villalobos, A. (2016). “A Study of the 2015 M w 8.3 Illapel Earthquake and Tsunami: Numerical and Analytical Approaches”. *Pure Appl. Geophys. 173 (2016), 1847–1858*

Conference abstracts

Villalobos, A.; Santibáñez I.; del Río, I.; González, G. (2014). “Paleoseismological assessment of the Mititus-Naguayán fault”. In *Scientific Contributions, APRU X International Multi-Hazards Symposium 2014*, Santiago, Chile.

Participation in research projects

Co-Investigator in CIMAR-25 Project “*Submarine neotectonic and paleoseimic investigation of the Magallanes-Fagnano Fault System*”, in the Strait of Magellan, Magdalena Channel and Tierra del Fuego. October 2019.

Co-Investigator in CIMAR-24 Project “*Submarine neotectonic and paleoseimic investigation of the LOFZ, Chile Triple Junction and implications for Seismic Hazard*” in the Patagonian Andes fjordland (Aysén, Quitralco, Exploradores, Puyuhuapi fjords). October 2018.

Bibliography

Arqueros, C. R. (2004). Evolución glacial de la Hoya del Río Coihaique: una aproximación a partir del análisis geomorfológico y morfoestratigráfico. Memoria de título Universidad de Chile, Escuela de Post Grado, Escuela de Ingeniería y Ciencias: 114 pp.

Bangs, N. L., & Cande, S. C. (1997). Episodic development of a convergent margin inferred from structures and processes along the southern Chile margin. Tectonics, 16(3), 489–503. https://doi.org/10.1029/97TC00494

Barnes, P. M., & Pondard, N. (2010). Derivation of direct on-fault submarine paleoearthquake records from high-resolution seismic reflection profiles: Wairau fault, New Zealand. Geochemistry, Geophysics, Geosystems, 11, Q11013. https://doi.org/10.1029/2010GC003254

Breuer, S., Kilian, R., Schörner, D., Weinrebe, W., Behrmann, J., & Baeza, O. (2013). Glacial and tectonic control on fjord morphology and sediment deposition in the Magellan region (53°S), Chile. Marine Geology, 346, 31–46. https://doi.org/10.1016/j.margeo.2013.07.015

Bull, J. M., Barnes, P. M., Lamarche, G., Sanderson, D. J., Cowie, P. A., Taylor, S. K., & Dix, J. K. (2006). High-resolution record of displacement accumulation on an active normal fault: Implications for models of slip accumulation during repeated earthquakes. Journal of Structural Geology, 28, 1146–1166. https://doi.org/10.1016/j.jsg.2006.03.006

Cembrano, J., Hervé, F., & Lavenu, A. (1996). The Liquiñe Ofqui fault zone: A long-lived intra-arc fault system in southern Chile. Tectonophysics, 259, 55–66. https://doi.org/10.1016/0040-1951(95)00066-6

Cembrano, J., Lavenu, A., Reynolds, P., Arancibia, G., López, G., & Sanhueza, A. (2002). Late Cenozoic transpressional ductile deformation north of the Nazca–South America–Antarctica triple junction. Tectonophysics, 354(3-4), 289–314. https://doi.org/10.1016/S0040-1951(02)00388-8

Douglass, D. C., Singer, B. S., Kaplan, M. R., Mickelson, D. M., & Caffee, M. W. (2006). Cosmogenic nuclide surface exposure dating of boulders on last-glacial and late-glacial moraines, Lago Buenos Aires, Argentina: interpretive strategies and paleoclimate implications. Quaternary Geochronology, 1(1), 43-58. https://doi.org/10.1016/j.quageo.2006.06.001

Erickson, S. N., & Jarrard, R. D. (1998). Velocity-porosity relationships for water-saturated siliciclastic sediments. Journal of Geophysical Research, 103(B12), 30,38530,406. https://doi.org/10.1029/98JB02128

Fernández R. A., Anderson J. B., Wellner J. S., Hallet B. (2011). Timescale dependence of glacial erosion rates: A case study of Marinelli Glacier, Cordillera Darwin, southern Patagonia. Journal of Geophysical Research: Earth Surface, 116, (F1), n/a–n/a. http://dx.doi.org/10.1029/2010jf001685.

Glasser, N. F., Harrison, S., Schnabel, C., Fabel, D., & Jansson, K. N. (2012). Younger Dryas and early Holocene age glacier advances in Patagonia. Quaternary Science Reviews, 58, 7–17. https://doi.org/10.1016/j.quascirev.2012.10.011

Hein, A. S., Hulton, N. R., Dunai, T. J., Sugden, D. E., Kaplan, M. R., & Xu, S. (2010). The chronology of the Last Glacial Maximum and deglacial events in central Argentine Patagonia. Quaternary Science Reviews, 29, 1212–1227. https://doi.org/10.1016/j.quascirev.2010.01.020

Hubbard, A., Hein, A. S., Kaplan, M. R., Hulton, N. R., & Glasser, N. (2005). A modelling reconstruction of the last glacial maximum ice sheet and its deglaciation in the vicinity of the Northern Patagonian Icefield, South America. Geografiska Annaler: Series A, Physical Geography, 87(2), 375-391. https://doi.org/10.1111/j.0435-3676.2005.00264.x

Lambeck, K., Esat, T. M., & Potter, E. K. (2002). Links between climate and sea levels for the past three million years. Nature, 419(6903), 199–206. https://doi.org/10.1038/nature01089

Lambeck, K., Rouby, H., Purcell, A., Sun, Y., & Sambridge, M. (2014). Sea level and global ice volumes from the Last Glacial Maximum to the Holocene. Proceedings of the National Academy of Sciences, 111, 15,296–15,303. https://doi.org/10.1073/pnas.1411762111

Maksymowicz, A., Contreras-Reyes, E., Grevemeyer, I., & Flueh, E. R. (2012). Structure and geodynamics of the post-collision zone between the Nazca–Antarctic spreading center and South America. Earth and Planetary Science Letters, 345-348, 27–37. https://doi.org/10.1016/j.epsl.2012.06.023

Pondard, N., & Barnes, P. M. (2010). Structure and paleoearthquake records of active submarine faults, Cook Strait, New Zealand: Implications for fault interactions, stress loading, and seismic hazard. Journal of Geophysical Research, 115, B12320. https://doi.org/10.1029/2010JB007781

Salamanca, M. A., & Jara, B. (2003). Distribución y acumulación de plomo (Pb y 210Pb) en sedimentos de los fiordos de la XI región. Revista Ciencia y Tecnología del Mar, 26, 61–71.

Smedley, R. K., Glasser, N. F., & Duller, G. A. T. (2016). Luminescence dating of glacial advances at Lago Buenos Aires (~ 46 S), Patagonia. Quaternary Science Reviews, 134, 59-73. https://doi.org/10.1016/j.quascirev.2015.12.010

Stoker, M. S., & Holmes, R. (1991). Submarine end-moraines as indicators of Pleistocene ice-limits off northwest Britain. Journal of the Geological Society, 148(3), 431–434. https://doi.org/10.1144/gsjgs.148.3.0431

Stoker, M. S., Pheasant, J. B., & Josenhans, H. (1997). Seismic methods and interpretation. T.A. Davies T. Bell A.K. Cooper H. Josenhans L. Polyak A. Solheim M.S. Stoker & J.A. Stravers In Glaciated continental margins; An Atlas of Acoustic Images , First, (9–26). London, U.K.: Chapman & Hall. https://doi.org/10.1007/978-94-011-5820-6_2

Sugden, D. E., & John, B. S. (1976). Glaciers and landscape: a geomorphological approach. E. Arnold.

Sugden, D. E., Bentley, M. J., Fogwill, C. J., Hulton, N. R. J., McCulloch, R. D., & Purves, R. S. (2005). Late-glacial glacier events in southernmost South America: A blend of “northern” and “southern” hemispheric climatic signals? Geografiska Annaler: Series A. Physical Geography, 87, 273–288. https://doi.org/10.1111/j.0435-3676.2005.00259.x

St-Onge, G., Chapron, E., Mulsow, S., Salas, M., Viel, M., Debret, M., Foucher, A., Mulder, T., Winiarski, T., Desmet, M., Costa, P. J. M., Ghaleb, B., Jaouen, A., & Locat, J. (2012). Comparison of earthquake-triggered turbidites from the Saguenay (Eastern Canada) and Reloncavi (Chilean margin) Fjords: Implications for paleoseismicity and sedimentology. Sedimentary Geology, 243-244, 89–107. https://doi.org/10.1016/j.sedgeo.2011.11.003

Syvitski, J. P. M., Burrell, D. C., & Skei, J. M. (1987). . J. P. M. Syvitski D. C. Burrell & J. M. Skei In Fjords; Processes and products, First(X). –215). , . New York: Springer-Verlag. https://doi.org/10.1007/978-1-4612-4632-9

Thomson, S. N. (2002). Late Cenozoic geomorphic and tectonic evolution of the Patagonian Andes Late Cenozoic geomorphic and tectonic evolution of the Patagonian Andes between latitudes 42°S and 46°S: An appraisal based on fission-track results from the transpressional intra-arc Liquiñe-Ofqui fault zone. Geological Society of America Bulletin, 114, 1159–1173. https://doi.org/10.1130/0016-7606(2002)114<1159

Thornburg, T. M., & Kulm, L. D. (1987). Sedimentation in the Chile Trench: Depositional morphologies, lithofacies, and stratigraphy. Geological Society of America Bulletin, 98(1), 33–52. https://doi.org/10.1130/0016-7606(1987)98<33:SITCTD>2.0.CO;2

Van Daele, M., Versteeg, W., Pino, M., Urrutia, R., & De Batist, M. (2013). Widespread deformation of basin-plain sediments in Aysén Fjord (Chile) due to impact by earthquake-triggered, onshore-generated mass movements. Marine Geology, 337, 67–79. https://doi.org/10.1016/j.margeo.2013.01.006

Vargas, G., Rebolledo, S., Sepúlveda, S., Lahsen, A., Thiele, R., Townley, B., Padilla, C., Rauld, R., Herrera, M. J., & Lara, M. (2013). Submarine earthquake rupture, active faulting and volcanism along the major Liquiñe-Ofqui Fault Zone and implications for seismic hazard assessment in the Patagonian Andes. Andean Geology, 40, 141–171. https://doi.org/10.5027/andgeoV40n1-a07

Veeken, P. C. (2006). P. C. Veeken Seismic stratigraphy, basin analysis and reservoir characterisation, Handbook of Geophysical Exploration: Seismic Exploration, (Vol. 37, First, (X–522). Amsterdam, The Netherlands: Elsevier.

Zhou, H. W. (2014). Practical seismic data analysis, First, Cambridge, U.K.: Cambridge University Press. https://doi.org/10.1017/CBO9781139027090